Differential cross-section measurements for four-lepton production and implications for new physics

Dan Ping (Joanna) Huang

A dissertation submitted to University College London
for the degree of Doctor of Philosophy

Abstract

This thesis describes the analysis design and results of the ATLAS four-lepton measurement, using 139 fb^{-1} of data collected in 13 TeV proton-proton collisions at the Large Hadron Collider. The measurement is designed for maximal model-independence and inclusivity. Defined solely in terms of the final state particles, any process leading to the creation of four or more leptons is considered to be a part of the signal. The results are presented in the form of inclusive and fiducial differential cross-sections, and are corrected for detector effects via an iterative Bayesian technique. The measurement is compared to state-of-the-art Standard Model predictions, and the two are found to be consistent. Secondly, two re-interpretation studies are presented where existing precision fiducial measurements, including the aforementioned four-lepton measurement, are used to set constraints on two beyond the Standard Model theories. The first is a generic model of vector-like quarks, and the second is a model with a gauged and spontaneously broken $B - L$ symmetry. These studies are conducted using the CONTUR re-interpretation toolkit. The derived limits are competitive with existing ATLAS limits, and exclude previously unexplored regions of parameter space.

Impact Statement

The research presented in this work plays a part in the continuous efforts of the particle physics community in refining the Standard Model, as well as searching for what lies beyond it. Using new LHC data collected by the ATLAS detector during Run 2, a measurement was made for events with a specific final state. Steps were taken to ensure the data are well preserved such that they may be re-used by the theoretical community. Two studies were performed to demonstrate the power of such re-use. The work carried out in this thesis is an advocate for re-interpretation. In maximizing the impact of the published data for years to come like so, researchers will be able to push the frontiers of particle physics even further. Outside of the academic world, the analysis techniques and experimental technologies developed have wide applications that improve and facilitate humans' quality of life. Particle accelerators are now used by most major medical centres for treatment and diagnosis, and the use of batch systems to handle unprecedented amounts of data is now adopted by many government and private industries.

Declaration

I confirm that the work presented in this thesis is my own. Where information has been derived from other sources, I confirm that this has been indicated in the thesis.

Dan Ping (Joanna) Huang

Acknowledgements

There are a large number of people who have provided me with tremendous support (either in my research or my personal life) during my time at UCL. First, I would like to thank my supervisor, Jon Butterworth, for offering me such a wonderful opportunity, and for guiding me along the research of this thesis. I am genuinely grateful for your constant encouragement, feedback, and support. None of this would have been possible without you. I extend my thanks to MCnet and the European Union's Horizon 2020 research and innovation programme under the Marie Sklodowska-Curie grant for funding this work.

A big thank you goes to the talented members of the ATLAS four-lepton analysis team for your support and patience with my work. Special thanks goes to to Zara Grout, Max Goblirsch, and Emily Nurse, who were the best mentors I could ask while working on the analysis. I am very thankful to Andy Buckley, Louie Corpe, and Puwen Sun. It was an absolute privilege working along your sides for the vector-like quarks project. Another thank you goes to the brilliant minds of the many CONTUR developers. In particular, thank you to David Yallup for your invaluable mentor-ship and friendship.

To the many UCL HEP students who have become my dear friends, thank you. Life in the office was so much more lively (and possibly less productive) because of you lot. I feel so lucky and inspired to be surrounded by so many amazing people. Thank for you the Friday post-work pub sessions, for the ridiculous office banter, and for the non-stop flow of memes throughout the pandemic to liven the mood. I am very grateful to Seb for the countless coffees and hugs. In retrospect, I wished I used the "one favour" coupon to ask you to write this thesis. Thank you to Caishan, whose smile never fails to be a ray of sunshine in my day, and who I can count on to bring my passport to the airport.

To my incredible group of friends that I met through the Imperial Outdoors club, thank you for the countless happy memories and becoming my second family. Thank you for roping me into climbing and taking me on my best, and scariest, adventures. Aina, your support and wisdom has seen me through hurdle after hurdle, and you've

taught me the versatility of cooking with onions, thank you. Dimitris, thank you for cheering me on (for work, climbs, and life), and for showing me how stylish an oversized fanny pack can be. Micol, thank you for always being so incredibly kind and caring to me, and for teaching me what good olive oil should taste like. Tom, thank you for having my back no matter what. I look forward to when we visit Chick'n.

Adélie, my deepest thank you for being so endlessly kind, and for being my rock throughout the last few years. You're worth more than diamonds more than gold.

Rasa, you've been with me through every obstacle. From the bottom of my heart, thank you for being more dedicated to our friendship than Drake is to his facial hair.

A profound thank you to Arthur for always giving me strength when I needed it, and for having a black hole as a stomach so I can cook endlessly to my heart's content.

My two little nuggets of joy, Aaron and Aiden, thank you for existing. If you two read this in the future, go and give your big sister a hug.

Finally, a most sincere thank you to my mom and dad, for all the hardship you have endured so that I can be where I am today. Thank you for always for supporting me through and through.

Contents

1. Introduction **1**

2. The Standard Model **3**

2.1. Particle content . . . 3
2.2. Gauge fields . . . 4
  2.2.1. Quantum electrodynamics . . . 4
  2.2.2. Quantum chromodynamics . . . 7
  2.2.3. Weak interactions and electroweak unification . . . 9
2.3. Spontaneous symmetry breaking and the Higgs mechanism . . . 11
  2.3.1. Spontaneous symmetry breaking . . . 11
  2.3.2. The Higgs mechanism . . . 14
  2.3.3. The Standard Model Higgs . . . 16
  2.3.4. Yukawa sector: fermion masses . . . 17

3. The Large Hadron Collider and the ATLAS experiment **21**

3.1. The Large Hadron Collider . . . 21
3.2. The ATLAS detector . . . 25
  3.2.1. The Inner Detectors . . . 26
  3.2.2. Calorimetry . . . 29
  3.2.3. The Muon Spectrometer . . . 31
  3.2.4. Magnet system . . . 33
  3.2.5. Trigger system . . . 34
3.3. Object reconstruction . . . 36
  3.3.1. Tracks and vertices . . . 36
  3.3.2. Clustering algorithms . . . 37
  3.3.3. Electrons . . . 40
  3.3.4. Muons . . . 42

4. $m_{4\ell}$: A measurement designed for re-interpretation **45**

4.1. Motivation for the $m_{4\ell}$ measurement . . . 45

4.2. Fiducial region 48
4.3. Measured observables 49
4.4. Event reconstruction and selection 51
4.5. Predictions from Monte Carlo Event Generators 54
    4.5.1. Overview of Monte Carlo Event Generators 54
    4.5.2. Monte Carlo samples 57
    4.5.3. $q\bar{q} \to 4\ell$ 57
    4.5.4. $gg \to 4\ell$ 57
    4.5.5. On-shell Higgs 58
    4.5.6. VVV and $t\bar{t}V(V)$ 58
    4.5.7. Corrections 59
4.6. Background estimation 59
    4.6.1. Defining leptons 59
    4.6.2. Fake Factor method 60
    4.6.3. Fake background uncertainties 61
4.7. Detector-level results 61
4.8. Correcting for detector effects 62
    4.8.1. Unfolding methodology 63
    4.8.2. Unfolding inputs 65
    4.8.3. Binning optimization 70
    4.8.4. Pre-unfolding weights 72
    4.8.5. Unfolding iterations optimization 73
    4.8.6. Closure tests 74
    4.8.7. Injection studies 75
4.9. Measurement uncertainties 81
    4.9.1. Statistical uncertainties 81
    4.9.2. Systematic uncertainties 84
4.10. Results 85
4.11. Interpretations 89
    4.11.1. $Z \to 4\ell$ branching fraction 103
    4.11.2. EFT couplings 104

5. Re-interpreting results from LHC measurements 113
5.1. CONTUR and related software tools 114
5.2. Sensitivity of LHC measurements to Vector-like Quarks 117
    5.2.1. Phenomenology of VLQs 117
    5.2.2. Comparison to ATLAS searches 122
    5.2.3. All quark generations 124

5.2.4. Role of the ATLAS $m_{4\ell}$ measurement 129
5.3. Sensitivity of LHC measurements to a gauged $B - L$ model 134
5.3.1. About the model 134
5.3.2. ATLAS limit from the $m_{4\ell}$ analysis 136
5.3.3. Updated CONTUR limit with new $m_{4\ell}$ measurement 137

6. Conclusion **145**

A. Unfolding inputs and studies **147**

Bibliography **187**

List of figures **205**

List of tables **223**

Chapter 1.

Introduction

What is the universe made of? This question has fascinated both philosophers and scientist alike for the past millennium. The best theory there is to date that answers this question is the Standard Model of Particle Physics, often abbreviated as the SM. All matter in the universe can be broken up into fundamental building blocks, the fundamental particles, which are governed by fundamental forces. The SM is the most accurate description that exists of how these particles and forces interact with one another. The construction of increasingly powerful particle colliders has led to the observation of a plethora of new particles. The SM has been able to bring to order the observed particles, as well as accurately predict the existence of postulated particles. In 2012, two experiments (ATLAS and CMS) at the Large Hadron Collider (LHC) announced the discovery of a new particle exhibiting the predicted properties of the Higgs boson, thus completing the SM. Despite its immense success, however, the SM is not without imperfections. For example, the reasoning behind dark matter, dark energy, gravity, and the matter-antimatter asymmetry (i.e. the excess of baryons over anti-baryons) are not incorporated within the model. Rather, the explanations for these phenomena are postulated by theorists as Beyond the Standard Model (BSM) theories.

Traditionally, the hunt for BSM physics at the LHC takes in the form of dedicated direct searches. A less labour-intensive, complementary probe for new physics involves exploiting the precision measurements made at the LHC of predicted SM processes. The work presented in this thesis focuses on the design and results of one such ATLAS precision measurement, and how it is used alongside other published LHC measurements to test new physics theories.

This thesis is structured as follows. Beginning with Chapter 2, a brief review of the phenomenology of the Standard Model is given. Chapter 3 explains the practical experimental aspects of the data used, including the LHC, the structure of the ATLAS detector, and how collision events are reconstructed. Chapter 4 is the main focus of this thesis: the ATLAS inclusive four-lepton analysis. The analysis design is described in detail, with particular attention paid to the unfolding procedure which corrects the data for detector effects. The results using the complete 139 fb^{-1} Run II data-set are presented along with several interpretation examples. Finally, Chapter 5 introduces the concept of reinterpretation and presents the constraints that LHC measurements have on two BSM scenarios.

Author contributions

The analysis presented in of Chapter 4 is performed as part of the ATLAS Collaboration with contributions from multiple international institutes. The results presented relies on the work of many engineers, technicians, experimentalists, and theorists alike. The data analysis itself is a sub-group effort, and would not have been possible without the hard work from every team member. The specific contributions from the author to the analysis are as follows:

- Validations studies of the Monte Carlo samples
- Binning definition of all observables
- Creation of unfolding inputs
- Monte Carlo closure tests
- Signal injection studies
- Unfolding the data and presentation of final results.

The author did not directly work on the evaluation of the background estimation, the evaluation of the uncertainties, or the in-house interpretations.

The VLQ re-interpretation study of Chapter 5 is a collaborative effort between UCL and the University of Glasgow with team members Andy Buckley, Jon Butterworth, Louie Corpe, and Puwen Sun. The results of the study is published in Reference [1]. Additionally presented are some updated CONTUR scans performed by the author, and an investigation the role of the new ATLAS four-lepton analysis. The CONTUR study on the gauged $B - L$ model of Chapter 5 was conducted by the author, following guidance from Reference [2] regarding what regions of parameter space to sample. The results are compared to the ATLAS limits, which the author did not work on.

The ATLAS author qualification task conducted by the author is not included explicitly in this thesis, however it is documented in Reference [3].

Chapter 2.

The Standard Model

The Standard Model (SM) of particle physics is a rather simplistic name for such a powerful theory. It is the closest theory that exists to a complete description of the universe at the most fundamental level, and is arguably the pinnacle of science. In this chapter, the aim is to provide a a brief overview of the SM, relying on the derivations of Reference [4]. For a more comprehensive description, one may refer to the above reference.

2.1. Particle content

The Standard Model is often depicted in compact diagrams similar to that of Mendeleev's Periodic Table of Elements. One such diagram is shown in Figure 2.1. In a nutshell, the particles put forward by the SM are truly elementary particles. Unlike the elements in the Periodic Table which can be further broken down, these elementary particles are (to our knowledge) point-like and contain no internal structure. Each particle has a unique set of properties - quantum numbers - that define it, and split into one of two categories: fermions and bosons.

Fermions are half-integer spin particles, and are usually thought of as matter particles. Each fermion has an anti-particle, with an identical mass but opposite electric charge. They are further classified as either leptons or quarks. Leptons are either negatively charged (-1), or neutral. The latter are referred to as neutrinos, which the SM predicts to be massless. Quarks have an electric charge of either $\frac{2}{3}$ or $-\frac{1}{3}$, and carry an additional colour charge of either red, blue, or green. The arrangement of fermions in the SM is generational. The first generation is found in everyday matter. For example the proton and neutron are made up of up and down quarks, and the electron which orbit nuclei. The second and third generation leptons have higher masses and are able to decay to lighter particles, but they otherwise behave identically.

Bosons are integer spin particles that mediate the interactions within the SM. Electromagnetism is arguably the most well-known forces, and is carried by the massless and chargeless photon γ. Electric charge is conserved during photon-mediated particle interactions, and the photon has infinite range. Eight gluons mediate the strong force of quantum chromodynamics. They are also massless and electromagnetically neutral, but carry a colour charge. Only quarks are able to interact with gluons, and unlike photons, gluons interact with each other as well as with quarks. This process is known as gluon self-interaction. The self-interaction leads properties characteristic of the strong interaction: namely asymptotic freedom and confinement. The weak force arises from the exchange of three massive force carriers: two charged $W^{\pm}$ bosons and a neutral Z boson. As its name suggests, the force is relatively weak compared to the EM and strong forces, and is only carried over short ranges. The photon, $W^{\pm}$ bosons, and Z boson are gauge bosons of spin 1. Completing the SM is the spin 0 scalar Higgs boson. The Higgs is electrically neutral, colourless, and massive. It plays a key role in the SM by providing mass to gauge bosons and fermions through electroweak symmetry breaking.

2.2. Gauge fields

The Standard Model is constructed upon the language of quantum field theory, where every elementary particle is described as excitations of a quantum field. It describes the strong and electroweak interaction from the $\mathrm{SU}(3)_C \otimes \mathrm{SU}(2)_L \otimes \mathrm{U}(1)_Y$ symmetry group, each with a conserved quantity (following Noether's theorem [6]) as indicated by the indices. All the interactions of the SM can be derived on the basis that the system is invariant under local gauge transformations. Imposing local gauge invariance under $\mathrm{SU}(3)$ and colour charge conservation returns Quantum Chromodynamics (QCD).

2.2.1. Quantum electrodynamics

To proceed toward a field theory for electrons and quantization of the Dirac field we wish to find a scalar Lagrangian that yields the Dirac equation. This turns out to be the Dirac Lagrangian, written as

$$\mathcal{L} = i\hbar c\bar{\psi}\gamma^{\mu}\partial_{\mu}\psi - mc^2\bar{\psi}\psi \tag{2.1}$$

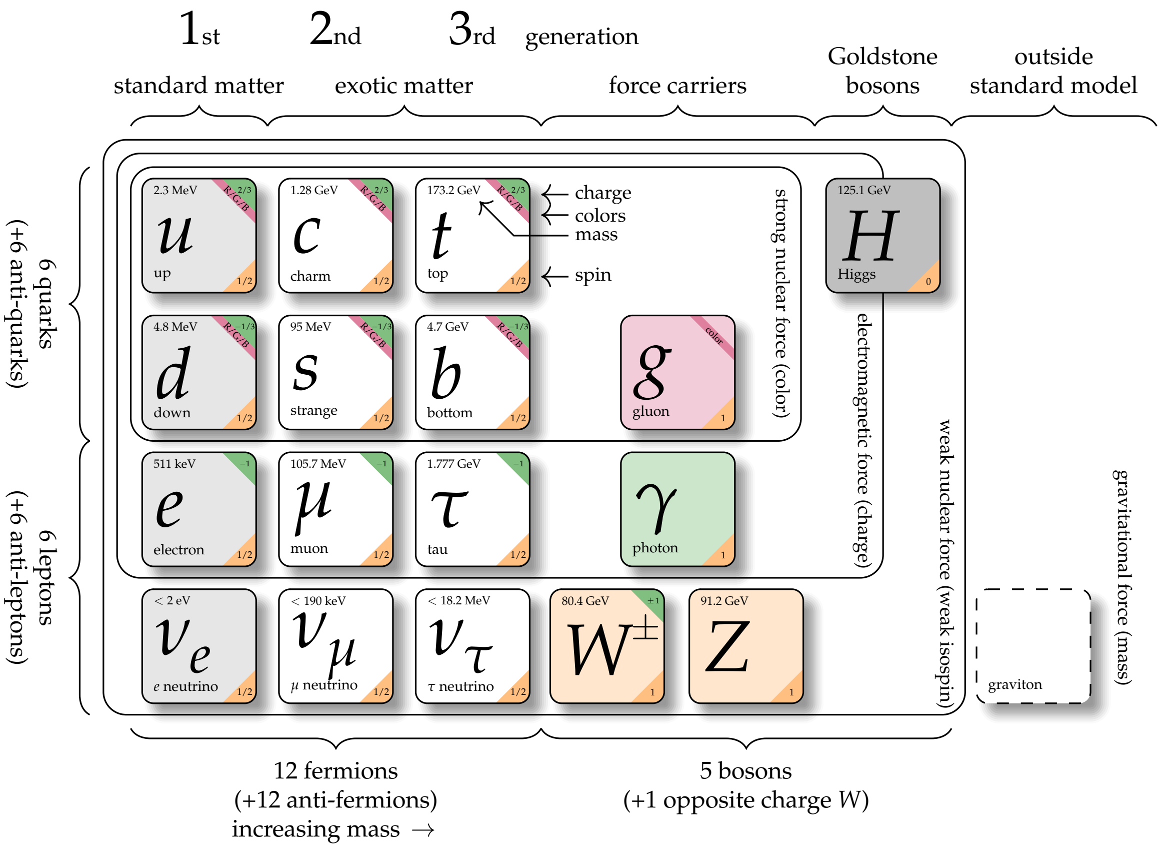
1st
2nd
3rd
generation
standard matter
exotic matter
force carriers
Goldstone bosons
outside standard model
6 quarks (+6 anti-quarks)
6 leptons (+6 anti-leptons)
2.3 MeV
2/3
R/G/B
u
up
1/2
1.28 GeV
c
charm
173.2 GeV
t
top
charge
colors
mass
spin
strong nuclear force (color)
125.1 GeV
H
Higgs
0
4.8 MeV
−1/3
d
down
95 MeV
s
strange
4.7 GeV
b
bottom
color
g
gluon
1
electromagnetic force (charge)
511 keV
−1
e
electron
105.7 MeV
μ
muon
1.777 GeV
τ
tau
γ
photon
weak nuclear force (weak isospin)
< 2 eV
ν_e
e neutrino
< 190 keV
ν_μ
μ neutrino
< 18.2 MeV
ν_τ
τ neutrino
80.4 GeV
±1
$W^\pm$
91.2 GeV
Z
graviton
gravitational force (mass)
12 fermions (+12 anti-fermions) increasing mass →
5 bosons (+1 opposite charge W)

Figure 2.1.: The particle content in the Standard Model. Included in the diagram is the graviton, however this is currently outside the scopes of the SM. This figure is from Ref. [5].

is invariant under a global gauge transformation $\psi \rightarrow e^{i\theta}\psi$, but not under a local gauge transformation where θ is a function of x^{μ}. Next, an additional term is be added to equation 2.1 to introduce a new gauge field A_{μ}.

$$\mathcal{L} = i\hbar c\bar{\psi}\gamma^{\mu}\partial_{\mu}\psi - mc^{2}\bar{\psi}\psi - q\bar{\psi}\gamma^{\mu}\psi A_{\mu} \tag{2.2}$$

This gauge field transforms under local gauge transformations in a way that renders equation 2.2 invariant. This is not yet complete, since the new vector field must include it's own "free" term. Since it is a vector field, the Proca Lagrangian is examined

$$\mathcal{L} = \frac{-1}{16\pi}F^{\mu\nu}F_{\mu\nu} + \frac{1}{8\pi}\left(\frac{m_{A}c}{\hbar}\right)^{2}A^{\nu}A_{\nu}. \tag{2.3}$$

Here it can be seen that the gauge field must be massless, because $A^{\nu}A_{\nu}$ is not invariant under local gauge transformation $A_{\mu} \rightarrow A_{\mu} + \partial\lambda$. Also introduced in equation 2.3 is the shorthand

$$F^{\mu\nu} \equiv \partial^{\mu}A^{\nu} - \partial^{\nu}A^{\mu}. \tag{2.4}$$

To summarize, in requiring local gauge invariance from the Dirac Lagrangian, a new vector field with no mass is introduced. In imposing local gauge invariance, the Lagrangian becomes

$$\mathcal{L} = i\hbar c\bar{\psi}\gamma^{\mu}\partial_{\mu}\psi - mc^{2}\bar{\psi}\psi + \frac{-1}{16\pi}F^{\mu\nu}F_{\mu\nu} - q\bar{\psi}\gamma^{\mu}\psi A_{\mu}. \tag{2.5}$$

The transformation rule of the new vector field corresponds to that of the field of the massless photon, and the Maxwell equations may be derived from this Lagrangian.

Going back to the free Dirac Lagrangian in equation 2.1, what if an alternate definition of the derivative, namely

$$\mathcal{D}_{\mu} \equiv \partial_{\mu} + i\frac{q}{\hbar c}A_{\mu} \tag{2.6}$$

were to replace ∂_{μ}? This is a practical definition that absorbs the gauge-fixing interaction term into the derivative itself. Suppose as well that $\mathcal{D}_{\mu}$, hereforth referred to as the covariant derivative, transforms like the field ψ itself:

$$\mathcal{D}_{\mu}\psi \rightarrow e^{i\theta(x_{\mu})}\mathcal{D}_{\mu}\psi. \tag{2.7}$$

It turns out that in doing so, the transformation of of A_μ,

$$A_\mu \to A_\mu - \frac{\hbar c}{q}\partial_\mu \theta \tag{2.8}$$

renders the Lagrangian locally invariant. A_μ brings along its own free Lagrangian, however, and the field must be massless to preserve local gauge invariance. All together this give the final Lagragian stated in equation 2.5, describing the interactions of fermions with charge q (Dirac fields) with photons (Maxwell fields), more commonly known as the Lagrangian for quantum electrodynamics.

2.2.2. Quantum chromodynamics

The coloured quark model dictates that each flavour (six in total) comes in three variations. Arbitrarily, a conserved colour charge is used to differentiate between these variations: for each quark flavour, there exists a red, blue, and green version. The quark field in its colour triplet is written in vector notation as

$$\psi_q \equiv \begin{pmatrix} \psi_q^r \\ \psi_q^b \\ \psi_q^g \end{pmatrix}, \quad \bar{\psi}_q = (\bar{\psi}_q^r, \bar{\psi}_q^b, \bar{\psi}_q^g) \tag{2.9}$$

such that the Lagrangian resembles the free Dirac Lagragian,

$$\mathcal{L} = i\bar{\psi}_q \gamma^\mu \partial_\mu \psi_q - m^2 \bar{\psi}_q \psi_q. \tag{2.10}$$

In order to maintain local gauge invariance under SU(3) gauge transformations of the form

$$\psi_q \to S\psi_q = e^{i\lambda_a \theta^a} \psi_q, \tag{2.11}$$

the Lagrangian must be modified. As with the case in QED, a covariant derivative is introduced to replace the ordinary derivative:

$$\mathcal{D}_\mu \equiv \partial_\mu + i g_s \lambda_a G_\mu^a \tag{2.12}$$

where λ_a with $a = 1, 2, ..., 8$ are the 3×3 Gell-Mann matrices, whose role for SU(3) is analogous to the role Pauli spin matrices play for SU(2). For the new gauge fields G^a, it will suffice to know the approximate transformation rule. For that the infinitesimal case is considered, where only first-order terms are kept. The transformation rule obtained is

$$G^a_\mu \to G^a_\mu - \frac{1}{g_s}\partial_\mu\theta_a - f_{ijk}\theta^j G^k_\mu \tag{2.13}$$

where f_{ijk} are the structure constants of SU(3).

The modified Lagrangian (with the covariant derivative replacing the derivative) is locally invariant under SU(3) transformations, and consequently eight new gauge fields are introduced (one for each λ_a)[1]. Unsurprisingly, these correspond precisely to the eight gluons. Lastly, the Proca-Lagrangian for the gluon fields must be added in to introduce a mass term. Here it is useful to define

$$G^{\mu\nu}_a \equiv \partial^\mu G^\nu_a - \partial^\nu G^\mu_a - g_s f_{ijk} G^\mu_j G^\nu_k, \tag{2.14}$$

which looks quite similar to the field strength tensor of QED, except for the vector product of the third term. This last term is a characteristic of quantum field theories based on non-Abelian groups; the gauge bosons carry charge and therefore may interact with one another. In the case of QCD the gluons are bicoloured; carrying both a colour and an anticolour. The final Lagrangian describing quantum chromodynamics is then

$$\mathcal{L} = [i\bar{\psi}\gamma^\mu\partial_\mu\psi - m\bar{\psi}\psi] - \frac{1}{4}G^{\mu\nu}_a G^a_{\mu\nu} - g_s\bar{\psi}\gamma^\mu\lambda_a\psi G^a_\mu. \tag{2.15}$$

Two important features of QCD are asymptotic freedom and confinement. Asymptotic freedom, describes the behaviour of quarks at high energies or, equivalently, at small distances. In this regime, quarks behave as if there were quasi-free particles since the coupling constant α_S becomes increasingly small. However, at small energies, or large distances, confinement occurs. The strong coupling constant grows continually thereby increasing the attraction among the quarks. Quarks can consequently not exist as coloured free particles but are confined into bound colourless states called hadrons.

---

[1] Note that that 3×3 Hermitian matrices with trace equal to zero is eight dimensional.

2.2.3. Weak interactions and electroweak unification

The global gauge transformation $\psi \to e^{i\theta}\psi$ where θ is any real number can be thought of as a matrix multiplication of the form

$$\psi \to U\psi \tag{2.16}$$

where $U^{\dagger}U = 1$ and in this case $U = e^{i\theta}$. The group of all possible unitary 1×1 matrices is called U(1). The same logic was applied in 1954 by Yang and Mills to the SU(2) group.

Experimental observations have shown that weak charged currents couple only to left-handed fermions and right-handed anti-fermions [7]. In order to extract the left- and right-handed components, it is useful to define the projection operators P_L and P_R, which act on fermion fields (expressed by Dirac spinors) in the following manner:

$$\psi_L = P_L\psi = \frac{1}{2}(1-\gamma_5)\psi, \quad \psi_R = P_R\psi = \frac{1}{2}(1+\gamma_5)\psi \tag{2.17}$$

The left-handed and right-handed fermion fields follow different definitions under SU(2). The former are arranged as doublets with isospin $I = \frac{1}{2}$, while the latter are singlets with isospin $I = 0$. The singlets are consequently unaffected by SU(2) local gauge transformation.

$$\ell_L = \begin{pmatrix} \nu_e \\ e \end{pmatrix}_L, \begin{pmatrix} \nu_\mu \\ \mu \end{pmatrix}_L, \begin{pmatrix} \nu_\tau \\ \tau \end{pmatrix}_L \qquad q_L = \begin{pmatrix} u \\ d' \end{pmatrix}_L, \begin{pmatrix} c \\ s' \end{pmatrix}_L, \begin{pmatrix} t \\ b' \end{pmatrix}_L \tag{2.18}$$

$$\ell_R = e_R, \quad \mu_R, \quad \tau_R \qquad q_R = u_R, \quad d_R, \quad c_R, \quad s_R, \quad t_R, \quad b_R \tag{2.19}$$

Notice that in equation 2.18 the the down type quark doublet partners are weak eigenstates that can transform into one another through interactions with W bosons [8]. The weak eigenstates d', s' and b' are related to the mass eigenstates d, s and b through a unitary 3×3 matrix - the Cabbibo-Kobayashi-Maskawa (CKM) matrix.

$$\begin{pmatrix} d' \\ s' \\ b' \end{pmatrix} = \begin{pmatrix} V_{ud} & V_{us} & V_{ub} \\ V_{cd} & V_{cs} & V_{cb} \\ V_{td} & V_{ts} & V_{tb} \end{pmatrix} \begin{pmatrix} d \\ s \\ b \end{pmatrix} \tag{2.20}$$

Similar to the QED and QCD case, a covariant derivative $\mathcal{D}_\mu$ is defined for the theory to retain its invariance under local gauge transformations:

$$\mathcal{D}_\mu \equiv \partial_\mu + ig_W \frac{\sigma^a}{2} W^a_\mu + ig' \frac{Y}{2} B_\mu \tag{2.21}$$

where g and g' represent the weak coupling constants, σ_a with $a = 1, 2, 3$ are the pauli matrices (i.e. the generators of SU(2)), and Y is the weak hypercharge (generator of U(1)). Y is the conserved quantity from the $\mathrm{U}(1)_Y$ symmetry and it is related to the electric charge Q by

$$Q = T_3 + \frac{Y}{2} \tag{2.22}$$

where T_3 is the third component of weak isospin. The Pauli matrices satisfy the condition

$$[\sigma_a, \sigma_b] = 2i\epsilon_{abc}\sigma^c. \tag{2.23}$$

In defining the covariant derivative, four new massless gauge fields $W^1_\mu, W^2_\mu, W^3_\mu$ and B_μ are introduced. The former corresponds to the three $\mathrm{SU}(2)_L$ generators, while the latter is associated with $\mathrm{U}(1)_Y$. The mixing of these four fields gives the electroweak bosons W^+, W^-, Z and γ. The charged bosons W^+ and W^- are linear combinations of W^1_μ and W^2_μ:

$$W^+_\mu = \frac{1}{\sqrt{2}}(W^1_\mu - iW^2_\mu) \tag{2.24}$$

$$W^-_\mu = \frac{1}{\sqrt{2}}(W^1_\mu + iW^2_\mu). \tag{2.25}$$

The remaining fields W^3_μ and B_μ combine to form the Z boson and the photon as follows:

$$A_\mu = B_\mu \cos\theta_w + W^3_\mu \sin\theta_w \tag{2.26}$$

$$Z_\mu = -B_\mu \sin\theta_w + W^3_\mu \cos\theta_w \tag{2.27}$$

where θ_w denotes the Weinberg angle.

The field strength tensors for $\mathrm{SU}(2)_L$ and $\mathrm{U}(1)_Y$ are defined as:

$$W^a_{\mu\nu} = \partial_\mu W^a_\nu - \partial_\nu W^a_\mu - g\epsilon^{abc} W^b_\mu W^a_\nu \tag{2.28}$$

$$B_{\mu\nu} = \partial_\mu B_\nu - \partial_\nu B_\mu. \tag{2.29}$$

The first line of equation 2.28 is reminiscent of QCD, where last term gives rise to self-couplings of the electroweak gauge bosons.

The electroweak interaction, invariant under $\mathrm{SU}(2)_L \times \mathrm{U}(1)_Y$ gauge transformations, has the following Lagrangian:

$$\mathcal{L} = \sum_j i\bar{\psi}_j \gamma^\mu \mathcal{D}_\mu \psi_j - \frac{1}{4} B_{\mu\nu} B^{\mu\nu} - \frac{1}{4} W^a_{\mu\nu} W^{\mu\nu}_a \tag{2.30}$$

where j iterates over all the fermion fields. The requirement of local gauge invariant led to the construction of this Lagrangian that unifies the electromagnetic and weak interactions, from which the the physical interactions between fermions and the electroweak gauge bosons are correctly reproduced. The electroweak Lagrangian above, however, does not allow for gauge field mass terms. While the photon (and the gluon) is indeed massless, the fermions, W, and Z bosons have been experimentally shown to be massive [9]. So, the question arises as to whether there is a way to address this issue in gauge theory such that massive gauge fields can be accommodated. The answer is yes, and it lies in the subtle procedure of exploiting spontaneous symmetry-breaking and the Higgs mechanism.

2.3. Spontaneous symmetry breaking and the Higgs mechanism

2.3.1. Spontaneous symmetry breaking

Broken discrete symmetry

The Lagrangian written in the classic form of a kinetic term minus a potential term, is:

$$\mathcal{L} = T - V \tag{2.31}$$

$$\mathcal{L} = \frac{1}{2}(\partial_\mu \phi)(\partial^\mu \phi) - (\frac{1}{2}\mu^2\phi^2 + \frac{1}{4}\lambda\phi^4). \tag{2.32}$$

For the potential to have a finite minimum, λ must be positive. The minimum of the potential $V(\phi)$ occurs at

$$\phi = \pm\sqrt{\frac{-\mu^2}{\lambda}}. \tag{2.33}$$

This potential is illustrated in Figure 2.2. A new field can be written as perturbations from the ground states, defined by

$$\eta \equiv \phi \pm \sqrt{\frac{-\mu^2}{\lambda}}. \tag{2.34}$$

If the Lagrangian of equation 2.32 is rewritten in terms of η as

$$\mathcal{L} = \frac{1}{2}(\partial_\eta \phi)(\partial^\eta \phi) - \mu^2\eta^2 \pm \mu\lambda\eta^3 - \frac{1}{4}\lambda\eta^4 + \frac{1}{4}\frac{\mu^4}{\lambda} \tag{2.35}$$

then the second term resembles a mass term, where the mass of the particle is

$$m = \sqrt{-2\mu^2} \tag{2.36}$$

the third and fourth term of equation 2.35 represent triple and quartic couplings, and the last term is an insignificant constant.

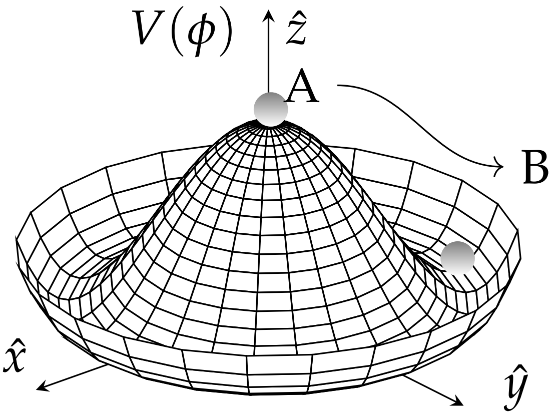

Figure 2.2.: Illustration of the Higgs potential. There is an infinite number of ground states. At point A, the global symmetry is unbroken. At point B, a local minimum is chosen and spontaneous symmetry breaking occurs. This figure is from Ref. [10].

Broken continuous symmetry

The previous section illustrates an example of spontaneous symmetry breaking. The original Lagrangian of equation 2.32 is invariant if $\phi \rightarrow -\phi$; it is even in ϕ. In the reformed Lagrangian of equation 2.35, however, this symmetry is broken because it is not even in η. The breaking is considered spontaneous because no external agent is required; the symmetry simply becomes hidden when selecting a particular ground state (the "vacuum"). In section 2.3.1 the broken symmetry was a discrete symmetry in context of a real scalar field. This section will apply spontaneous symmetry breaking to a complex scalar field.

Consider the following complex scalar field, written neatly as a combination of two real fields:

$$\phi \equiv \frac{1}{\sqrt{2}}(\phi_1 + i\phi_2) \tag{2.37}$$

$$\phi^*\phi = \frac{1}{2}(\phi_1^2 + \phi_2^2). \tag{2.38}$$

The Lagrangian written with respect to the two fields ϕ_1 and ϕ_2 is

$$\mathcal{L} = \frac{1}{2}(\partial_\mu\phi_1)(\partial^\mu\phi_1) + \frac{1}{2}(\partial_\mu\phi_2)(\partial^\mu\phi_2) - \left[\frac{1}{2}\mu^2(\phi_1^2 + \phi_2^2) + \frac{1}{4}\lambda(\phi_1^2 + \phi_2^2)^2\right] \tag{2.39}$$

where the terms in the square brackets is the potential energy function V. The minima of V is a circle with the equation

$$\phi_1^2 + \phi_2^2 = \frac{-\mu^2}{\lambda} = \nu^2 \tag{2.40}$$

where ν corresponds to the ground states. Arbitrarily one can choose

$$\phi_1 = \nu, \qquad \phi_2 = 0 \tag{2.41}$$

and introduce fluctuations about this vacuum state as new fields

$$\eta \equiv \phi_1 - \nu, \qquad \xi \equiv \phi_2. \tag{2.42}$$

Now equation 2.39 can be rewritten in terms of η and ξ:

$$\mathcal{L} = \left[\frac{1}{2}(\partial_\mu\eta)(\partial^\mu\eta) - \mu^2\eta^2\right] + \left[\frac{1}{2}(\partial_\mu\xi)(\partial^\mu\xi)\right] + \text{higher order terms}. \tag{2.43}$$

The first term is the free Lagrangian for the field η, which includes a mass term, giving $m_\eta = \sqrt{2}\mu$. The second term describes field ξ, which unlike η, turns out to be massless. This is Goldstone's theorem - the appearance of a massless spin-0 Goldstone boson is the result of a spontaneous broken continuous global symmetry [4].

2.3.2. The Higgs mechanism

The Higgs mechanisms involves spontaneous symmetry breaking of the complex field in equation 2.38 in a Lagrangian that is locally gauge invariant. Consider the Lagrangian in equation 2.39: it is invariant under global U(1) transformation $\phi \rightarrow e^{iq\theta}\phi$, however not invariant under local U(1) gauge transformation $\phi \rightarrow e^{iq\theta(x)}\phi$. In order to impose local gauge invariance, the derivatives must be replaced by the appropriate covariant derivatives

$$\partial_\mu \rightarrow \mathcal{D}_\mu = \partial_\mu + igA_\mu \tag{2.44}$$

where a new gauge field A_μ is introduced and transforms as

$$A_\mu \rightarrow A_\mu - \partial_\mu \theta(x). \tag{2.45}$$

The locally invariant Lagrangian for the complex scalar field ϕ becomes

$$\mathcal{L} = (\mathcal{D}_\mu \phi^*)(\mathcal{D}^\mu \phi) - \mu^2\phi^2 - \lambda\phi^4 - \frac{1}{4}F_{\mu\nu}F^{\mu\nu} \tag{2.46}$$

where the additional term is the Proca Lagrangian acccompanying the gauge field.

As with the previous section, when $\mu^2 < 0$ in the potential, the choice of a physical degenate vacuum state breaks the symmetry of the Lagrangian. The complex scalar field can be rewritten by substituting equation 2.42 into equation 2.38 to get:

$$\phi(x) = \frac{1}{\sqrt{2}}\Big[v + \eta(x) + i\xi(x)\Big]. \tag{2.47}$$

The definition above is used to rewrite the Lagrangian on equation 2.46 as

$$\begin{aligned}\mathcal{L} =& \frac{1}{2}(\partial_\mu \eta)(\partial^\mu \eta) - \lambda v^2 \eta^2 + \frac{1}{2}(\partial_\mu \xi)(\partial^\mu \xi) - \frac{1}{4}F_{\mu\nu}F^{\mu\nu} + \frac{1}{2}g^2 v^2 A_\mu A^\mu \\ &+ g v A_\mu (\partial^\mu \xi) + \text{interaction terms}\end{aligned} \tag{2.48}$$

where the first two terms represent the massive scalar field η, the third term corresponds to the massless Goldstone boson ξ, and the fourth and fifth terms describes the gauge field A_μ which has now acquired a mass. Additional three and four point interactions terms also exist the fields. The is the exact same Lagrangian as equation 2.46; ϕ has simply been expanded about the vacuum state. The underlying symmetry of the U(1) gauge group has consequently been broken.

The final step involves the choice of an appropriate gauge which eliminates the Goldstone field completely from the Lagrangian. This is motivated by the $qvA_\mu(\partial^\mu\xi)$ term, which reads as a coupling between the spin-1 gauge field A_μ and the spin-0 scalar Goldstone field ξ, where one field can transform into another. Such bilinear terms indicate that the fundamental fields have been misidentified [4]. If it is read as an interaction, it leads to a vertex in which ξ transforms into A_μ, meaning neither exist independently. This can be resolved by exploiting the freedom in gauge choice and setting

$$\theta(x) = -\frac{\xi(x)}{gv}, \tag{2.49}$$

which leads the complex scalar field to transform as

$$\phi(x) \rightarrow e^{-ig\frac{\xi(x)}{gv}}\phi(x). \tag{2.50}$$

Writing equation 2.47 to to first order as $\phi \approx \frac{1}{\sqrt{2}}\Big[v + \eta(x)\Big]e^{i\frac{\xi(x)}{v}}$, the gauge transformation on ϕ transforms away the Goldstone field completely:

$$\phi(x) \rightarrow e^{-i\frac{\xi(x)}{v}}\frac{1}{\sqrt{2}}\Big[v + \eta(x)\Big]e^{i\frac{\xi(x)}{v}} = \frac{1}{\sqrt{2}}\Big[v + h(x)\Big]. \tag{2.51}$$

This choice of gauge renders ϕ to be entirely real, and is called the unitary gauge. Here the field $\eta(x)$ can be rewritten as $h(x)$, corresponding to none other than the Higgs field. The mass term for the scalar Higgs field is

$$m_H = gv \tag{2.52}$$

and the mass of A, the gauge boson associated with the local gauge symmetry, is given by

$$m_A = \sqrt{2\lambda}v. \tag{2.53}$$

2.3.3. The Standard Model Higgs

This final subsection will apply the Higgs mechanism to the electroweak sector of the Standard Model, with a $\mathrm{SU}(2)_L \times \mathrm{U}(1)_Y$ local gauge symmetry.

$$\phi = \begin{pmatrix} \phi^+ \\ \phi^0 \end{pmatrix} = \frac{1}{\sqrt{2}} \begin{pmatrix} \phi_1 + i\phi_2 \\ \phi_3 + i\phi_4 \end{pmatrix} \tag{2.54}$$

$$\mathcal{L} = (\mathcal{D}_\mu \phi)(\mathcal{D}^\mu \phi)^\dagger - V(\phi^\dagger \phi) \tag{2.55}$$

$$\frac{1}{2}(\phi_1^2 + \phi_2^2 + \phi_3^2 + \phi_4^2) = \frac{v^2}{2} \tag{2.56}$$

The Lagrangian has an infinite set of ground states, and choosing any particular ground state will break the symmetry. The vacuum state chosen is

$$\langle 0|\phi|0\rangle = \frac{1}{\sqrt{2}} \begin{pmatrix} 0 \\ v \end{pmatrix} \tag{2.57}$$

which keeps the ground state electrically neutral, and consequently the photon massless. Expanding the ground state as before, ϕ is redefined as

$$\phi(x) = e^{\frac{\xi_a(x)\sigma_a}{2v}} \frac{1}{\sqrt{2}} \begin{pmatrix} 0 \\ v + h(x) \end{pmatrix}. \tag{2.58}$$

Choosing a unitary gauge, the Higgs doublet is rewritten such that the massless Goldstone fields are "eaten" by the gauge fields and the dependence on ξ_a is removed.

$$\phi(x) \to e^{-\frac{\xi^a(x)\sigma^a}{2v}} \phi(x) = \frac{1}{\sqrt{2}} \begin{pmatrix} 0 \\ v + h(x) \end{pmatrix}. \tag{2.59}$$

Applying equation 2.59 on the kinematic part of the Lagrangian in equation 2.55 and expanding generates the mass terms of the gauge boson fields. In the unitary gauge,

$\mathcal{D}_\mu\phi$ is

$$\mathcal{D}_\mu\phi = \left[\partial_\mu + ig_W\frac{\sigma^a}{2}W^a_\mu + ig'\frac{Y}{2}B_\mu\right]\phi \tag{2.60}$$

$$= \frac{1}{\sqrt{2}}\begin{pmatrix} \partial_\mu + \frac{ig_W}{2}W^3_\mu + \frac{ig'}{2}B_\mu & \frac{ig_W}{2}(W^1_\mu - iW^2_\mu) \\ \frac{ig_W}{2}(W^1_\mu + iW^2_\mu) & \partial_\mu - \frac{ig_W}{2}W^3_\mu + \frac{ig'}{2}B_\mu \end{pmatrix}\begin{pmatrix} 0 \\ v+h \end{pmatrix} \tag{2.61}$$

$$= \frac{1}{\sqrt{2}}\begin{pmatrix} \frac{ig_W}{2}(W^1_\mu - iW^2_\mu)(v+h) \\ (\partial_\mu - \frac{ig_W}{2}W^3_\mu + \frac{ig'}{2}B_\mu)(v+h). \end{pmatrix} \tag{2.62}$$

The kinetic term $(\mathcal{D}_\mu\phi)(\mathcal{D}^\mu\phi)^\dagger$ is

$$(\mathcal{D}_\mu\phi)(\mathcal{D}^\mu\phi)^\dagger = \frac{1}{2}(\partial_\mu h)(\partial^\mu h) + \frac{1}{8}g_W^2(W^1_\mu + iW^2_\mu)(W^{1\mu} - iW^{2\mu})(v+h)^2 \tag{2.63}$$

$$+ \frac{1}{8}(g_W W^3_\mu - g'B_\mu)(g_W W^{3\mu} - g'B^\mu)(v+h)^2, \tag{2.64}$$

where the terms proportional to v^2 correspond to the mass terms of the gauge bosons, namely

$$m_W = \frac{1}{2}g_W v \tag{2.65}$$

$$m_Z = \frac{1}{2}v\sqrt{g_W^2 + g'^2} \tag{2.66}$$

$$m_A = 0. \tag{2.67}$$

The spontaneous breaking of the $\mathrm{U}(1)_Y \times \mathrm{SU}(2)_L$ symmetry lets the W and Z bosons acquire mass, while the $\mathrm{U}(1)_Q$ symmetry remains unbroken thus leaving the photon massless.

2.3.4. Yukawa sector: fermion masses

The fermionic mass term given by

$$-m\bar{\psi}\psi = -m(\overline{\psi}_R\psi_L + \psi_R\overline{\psi}_L) \tag{2.68}$$

is not invariant under a local gauge transformation due to different transformation properties of its left- and right-handed chiral components. The left-handed states transform as weak isospin doublets under $\mathrm{SU}(2)_L$, while the right-handed states transform as singlets.

It is possible to add interaction terms between the Higgs field and the fermions to the Lagrangian of equation 2.55 while preserving the $\mathrm{SU}(2)_L \times \mathrm{U}(1)_Y$ symmetry. Starting with leptons, this is done by writing the term

$$\mathcal{L}_{\text{Yukawa},\,\ell} = -c_\ell(\overline{\psi}_R\phi^\dagger\psi_L + \psi_R\phi\overline{\psi}_L) \tag{2.69}$$

where c_ℓ is the Yukawa coupling constant between the specified lepton and the Higgs field. Next, the Higgs doublet ϕ is replaced with the ground state written in unitary gauge as per equation 2.59, and the Lagrangian becomes

$$\begin{aligned}
\mathcal{L}_{\text{Yukawa},\,\ell} &= -\frac{c_\ell}{\sqrt{2}}v(\overline{\psi}_R\psi_L + \psi_R\overline{\psi}_L) - \frac{c_\ell}{\sqrt{2}}h(\overline{\psi}_R\psi_L + \psi_R\overline{\psi}_L) && (2.70)\\
&= -\frac{c_\ell}{\sqrt{2}}v\overline{\psi}\psi - \frac{c_\ell}{\sqrt{2}}\overline{\psi}\psi h && (2.71)\\
&= -m_\ell\overline{\psi}\psi - \frac{m_\ell}{v}\overline{\psi}\psi h. && (2.72)
\end{aligned}$$

The first term is a mass term for the lepton, and the second term represents the coupling of the lepton to the Higgs boson.

The same mechanism generates mass for the case of down-type quarks. Up-type quarks require something a little different. The vacuum expectation value for the Higgs doublet is zero in the upper component, and therefore cannot generate mass for the up-type quarks and neutrinos[2]. Focusing on the case of the up-type quarks ψ_u, it is useful to define the conjugate doublet ϕ_C

$$\phi_C = -i\sigma_2\phi^* = \begin{pmatrix} -\phi^{0*} \\ \phi^- \end{pmatrix} = \frac{1}{\sqrt{2}}\begin{pmatrix} -\phi_3 + i\phi_4 \\ \phi_1 - i\phi_2 \end{pmatrix}. \tag{2.73}$$

which transforms exactly like ϕ. Now a gauge invariant Yukawa term can be written for the quark families as

$$\mathcal{L}_{\text{Yukawa},\,q} = -c_u(\overline{\psi}_{u,R}\phi_C^\dagger\psi_{u,L} + \psi_{u,R}\phi_C\overline{\psi}_{u,L}) - c_d(\overline{\psi}_{d,R}\phi^\dagger\psi_{d,L} + \psi_{d,R}\phi\overline{\psi}_{d,L}) \tag{2.74}$$

---

[2] The question of neutrino masses will not be addressed in this thesis.

which becomes

$$\begin{aligned}\mathcal{L}_{\text{Yukawa},\,q} &= -\frac{c_u}{\sqrt{2}}\nu\overline{\psi}_u\psi_u - \frac{c_u}{\sqrt{2}}\overline{\psi}_u\psi_u h - \frac{c_d}{\sqrt{2}}\nu\overline{\psi}_d\psi_d - \frac{c_d}{\sqrt{2}}\overline{\psi}_d\psi_d h &(2.75)\\ &= -m_u\overline{\psi}_u\psi_u - \frac{m_u}{\nu}\overline{\psi}_u\psi_u h - m_d\overline{\psi}_d\psi_d - \frac{m_d}{\nu}\overline{\psi}_d\psi_d h &(2.76)\end{aligned}$$

after spontaneous symmetry breaking. The Yukawa constants c_q, c_ℓ are not predicted by theory, and are assigned values that are consistent with experimental fermion mass measurements.

Chapter 3.

The Large Hadron Collider and the ATLAS experiment

3.1. The Large Hadron Collider

This massive fruit of labour, decades in the making from the hundreds of institutions which make up CERN, lies hidden 100 meters below the surface of the Switzerland-France border. Sandwiched between Geneva and the Jura Mountains is a 27 km ring of superconducting magnets and radio-frequency (RF) cavities, which bend and accelerate particles to near light speed. More specifically, it is approximately 3 metres per second slower. This remarkable achievement is none other than the Large Hadron Collider (LHC). The LHC lives up to its name; it is the largest machine built by humankind, and unsurprisingly the most powerful high-energy particle collider in the world. The four main interaction points around the ring where particles collide mark the four main experiments: ATLAS, CMS, LHCb, and ALICE [11]. The former two are general purpose detectors with a similar goal: to precisely study the Standard Model and to search for evidence of new physics. The latter two have specialized purposes. LHCb is dedicated to probing physics involving b-hadrons in pp collisions, and ALICE's aim is to shed light on the physics of the quark-gluon plasma by investigating heavy-ion collisions.

The protons used in the collisions originally come from hydrogen gas. The gas is housed in tanks and stripped of orbital electrons through of ionization. Prior to the injection into the LHC, the protons first pass through a series of smaller machines which boost them to higher and higher energy. The first in the chain is LINAC2, a linear accelerator in which beams of protons are formed, and given an energy of 50 MeV. Next the protons are piped into the Proton Synchrotron Booster, the Proton Synchrotron, and finally into the Super Proton Synchrotron . Through this chain the protons get

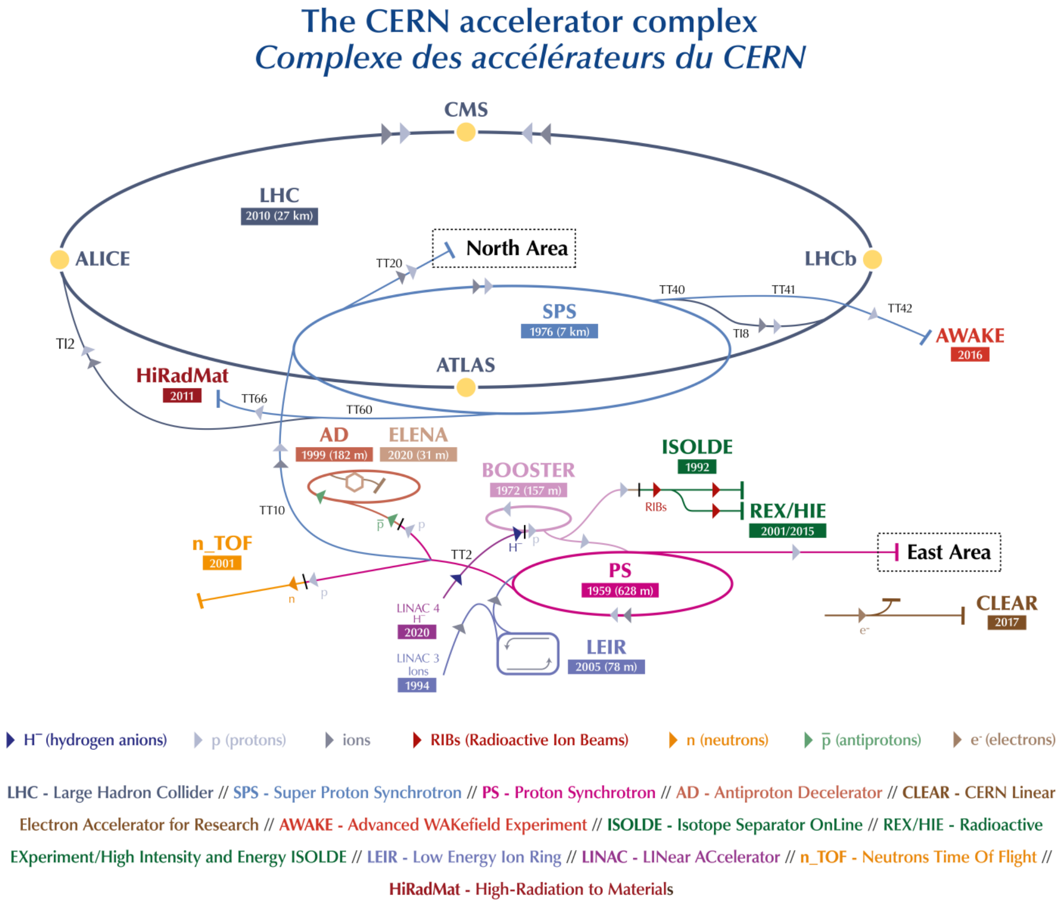
The CERN accelerator complex
Complexe des accélérateurs du CERN
CMS
LHC
2010 (27 km)
ALICE
North Area
LHCb
TT20
TT40
TT41
TT42
SPS
1976 (7 km)
TI8
AWAKE
2016
TI2
ATLAS
HiRadMat
2011
TT66
TT60
AD
1999 (182 m)
ELENA
2020 (31 m)
ISOLDE
1992
BOOSTER
1972 (157 m)
RIBs
REX/HIE
2001/2015
TT10
n_TOF
2001
TT2
East Area
PS
1959 (628 m)
CLEAR
2017
LINAC 4
H⁻
2020
LINAC 3
Ions
1994
LEIR
2005 (78 m)
H⁻ (hydrogen anions)
p (protons)
ions
RIBs (Radioactive Ion Beams)
n (neutrons)
p̄ (antiprotons)
e⁻ (electrons)
LHC - Large Hadron Collider // SPS - Super Proton Synchrotron // PS - Proton Synchrotron // AD - Antiproton Decelerator // CLEAR - CERN Linear Electron Accelerator for Research // AWAKE - Advanced WAKefield Experiment // ISOLDE - Isotope Separator OnLine // REX/HIE - Radioactive EXperiment/High Intensity and Energy ISOLDE // LEIR - Low Energy Ion Ring // LINAC - LINear ACcelerator // n_TOF - Neutrons Time Of Flight // HiRadMat - High-Radiation to Materials

Figure 3.1.: The CERN accelerator complex, where the LHC is the largest ring. The four main collision points corresponding to the main experiments are dotted in yellow. This figure is from Ref. [12].

boosted to 1.4 GeV by the PSB, then further to 25 GeV by the PS, to a final 450 GeV by the SPS before entering the LHC. Inside the pipes of the LHC, the protons take a short 20 minutes to reach 6.5 TeV.

The impressive feat of accelerating particles is made possible through the use of radio-frequency cavities. The idea was first crafted by the young Rolf Wideröe [13] for his PhD thesis and later caught the eye of the brilliant E. Lawrence, recipient of the Nobel Prize in Physics in 1939 for the invention of the cyclotron. RF cavities are round chambers along the beam. A voltage generator generate a voltage which oscillates at 400 MHz, inducing an electric field inside the RF cavity. As particles pass through they experience the force of the field and are accelerated along the beam pipe. In total the LHC uses 8 RF cavities per beam (so 16 in total), with each cavity capable of delivering two megavolts of energy. Protons travelling through the cavity increase their energy to 14 times the injection amount, from 450 GeV to 6.5 TeV. Once protons get up to speed, a proton that has perfect timing are left alone, while protons that arrive slightly earlier/later will be accelerated/decelerate. The result is a beam of protons sorted into smaller segments of proton bunches. The LHC produces two such proton beams, one circulating clockwise and the other counterclockwise.

A key concept in particle physics is luminosity. It is a factor that relates the cross-section to the number of event per second, written as follows:

$$\mathcal{L} = \frac{1}{\sigma} \cdot \frac{dN}{dt} \tag{3.1}$$

where $\mathcal{L}$ is the luminosity, N is the number of events, and σ is the production cross section. The dimension of luminosity is events per unit time and unit area $\text{cm}^{-2}\ \text{s}^{-1}$.

There are two properties used to describe a particle beam: its emittance ϵ, and its β function. The emittance can be thought of as the area occupied by the particle beam in the position momentum plane. A lower emittance means the distance between particles and the difference in momentum between the particles are small. The β function is also known as the amplitude function. It is a function related to the transverse size of the particle beam, and it is proportional to the width of the beam squared divided by the emittance. With low β, the beam is narrowere and squeezed. When high β, the beam is wider. The cross sectional sizes of the beam σ_i $(i = x, y)$ are written as

$$\sigma_i = \sqrt{\frac{\beta_i \cdot \epsilon_i}{\pi}} \tag{3.2}$$

The beams are assumed to be Gaussian distributed, meaning that in collisions, the centres of the beams contribute most while the edges have minimal impact. Following this the luminosity is

$$\mathcal{L} = \frac{N_1 N_2 f_{rev} N_b}{2\pi \Sigma_x \Sigma_y} \tag{3.3}$$

where N_1 and N_2 are the number of particles for each bunch, N_b is the number of bunches, f is the revolution frequency, and Σ_x, Σ_y represent the convolution of the beam sizes. They can be expressed as

$$\Sigma_x = \sqrt{\sigma_{x1}^2 + \sigma_{x2}^2}, \quad \Sigma_y = \sqrt{\sigma_{y1}^2 + \sigma_{y2}^2}. \tag{3.4}$$

Assuming that the beam sizes are identical and round, $\sigma_{x1} = \sigma_{x2} = \sigma_{y1} = \sigma_{y2}$, and the luminosity becomes

$$\mathcal{L} = \frac{N_1 N_2 f_{rev} N_b}{4\pi\sigma^2} = \frac{N_1 N_2 f_{rev} N_b \gamma}{4\pi\epsilon_N \beta^*}, \tag{3.5}$$

where β^* is the amplitude function at the interaction point. The LUCID-2 detector of the LHC consists of several small Cherenkov detectors that consists only of photomultipliers with quartz windows, and it is responsible for luminosity measurements and luminosity monitoring [14].

When proton beams cross at the LHC, there are many collisions which occur other than the hard-scatter of interest. While increasing the number of particles per bunch increases the likelihood of a rare interaction, it also increases the pile-up of multiple interactions. The number of pile-up events, denoted as μ, is one of the biggest obstacles for LHC experiments; the more there is, the more difficult it becomes to disentangle the events of interest from the sea of low energy collisions. It is, however, an inevitable consequence that accompanies increasing the instantaneous luminosity. The contribution to pile-up events can be separated into two main categories:

- In-time pile-up refers to simultaneous proton-proton collisions occurring in the same bunch crossing as the hard scatter of interest;
- Out-of-time pile-up is the overlay of events from neighbouring bunches which contaminate signal events, attributed to detector electronics latency.

There are also less-substantial contributions from the cavern background, beam halo events, and beam gas events. The cavern background is the cloud of gas that floods the LHC cavern during operation. Beam halo events are from when the proton beam interacts with the collimating instrumentation, and the beam gas events describe interactions between the beam and the residual gas in the beam pipe.

The LHC was originally designed to reach a peak instantaneous luminosity and average pile-up of 10^{34} cm^{-2}s^{-1} and $\langle\mu\rangle = 19$ respectively. In Run II, the LHC reached peak luminosity of 2×10^{34} cm^{-2}s^{-1}, and peak pile-up of $\mu = 60$ [15]. Figure 3.2 shows the profiles of pile-up conditions in the four years of operation.

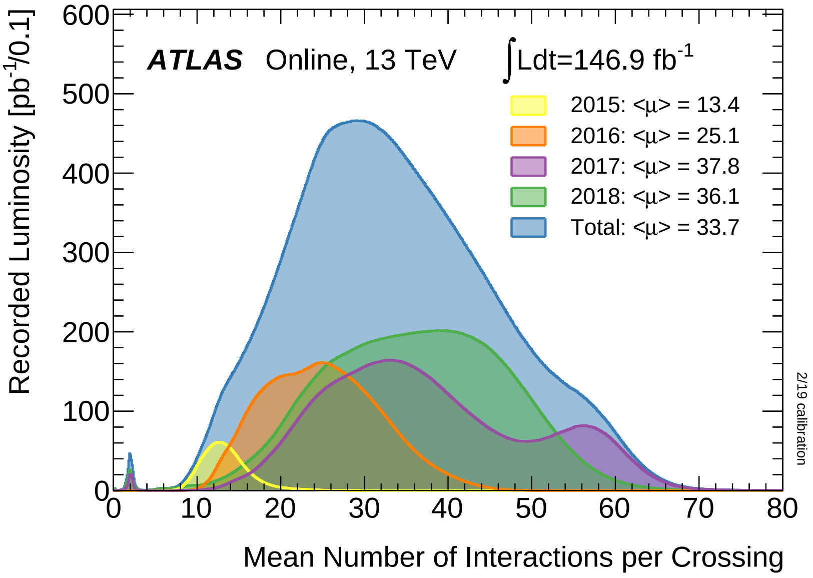

Figure 3.2.: The pile-up, μ, is the mean number of collisions per bunch crossing. Shown are the pile-up distributions from 2015-2018, where each distribution is luminosity weighted. This figure is from Ref. [16].

3.2. The ATLAS detector

Measuring forty-six meters in length, twenty five meters in height and width, and weighing in at a hulking seven thousand tons, the ATLAS (A-Toroidal-LHC-ApparatuS) detector is the Mount Everest of particle detectors. Built with a cylindrical and symmetric structure around the beam pipe, it's detection region covers nearly the entirety of the 4π solid angle of the collision point. ATLAS is a general purpose detector, and combines a multitude of detector technologies to conduct searches for new phenomena, and to make high-precision measurements of the Standard Model.

The right-handed coordinate system used by the ATLAS detector, and also very commonly in particle physics, is illustrated in figure 3.3. The z-axis is parallel to the beam pipe, the y-axis points vertically to the sky, and the x-axis points to the centre of the LHC ring. The xy-plane is often referred to as the transverse plane, and the frequently encountered variables p_T and E_T refer to the momentum and energy in the transverse direction respectively. The azimuthal angle in the transverse plane is denoted as ϕ, and polar angle θ denotes the angle offset from the beam pipe. Another commonly used coordinate is the rapidity, y, of an object:

$$y = \frac{1}{2} \ln \frac{E + p_Z}{E - p_Z}, \tag{3.6}$$

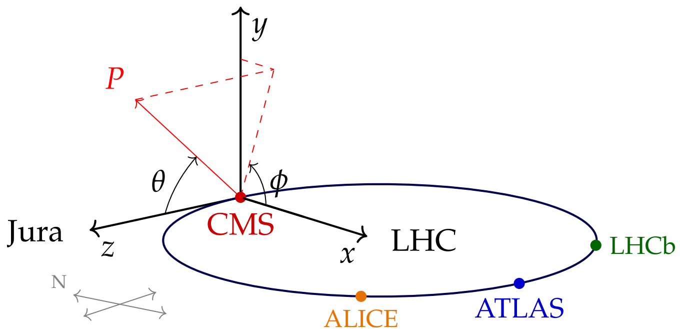

Figure 3.3.: The coordinate system used at the LHC in the perspective of the CMS experiment. Figure taken from [18].

where E is the object's energy and p_Z is the momentum in the z-direction. Rapidity differences are invariant with respect to Lorentz boosts along the beam axis. This is the key reason why rapidities are so crucial in accelerator physics [17]. Alternatively there is the pseudorapidity η in the massless limit:

$$\eta = -\ln \tan \frac{\theta}{2}. \tag{3.7}$$

Both rapidity and pseudorapidity are more commonly used than polar angle θ. The separation of two detected objects, ΔR, is given by

$$\Delta R = \sqrt{\Delta y^2 + \Delta\phi^2}, \tag{3.8}$$

which is Lorentz invariant under a boost along the longitudinal (beam) direction.

The rest of this section will review the three sub-detectors of ATLAS- the Inner Detector, the Calorimeter, and the Muon Spectrometer - as well as the Magnet System. A cross-sectional diagram illustrating the sub-detector systems is shown in Figure 3.4. The sub-detectors are made up of concentric barrels that wrap around the beam pipe, and circular endcaps placed at either end of the barrels. The barrels are designed to detect the particles that travel through the central $|\eta|$ region, and the endcaps broadens the angular coverage for particles whose trajectories run close to parallel to the beam.

3.2.1. The Inner Detectors

The Inner Detector (ID) is able to measure the momentum of charged particles passing through it. The trajectories of the charged particles as they cross through are curved by a superconducting solenoid magnet with a 2 Tesla magnetic field [20]. The direction

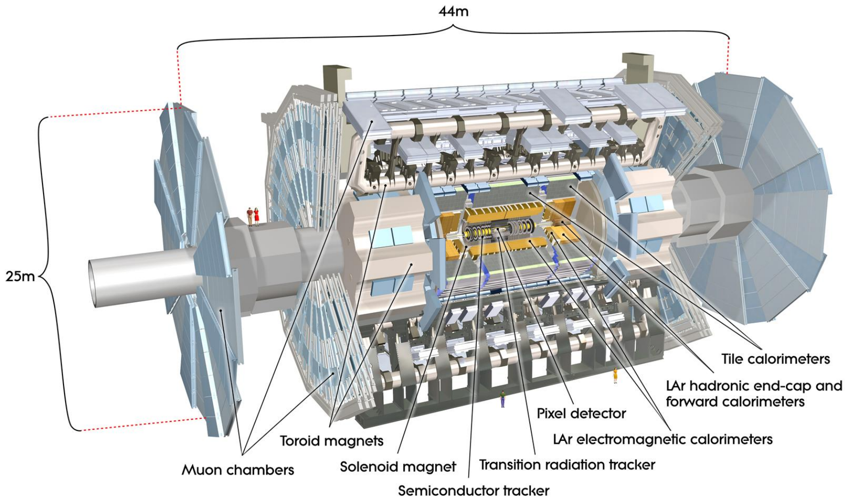
44m
25m
Tile calorimeters
LAr hadronic end-cap and forward calorimeters
Pixel detector
LAr electromagnetic calorimeters
Toroid magnets
Muon chambers
Solenoid magnet
Transition radiation tracker
Semiconductor tracker

Figure 3.4.: The ATLAS detector and its sub-components. This figure is from Ref. [19].

of curvature indicates the particle's charge, while the degree of curvature indicates momentum. The Inner Detector is the smallest sub-detector of ATLAS, stretching out to a radius of only 1.15 meters, with a total length of 7 meters. The barrel arrangement consists of concentric cylinders wrapped around the beam axis, and the end-cap components are attached as disks normal to the beam axis. The inner detector has three main components: the Pixel Detector, the Semiconductor Tracker (SCT), and the Transition Radiation Tracker (TRT).

Pixel Detector

The Pixel Detector is the innermost part of the Inner Detector. It is the part of ATLAS that is closest to the interaction point where particles collide. It was designed with extremely high granularity in mind in order to accurately resolve primary and secondary vertices, determine impact parameter resolution, and identify short-lived particles such as b-hadrons and tau leptons. Prior to Run 2, the pixel detector consisted of three concentric layers in the barrel, and three disks in the end-cap regions. During the long shutdown prior to Run 2, an additional layer called the Insertable B-layer (IBL) [21] was added to the Pixel Detector closest to the beam pipe, making a total of four layers. The pixel detector are made up of sensor modules, each consisting of 46,080 active silicon pixels measuring 50 micrometers in width (ϕ direction) and 400 micrometers in length (z direction). Each module consist of the active sensor medium (in this case silicon), and front-end electronics for readout. In total, the pixel detector hosts an astonishing eighty million readout channels. All together, the pixel detector achieves a resolution of 10 µm in the ϕ-direction and 115 µm in the z-direction.

Semi-conductor tracker

The second layer of the inner detector is the SemiConductor Tracker (SCT), made up of two-sided modules of silicon microstrip sensors arranged back to back and tilted by a stereo angle of 40 mrad [22]. It wraps around around the pixel detector and has in total 4088 modules, assembled in four cylindrical layers in the barrel region, and two end-caps containing nine disks each [23]. The stereo angle enables the module to provide information about where along the strip the hit occurred. This is turn gives resolution in the z-plane in the barrels, and in R along the endcaps. The spatial resolution of the detector is 17 μm in $R - \phi$ coordinate and 580 μm in the z coordinate in the barrel (R in the endcaps) [24]. In total the SCT hosts 4088 modules, assembled in four cylindrical layers in the barrel region, and two end-caps containing nine disks each [23].

Transition Radiation Tracker

The third and outermost layer of the inner detector is the Transition Radiation Tracker (TRT). Unlike the ID and the SCT, it uses a straw drift tube technology, and exploits transition radiation emission for additional particle identification. Each module consists of 4 millimetre diameter straw tubes filled with xenon, carbon dioxide, and oxygen (70%, 27%, and 3%) [25] bundled together. In order to collect charge from ionisation, a tungsten wire extends axially through the centre of each tube. In the barrel the drift tubes run parallel with the beam axis, and in the endcaps they run radially. In total there are 351,000 readout channels, and the resulting position resolution is weaker than the Pixel Detector or the SCT. The TRT is only capable of performing measurements in the $R - \phi$ coordinate, with a resolution of 130 μm [25].

Despite the lower resolution and the lack of sensitivity in the z coordinate, the hits in the TRT contribute significantly to momentum resolution due to the a larger number of measurements and an extended measured track length. There are 73 parallel planes of straw-tubes in the barrel and 80 planes in each endcap. Furthermore, the barrel straws are inter-weaved in a matrix of polypropylene fibres, and the endcap disks are wedged in between polypropylene foils, creating numerous material boundaries. As highly relativistic particles pass through the boundaries they emit transition radiation photons; predominantly in the X-ray energy regime [26]. These photons are absorbed by the gas mixture inside the tubes, and yield higher signal amplitudes than the signal of hits from minimum-ionizing particles. The energy of the transition radiation photon is strictly proportional to the relativistic factor $\gamma = E/m$ of the incident particle. For a given momentum, it is much higher for electrons than it is for pions or muons, a useful difference that is exploited for particle identification.

3.2.2. Calorimetry

Immediately after the particles exit the inner detector, they reach a set of calorimeters whose aim is to measure the particles' energies by fully absorbing them. In contrast to the Inner Detector, the calorimeters can detect both charged and neutral particles. Neutrinos and muons, however, pass through the calorimeters unaffected as they are minimally ionizing particles (MIPs) at the LHC energy scale. The ATLAS calorimeters use sampling calorimeter technology. This is a design choice where layers of an active sensing material alternate with layers of a dense absorber material. Particles crossing the calorimeters will interact with the absorber medium and lose its energy through interactions. The initial traversing particle eventually creates a cascade of many lower energy particles - a particle shower. The sensitive detector medium sandwiched between will generate a signal proportional to this shower, with readout done through ionization or scintillation. There are two types of particle showers: electromagnetic and hadronic, depending on the nature of the source. Electromagnetic showers are primarily initiated by electrons or photons and develop mainly through Bremsstrahlung ($e \rightarrow \gamma e$) and pair production ($\gamma \rightarrow e^+ e^-$), while hadronic interactions are more complex, developing through the strong interaction between the hadrons and the absorber material's nuclei. They differ radically, and thus require separate detector technologies for high-precision detection. In order to meet these needs, there are two types of calorimeters that are hermetic along the ϕ coordinate and cover up to $|\eta| < 4.9$. As depicted in Figure 3.5, these are the electromagnetic and the hadronic calorimeters.

The Electromagnetic Calorimeter

The electromagnetic calorimeter wraps immediately around the inner detector as illustrated in Figure 3.5. The material used for the active sensing medium is liquid Argon (LAr), chosen for its high intrinsic uniformity, long-term stability of signal response, as well as radiation hardness [28]. Lead plates are used as absorbers, chosen for its high hadronic interaction length to radiation length ratio. The resulting electromagnetic

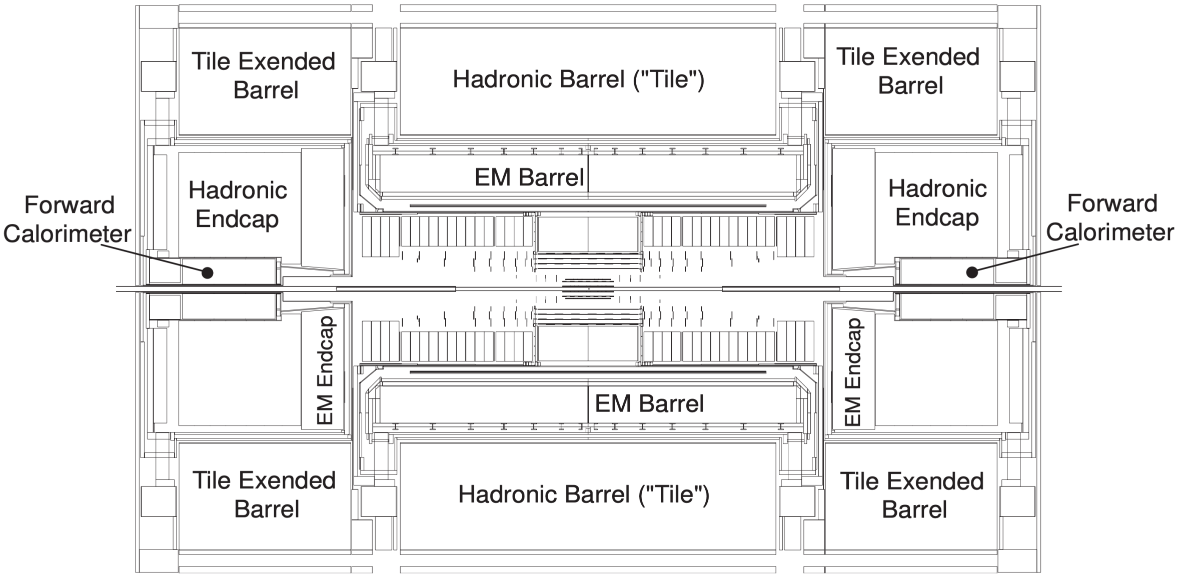
Tile Exended Barrel
Hadronic Barrel ("Tile")
Tile Exended Barrel
EM Barrel
Forward Calorimeter
Hadronic Endcap
Hadronic Endcap
Forward Calorimeter
EM Endcap
EM Endcap
EM Barrel
Tile Exended Barrel
Hadronic Barrel ("Tile")
Tile Exended Barrel

Figure 3.5.: Cross-sectional view of the calorimetry system in the ATLAS detector. This figure is from Ref. [27].

calorimeter has a total thickness that covers 22 times the radiation length, which corresponds to less that one hadronic interaction length, preventing hadronic showers from forming. The liquid Argon and lead layers and arranged in an accordian-like geometry, ensuring a full azimuthal coverage with minimal gaps in acceptance . The barrel sector consists of three layers of varying granularity and has coverage up to $|\eta| < 1.475$.

The first layer has a granularity of $\Delta\eta \times \Delta\phi = 0.0031 \times 0.098$. The high $\Delta\eta$ resolution acts as a powerful discriminator between showers originating from single isolated photons and those originating from multiple photons, from decays of neutral mesons within jets . The second layer is the thickest of the three, and it absorbs the vast majority of the shower's energy. It has a granularity of $\Delta\eta \times \Delta\phi = 0.025 \times 0.025$. Lastly, a thinner, lower-granularity final layer with $\Delta\eta \times \Delta\phi = 0.05 \times 0.025$ is used to estimate the energy that leaks beyond the electromagnetic calorimeter and into the hadronic calorimeter. In order to correct for energy lost by electrons and photons when they interact with the inner detector and magnet, a liquid Argon pre-sampler is installed upstream of the calorimeter. The pre-sampler is one single sensitive layer of liquid Argon and covers the range $|\eta| < 1.8$. The electromagnetic calorimeter end-caps are made up of four wheels; an inner and outer wheel on either side of the interaction point. These are each divided into eight wedge shaped modules and cover the range $1.375 < |\eta| < 3.2$. Like the barrel modules, the end-cap modules consist of three layers of varying granularity.

The Hadronic Calorimeter

Hadrons lose energy through inelastic interactions with the detector medium, which result in the production of secondary strongly interacting particles, giving rise to hadronic showers. The main purpose of the hadronic calorimetry system is to measure the energy of such hadrons. Its performance is essential for precision measurements of jets as well as reconstruction of missing energy [29]. The hadronic calorimeter incorporates modules of varying technologies, the barrel region hosts a tile calorimeter and the end-caps host a liquid-argon hadronic calorimeter.

The Tile Calorimeter, covering the central region of ATLAS, is further separated into two sub-detectors. In the $|\eta| < 1.0$ region there is the hadronic tile barrel, and the extended tile barrel resides between $0.8 < |\eta| < 1.7$. Both regions use alternating tiles of steel absorbers and scintillating sensing elements, arranged parallel to the beam axis. A total of 64 modules wedge together to give full azimuthal angle coverage. In the transverse direction there are three layers of varying granularity. The first and second layers have resolution 0.1×0.1 in $\Delta\eta \times \Delta\phi$, and the third layer a coarser resolution of $\Delta\eta \times \Delta\phi = 0.2.1$. As an ionising particle crosses the scintillating medium, ultraviolet scintillation light is produced. Using wavelength-shifting optical fibers, this light is collected and converted into visible light. Next it is guided towards photomultiplier tubes at the top of each module, where the optical signal is measured.

The hadronic end-cap calorimeter is a liquid argon sampling calorimeter, similar to the electromagnetic counterpart. The coverage reaches the $1.5 < |\eta| < 3.2$ range in the forward region, where the more radiation resistant liquid argon technology is better suited than a tile calorimeter. The absorber in the hadronic end-cap, however, is copper rather than lead. Each end-cap consists of two separate wheels. The inner wheel has 8.5 millimetre liquid argon gaps wedged between 25 millimetre thick copper plates, whereas for the outer wheel the copper is 50 millimetre thick. The granularity is 0.1×0.1 in $\Delta\eta \times \Delta\phi$ for $1.5 < |\eta| < 2.5$, and $\Delta\eta \times \Delta\phi = 0.2 \times 0.2$ for $\Delta\eta \times \Delta\phi$ for $2.5 < |\eta| < 3.2$.

3.2.3. The Muon Spectrometer

The outermost layer of the ATLAS detector system is the muon spectrometer, which as the name suggests, is designed to provide efficient, high-resolution measurements of muons' trajectory and momenta. Energetic muons are minimum ionizing particles, and can penetrate through the calorimeters. Installing this tracking system wrapping around the other sub-detectors gives muons a very distinctive detector signature, leading to a high purity and efficiency in their reconstruction. Figure 3.6 shows the layout of the muon system, which consists of four gaseous tracking chambers installed between the eight coils of the barrel toroidal magnetic system, as well as before and after the toroid magnets of the endcaps. Two of these are precision tracking chambers made for precision momentum measurements, and the other two act as an efficient trigger system for fast response [30].

- Monitored Drift Tubes (MDT): To provide precision coordinate measurements in the bending plane of the the muon spectrometer, Monitored Drift Tube (MDT) chambers are installed over the full pseudorapidity range $|\eta| < 2.7$. Each MDT component consists of a 3 cm diameter pressurised aluminium drift tube filled with 93% argon and 7% carbon dioxide gas at three bar [31]. As a muon passes through a drift tube, ionisation electrons drift towards the centre where a wire stretches through the longitudinal axis.
- Cathode Strip Chambers (CSC): The number of MDTs is reduced in the forward region $2.0 < |\eta| < 2.7$, where particle flux is twenty times higher than the average in the rest of the MS. Here, Cathode-Strip Chambers (CSC) aid momentum measurement. The CSC are multi-wire proportional chambers, with the cathode segmented into strips, and the direction of the strip is perpendicular to one of the wires. This allows for two independent measurements of the muon: one for the ionisation electrons that are collected at the wire, the other one from the induced signal collected at the strips.
- Resistive Plate Chambers (RPC): Installed in the barrel region, these chambers provides fast tracking in the $\eta < 1.05$ region. Each chamber is made up of two gaseous volumes, Bakelite plates, and read-out electronics [30].
- Thin Gap Chambers (TGC): Installed in the endcaps, TGCs makes up the second part of the muon trigger system. In total each endcap has seven layers of TGC. Each layer is made up of two resistive grounded cathode planes, with a sheet of closely spaced wires sandwiched inside [32]. A positive high voltage is applied to the wire anode. The gap between the anode to cathode plane is thinner than the wire to wire spacing (1.4 mm and 1.8 mm respectively), a characteristic reflected in the name of these chambers. TGCs act as a level-1 trigger, and provide high efficiency and excellent time resolution in a high-background environment [33].

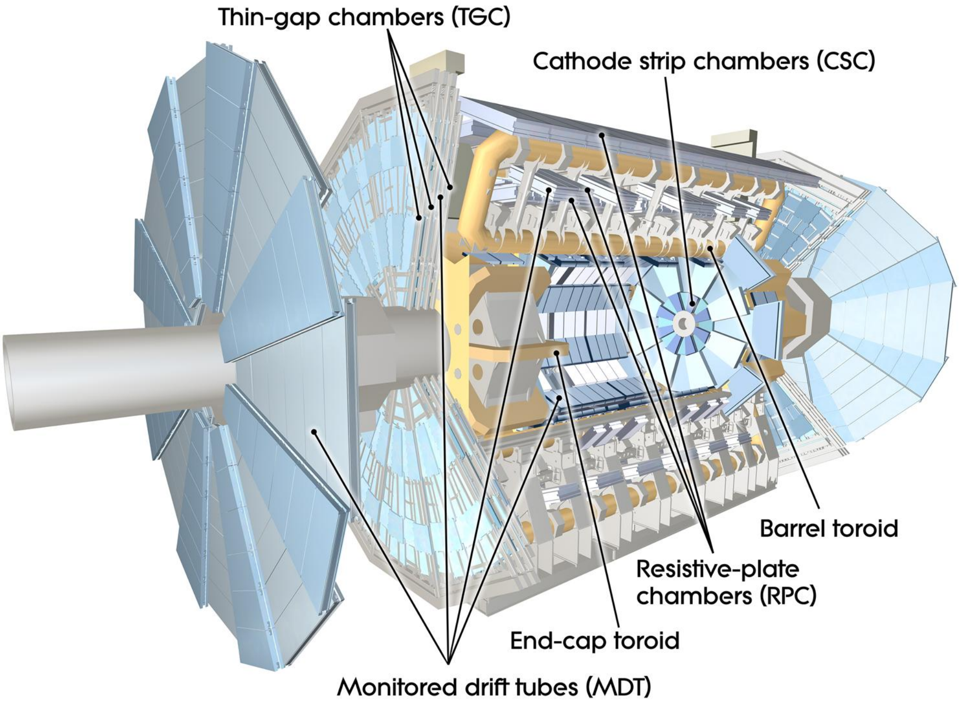
Thin-gap chambers (TGC)
Cathode strip chambers (CSC)
Barrel toroid
Resistive-plate chambers (RPC)
End-cap toroid
Monitored drift tubes (MDT)

Figure 3.6.: A section view of the ATLAS Muon Spectrometer and its sub-components. This figure is from Ref. [34]

3.2.4. Magnet system

The ATLAS detector incorporates a powerful magnet system that bends the trajectory of charged particles in order to measure their momentum with high accuracy. The momentum is deduced via the radius of curvature of the tracks seen within the detector systems. A pictorial representation of the ATLAS magnet system is shown in Figure 3.7. It is a system comprised of four separate superconducting magnets - one barrel toroid and two endcap toroids incorporated in the muon spectrometer, and one central solenoid surrounding the inner detector. All four magnets are indirectly cooled, through conducting, by circulating helium at 4.5 K in the tubes welded onto the aluminum structure that encloses the coils [35].

The central solenoid is cylindrical in shape, and designed with minimal thickness in order to reduce energy loss before the particles enter the calorimeter. It is a superconducting magnet constructed from niobium-titanium alloy. It provides a magnetic field of 2 T to the inner detector axially (parallel to the $z-$axis), deflecting charged tracks along the ϕ coordinate. The strength of the central solenoid's magnet field is near constant along the radial direction, however it decreases on the axial edges due to the finite length of the magnet.

The air toroid system is composed of three magnets: one forming a barrel section, and the others two end-caps. Each is composed of eight coils positioned in azimuthal symmetry around the beam axis. The toroids bend charged particles in the muon spectrometer. Unlike the central solenoid, however, the magnetic field strength varies. In the barrel it is between 0.15 Tesla and 2.5 Tesla, and in the endcaps it starts at 0.2 Tesla and reaches up to 3.5 Tesla . The toroids' generated magnetic fields are orthogonal to that of the solenoid. This has the advantage that independent measurements of muon momenta can be made in the inner- and outer-most regions of the detector.

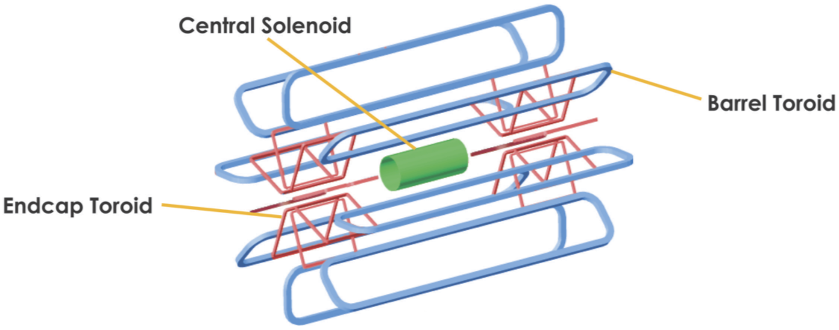

Figure 3.7.: Schematic representation of the ATLAS magnet system. This Figure is from Ref. [36].

3.2.5. Trigger system

ATLAS does not record every single collision that the LHC produces. This is partially because most events are uninteresting low-energy processes, and partially because the amount of bandwidth and computing resources required make it impossible to do so. During run 2 the LHC had a bunch crossing rate of twenty five nanoseconds, corresponding to a collision frequency of forty megahertz. That's on the order of a few thousand gigabytes of data per second! It is neither feasible or practical to read out and record data at this frequency, and here the nifty trigger system comes into play. The ATLAS triggers act like a fine sieve and select only rare, interesting events. Typically, interesting events involve objects that have high momentum or energy in the transverse direction. The ATLAS trigger system throughout run 2 effectively reduces the crossing rate from forty megahertz to one kilohertz through two triggers. The first is the level-1 (L1) trigger, a hardware based trigger that uses coarse objects from the calorimeters and the muon spectrometer, which reduces the rate to 100 kilohertz. The second is a software based high level trigger (HLT), which makes further selection choices bringing the final rate to one kilohertz [37].

Level-1 trigger

The level-1 trigger consists of several subsystems. The level-1 calorimeter (L1Calo) and level-1 muon (L1Muon) subsystems operate separately with calorimetry and muon spectrometry information. The L1Calo trigger receives reduced resolution analogue signals from calorimeter trigger towers. These are formed by $\eta \times \phi = 0.1 \times 0.1$ regions in the barrel and $\eta \times \phi = 0.4 \times 0.4$ regions in the endcaps [9], separately for the electromagnetic and the hadronic calorimeter [38]. In the central region $|\eta| < 3.2$, L1Calo uses a sliding window algorithm to search for local maximum and forms regions of interests (ROIs) around them, which are sent for further processing to the HLT. L1Muon looks for coincident hits in the muon spectrometer; more specifically in the resistive plate chambers of the barrel region and and thin gap chambers in the endcaps, see Section 3.2.3. Finally there is the level-1 topological trigger (L1Topo), which makes use of takes trigger objects from both L1Calo and L1Muon and combines them into topological information. For example, one can require that two leptons have small angular separation $\Delta R < 0.1$. The L1 trigger makes a binary accept or reject decision via the the central trigger processor (CTP) which takes input from the three L1 subsystems. The acceptance rate reaches up to 100 kHz, and the data latency is 2.5 μs.

High level trigger

Once the level-1 trigger has accepted an event, it passes the baton onto the software-based high level trigger (HLT) for processing. The HLT uses the ROIs provided by the L1 trigger to seed regional event reconstruction with full detector granularity, including tracking information from the inner detector. Upon receiving an accept signal from the L1 trigger, the front-end electronics sent data out to the readout system via readout drivers. Reconstructing events is computationally expensive, thus the HLT is a built as a series of numerous individual trigger chains. At each stage an event may be rejected should it fail to meet the criteria of the chain. Rejected events are aborted, avoiding the need to run more CPU intensive algorithms. Once the HLT decides to accept an event, the full event data from various detectors are gathered and transferred to the tier-0 facility at CERN for preliminary analysis. The final event acceptance rate is reduced to an average of 1.5 kHz, a much more bearable 1.5 GB per second [37]. Not all triggers need run, or indeed can run, at their full rate. Here the trigger prescales come into play. The prescale value determines the fraction of events an HLT algorithm is being executed on, including when it is deactivated. This feature is both essential during the commissioning phase of the HLT as well as for adjusting the mixture of recorded physics events during an LHC run [39].

3.3. Object reconstruction

The ATLAS detector's raw readout signals must be translated into meaningfiul physics information before delivered to analysis teams. The responsibility for this task falls upon the offline reconstruction system, which combines information from all sub-detectors to reconstruct and identify particles with the highest possible efficiency.

3.3.1. Tracks and vertices

Reconstruction of complex physics objects, such as electrons and muons, begins with the construction of more basic inputs such as tracks, vertices, and calorimeter clusters. Charged particle trajectories are called tracks, and their reconstruction is crucial for many reasons. They are explicit inputs in the identification, reconstruction and isolation of electrons and muons, which is the signal process for the analysis of this thesis. The basic building block of a track is the detection of a signal above threshold, a hit, in the inner tracking detectors. In the pixel detector and semi-conductor tracker, the hits are first assembled into clusters of energy deposits that share common corners and edges, called space points. Tracks are seeded with a triplet of space points and are extended by matching subsequent pixel and SCT hits. This is done using a Kalman filter [40], which searches for adjacent clusters both outwards and inwards in the radial direction while attempting to smooth the trajectory.

When describing a track, five parameters are used: d_0 and z_0, the transverse and longitudinal impact parameters, ϕ and θ, the azimuthal and polar angle, and q/p describing the charge [41]. Together these are known as the perigee parameters. The two impact parameters are illustrated in figure 3.8. The transverse d_0 is the transverse distance from the primary vertex to the point of closest approach in the $\eta - \phi$ plane, while the z_0 is the distance from the $z-$axis. The momentum can be deduced from the track using the radius of curvature and the solenoid field strength. High momentum particles have less curved trajectories than low momentum particles. The collision vertex is the intersection of multiple particle trajectories at their origin. For vertex finding at least two reconstructed tracks are required as input. The primary vertices are

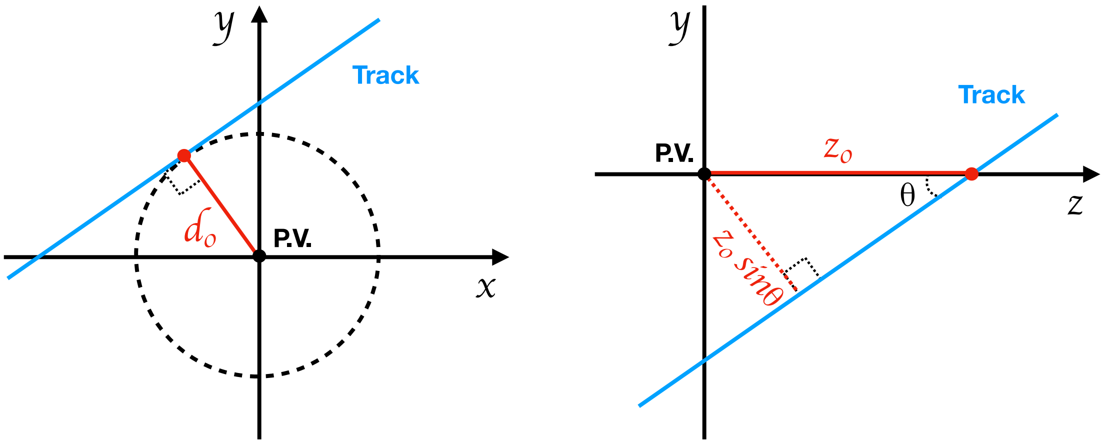

Figure 3.8.: Drawn in blue is the particle track, with the transverse and longitudinal impact parameters illustrated on the left and right graph respectively. The primary vertex (P.V.) is defined to be at the origin.

points in space where proton–proton interactions have occurred [42]. Track to vertex association is split into two stages:

- Vertex finding associates reconstructed tracks to potential vertex candidates
- Vertex fitting is the reconstruction of the vertex position, as well as an estimate on the quality of the fit [43].

These two steps are often interlaced in the algorithms. With a set of selected tracks and a vertex seed position, an iterative procedure is used to find the best vertex position. After the vertex position is computed, incompatible tracks are removed and regrouped with the non-selected tracks to be used in finding and fitting or another vertex.

3.3.2. Clustering algorithms

In the calorimeters, the signals are collected into related clusters. This is done to extract the significant signal coming from the hard scattering process from the noise [44]. In the calorimeters, the noise arises from two main sources: the readout electronics, and pile-up from non-primary interactions [45]. The clustering algorithms aim to group together the calorimeter cells, in three dimensions, in which incoming particles have deposited their energy. The clustering allows for the computation of the sum of the total energy deposited. Within ATLAS, there are two clustering algorithms: the sliding-window algorithm, and the topological algorithm. Both are summarised below and are described in detail in reference [45].

Sliding-window algorithm

The sliding-window algorithm first divides the $\eta - \phi$ space into a grid. All longitudinal cells' energies in each grid element is summed together to form rectangular prisms called towers. Next, a fixed sized window of $N_\eta \times N_\phi$ towers is used to scan across the grid in search of a local maximum above a chosen energy threshold. once found, it is used as a seed for the final step; cluster formation. Depending on the hypothesised particle type and the location in the calorimeter, the clusters pre-defined size in $\eta - \phi$ space varies [45]. Clusters are built by summing the energies of all cells within the defined size.

In cluster formation, the sliding window algorithm can form overlapping clusters if they share common cells. In these cases, the reconstruction algorithm (by default) includes the overlapping cells in both clusters, thus resulting in a double count of the energies of the shared cells. The disadvantage of this approach is that objects can be reconstructed with a larger energy that it had initially, due to the double counting.

Topological clustering

Unlike the sliding-window algorithm, topological clustering results in clusters that have variable cell sizes. The building of clusters starts by examining the cell signal significance ζ_{cell}, defined as

$$\zeta_{\text{cell}} = \frac{E_{\text{cell}}}{\sigma_{\text{noise,cell}}} \tag{3.9}$$

where the numerator is the energy deposited in the cell and the denominator is the average expected noise in the cell [44]. In building the topological clusters, three thresholds are defined. The seed threshold ζ_{seed}, the neighbour threshold $\zeta_{\text{neighbour}}$, and the baseline cell threshold ζ_{base}. Any cell whose cell significant is above the seed threshold is labelled as a seed cell, and forms a proto-cluster. The seed cells are ranked from high to low based on their ζ_{cell} value. From there, neighbouring cells that have not been used as a seed cell are added to the proto-cluster if their energy is above $\zeta_{\text{neighbour}}$, and also added to the neighbour seed list. If a neighbour cell is next to two

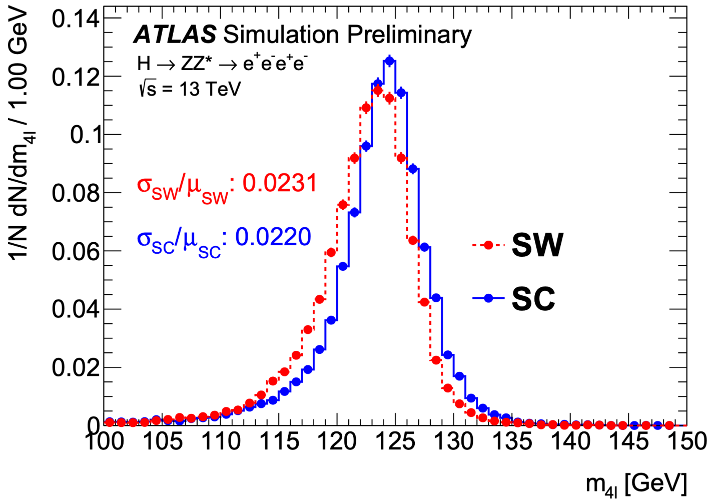

Figure 3.9.: Simulated 4 lepton invariant mass distributions using the super-cluster (SC) and sliding window (SW) algorithms, in the $4e$ channel. This figure is from Ref. [46].

proto-clusters, then the proto-clusters are merged. If ζ_{cell} is below $\zeta_{\text{neighbour}}$ but still above ζ_{base}, then the cell is added to the nearest neighbouring proto-cluster. After the original seed list is processed, it is discarded and the same procedure is repeated for neighbour seed list. This is done until no cells remain unprocessed.

The advantage to the topological clustering method, as opposed to the sliding window method, is that it allows for a more organic growth of clusters rather than pre-defining its size and shape. The algorithm is formed so that it closely traces the spatial signal-significance patterns generated by particle showers [46]. Furthermore, topological clustering requires smaller energy loss corrections. It has a very efficient energy resolution and collects more energy on average than sliding window clustering [46]. It is more complex to implement, however, and due to the dependency on noise levels, uncertainties from the electronics and pile-up directly affect the algorithm's reconstruction efficiency [45].

In reference [46], a topological clustering algorithm for electron and photon reconstruction is presented. It is demonstrated that this algorithm improves the energy resolution when compared to the traditional sliding window method. Figure 3.9 shows the resolution improvements in the $H \to 4\ell$ channel, taken from reference [46]. The topological cluster approach has a more narrow Higgs peak, and the peak is also closer to the true Higgs mass. After performing a fit with a double Crystal Ball function, the $4e$ channel shows a 5% improvement in resolution.

3.3.3. Electrons

Electron reconstruction

Following track candidate and calorimeter cluster candidate reconstruction as described in sections 3.3.1 and 3.3.2 comes the final procedure in electron reconstruction: the matching of a track candidate to a topo-cluster and the finalisation of the cluster size [47]. The algorithm prepares for reconstruction by first selecting the topo-custers and tracks it will use. The tracks are then refitted using a Gaussian sum filter (GSF) method [48] to accommodate for the energy loss due to bremsstrahlung radiation, which affects electrons more significantly than muons due to their lighter mass. As an electron loses its energy, its transverse momentum also decreases, and the curvature of its track becomes more prominent. The refit improves electron reconstruction efficiencies by correcting for this effect and improving the track parameters.

By extrapolating the track from the perigee to the second calorimeter layer and using the track's momentum, re-fitted tracks are matched to topological clusters. Sometimes the momentum of the track is rescaled to match the energy of the cluster, which improves matching accuracy for electron candidates that lose a portion of their energy to bremsstrahlung radiation [49]. In order for a track to match, the requirements $|\Delta\eta| < 0.05$ and $-0.10 < q \cdot (\phi_{\text{track}} - \phi_{\text{cluster}}) < 0.05$ must be fulfilled, where q is the charge of the track. The asymmetry of the latter requirement is due to radiated photons which clusters are able to measure, but tracks may miss [49].

Electron identification

Electron identification is done using a likelihood method that takes calorimeter shower shapes, tracking information, and cluster-track matching information as inputs. The advantages of this approach, as opposed to a cut-based approach, are twofold. The first is that a prompt electron may fail to be identified if it does not pass a singular selection criterion for cut-based identification. In a likelihood-based method, however, the electron may still be identified. Secondly, discriminants that are too similar to be used in a cut-based approach (because it would result in drops in efficiency) are easily added to the likelihood-based approach without penalty [47].

The ATLAS experiment carries out many physics analyses which require different signal efficiencies and background rejection rates. For this reason, the likelihood-based discriminant takes on fixed values for discrete working points [47]. These working points are namely loose, medium, and tight, each corresponding to increasingly stringent thresholds. In Run 2, the electron candidates satisfying the tigher criteria are a subset of those satisfying the looser criteria. The efficiencies are 93%, 88%, and 80% for identifying a 40 GeV electron in the loose, medium, and tight working points respectively. The medium and tight operating points have lower efficiencies and consequently a factor of 2.5 and 5 times higher fake electron rejection rates, respectively.

For the ATLAS four lepton analysis of this thesis, the Loose electron identification working point is chosen following the studies of the $H \rightarrow 4\ell$ analysis [50]. In terms of tracking criteria, this requires a minimum of two hits in the pixel detector, and seven total hits in the pixel and SCT combined. The Loose likelihood selection originally made to match and improve the previous ATLAS Multilepton working point, a cut-based selection optimized for the $H \rightarrow 4\ell$ analysis [51].

Electron isolation

Isolation is an important step in distinguishing prompt electrons in signal processes, from misidentified hadrons, semi-leptonic heavy quark decays, and other such background processes. Signal processes are usually characterized as being well isolated; there is little activity in the surrounding cells of the signal object in the calorimeter and the inner detector alike. In order to quantify the amount of activity surrounding the object of interest, a cone is defined around the electron's trajectory and the signal inside that cone (excluding the electron itself) is summed. There are two types of variables considered for isolation, one that is calorimeter-based and one that is track-based [47].

The calorimeter isolation, $E_{\mathrm{T}}^{\mathrm{iso}}$, is the transverse energy sum of topological clusters in a cone around the electron candidate. The value is fully corrected by subtracting the E_{T} of the underlying event and effects from pile-up [47,52]. The track isolation, $p_{\mathrm{T}}^{\mathrm{iso}}$, is similarly obtained by taking the scalar p_{T} sum of $p_{\mathrm{T}} > 1$ GeV tracks that satisfy basic quality requirements in a cone around the electron candidate. To minimise the effects from pile-up, a requirement on the product of the longitudinal impact parameter and the sine of the polar track angle, $|z_0 \sin\theta| < 3$ mm, is imposed [47]. This requirement selects tracks whose vertex is also the relevant vertex of the process.

The various working points for track isolation are described in detail in references [47,49]. The leptons in the relevant analysis of this thesis use the FixedCutPflowLoose isolation working point, with $E_{\mathrm{T}}^{\mathrm{iso}}/E_{\mathrm{T}} < 0.2$ and $p_{\mathrm{T}}^{\mathrm{iso}}/p_{\mathrm{T}} < 0.15$ for electrons.

3.3.4. Muons

Muon reconstruction

Muons come in various types depending on the what subdetector information was used in reconstruction [53]. In total there are four classes of muons: combined, segment-tagged, calorimeter-tagged, and extrapolated. Most reconstructed muons are combined muons, indeed, these are the purest of the four identification categories with the smallest percentage of fakes. Combined muons have tracks reconstructed independently in the inner detector and the muon spectrometer, and a global refitting procedure is used to combine the tracks. Segment-tagged (ST) muons are those with a track in the inner detector that is outwards extrapolated to at least one matched track segment in the muon spectrometer. Segmented tracks occur to muons with lower momentum, and in regions of the muon spectrometer with acceptance holes. Calorimeter tagged muons refer to a muon with an identified track in both the inner detector that is matched to a MIP-like energy cluster in the calorimeter. Of all the muon types this is the one with the lowest purity. As it does not rely on the muon spectrometer, its role is to recover the coverage gap around $\eta = 0$. Lastly, extrapolated muons (synonymously standalone muons) are reconstructed without an inner detector track, and are based only a full muon spectrometer track. These types are mainly used to extend the muon coverage in the high-η region where the inner detector has no coverage.

These four types of muons exists because muons offer an extremely clean signal in the detector, and therefore they can afford to be further categorised. Figure 3.10 illustrates the detector profiles of each type of muon. In the high multiplicity four lepton channel, the signal is particularly sensitive to changes in lepton acceptance. For the 4μ channel (the flavour channel with the highest resolution), the slightest improvement in muon acceptance will cascade into a significant overall acceptance.

Muon identification

Muon identification is carried out with a cut-based approach [55]. The main backgrounds coming from hadron decays (mostly charged pion and kaon decays) are suppressed by applying quality requirements that select for prompt muons with high efficiency that provide robust momentum measurements.

There are three identification variables used in discriminating a prompt muon from a background muon. These are:

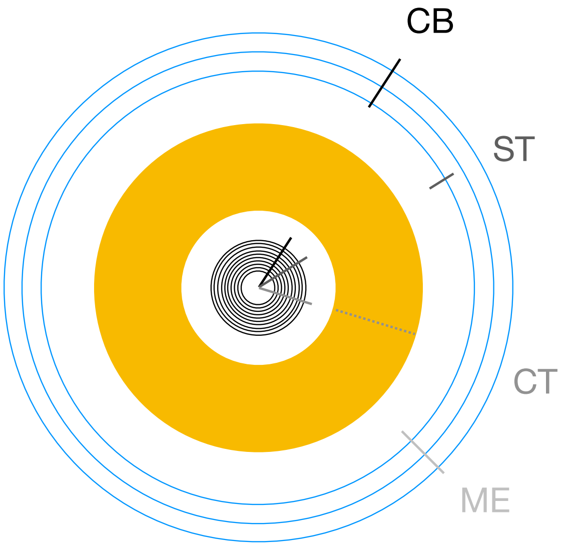

Figure 3.10.: Cross-sectional view of the ATLAS detector and how muon types are identified. The inner black lines represent the inner detector, the yellow is the calorimeter, and the outer blue lines are the muon spectrometer. This figure is adapted from [54].

- the q/p significance, $\frac{q/p}{\sigma_{q/p}}$, the absolute value of the difference between the muon's charge to momentum ratio as measured in the inner detector and the muon spectrometer, divided by the sum in quadrature of the corresponding uncertainties $\sigma_{q/p}$;
- $\rho' = \frac{p_{\mathrm{T}}^{\mathrm{ID}} - p_{\mathrm{T}}^{\mathrm{MS}}}{p_{\mathrm{T}}^{\mathrm{CB}}}$, the absolute value of the difference between the transverse momentum measurements in the inner detector and the muon spectrometer, divided by the transverse momentum of the combined track;
- the nomalized χ^2 of the fit of the combined track.

Together these variables are sensitive in filtering out candidates from charged hadron in-flight decays in the inner detector. These have a topological "kink" that results in a combined track with poor fit quality, and incompatible momentum measurements coming from the inner detector and muon spectrometer.

Various identification criteria are employed to target the diverse needs of physics analyses. Just like electron identification, the Loose, Medium, and Tight muon identification working points define progressively more restrictive requirements. Unlike the electrons, however, these working points differ not in the thresholds of a likelihood.

Rather, they differ in the type of candidate muons permitted and in the requirements on the three variables defined above.

The Loose muon identification criteria are chosen for the ATLAS work of this thesis, where all four types of reconstructed muons are used. The calorimeter tagged and segment tagged muons are restricted to a smaller region of $|\eta| < 0.1$. This working point is designed to maximise reconstruction efficiency all the while providing good-quality tracks [56]. They were specifically optimised for an ATLAS Higgs analysis in the four-lepton final state [50].

Muon isolation

Just like electrons, muons have additional isolation requirements imposed to reject background, because muons originating from vector boson decays are often isolated while those originating from semileptonic decays are often embedded in jets. The activity around a muon candidate is therefore measured, in a similar manner to that of the electrons, by summing a cone of transverse momentum and transverse energy in the tracking detector and calorimeter respectively.

The tracking isolation is $p_{\mathrm{T}}^{\mathrm{varcone30}}$, defined as the scalar transverse momenta sum of tracks with $p_{\mathrm{T}} > 1$ GeV in a cone of size $\Delta R = \min\left(\frac{10}{p_{\mathrm{T}}^{\mu}}, 0.3\right)$ around the muon candidate. The contribution from the muon track itself is subtracted. The variability in cone size is to ameliorate performance for high p_{T} muons [56]. Likewise, the calorimeter isolation variable, $E_{\mathrm{T}}^{\mathrm{topocone20}}$, is the sum of the topological energy clusters in a $\Delta R = 0.2$ cone around the muon, with the energy deposit of the muon and pile-up effects subtracted. Various definitions for the discriminant variables are used to setup different working points. For the four lepton analysis, the FixedCutLoose working point is chosen, with $p_{\mathrm{T}}^{\mathrm{varcone30}}/p_{\mathrm{T}}^{\mu} < 0.15$ and $E_{\mathrm{T}}^{\mathrm{topocone20}}/p_{\mathrm{T}}^{\mu} < 0.30$. The details of the various muon isolation working points can be found in reference [56].

Chapter 4.

$m_{4\ell}$: A measurement designed for re-interpretation

4.1. Motivation for the $m_{4\ell}$ measurement

The four lepton final state is a particularly interesting channel to study as it receives contributions from many physics processes. The predicted cross-sections for these processes are shown as a function of the invariant four-lepton mass in Figure 4.1. First and foremost, there is the production of a pair of Z-bosons via quark-antiquark interactions in both the t- and u-channel, drawn in red in Figure 4.1. The t-channel diagram is shown in Figure 4.2a, and represents, by far, the largest contribution to the ZZ production and thus to the $m_{4\ell}$ distribution. At low masses where $m_{4\ell} = m_Z$, single resonant $Z \to 4\ell$ production through QED radiative processes leads to a peak in the spectrum via the s-channel diagram in Figure 4.2b. At $m_{4\ell} = 180$ GeV and beyond, the threshold for the on-shell production of two Z bosons is reached and results in a peak in the four lepton invariant mass spectrum.

Second in magnitude is the gluon-induced production of a Z boson pair as shown in dark blue in Figure 4.1, and the corresponding Feynman diagram is shown in Figure 4.2c. This occurs via a triangle or box quark loop, which results in a factor α_s^2 suppression. It still plays a substantial role, however, because at small x[1] gluon-gluon luminosity is higher than the quark-antiquark luminosity [58]. The contribution from this process in on the order of ten percent [59].

---

[1] Here x is the component of the proton's momentum carried by the struck quark. At the LHC the protons have very high energies; therefore the LHC can be described as a small x collider [57]

Aside from Z boson pair contributions, there is a small contribution from decaying Higgs bosons. The Higgs bosons are produced also via gluon fusion, as illustrated in Figure 4.2d. There is resonant Higgs production at $m_{4\ell}$=125 GeV, and a non-resonant enhancement at $m_{4\ell} = m_t = 350$ GeV from the top quark loop. Beyond 350 GeV, the Higgs-mediated Z boson pair production process destructively interferes with continuum production of on-shell Z bosons [60]. The Higgs contribution is illustrated by the cyan line in Figure 4.1.

Finally there are small SM contributions from top-quark pair production in association with a dilepton pair (orange line in Figure 4.1), from triboson processes where at least two bosons decay leptonically (purple line in Figure 4.1), and from events where τ-leptons decay to muons or electrons.

The $m_{4\ell}$ distribution can be a useful probe for certain new physics scenarios. Take for example, the high mass tail of the invariant mass spectrum. This region is dependent on the couplings of the Higgs to incoming and outgoing particles while independent of the Higgs boson width [60], a unique property that can be exploited to derive model-independent limits on the Higgs couplings, and on the contribution of new states in the Higgs to gluon coupling [61]. It has also been previously exploited to derive model-independent constraints on the Higgs boson width [62].

A previous iteration of the $m_{4\ell}$ by the ATLAS collaboration using 36 fb^{-1} of data can be found in Reference [63]. For the analysis presented in this chapter, the data used corresponds to 139 fb^{-1} at $\sqrt{s} = 13$ TeV, including the 36 fb^{-1} of the previous iteration, collected by the ATLAS detector during Run 2 of the LHC between 2015 and 2018. Compared to the previous round, the new $m_{4\ell}$ measurement takes advantage of the increased data statistics and focuses on improving inclusivity and acceptance (particularly in the low mass region), and maximizing reinterpretability. Unlike the previous iteration of the four-lepton analyses and other dedicated $ZZ \to 4\ell$ analyses [64, 65], the new inclusive $m_{4\ell}$ analysis does not have an upper mass cut on the lepton pairs. In addition, the lower $m_{\ell}\ell$ limit has been simplified to be 5 GeV for all lepton pairs. In the previous round of Reference [63], the $m_{4\ell}$ mass lower limit was at 80 GeV. With improved statistics this is now at 20 GeV. The full set of changes in comparison to the previous analysis can be found in the internal note [66].

This chapter presents the inclusive four-lepton measurement using 139 fb^{-1} of data in full, with a stronger focus on the unfolding studies on which the author contributed. The analysis is published in Reference [67], from which certain sections are adapted.

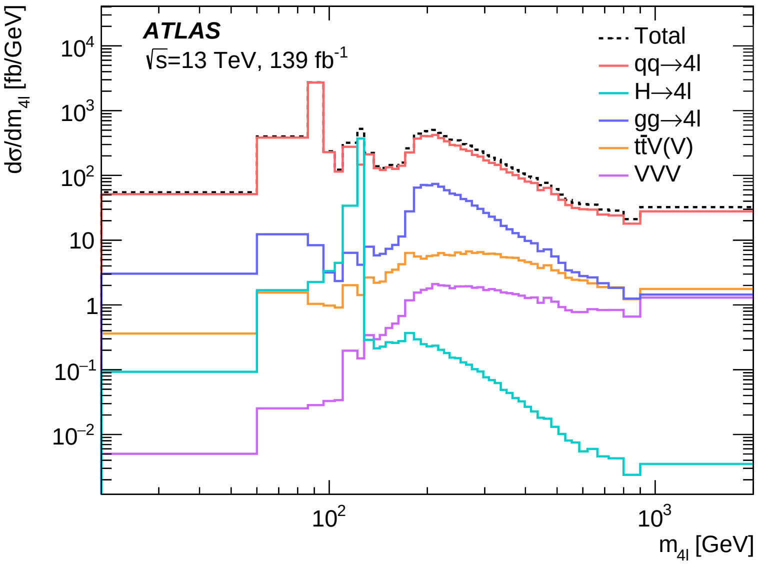

Figure 4.1.: Breakdown of contributing processes in the $m_{4\ell}$ distribution as modelled by Monte Carlo simulation are shown in the solid coloured lines. The total of all processes is represented by the dotted black line.

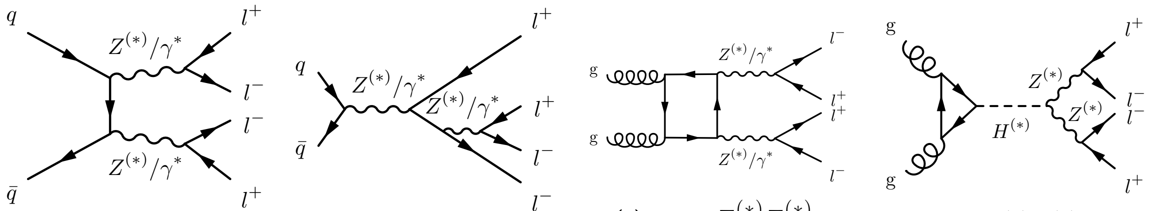
q
$\bar{q}$
$Z^{(*)}/\gamma^*$
$Z^{(*)}/\gamma^*$
l^+
l^-
l^-
l^+
q
$\bar{q}$
$Z^{(*)}/\gamma^*$
$Z^{(*)}/\gamma^*$
l^+
l^+
l^-
l^-
g
g
$Z^{(*)}/\gamma^*$
$Z^{(*)}/\gamma^*$
l^-
l^+
l^+
l^-
g
g
$H^{(*)}$
$Z^{(*)}$
$Z^{(*)}$
l^+
l^-
l^-
l^+

(a) $q\bar{q} \to Z^{(*)}Z^{(*)}$ **(b)** $Z \to 4\ell$ **(c)** $gg \to Z^{(*)}Z^{(*)}$ **(d)** $H \to Z^{(*)}Z^{(*)} \to 4\ell$

Figure 4.2.: Feynman diagrams for quark- and gluon-induced ZZ production. The processes shown are the main contributors. This figure is from Ref. [67].

4.2. Fiducial region

The motivation behind this analysis is to make a measurement as inclusive and as model-independent as possible. Any process leading to a final state of four leptons - made up of two same flavour opposite sign electron or muon pairs - is considered to be part of the signal. Electrons or muons originating from fully leptonic decays of taus are counted towards the signal. This section describes the fiducial region definition of the analysis, summarized in Table 4.1, which follows closely the acceptance of the detector.

The signal is defined solely in terms of final state particles as opposed to targeting a specific process. Beyond the requirement of two same flavour opposite sign lepton pairs, the measurement is inclusive to additional particles such as additional leptons, jets, and invisible particles. Contributions from triboson production and vector boson production in association with top quarks are considered to be part of the signal since they produce four or more prompt leptons. In general, it is good practice to avoid the subtraction of so-called "irreducible backgrounds" (which invariably introduces a theory dependence) and instead make measurements defined solely in terms of the final state signature.

In context of this analysis, a prompt lepton simply means the lepton did not originate from a hadron. Prompt leptons are further classified into three categories depending on their association with emitted photons. These three categories are:

- Born leptons: leptons prior to QED Final State Radiation (FSR);
- Bare leptons: leptons after QED FSR;
- Dressed leptons: leptons after QED FSR, that then have the four momenta of nearby radiated photons added.

All experiments make lepton measurements after QED FSR has occurred. It is for this reason that Born leptons are not the best choice. It is more realistic to perform measurements involving only final state particles, and objects constructed from final state particles, such as dressed leptons [68]. In this analysis, a choice of dressing electrons but leaving muons bare was made to closer mimic what is seen by the detector. This choice is studied in detail in the internal note of the analysis [66]. The leptons are required to satisfy p_T and $|\eta|$ requirements motivated by detector acceptance. For electrons, the p_T must be greater than 7 GeV and $|\eta| < 2.47$. Muons must have p_T >5 GeV and $|\eta| < 2.7$.

Events must contain a minimum of four leptons formed of two same-flavour, opposite-sign electron or muon pairs. Additional requirements are set on the transverse

Electrons	Dressed, $p_T > 7$ GeV, $\lvert\eta\rvert < 2.47$
Muons	Bare, $p_T > 5$ GeV, $\lvert\eta\rvert < 2.7$
Four-lepton signature	Minimum four leptons Two same-flavour, opposite-sign electron or muon pairs
Lepton kinematics	Leading lepton $p_T > 20$ GeV Sub-leading lepton $p_T > 10$ GeV
Lepton separation	$\Delta R > 0.05$ between all leptons
J/ψ-Veto	$m_{\ell\ell} > 5$ GeV for all SFOS pairs
Truth isolation	$\frac{p_T(\Delta R = 0.3)}{p_T(\text{lepton})} < 0.16$
Quadruplet selection	The two SFOS pairs closest to m_Z are assigned as the primary and secondary pair

Table 4.1.: Fiducial region definition at truth level.

momentum of the leading and sub-leading lepton to be higher than 20 GeV and 10 GeV respectively. A lepton angular separation requirement of $\Delta R > 0.05$ is applied to all leptons. A cut on the invariant mass of all SFOS lepton pairs is made at 5 GeV. The motivation behind these cuts and described in Section 4.4.

Finally, an emulation of the reconstruction-level isolation criteria is included in the fiducial region definition. Although the particle-level application is a simplification, it nevertheless returns a result that is closer to what is actually measured. The particle-level truth isolation criteria requires the sum of the transverse momentum of all charged particles inside a $\Delta R = 0.3$ cone of the lepton, divided by transverse momentum of the lepton itself, to be less than 0.16. If any other selected leptons are within the cone, their momenta is not included.

4.3. Measured observables

The star observable of the analysis is none other than the four lepton invariant mass, $m_{4\ell}$. It has been measured previously by both the ATLAS and the CMS experiment [63,69,70]. As with the previous round of the analysis, the $m_{4\ell}$ distribution is also measured double-differentially, in slices of the transverse momentum of the four lepton system, the absolute rapidity of the four lepton system, and the flavour channel of the four lepton system. These double-differential distributions provide a greater sensitivity to the $gg \to Z^{(*)}Z^{(*)}$ production rate. The $p_{\mathrm{T},4\ell}$ observables provide insight into the potential presence of anomalous triple gauge couplings, while the contribution by the off-shell s-channel Higgs boson mediated production channel can be probed with the $m_{4\ell}$–$y_{4\ell}$ distribution. The double differential with respect to lepton flavour channel allows for lepton universality cross-checks [63].

New to this round of the analysis is the division of the four lepton invariant mass spectrum into four separate regions, each dominated by a different process. From 60 GeV-100 GeV resonant single Z production reigns, similarly the 120 GeV–130 GeV region is dominated by Higgs production, and the high mass region from 180 GeV–2000 GeV by on-shell ZZ production. Lastly filling the gaps between 20 GeV–60 GeV, 100 GeV–120 GeV, and 130 GeV–180 GeV is the off-shell ZZ region. This is summarized in Table 4.2. A number of observables are measured within these mass slices, largely motivated by the ATLAS 13 TeV $ZZ \to 4\ell$ measurement [65]. Some of them are particularly motivated: the azimuthal-angle separation and rapidity difference between the Z boson candidates probe their angular correlations and may help extract the contribution of double-parton-scattering $Z\,Z$ production [65]. The azimuthal-angle separation is also sensitive to radiation of partons and photons produced in association with the $Z\,Z$ pair [65].

All the measured distributions are listed below. First are the single differential $m_{4\ell}$ distribution and the distributions measured as a function of $m_{4\ell}$:

- Single-differential $m_{4\ell}$
- $m_{4\ell}$ in slices of the four-lepton quadruplet transverse momentum, $p_{\mathrm{T},4\ell}$
- $m_{4\ell}$ in slices of the absolute rapidity of the quadruplet $y_{4\ell}$
- $m_{4\ell}$ in the decay channels $4e, 4\mu$, and $2e2\mu$.

The following variables are measured double differentially in the four $m_{4\ell}$ regions:

- Cosine of angle θ^*, where θ^* is the angle between the negative lepton in the di-lepton rest frame (leading pair) and the di-lepton pair in the lab frame (sub-leading pair). This angle is sensitive to the polarization of the decaying boson. This is measured for the primary and secondary lepton pair, $\cos\theta^*_{12}$ and $\cos\theta^*_{34}$
- The difference in rapidity between the lepton pairs $|\Delta y_{\mathrm{pairs}}|$

Region	$m_{4\ell}$interval(s)
$Z \to 4\ell$	60 GeV < $m_{4\ell}$< 100 GeV
$H \to 4\ell$	120 GeV < $m_{4\ell}$< 130 GeV
on-shell ZZ	180 GeV < $m_{4\ell}$< 2000 GeV
off-shell ZZ	20 GeV < $m_{4\ell}$< 60 GeV, 100 GeV < $m_{4\ell}$< 120 GeV, and 130 GeV < $m_{4\ell}$< 180 GeV

Table 4.2.: The four $m_{4\ell}$ regions dominated by the single Z, Higgs, on-shell ZZ and off-shell ZZ processes.

- The difference in azimuthal angle between the lepton pairs, and between leading leptons, $|\Delta\phi_{\text{pairs}}|$, $|\Delta\phi_{\ell\ell}|$
- The invariant mass of the lepton pairs m_{12} and m_{34}
- The transverse momentum of the lepton pairs $p_{\text{T},12}$ and $p_{\text{T},34}$

4.4. Event reconstruction and selection

A critical aspect of any analysis is its event selection. The dominant backgrounds are shaped by the selection choices, and signal sensitivity are enhanced with optimized cuts. The objective of the selection in this analysis is to efficiently identify the four lepton final states while keeping the background at a minimum. This is achieved through a combination of online trigger (described in detail in Section 3.2.5) and offline event selection cuts. As with all ATLAS analysis, basic requirements on the event cleaning are imposed. Only data recorded with stable beam conditions and with all relevant information from sub-detectors present are considered.

The requirements on event selection are outlined in Tables 4.4 and 4.5. The cuts are largely based on the fiducial region definition of Table 4.1 combined with the limited acceptance and efficiency of ATLAS's object reconstruction. This ensures that there is little to no extrapolation into unmeasured regions on phase space when unfolding.

First there is the selection of baseline electrons and muons. For both the Loose identification working point is used. For electrons there is a minimum requirement of p_T >7 GeV and $|\eta| > 2.7$. For muons it is p_T >5 GeV and $|\eta| > 2.47$, and if the muon is a calorimeter-tagged muon there is a more stringent p_T >15 GeV requirement to account for their lower purity. The vertex association requirement ensures that the leptons are associated to the primary vertex in the event. Lastly a lepton-favoured overlap removal is applied to ensure that objects are reconstructed with some distance in between. In the event where a lepton and a jet overlap, priority is given to the lepton. The events that pass these criteria (listed in Table 4.4) are classified as baseline leptons.

Additional lepton kinematic requirements are imposed on the leptons after overlap removal. The leading and sub-leading lepton must have a transverse momentum higher than 20 GeV and 10 GeV respectively in order to maintain a high trigger 449 efficiency and minimize the reducible background in the low mass region. The minimum separation between leptons is set at $\Delta R = 0.05$ in order to suppress contributions from fake leptons. A J/ψ mass cut at 5 GeV is imposed on all same-flavour-opposite-sign lepton pairs, and also due to generator-level cuts in the MC samples used. The Υ contribution is very small, and no mass cut is imposed to suppress it. It is instead subtracted alongside the reducible background from the SM predictions prior to unfolding.

Next, a quadruplet is formed from the baseline leptons containing two same-flavour, opposite-sign (SFOS) lepton pairs. The lepton pair with an invariant mass closest to the Z mass is the primary pair. Of the remaining leptons, the SFOS pair with an invariant mass closest to the Z mass is designated as the secondary pair. These are synonymously referred to as the leading and sub-leading lepton pair, respectively. The baseline leptons chosen to form the quadruplet undergo a final set of selection cuts outlined in Table 4.5. An isolation requirement is imposed to ensure robustness against pile-up. Contributions from other baseline leptons in the vicinity are subtracted from the isolation variables to ensure that the analysis remains sensitive to highly collimated leptons. Background from cosmic-ray muons is suppressed by requiring that a muon's transverse impact parameter $|d_0| < 1$ mm. Each lepton's impact parameter must satisfy a requirement on its significance with respect to the beam line,

$$\mathrm{S}_{d_0} \equiv \frac{d_0}{\sigma_{d_0}} \tag{4.1}$$

where d_0 is the transverse impact parameter and σ_{d_0} is the associated uncertainty. S_{d_0} must be smaller than three for muons, and five for electrons. Finally, electrons are subjected to an additional identification criterion requiring a hit in the innermost pixel layer. LooseBLayer is a variation of the Loose working point [67].

Like so, the signal region used in the measurement is defined as the subset of events where all four baseline leptons pass all the signal lepton cuts. Those with baseline lepton(s) that fail the additional cuts of Table 4.5 are not included in the measurement.

Category	Requirement
Event Preselection	Fire at least one lepton trigger $\geq$1 vertex with 2 or more tracks
Four-lepton signature	At least 4 leptons (e, μ)
Lepton kinematics	$p_{\mathrm{T}} > 20/10$ GeV for leading two leptons
Lepton separation	$\Delta R_{ij} > 0.05$ for any two leptons
J/ψ-Veto	$m_{ij} > 5$ GeV for all SFOS pairs
Trigger matching	Baseline leptons matched to at least one lepton trigger
Quadruplet formation	At least one quadruplet with 2 Same-Flavour, Opposite-Sign (SFOS) pairs
Quadruplet categorisation	4 signal, 0 non-signal: signal region $\leq$ 3 signal, $\geq$ 1 non-signal: background control region

Table 4.3.: Definition of the reconstruction-level event selection. This table is from Reference [66].

Category	Requirement	
Kinematics	Muons :	$p_{\mathrm{T}} > 5$ GeV
		If CaloTag: $>$15 GeV
		$\lvert\eta\rvert < 2.7$
	Electrons:	$p_{\mathrm{T}} > 7$ GeV
		$\lvert\eta\rvert < 2.47$
Vertex association	Both :	$\lvert z_0 \sin\theta\rvert <$0.5 mm
Identification:	Muons:	Loose ID
	Electrons:	LooseLH ID
Overlap removal: Lepton-favoured		
Additional kinematics	Leading lepton	$p_{\mathrm{T}} > 20$ GeV
	Sub-leading lepton	$p_{\mathrm{T}} > 10$ GeV

Table 4.4.: Definition of the baseline lepton event selection. This Table is from Reference [66]

Input objects	Baseline electrons and muons that are part of the quadruplet
Isolation	FixedCutPflowLoose working point *Contribution from all other baseline leptons is subtracted*
Cosmic muon veto	Muons: $\lvert d_0 \rvert$ <1 mm
Impact Parameter	Muons: d_0/σ_{d_0} <3 Electrons: d_0/σ_{d_0} <5
Stricter Electron ID	Electrons: LooseBLayerLH ID

Table 4.5.: Definition of the signal lepton selection criteria applied to data. This table is from Reference [66].

4.5. Predictions from Monte Carlo Event Generators

4.5.1. Overview of Monte Carlo Event Generators

Monte Carlo Event Generators (MCEG) play an important role in high energy physics. Generators such as Herwig [71], PYTHIA8 [72] and SHERPA [73] amongst others are essential in data analysis. Together with programs that simulate the detector effects, they are used to estimate the signal and background distributions of various processes. This section gives a brief review of how MCEGs simulate proton-proton collisions, drawing from References [9,74,75], to which the readers may refer to for for an in-depth review.

Protons are composite particles. In order to model how they collide on an event-by-event basis at the LHC, one must model how the partons (valence quarks, sea quarks, and gluons) behave. To achieve this complex goal, the event must be broken up into several phases, each produced via different techniques and occupying a unique region in phase space. QCD is weakly interacting at short distances. Therefore the components of the MCEG dealing with short-distance physics are based on perturbation theory [76]. At larger distances, all soft hadronic phenomena such as hadronization and the formation of the underlying event in hadron collisions cannot be computed from first principles [76]. Instead, one must rely upon other models. This is the general idea behind the factorization theorem [77]. Schematically, a hadron-hadron cross section can be written as

$$\sigma^{\text{h-h}} = \sum_{i,j} \int dx_1 dx_2 f_i(x_1, \mu_F^2) f_j(x_2, \mu_F^2) \hat{\sigma}_{ij}(x_1, x_2, Q^2/\mu_F^2, \ldots). \tag{4.2}$$

An important concept of the factorization theorem is the Parton Distribution Function (PDF). Written as $f_i(x, \mu_F^2)$, this corresponds to the probability to find a parton of flavour i in the proton as a function of the fraction x of the proton's momentum carried by the parton and μ_F^2 the energy scale of the hard interaction. μ_F is often referred to as the factorization scale. Since QCD does not predict the parton content of the proton, the dependence of the PDFs on energy scale and momentum fraction are determined by a fit to data from experimental observables in various processes [78].

The event simulation starts at the heart of the collision: the hard scatter. In Figure 4.3, this is the central blob in red. The hard scatter is the one with the largest transfer of energy between the two colliding partons. This is relatively straight-forward to simulate to some fixed order via the matrix element prescription. Nowadays for matrix element calculators, it is standard for most processes to calculate up to Next-to-Leading-Order (NLO), so as to include loop radiative correction. While including higher-order corrections reduces theory uncertainty [79], it is computationally expensive.

Another important aspect of event generation is the parton shower, which connects the matrix element to the produced and observed hadrons. These are the squiggly branch structures illustrated in Figure 4.3. The parton shower describes what happens to the incoming and outgoing parton of the hard collision [74]. Since partons are coloured, they behave in a Bremsstrahlung-like fashion and radiate gluons as they move through a collision. Recall from Section 2.1 that gluons can also self interact and emit another gluon, leading to an extended shower of partons that is made up of mostly soft gluons [74]. The parton shower develops with decreasing values of a parameter that is a measure of the hardness of interactions [80]. It is an evolution in momentum transfer scale that starts from the hard process and works to lower momentum until a point is reached where perturbation theory breaks down [74].

As the parton shower branches, the QCD force grows until confinement takes over and results in the partons grouping together into colour-singlet hadrons, illustrated in bright green in Figure 4.3. This process is described using hadronization models. The hadrons simulated may not be stable, meaning that they decay inside the detector volume. The decays are modelled inside the simulations using information about hadron lifetime, branching ratios and hadron decay width [81]. Of course, aside from the hard collision there are lots of secondary interactions between the proton remnants [74]. This is referred to as the underlying event, sketched in purple in Figure 4.3. It produces soft hadrons everywhere in the event, which overlie and contaminate the hard process that was already simulated [74].

The MCEGs used to simulate four-lepton events for this analysis, along with key parameters such as PDF set and NLO corrections, are summarized in the next section. The MC samples are used in the design and optimization of the analysis, in evaluating the uncertainties, and in correcting the data from detector inefficiency and resolution effects.

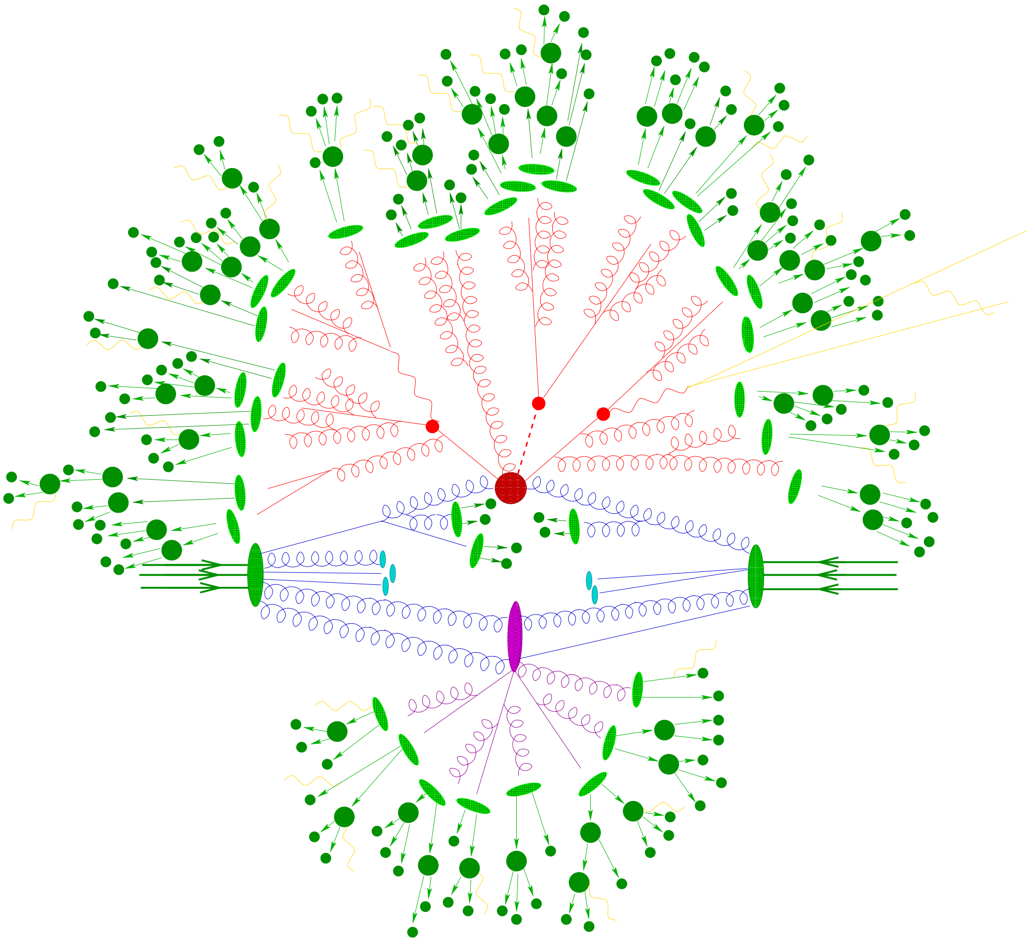

Figure 4.3.: This is a diagram of a simulated proton-proton collision. The hard collision is shown in the centre in red. In purple is the secondary hard scattering event. The parton shower is drawn in blue. Hadronisation is sketched in light green, and the subsequent hadron decays and final state particles are shown in dark green. Finally, the electromagnetic radiation is presented in yellow. This figure is from Reference [75].

Validation of V+jets production in Herwig7 with NLO multi-jet merging

As part of the ATLAS author qualification task, multi-leg merging at next-to leading order accuracy using the Matchbox framework [82] in Herwig7 was explored, with a focus on the vector boson plus jets process. Further details of the task and progression can be found on JIRA (AGENE-1453), and in the technical report of Reference [3].

4.5.2. Monte Carlo samples

This section provides a description of the event samples that are used for this analysis in the standard description of the ATLAS collaboration. These state-of-the-art predictions used to model the signal processes at detector-level and particle-level for this analysis, and to construct the response matrices that correct the data for detector effects.

4.5.3. $q\bar{q} \to 4\ell$

The dominant $q\bar{q} \to 4\ell$ process is simulated using the SHERPA2.2.2 event generator [83] with the `NNPDF3.0nnlo` set of PDFs [84]. The matrix elements are calculated at next-to-leading order accuracy for final states with zero and one jet, and at leading order accuracy for two- and three-jet final states. The different parton multiplicities are merged together and matched to the SHERPA parton shower model based on the Catani-Seymour dipole factorization [85] using the MEPS@NLO prescription [86–88]. A dedicated set of tuned parton-shower parameters developed by the SHERPA authors are used. An alternate sample of the $q\bar{q} \to 4\ell$ process is generated using POWHEGBOX v2 [89–91]. The sample is generated at NLO accuracy and interfaced to PYTHIA8 8.186 for the simulation of the parton shower, hadronization, and underlying event. The tuning parameters are set according to the AZNLO tune [92]. The sample is corrected to higher order effects using a k-factor obtained with MATRIX NNLO QCD prediction [93–96]. The k-factor is defined as the ratio of the NNLO cross-section to the NLO cross-section and applied as a function of $m_{4\ell}$. Virtual electroweak NLO effects are accounted for by reweighting both samples with a mass-dependent k-factor. The high-order real electroweak contribution of ZZ plus two jets is modelled separately in a SHERPA 2.2.2 sample.

4.5.4. $gg \to 4\ell$

The gluon-gluon initiated $gg \to 4\ell$ process is modelled by SHERPA 2.2.2 at leading order QCD for up to one additional parton emission. The SHERPA parton shower model based on the Catani-Seymour dipole factorisation is used. Also included in this sample is the s-channel Higgs signal $gg \left(\to H^{(*)} \right) \to Z^{(*)}Z^{(*)} \to 4\ell$ and its interference with the

SM box diagram, which has a sizeable contribution above 130 GeV. For particle-level masses below 130 GeV the sample includes on the $gg \rightarrow 4\ell$ box diagram because the role of interference is negligible. An NLO QCD K-factor is derived using the ratio of the SHERPA sample to an MCFM NLO sample [97]. This is applied as a mass-dependent weight. An additional constant K-factor of 1.2 is applied to account for NNLO effects on the off-shell Higgs production cross-section [98,99]. The sample has a generator cut of $m_{\ell\ell} > 10$ GeV for same-flavour, opposite-charge lepton pairs. The contribution is below this cut is accounted for through the reweighting to MCFM prediction. Scale and PDF uncertainties are derived in the same way as for the SHERPA $q\bar{q} \rightarrow 4\ell$ sample.

4.5.5. On-shell Higgs

The resonant Higgs-boson production is an important process and is generated independently using the most precise description available. The SM Higgs can be produced via gluon-gluon fusion, vector-boson fusion (VBF), Higgstrahlung (VH), and in association with a top quark pair ($t\bar{t}H$). The `PDF4LHC15nnlo` and `PDF4LHC15nlo` PDF set [100] are used, alongside AZNLO tune for all on-shell Higgs samples. The dominant gluon–gluon fusion production channel is simulated using the POWHEG NNLOPS program [89,101–104] at NNLO accuracy in QCD, and matched to PYTHIA8 [105] for the simulation of the parton shower and non-perturbative effects. The sample is normalized to N^{3}LO in QCD cross-sections, which has been calculated for the gluon-fusion process, and corrected for NLO electroweak effects [99,106–115]. POWHEG [89,103,104,116] is interfaced to PYTHIA8 for the vector-boson fusion process, the WH and ZH production process, and the small contribution from associated productions with a $t\bar{t}$ pair. All are estimated with matrix elements up to NLO in QCD. For VBF, the prediction is reweighted to an approximate-NNLO QCD cross-section with NLO electroweak corrections [117–119]. For VH, the prediction is normalized to an NNLO QCD cross-section calculation with electroweak NLO corrections [120–124]. The uncertainties for the on-shell Higgs samples are identical of that of a previous Higgs analysis, the largest of which are from the QCD scale and PDF uncertainties. A detailed description can be found in Reference [125].

4.5.6. VVV and $t\bar{t}V(V)$

A smaller contribution to the four-lepton final state originates from triboson processes, and vector-boson production in association of top-quark pairs. These are referred to as VVV (for WWZ, WZZ and ZZZ) and $t\bar{t}V(V)$ (for $t\bar{t}Z$ and $t\bar{t}WW$) respectively. The tribon processes are modelled with SHERPA 2.2.2 at NLO accuracy in QCD, with a Catani–Seymour dipole factorization based parton shower provided by SHERPA. Two samples are provided for the $t\bar{t}V(V)$ contribution. The first is simulated with SHERPA 2.2.0 at LO accuracy up to final states with one additional jet. This sample is used to construct the response matrix used to correct the data for detector effects. The second prediction is produced with the MADGRAPH5_aMC@NLO 2.3.3 [126] generator at NLO accuracy interfaced to PYTHIA88.210 [105]. This particle-level predictions of this sample is used to compared against the data for the interpretations of Section 4.11. A flat uncertainty of ± 15% to account for the differences between the two samples is is assigned.

4.5.7. Corrections

All MC events are processed through GEANT4 [127] to simulate the expected response of the ATLAS detector. Next, the samples are passed through the same object reconstruction and identification algorithms as the data and the analysis selection is applied. Pile-up is simulated with PYTHIA8 8.186 as inclusive inelastic pp collisions. The events are then reweighted to reproduce the distribution of the mean number of interactions per brunch crossing (33.7 on average for the whole dataset). Lastly, events are reweighted to account for the differences of the lepton reconstruction, identification, isolation, and vertex-matching efficiencies between data and simulation.

4.6. Background estimation

4.6.1. Defining leptons

The four lepton channel is quite the golden channel, as it has a very clean signature with minimal background. The dominant background in this analysis is when one or more of the reconstructed leptons in the quadruplet are not real leptons; rather they are misidentified objects in the detector mimicking the same signature [128]. These "leptons" are non-prompt, and can be referred to as a fake lepton, whereas a lepton produced from the hard scatter is a prompt, real lepton. One source of fake leptons is from hadron decays. In the case of the electron, photon conversion and hadronic jets misidentified due to their large and narrow deposit in the electromagnetic calorimeter can also play a role. In this analysis, around three-quarters of the fakes originate from -hadron decays in Z+jets and $t\bar{t}$ events.

The size and behaviour of the fake lepton background - also referred to as the reducible background - is usually estimated using data-driven methods because they are not well modelled by simulation [128]. One such method is the Fake Factor method. This method depends on two sets of lepton criteria: a tight criteria that selects leptons which make it into the signal region, and a loose criteria that is similar but less restrictive. The leptons selected by the latter are referred to as baseline leptons, and the baseline leptons that additionally pass the tight criteria are the signal leptons. The rest of this section will also touch on baseline-not-signal leptons; these are leptons that pass the "baseline" loose selection, but do not make the "signal" tight selection.

4.6.2. Fake Factor method

The Fake Factor method relies on the calculation of a fake efficiency, f, which is the fraction of fake baseline leptons pass the tight selection criteria and become signal leptons. Because fake leptons not well modelled in simulation, the fake efficiency is calculated in data, in an alternative region of phase space that is enriched with fake leptons.

Using the Fake Factor F, the number of baseline leptons, and the number of real baseline leptons, the number of fake signal leptons can be calculated as

$$N_{\text{fake}}^{\text{signal}} = F(N^{\text{baseline}} - N_{\text{real}}^{\text{baseline}}). \tag{4.3}$$

Note that the FF method assumes good modelling in the real component of the simulation since $N_{\text{real}}^{\text{baseline}}$ is taken from MC. The method is described in detail in Reference [129].

Smoothing on the raw output of the reducible background estimate is performed. The raw output, due to low statistics in certain bins, have pronounced, jagged features that resemble resonances. Of course, resonant peaks should not exist. The smoothing procedure is therefore used to obtain a more even shape, minimizing the impact of any outlier bins that had a large Fake Factor weight. In order to smooth the distribution, an intermediate, finer binning is assigned to each observable and the background estimate is run. The fine-binned intermediate background distribution is smoothed with Friedman's super smoother [130]. Lastly, the final background estimate is obtained by integrating over the smoothed distribution using the coarser, original binning.

4.6.3. Fake background uncertainties

In the fake-factor background estimate, there are five sources of uncertainty considered:

1. Dominant in the low- and high-mass tails where $m_{4\ell}$< 150 GeV and $m_{4\ell}$> 350 GeV is the statistical uncertainty of the number of events with in the control region. This is propagated through the measurement via the bootstrap method [131].
2. The dominant uncertainty in the mid-range region 150 < $m_{4\ell}$< 350 GeV are the theory uncertainties associated with the subtraction of prompt-leptons in the control region. These come primarily from QCD scale variations in WZ events.
3. A smaller contribution comes from the uncertainties in the Monte-Carlo predictions. This covers the modelling of prompt baseline-not-signal leptons, which get subtracted from the background estimation.
4. Fourth is the statistical uncertainty in the control region data used for the calculation of the fake factor. This contribution is subdominant.
5. Lastly there is a very small uncertainty from the arbitrary choice of number of intermediate bins used in the background smoothing procedure. It is accounted for by comparing the nominal prediction using 500 bins with alternate predictions using 250 or 1000 bins.

4.7. Detector-level results

In this section the detector-level selected events are presented and compared to the SM predictions for the single Z, Higgs, on-shell ZZ and off-shell ZZ mass regions, and for the inclusive $m_{4\ell}$ distribution. The reducible background described in Section 4.6 is also included.

The number of selected events in the four $m_{4\ell}$ regions over the full fiducial phase space is presented in Table 4.6, along with the predicted number of events, and the predicted background contribution from non-prompt leptons. For the $q\bar{q} \rightarrow 4\ell$ process the SHERPA simulation is used. The combined uncertainties (systematic and statistical) are also quoted. The uncertainty in the total prediction takes into account correlations between processes, and therefore contributions in a given column do not trivially add up in quadrature to give the total. Uncertainties in the predictions arise from the sources discussed in Sections 4.6 and 4.9.

	Region				
	Full	$Z \to 4\ell$	$H \to 4\ell$	Off-shell ZZ	On-shell ZZ
$q\bar{q} \to 4\ell$	6100 ± 500	1490 ± 120	128 ± 10	800 ± 60	3640 ± 280
$gg \to 4\ell$	680 ± 90	10.8 ± 2.9	3.9 ± 0.7	49 ± 6	620 ± 80
$H \to 4\ell$	245 ± 20	2.16 ± 0.18	207 ± 17	33.5 ± 3.1	1.98 ± 0.20
VVV	35 ± 4	0.018 ± 0.005	0.127 ± 0.018	2.05 ± 0.22	32.9 ± 3.4
$t\bar{t}V$ (V)	123 ± 19	1.37 ± 0.22	1.2 ± 0.2	15.5 ± 2.4	105 ± 16
Background	330 ± 50	44 ± 8	26 ± 5	129 ± 19	139 ± 30
Total Pred.	7500 ± 500	1540 ± 110	367 ± 19	1030 ± 60	4530 ± 290
Data	7755	1452	379	1095	4828

Table 4.6.: Predicted reconstruction-level yields per process and in total, compared with observed data counts, over the full fiducial phase space and in the following regions of $m_{4\ell}$: $Z \to 4\ell$ ($60 < m_{4\ell} < 100$ GeV), $H \to 4\ell$ ($120 < m_{4\ell} < 130$ GeV), off-shell ZZ ($20 < m_{4\ell} < 60$ GeV or $100 < m_{4\ell} < 120$ GeV or $130 < m_{4\ell} < 180$ GeV) and on-shell ZZ ($180 < m_{4\ell} < 2000$ GeV). The background row is events with non-prompt leptons, including those from $Z + \mathrm{Y}$ events. The $H \to 4\ell$ row includes only the on-shell Higgs boson contribution, with off-shell contributions included in $gg \to 4\ell$. This table is from Reference [66].

Figure 4.4 shows the inclusive $m_{4\ell}$ distribution at the detector level. The data are plotted in black along with the uncertainties. The SM prediction is separated into the individual dominant processes described in Section 4.1 and plotted as stacked histograms. Overall the data are in good agreement with the predictions, with some minor fluctuations in the high mass bins due to low statistics. The detector-level plots for the rest of the observables are not shown in the scope of this thesis, but are published in Reference [67].

4.8. Correcting for detector effects

When an observable is measured by a particle physics experiment, it is important to note that the measured distribution, (i.e. what the particle detector sees) is not what truly occurs at the particle-level. Rather, it is a convolution of the underlying physics process with the effects of the detector. The ATLAS detector, although an astonishing feat of technology, is still subject to resolution, acceptance, and efficiency limitations. The data at the detector level is smeared and includes the effects of these limitations. For an inclusive measurement such as the four-lepton invariant mass distribution, it is often desirable to correct for these detector effects and present the data at the particle-

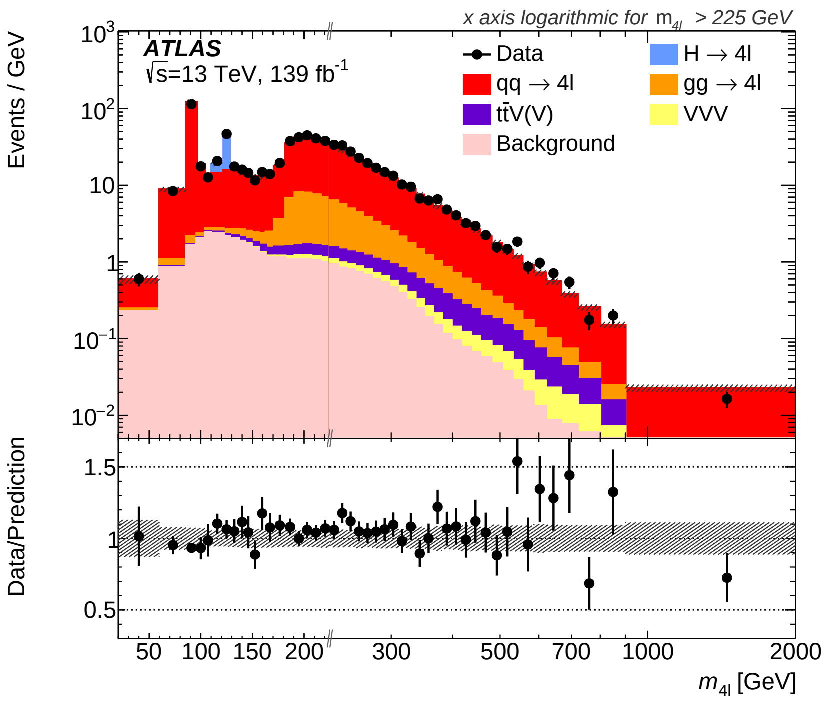

Figure 4.4.: Observed reconstruction-level $m_{4\ell}$ distribution compared with the SM prediction, using SHERPA for the $q\bar{q} \rightarrow 4\ell$ simulation. The statistical uncertainty of the data is displayed as error bars and systematic uncertainties in the prediction are shown as a grey hashed band. The ratio of the data to the prediction is shown in the lower panel. The x-axis is on a linear scale until $m_{4\ell} = 225$ GeV, where it switches to a logarithmic scale, as indicated by the double dashes on the axis. There is one additional data event reconstructed with $m_{4\ell} = 2.14$ TeV, while 0.4 events are expected from simulation for $m_{4\ell} > 2$ TeV. This figure is from Ref. [67].

level. In high energy physics, the term coined for this correction procedure is unfolding. Unfolding measurements and presenting them at the particle level has many advantages. In doing so, the measurement may be directly compared to theoretical predictions, as well as particle-level results from other experiments, in the years to come. Furthermore, they can be rapidly compared to newly available BSM simulations in re-interpretation studies. The concept of re-interpretation is further explored in Chapter 5.

4.8.1. Unfolding methodology

Unfolding in particle physics can be more generally referred to as a deconvolution. The generic problem statement of deconvolution is to derive a relationship between the true distribution $T(x)$ and the recorded distribution $D(y)$. The two are related by a smearing function $R(x,y)$, which encompasses the instrumentation effects in making the measurement.

$$T(x) = \int S(x,y)D(y)dy \tag{4.4}$$

Due to the discretised nature of histograms, the unfolding problem can be stated as a matrix equation:

$$x_i = S_{ij}y_j \tag{4.5}$$

where S represents the a smearing matrix of sorts, x_i is the true histogram at particle-level, and y_i is the reconstructed histogram at detector-level.

For the four-lepton invariant mass analysis, an iterative unfolding method motivated by Bayesian statistics, popularised by Giulio D'Agostini [130], is chosen. The method iteratively applies the three inputs described above to the measured distributions while using the particle-level SM prediction as a prior.

An iterative Bayesian approach to unfolding

Let there be a set of causes C_i, that can produce one effect E.

$$P(C_i|E) = \frac{P(E|C_i) \cdot P(C_i)}{\Sigma_{k=1} P(E|C_k) \cdot P(C_k)} \tag{4.6}$$

- $P(C_i|E)$: given the effect, the conditional probability that it was produced from the i-th cause.
- $P(E|C_i)$: for the i-th cause, the conditional probability that the effect is produced.
- $P(C_i)$ is the initial probability of the i-th cause.

If there are multiple possible effects for the causes, then the formula can be generalized to be:

$$P(C_i|E_j) = \frac{P(E_j|C_i) \cdot P(C_i)}{\sum_{k=1} P(E_j|C_k) \cdot P(C_k)} \tag{4.7}$$

The number of expected events for each cause C_i can be obtained by multiplying the number of observations made for effect j with the probability it had been due to cause i, and summing over all effects:

$$N(C_i) = \sum_j N(E_j) \cdot P(C_i|E_j). \tag{4.8}$$

Here a parallel can be drawn back to equation 4.5, where $N(C) = N(C_1), N(C_2), ..., N(C_n)$ represents the number of events in the n bins of the true histogram x_i, and $P(C_i|E_j)$ corresponds to R. Combining these equations, the procedure for estimating the true histogram can be written as:

$$x_i = \sum_{j=1}^{n} \frac{R_{ij} \cdot P(x_i)}{\sum_{k=1}^{n} R_{kj} \cdot P(x_k)} y_j. \tag{4.9}$$

Here the matrix defined as R_{ij} is the called the response matrix. The denominator in the equation is a normalization factor using the y-projection of the matrix. $P(x_i)$ is the prior, which is updated in each iteration with the unfolded true distribution x_i, also known as the posterior.

4.8.2. Unfolding inputs

Below is a summary of the terminology commonly used inputs in the unfolding procedure. These inputs are generated using the Monte Carlo simulations described in Section 4.5.2.

- Fiducial fraction f_i: this is a one-dimensional correction that accounts for events which do not enter into the fiducial region, but pass the detector-level selection nonetheless. These occur due to the finite resolution in the measurement the variables used to select events. The fiducial fraction is defined as the ratio of events that pass both fiducial and detector-level selection to events that pass detector-level selection only.

- Reconstruction efficiency ϵ_i: this accounts for the acceptance and efficiency of the detector in reconstructing an event. Of all the events that pass the fiducial selection, only a fraction will be successfully reconstructed and visible to the detector. Formally the reconstruction efficiency is also a one-dimensional correction; defined as the ratio of events which pass both the fiducial and detector-level selection to events that pass fiducial-level selection only.

- Migration matrix M_{ij}: each bin in the histogram of the measured observable represents a sub-range of observable values. Sometimes the detector may smear the observable's value high or low enough such that it gets filled to different bins in particle-level and detector-level. These are referred to as bin-to-bin migrations, and is corrected for by the migration matrix. This is constructed as a two-dimensional matrix using events which pass both fiducial and detector-level selection, with the value at particle-level on one axis and the value at detector-level on the other. The matrix, M_{ij}, represents the probability that an event which falls into bin i at particle-level will fall into bin j when reconstructed at the detector-level. The diagonal elements of the migration matrix is defined as the unfolding stability; the fraction of events in a particle-level bin which are reconstructed in same bin at detector level.

- Fiducial purity: similar to the unfolding stability, but not the same. The fiducial purity accounts for the probability that an event in the detector-level bin i originated from the same particle-level bin i.

The construction of the response matrix R_{ij} is done using the above inputs. It is defined as:

$$R_{ij} = M_{ij}\epsilon_j f_i. \tag{4.10}$$

The unfolding software used for this analysis (VIPUnfolding) takes the migration matrix, reconstruction efficiency, and fiducial fraction as inputs, and constructs the response matrix within the software.

Figure 4.5 shows the unfolding inputs for the inclusive $m_{4\ell}$ distribution. In the left panel there are the detector-level and particle-level yields, and in the right panel the fiducial fraction, reconstruction efficiency, and fiducial purity are plotted. The inputs here include the application of the pre-unfolding weight (see Section 4.8.4). The event count on the $y-$axis shows events per bin and serves as a visual check to ensure all bins have fourteen or more events. The fiducial purity in yellow, likewise, should always be above 0.6. The purity tends to be lower in the middle mass range and around the Z and Higgs peaks due to narrow bin widths. The fiducial fraction in blue is above 85% in all bins, levelling out to 95% for $m_{4\ell} > 200$ GeV. The efficiency in red is lowest below 80% for the first two mass bins, due to the higher inefficiency when reconstruction low mass electrons and muons.

The residual efficiency correction taking into account the pre-unfolding weights and the fiducial fraction for the full fiducial phase-space as well as for each of the four $m_{4\ell}$ slices are shown in Table 4.7. In order to illustrate the effect of the pre-unfolding and to show what the size of corrections would be if pre-unfolding were not applied, Tabe 4.8 shows the efficiency corrections and fiducial fractions before pre-unfolding.

Region	Eff. correction	Fid. fraction
Full fid. phase-space	0.879 ± 0.021	0.9521 ± 0.0033
$Z \to 4\ell$ region	0.79 ± 0.04	0.914 ± 0.009
$H \to 4\ell$ region	0.898 ± 0.028	0.937 ± 0.005
Off-shell region	0.842 ± 0.028	0.919 ± 0.006
On-shell region	0.930 ± 0.012	0.9754 ± 0.0017

Table 4.7.: Efficiency correction taking into account the pre-unfolding weights and fiducial fraction for the full fiducial phase space and the $m_{4\ell}$ slices. The quoted uncertainties take into account the full set of systematics discussed in Section 4.9

Region	Eff. correction	Fid. fraction
$Z \to 4\ell$ region	0.425 ± 0.019	0.930 ± 0.009
$H \to 4\ell$ region	0.534 ± 0.017	0.948 ± 0.005
Off-shell region	0.498 ± 0.017	0.934 ± 0.006
On-shell region	0.677 ± 0.009	0.978 ± 0.002

Table 4.8.: Efficiency correction and fiducial fraction for the full fiducial phase space and the $m_{4\ell}$ slices, without the pre-unfolding weights applied. The quoted uncertainties take into account the full set of systematics discussed in Section 4.9

Figure 4.6 shows the migration matrix for the inclusive $m_{4\ell}$ distribution. The $x-$axis has the detector-level bins, the $y-$axis has the particle-level bins, and the matrix is normalized to the $y-$axis. The numbers in each square is the percentage probability that an event in particle-level bin i ends up in detector bin j. The migration matrix of Figure 4.6 is very diagonal. This is a desirable trait in unfolding, as it means the distribution has relatively low amounts of bin-to-bin migrations. Most of the bin migrations are contained within the two neighbouring bins on either of the bin edge. Similarly in Figure A.13 there is the migration matrix of the four mass regions dominated by single Z, Higgs, off-shell ZZ, and on-shell ZZ, in that order. Here the migrations are highest for the off-shell mass slice. This is an expected effect since the off-shell slice consists of three discontinuous mass regions that neighbour all of the three other mass slices.

The remaining plots of the unfolding inputs and migration matrices for all other observables are available in Appendix A.

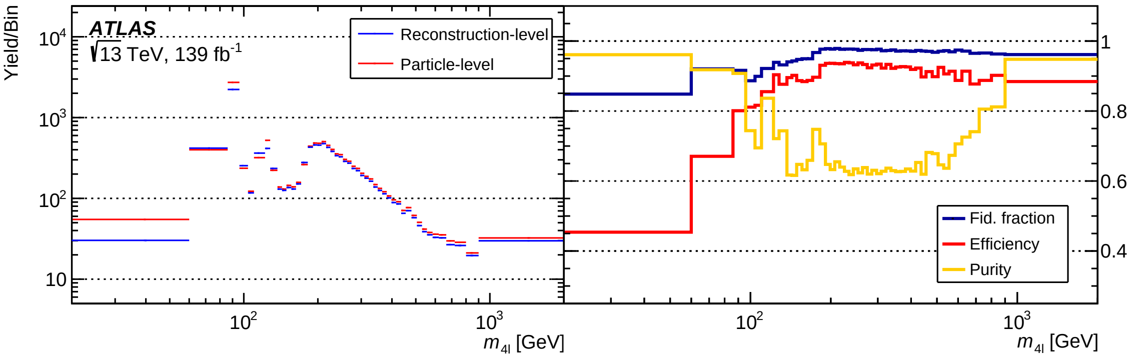

Figure 4.5.: In the left-hand panel, the number of predicted events passing the reconstruction- and fiducial- level selections are displayed as the detector yield and particle yield, respectively. They are given as a function of inclusive $m_{4\ell}$ bins. The right-hand panel shows the efficiency, fiducial purity and fiducial fraction in each of the same $m_{4\ell}$ bins.

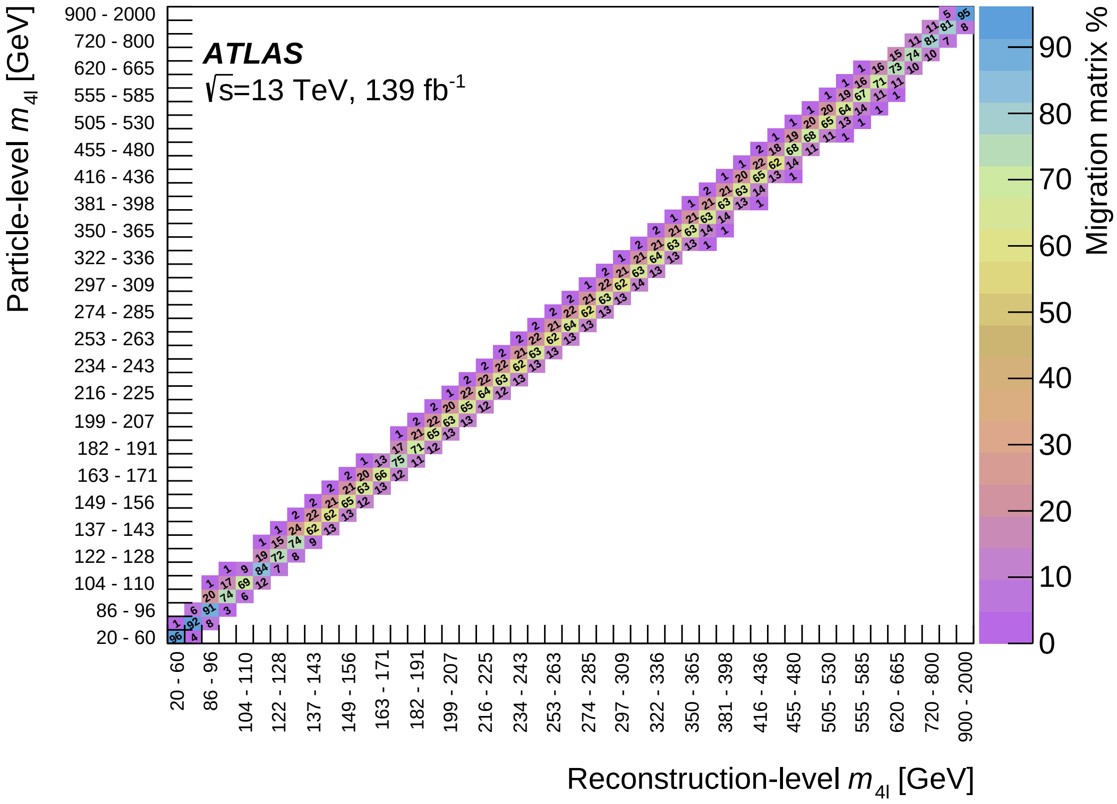

Figure 4.6.: Migration matrix for the inclusive $m_{4\ell}$ distribution.

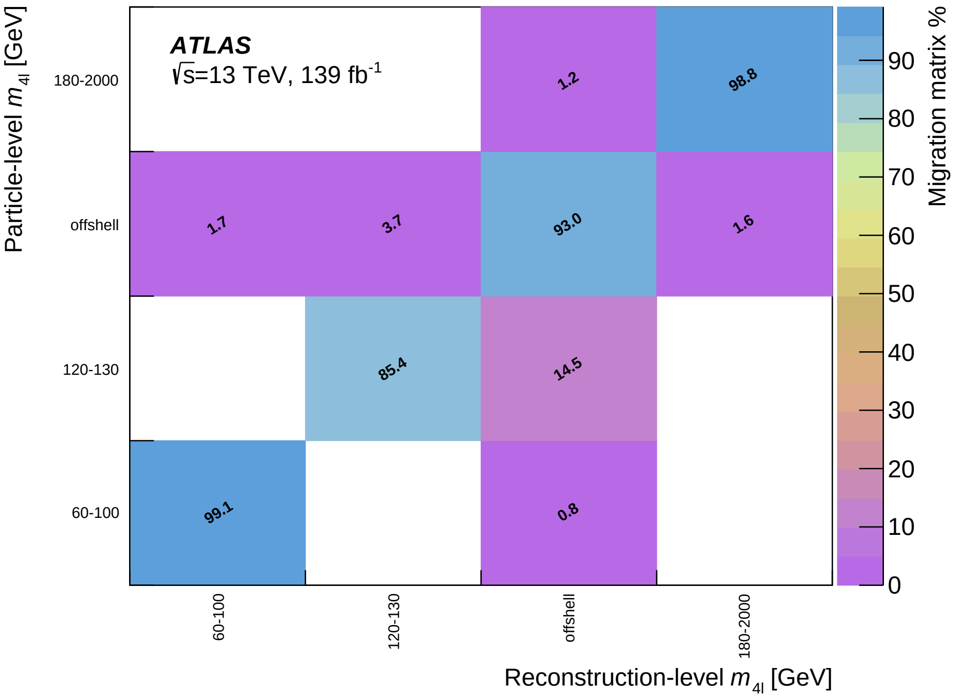

Figure 4.7.: Migration matrices for the four $m_{4\ell}$ regions between the slices.

Number of Bayesian iterations

When using the iterative Bayesian method to unfold, the number iterations performed is a key parameter and must be optimized. The method, which uses the nominal MC distribution as an initial prior, results in a bias towards the original shape of the nominal prediction. A way to minimize this effect is to use the obtained unfolded distribution from the previous iteration as the prior for the subsequent unfolding iteration. The more iterations there are, the less dependence there is on the prior, and therefore the smaller the bias. A side effect, however, is that increasing the number of iterations also increases the statistical uncertainty. Fluctuations caused by limited statistics become amplified by the feedback in the algorithm. These effects are thoroughly studied in order to strike a balance between minimizing the bias at the cost of increasing the statistical uncertainties.

One thousand toy distributions are generated using the detector-level Standard Model prediction where the value of each bin is randomly drawn from a Gaussian distribution. Each toy is unfolded following the procedure outlined in section 4.8.1, where the nominal SM predictions are used to construct the response matrix and for the prior. The bias, written as

$$\text{Bias}_i = \frac{\sum_{j=1}^{n} M_{ij} \cdot x_j - y_i \cdot f_i}{y_i \cdot f_i}, \tag{4.11}$$

measures the difference between the product of the migration matrix and the unfolding output, and the product of the detector-level toy and the fiducial fraction. It is an assessment of the strength of the pull that the shape of the SM prior has on the unfolded toy result . Additional, a statistical uncertainty from the unfolding procedure for each individual toy in each bin is quoted. Next, the bias significance per bin is defined as the quotient of the bias and the statistical uncertainty. After sampling over all toys, the root-mean-square (rms) of the bias significance in each bin is calculated. Through the rms bias significance, the size of the bias in comparison to that of the statistical uncertainty is quantified and used as a criterion in determining the number of iterations. The requirement is to use the minimum number of iterations needed for a bias significant lower than 0.5.

For the inclusive $m_{4\ell}$ distribution, the minimum number of iterations for which the criterion is met is three. For the majority of the other measured distributions, three iterations of the unfolding are also found to be optimal. Two iterations are found to be sufficient for the following observables: m_{12}-$m_{4\ell}$, $|\Delta\phi_{\ell\ell}|$-$m_{4\ell}$, and $|\Delta y_{\text{pairs}}|$-$m_{4\ell}$.

4.8.3. Binning optimization

The binnings of the measured distributions were optimized based on two factors: the number of events and the purity of each bin. Here the purity refers to the diagonal of the migration matrix normalised along truth, thus representing the fraction of truth events that end up in the same reconstructed event bin.

The first iteration of the binnings were run with the nominal criteria. Here, depending on the number of events in the bin, the purity requirement varies. Bins with lower statistics have a high purity requirement to reduce bin-to-bin migrations. The minimum number of events required for each bin is 14. Between 14 and 20 events, the purity was required to be at least 80%. Between 20 and 25 events the purity must be 70% or higher. Finally for the higher statistics bins with more than 25 events the purity cut was 60%.

The binning algorithm is as follows. For the full $m_{4\ell}$ differential mass distribution from 20 - 2000 GeV, the distribution is first split into very fine steps of 1 GeV bins from

20 -450 GeV. From 450 -2000 GeV wider steps of 5 GeV bins were used. Due to the fine nature of the bin widths, this initial binning failed to meet any of the binning criteria. Next, the binning algorithm starts from the low mass end and starts to merge adjacent bins together if the criteria were not met. For example, if bin number 1 [20,21] GeV has > 10 events, the algorithm merges bin number 1 with the next bin. The new bin number 1 is now [20,22] GeV. Once again, if this bin has > 10 events, it will merge again and become [20,23] GeV, and so on and so forth until 10 events has been reached. Of course the purity must also pass the required percentage for the number of events in the bin, otherwise further bin merging occurs. The bin edges are first fixed to be symmetric around the resonance masses at 90 GeV and 125 GeV while passing all requirements. Once this is complete, the remaining bins in between the resonances are passed through the same algorithm. The results of the final binning for the $m_{4\ell}$ distribution is given in Table 4.10.

Next there are the $m_{4\ell}$ distributions in double differential slices of $p_{\mathrm{T},4\ell}$, $y_{4\ell}$, and flavour channel. For these distributions, the fine binning is defined as the the binning of the inclusive $m_{4\ell}$ differential mass distribution, i.e. the output of the algorithm described in the previous paragraph. Bins are once again checked for number events and purity, and merged as needed. This is implemented so that all $m_{4\ell}$ in each of the $p_{\mathrm{T},4\ell}$, $y_{4\ell}$, and flavour slices will have bin edges that match with the inclusive distribution.

For the distributions measured double differentially in the four $m_{4\ell}$ regions corresponding to Z, Higgs, on-shell ZZ, and off-shell ZZ, the same procedure is followed for binning optimization. Each distribution has a fine binning defined, and the bins are merged from left to right of the x-axis until the criteria are met. For the polarization variables $\cos\theta^*_{12}$and $\cos\theta^*_{34}$, an additional requirement for the bins to be symmetric about zero is imposed.

	Nominal	High statistics
Minimum number of events	14 if purity > 0.8 20 if purity > 0.7 25 if purity > 0.6	100 (purity > 0.6)

Table 4.9.: Two different versions of binning with varying event count and purity criteria. The nominal version is what is for the unfolded results. The high statistics version is used as a cross-check for interpretation studies.

	$m_{4\ell}$ bins [GeV]
$m_{4\ell}$	[20, 60, 86, 96, 104, 110, 122, 128, 137, 143, 149, 156, 163, 171, 182, 191, 199, 207, 216, 225, 234, 243, 253, 263, 274, 285, 297, 309, 322, 336, 350, 365, 381, 398, 416, 436, 455, 480, 505, 530, 555, 585, 620, 665, 720, 800, 900, 2000]

Table 4.10.: The binning used in the $m_{4\ell}$ distribution. Each bin satisfies the minimum number of events and purity criteria. The bins containing resonance peaks are symmetric around the peak.

There were a few iterations of the binning that were run with varying criteria, summarized in table 4.9. The nominal criteria is what is presented in the final version of the analysis. The high statistics criteria was an alternative check used to investigate the effects of bins with low event statistics in the interpretations studies of Section 4.11.

4.8.4. Pre-unfolding weights

When correcting the data for detector effects, one of the things to take into account is the efficiency correction. Recall from section 4.8.1 that the efficiency correction is the fraction of reconstructed events that also pass the fiducial selection cuts. A significant contribution to this is the efficiency correction is efficiency in identifying, reconstructing, isolating, and track-to-vertex-association of (TTVA) leptons. These are dependent on lepton kinematics and calculated from Monte Carlo simulation, therefore they may not be accurate if the data differs from the prediction. To correct for this effect, the lepton efficiencies are measured as a function of the lepton transverse momentum (p_{T}) and pseudorapidity (η), and the inverse of this is applied as a per-lepton weight in the data. The term coined for this weight is the pre-unfolding weight, and as the name suggests it is applied prior to the unfolding procedure detailed in 4.8.1.

Figure 4.8 shows the detector yield from simulation with and without the application of the pre-unfolding weights, compared to the particle yield. It is readily apparent that the detector yield comes much closer to the particle yield when pre-unfolding weights are applied. In some cases, the detector yield surpasses the particle yield around the resonance peaks. This is attributed to bin migrations, and has negligible effects on the final unfolded result. Also shown is the efficiency correction with and without the pre-unfolding weights. In general, a significant increase in efficiency throughout the whole $m_{4\ell}$ spectrum, ranging from 10% at low mass, up to 25% at high mass. The conclusion drawn from these plots is that a large portion of the event inefficiency can be

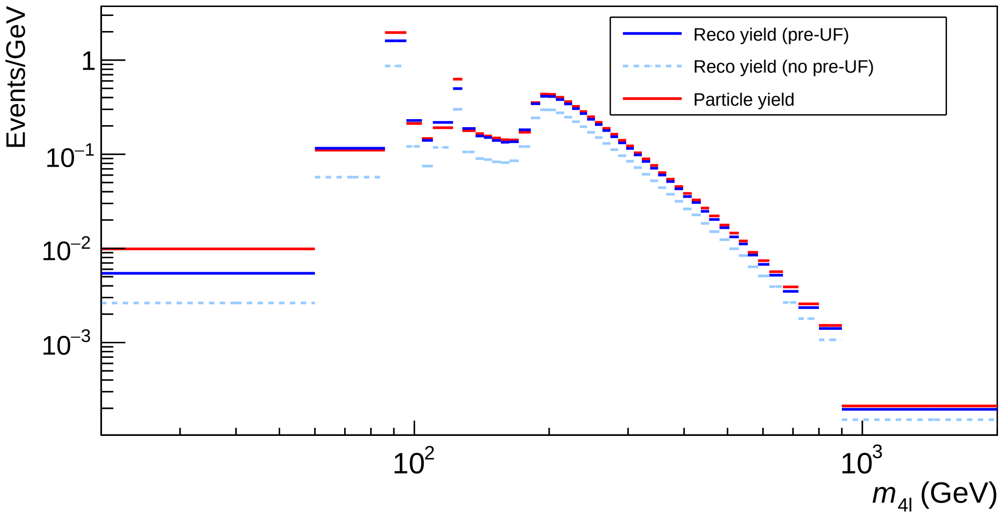

(a)

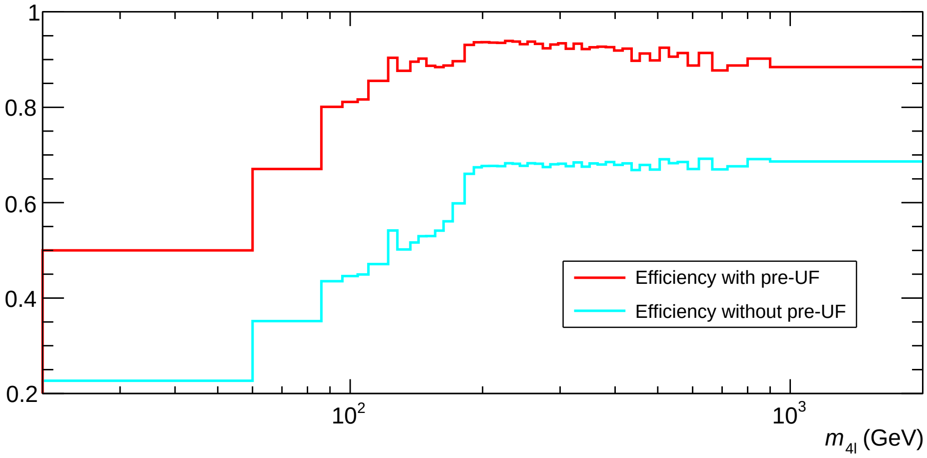

(b)

Figure 4.8.: In the top panel is the effect of the pre-unfolding weights on the predicted detector level (also called reco level) yield, compared to the particle level yield. The bottom panel shows the reconstruction efficiency with and without application of the pre-unfolding weights. The pre-unfolding weights brings the detector yield closer to the particle yield, consequently the efficiency is much higher.

accounted for using per-lepton corrections, bringing the reconstructed and particle level yield closer to one another, and minimising the correction needed when unfolding.

4.8.5. Unfolding iterations optimization

With the observable binnings defined and the pre-unfolding weights applied, the next step is to optimize the number of iterations used in the unfolding. As described in

Section 4.8.1, the iterative Bayesian approach to unfolding uses the Standard Model prediction as an initial prior and therefore has a dependence on it. Fewer numbers of iterations therefore correspond to a larger regularizaton bias on the unfolded result. Contrarily, increasing the number of iterations reduces the bias at the cost of a larger statistical uncertainty and results that are more prone to large bin-to-bin fluctuations. The rest of this section describes the metric used to balance these effects and converge on an optimal number of iterations.

First, one thousand toy distributions are generated from the Standard Model predicted yield at the detector level by drawing random Gaussian distributed values for each bin. Under the assumption that the SM accurately describes the underlying physics, each toy distribution represents a possible observation. The toy distributions are unfolded using the nominal unfolding method (Section 4.8.1). The bias of the unfolded toy result is defined using the migration matrix M, the unfolded yield of the toy U_j , detector-level yield of the toy R_i, and the fiducial fraction f_i as:

$$\text{Bias}_{\text{reco bin } i} = \frac{\sum_{\text{truth bin } j} M_{ij} \times U_j - R_i \times f_i}{R_i \times f_i},$$

The bias significance of the toy is then be calculated in each bin as the ratio of the bias and the estimated statistical uncertainty of the unfolding procedure. This ratio is a comparison of the sizes of the two effects.

Next, the bias significance of the one thousand toys are combined into a singular root-mean-square value in each bin. As a result, a metric indicating how significant the bias is expected to be across a range of toy datasets assuming an underlying SM physics is created. The number of iterations is chosen to be the smallest possible while maintaining a root-mean-square bias significance of 0.5 or below. This choice corresponds to a factor two suppresion of the bias compared to the statistical uncertainty. For the majority of distributions, three iterations of the unfolding comfortably satisfy this criteria, whilst for m_{12}-$m_{4\ell}$, $|\Delta\phi_{\ell\ell}|$-$m_{4\ell}$ and $|\Delta y_{\text{pairs}}|$-$m_{4\ell}$ two iterations is sufficient.

4.8.6. Closure tests

Monte Carlo closure tests

As detailed in Section 4.8.1, the unfolding procedure uses a response matrix that has been derived from Standard Model Monte Carlo predictions. A simple test that can be performed to check the validity of the unfolding method is to use the same SM MC prediction at reconstruction level as pseudo-data, unfold it, and compare it to the truth level prediction. This is a self-consistency check, and should yield the trivial result that the unfolded pseudo-data be identical to the truth distribution. This is the full MC closure test, and acts as a sanity check for the unfolding procedure. The test is shown in Figure 4.9a for the inclusive $m_{4\ell}$ distribution. Full closure is achieved as the unfolded distribution and the particle-level distribution are identical. This is the case for all other distributions as well.

Another similar validation, the half MC closure test, is also performed. This time, the SM samples are divided in two sets A and B based on whether their tagged event number is odd or even. Set A is used to construct the fiducial fraction, reconstruction efficiency, and migration matrix, while set B is used as pseudo-data and unfolded with the inputs from the set A. The unfolded distribution of the set B is then compared to the true distribution of the set B. The statistical uncertainties on both sub-samples are evaluated via the bootstrap method [131]. Figure 4.9b shows the test result for the inclusive $m_{4\ell}$ spectrum. For this and all other distributions, closure is generally achieved within the statistical uncertainties in each bin, with no significant discrepancies.

Data-driven closure tests

In order to assess the potential bias in the unfolding method, a data-driven closure test is performed separately for each measured distribution. For this test, a reweighting is conducted on the particle-level MC prediction such that the detector-level prediction represents more accurately the data. The function used for the reweighting is a smoothed function of the data to MC ratio. The reweighted prediction is used as pseudo-data and propagated through the nominal unfolding procedure. The difference between the reweighted particle-level prediction and the unfolded result in each bin is taken to be the systematic uncertainty of the unfolding method. The associated systematic uncertainty is below 0.3% across the full mass range. For the double differential observables, the derived systematic uncertainties averaging much less than 1% but reaching 3% in a few bins. Overall, it remains subdominant compared to other sources of uncertainty.

4.8.7. Injection studies

Section 4.8.6 demonstrates that the unfolding procedure has closure when unfolding pseudo-data that agree with the Standard Model. Since the SM predictions themselves

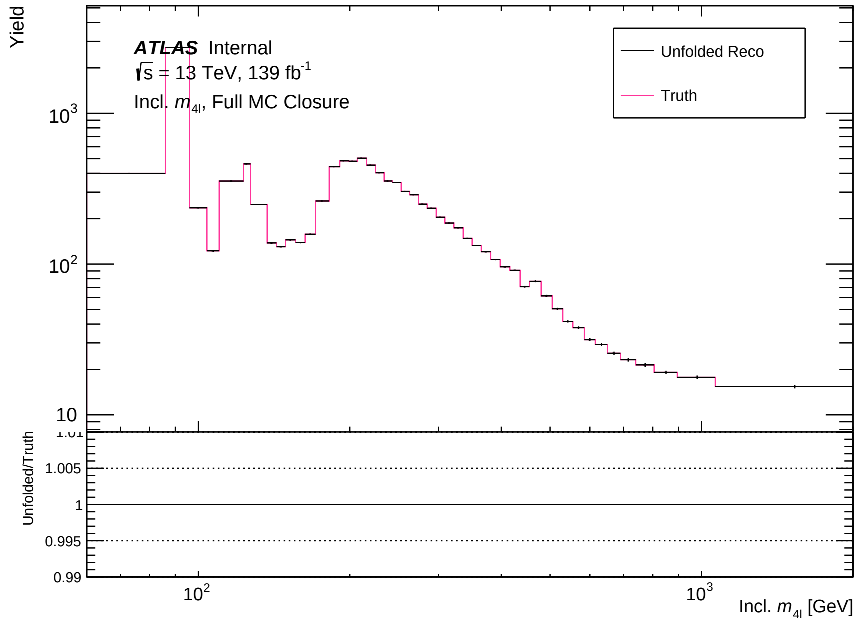

(a)

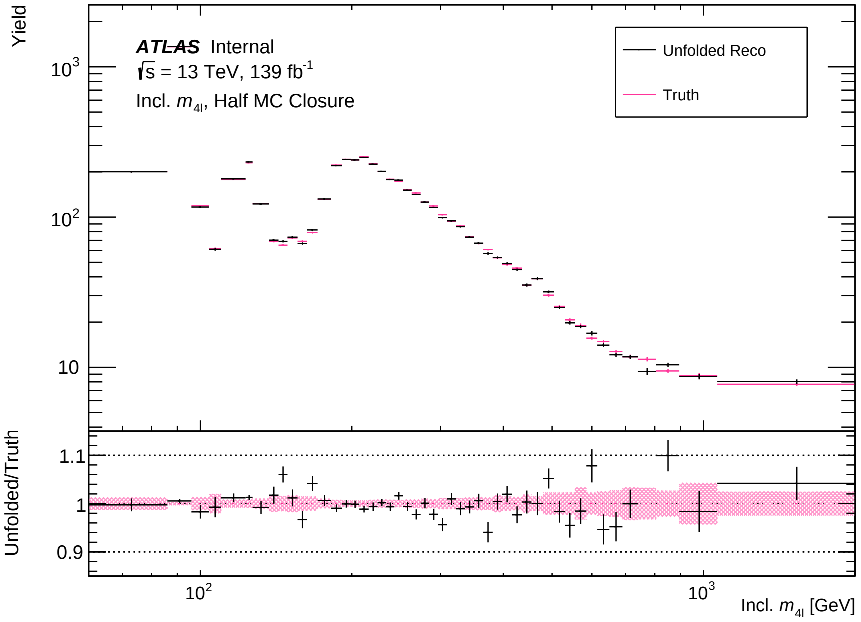

(b)

Figure 4.9.: Monte Carlo closure tests performed on all bins in the inclusive $m_{4\ell}$ distribution. The top figure uses the full MC to unfold itself. The bottom figure splits the MC in half, and uses one set to unfold the other. The pink hash in 4.9b is the MC statistical uncertainty. Closure is achieved in all bins.

Injected samples	
Gluon-gluon fusion heavy Higgs (Narrow width)	$m_{\text{res}} = 300, 800, 1400$ GeV
Gluon-gluon fusion heavy Higgs (15% width)	$m_{\text{res}} = 300, 800, 1400$ GeV
Vector-boson fusion heavy Higgs	$m_{\text{res}} = 300, 800, 1400$ GeV
$gg \rightarrow Z^{(*)}Z^{(*)}$ Enhancement	$c \times$ nominal, $c = 1.1, 1.2, 1.5, 2, 5, 1$

Table 4.11.: Modifications made to the nominal SM prediction for injection studies.

were used to derive the corrections and matrix used for unfolding, this is the expected case. The shape of real data is unknown, however, and may be different than the Standard Model prediction. Should the $m_{4\ell}$ spectrum be host to contributions that differ from the SM prediction, it is necessary to check that the unfolding procedure is nonetheless able to provide an accurate and unbiased particle-level result. In order to do this a number of injection tests were performed. The first step is to take the nominal SM prediction, and inject some amount of BSM signal into it. The reconstruction level yield of this modified sample is used as pseudo-data. It is run through the standard unfolding workflow in entirety, and compared to the particle level yield of the modified sample. Conceptually, this procedure is very similar to that of the Monte Carlo closure tests. These studies also check for the impact and benefit of pre-unfolding weights described in Section 4.8.4. The weights are designed to minimize bias in the unfolding procedure, particularly in cases where the predicted SM signal composition does not match the composition observed in data.

A number of modifications were made to the nominal SM prediction, one set had the addition of a gluon-gluon fusion produced heavy Higgs boson with a mass of 300, 800, or 1400 GeV with either a narrow width or a width 15% of its mass, and another set where the heavy Higgs was produced via vector-boson fusion. The $gg \rightarrow Z^{(*)}Z^{(*)}$ process was also modified to have a larger event weight with respect to the SM prediction. These are described in full in Table 4.11. All of the models describe BSM scenarios with extremely large enhancements or resonances.

For each of the variations listed in Table 4.11, a range of cross-sections were injected and then unfolded with and without application of the pre-unfolding weights. In order to carve a more realistic scenario, one of the injected cross-sections for the heavy Higgs samples was set to be just within the two-sigma band of the data uncertainty. This was done by increasing the injected cross-section and calculating the p-value between the

BSM prediction and the data until a p-value smaller than or equal to 0.05 is reached. This is the p-value corresponding to a two-sigma significance. The results from the injection tests corresponding to a two-sigma injected amount for all the gluon-gluon fusion BSM samples are shown in Figure 4.10. The nominal SM prediction and the modified BSM + SM prediction at particle level are shown (SM truth and BSM truth respectively), along with two unfolded BSM distributions, one with pre-unfolding (pre-UF) weights applied and one without. The lower panel is the ratio of the unfolded BSM distribution to the true BSM distribution and is interpreted as the bias.

Figure 4.11a is also published in Reference [67]. It shows the result of the injection test using a BSM model with a resonance mass of $m_{\text{res}} = 300\ GeV$ and width 15% of the mass, with a cross-section of 6.18 fb^{-1}. Looking at the ratio panel, the bias goes up to 2.2% without the application of the pre-unfolding weights (in green). With the weights applied, the bias is smaller and remains within a $\pm 0.8\%$ range (in black). The same trend holds true for the rest of the 15% width samples, see Figures 4.11b-4.11c. Application of the pre-unfolding weights tend to result in a smaller bias, especially for 300 GeV and 800 GeV resonances. For the highest resonance mass at 1400 GeV, the pre-unfolding has a notable effect only in the last $m_{4\ell}$ mass bin, where it reduces the bias from 10% to 4%.

The gluon-gluon fusion narrow-width heavy Higgs models' injection test results are presented in Figures 4.11d-4.11f. The unfolding method is much more sensitive to, and therefore less robust to, the presence of narrow resonances. Here, the pre-unfolding is not as effective in mitigating the effects of the BSM signal. The differences between the unfolded BSM and the truth BSM, however, is still within 6% bias for the 300 GeV and 1400 GeV resonance mass models. For the 800 GeV model this goes up to 16%. In all cases, the bias is well within the total uncertainty in the corresponding $m_{4\ell}$ mass bin. Similar conclusions are drawn for the the narrow-width VBF samples.

Lastly, the results from enhancing the $gg \to Z^{(*)}Z^{(*)}$ component of the SM prediction are shown in Figure 4.11. The range of the enhancements vary starting from 1.1 times the nominal amount, to 10 times the nominal amount. Once again, the unfolded spectra are compared with and without the application of pre-unfolding weights. Looking at the bottom ratio pad, it is immediately evident from Figure 4.11 that application of pre-unfolding weights leads to a smaller bias (i.e. a smaller difference between the true histogram and the unfolded histogram), especially at high mass. The unfolding procedure is very robust even for a $gg \to Z^{(*)}Z^{(*)}$ enhancement ten times the SM amount; the bias for all bins are within 4%.

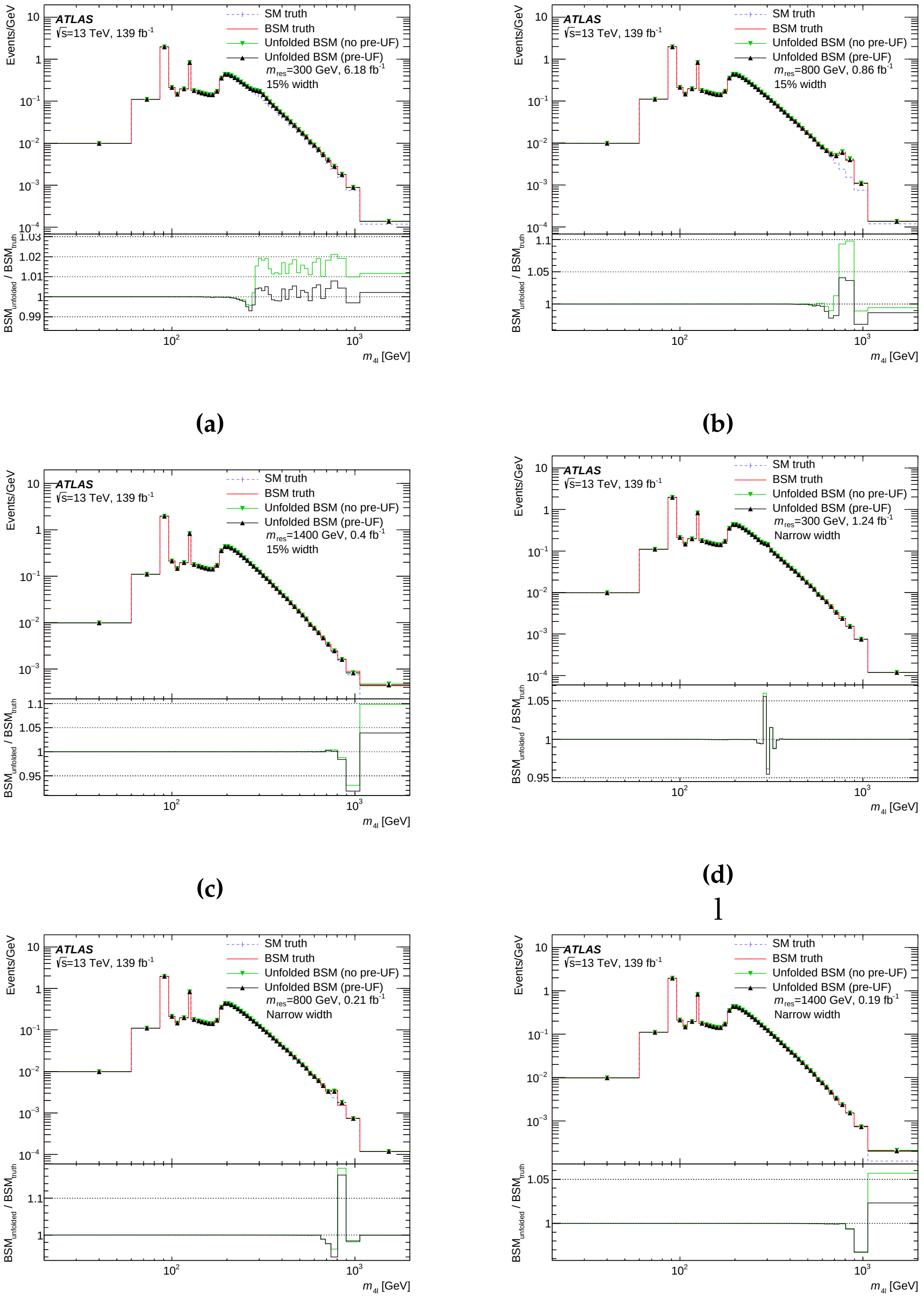

(a) **(b)** **(c)** **(d)** **(e)** **(f)**

Figure 4.10.: This figure shows the results of the BSM signal injection studies performed on the $m_{4\ell}$ distribution. Six BSM models are considered, with resonance masses at 300 GeV, 800 GeV, and 1400 GeV, and with narrow widths or a width 15% of the resonance mass. The cross-sections correspond to a 2σ signal significant with respect to the data uncertainty. Two unfolded distributions are shown with and without pre-unfolding (pre-UF) weights applied. The bottom panel shows the size of the bias.

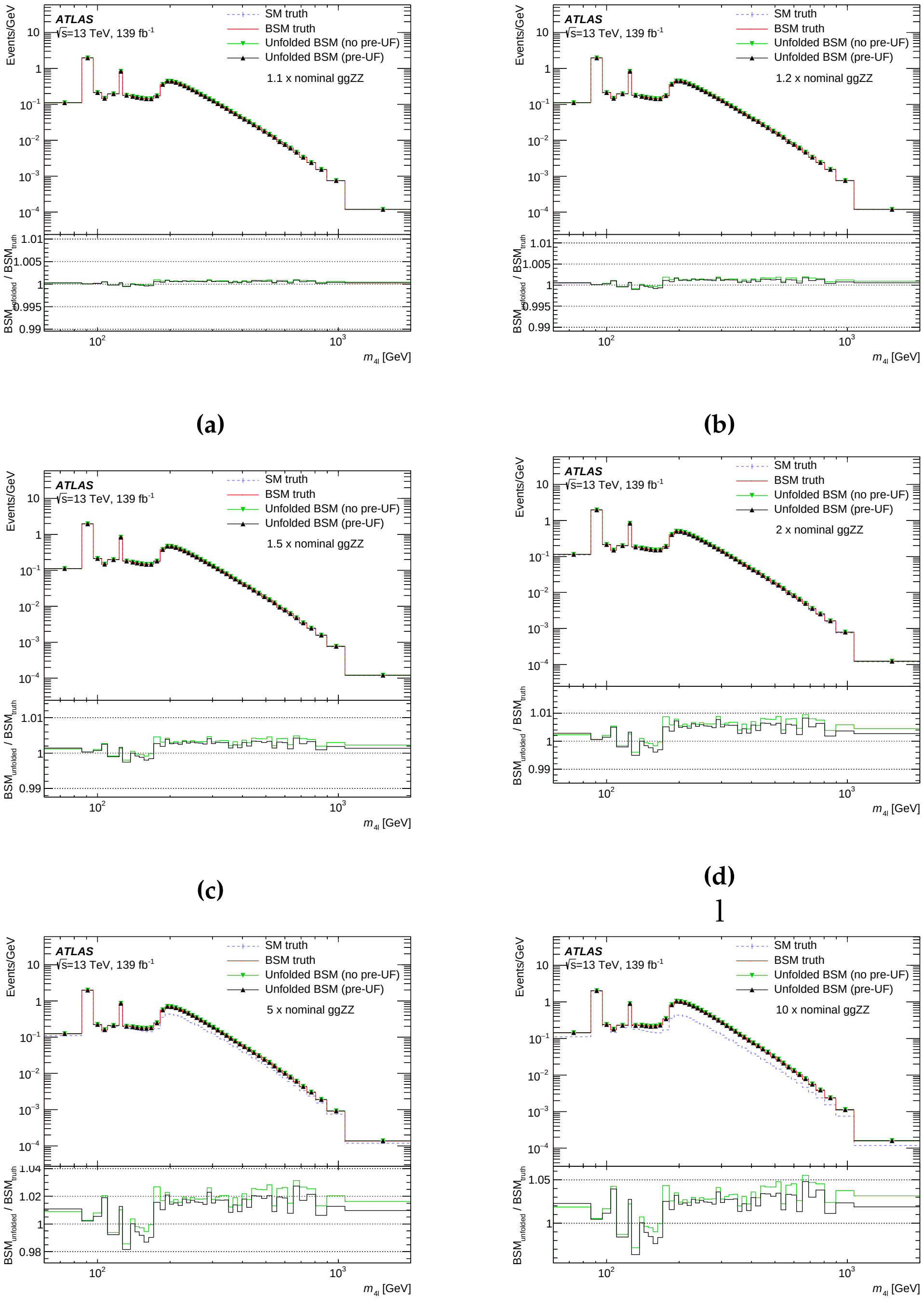

(a) **(b)**

(c) **(d)**

(e) **(f)**

Figure 4.11.: This figure shows the results of the enhanced $gg \rightarrow Z^{(*)}Z^{(*)}$ injection studies performed on the $m_{4\ell}$ distribution. The nominal $gg \rightarrow Z^{(*)}Z^{(*)}$ contribution is enhanced by 1.1–10 times. Two unfolded distributions are shown with and without pre-unfolding (pre-UF) weights applied. The bottom panel shows the size of the bias.

4.9. Measurement uncertainties

An important aspect of an experimental measurement is characterizing its uncertainty. Broadly speaking, uncertainties can be divided into two types. The first is the statistical uncertainty, which is caused by inherently unpredictable fluctuations and can be reliably estimated by making repeated measurements [68]. The second is the category of systematic uncertainties, which arise in the estimation of systematic effects such as background, selection bias, scanning efficiency, energy resolution, angle resolution, variation of counter efficiency with beam position and energy, dead time, etc [132]. Systematic uncertainties are generally more difficult to determine, and cannot be calculated simply from sampling fluctuations [133]. The total uncertainty of the measurement is the sum in quadrature of each individual component.

The breakdown and contribution of the uncertainty sources is shown in Figure 4.12 for the inclusive $m_{4\ell}$ spectrum. The dominant is the statistical uncertainty in all but the third mass bin with resonant single Z production, where the lepton efficiencies' uncertainty prevails. Table 4.12 shows the breakdown of the uncertainties on the total fiducial unfolded cross-section, as well as the fiducial cross-section in the four $m_{4\ell}$ regions. The data statistical uncertainty plays a dominant role, followed by the uncertainty from the choice of generator. The rest of this section will discuss the different sources of uncertainty and how they are propagated.

4.9.1. Statistical uncertainties

Predominantly, the statistical uncertainty is the dominant uncertainty in most bins of the measured differential and double differential cross-sections. The bootstrap method [131] is used to calculate the statistical uncertainty on the data, and the MC. It is first necessary to construct pseudo-data (also called toys). For each set of pseudo-data, a random value is drawn in each bin following a Poisson distribution where the expectation value is the observed event count that that bin. In total, 3500 pseudo-datasets are generated. Each of these are propagated through the unfolding procedure described in Section 4.8. The root mean square of the difference between the unfolded pseudo-data and the unfolded data is taken as the statistical uncertainty in each bin. The statistical uncertainties obtained in this way are equivalent to frequentist confidence intervals in the large-sample limit, while in the bins with few entries, the quoted bands are known to be up to 10% narrower than a frequentist confidence interval.

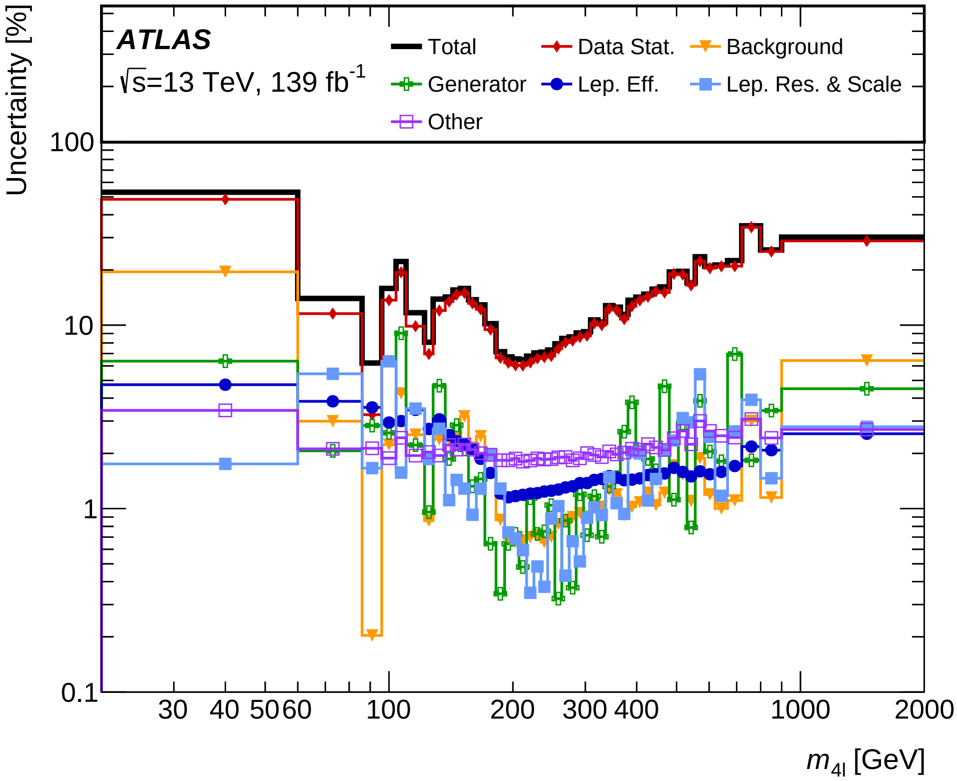

Figure 4.12.: Unfolded systematics for the inclusive $m_{4\ell}$ spectrum. The data statistical uncertainty is the dominant source in all but the third bin. This figure is from Ref. [67]

Region $m_{4\ell}$ [GeV]	Inclusive any	$Z \to 4\ell$ 60-100	on-shell H 120-130	off-shell ZZ 20-60/100-120 /130-180	on-shell ZZ 180-2000
DD Closure	0.088%	0.35%	0.13%	0.45%	0.035%
Electron ID	0.94%	**1.9**%	**1.5**%	**1.3**%	0.49%
Electron Isolation	0.52%	**1.1**%	0.79%	0.73%	0.18%
Electron Reco	0.84%	**1.7**%	**1.3**%	**1.2**%	0.31%
Electron Res. & Scale	0.46%	**1.1**%	0.83%	0.54%	0.12%
Generator	**1.3**%	**2.6**%	**1.3**%	**2.7**%	0.13%
MC Stat.	0.087%	0.22%	0.38%	0.26%	0.088%
Muon Isolation	0.96%	**1.6**%	**1.2**%	**1.2**%	0.58%
Muon Reco & ID	0.83%	**1.1**%	0.91%	0.89%	0.82%
Muon Res. & Scale	0.3%	0.65%	0.55%	0.53%	0.13%
Muon TTVA	0.21%	0.46%	0.28%	0.31%	0.071%
Non-Generator Theory	0.27%	0.31%	0.23%	0.45%	0.27%
Pile-up	0.73%	**1.2**%	**1**%	0.81%	0.47%
Reducible	0.8%	0.55%	**1.7**%	**2.5**%	0.74%
Trigger	0.33%	0.8%	0.44%	0.44%	0.084%
Total Systematic	2.6%	4.8%	3.7%	4.6%	1.5%
Luminosity	**1.7**%	**1.6**%	**1.6**%	**1.6**%	**1.7**%
Data Stat.	**1.3**%	**2.9**%	**6.2**%	**4.1**%	**1.5**%
Total	3.3%	5.8%	7.4%	6.4%	2.7%

Table 4.12.: Uncertainties on the unfolded fiducial cross-section inclusively as well as in the four $m_{4\ell}$ slices studied in this analysis, split by source. Uncertainty contribution larger than 1% are marked in bold to guide the eye. This table is from Ref. [66].

The above method of estimating the statistical uncertainty is used as the quoted uncertainty in the measurements. When testing the observed cross-sections against the Standard Model, however, a secondary approach - where the expected number of events is used in place of the observed number of events - is preferred. That is, the 3500 pseudo-datasets follow a Poisson distribution with the mean equal to the predicted reconstruction-level SM event yield. This was motivated by studies in constraining SM effective field theory coefficients where the former approach resulted in unreliable limits. For more details see Section 4.11.

4.9.2. Systematic uncertainties

Systematic uncertainties arise in nearly every step of the measurement. It is the result of measuring something, or estimating something that is not perfectly known because of certain limitations [134]. Systematic uncertainties are either experimental or theoretical in nature. The former is common to all analyses and pertains to to the ATLAS detector, while the latter relates to the simulation of physics processes as well as to analysis techniques.

Experimental sources

The flat uncertainty on the integrated luminosity for the for the 2015-2018 datasets of 139 fb^{-1} is $\pm 1.7\%$. The integrated luminosity and uncertainty for the whole Run 2 data-taking period is derived based on a calibration of the luminosity scale using $x-y$ beam-separation scans, following a methodology similar to that detailed in reference [135], and using the LUCID-2 detector for the baseline luminosity measurements [136]. While this uncertainty is not relevant in the unfolding, it applies when converting event counts into a cross-section result as well as during the interpretations.

There is an uncertainty associated with pile-up reweighting, which refers to the reweighting of the Monte Carlo samples in order to reproduce the distribution of the number of pp collisions per bunch crossing (μ) observed in the data [137]. The uncertainty arises from the modelling of pileup events, including uncertainties in the pp inelastic cross-section. The resulting effects on the measured distributions of this analysis is small.

Lepton identification, reconstruction and isolation, and lepton energy/momentum resolution and scale efficiencies and their uncertainties are derived from data using large samples of $J/\psi \to \ell\ell$ and $Z \to \ell\ell$ decays. The uncertainties on the performance are derived following the method reported in reference [56] for muons and references [49], [47] for electrons. Typical uncertainties on the identification efficiencies are in the range between 0.5% to 1.0% for muons and 1.0% to 1.3% for electrons.

The uncertainty from the non-prompt lepton background estimate has a size-able effect in the low- and high-mass tails of the $m_{4\ell}$ distribution, reach up to 11% and 6.5% in the first and last bins respectively. The details of the uncertainty estimate on the Fake Factor method is detailed in Section 4.6.3.

Theoretical sources

The choice of the generator used for the simulation of the $q\bar{q} \to 4\ell$ process in constructing the response matrix for unfolding (see Section 4.8.1) is the largest source of theory-related systematic uncertainty. The uncertainty arises from the difference in the modelling of the final-state radiation of photons between the SHERPA prediction and the POWHEG + PYTHIA8 prediction. To assess the uncertainty, the POWHEG + PYTHIA8 sample is reweighted to match the SHERPA sample. This is done so no double counting of the unfolding method uncertainty occurs. The data is then unfolded via the standard procedure using the reweighted POWHEG + PYTHIA8 input. The envelope of the observed ratio between this result and the nominal unfolded result is taken as the generator uncertainty. From the choice of unfolding method, the uncertainty is evaluated using the data-driven closure test detailed in Section 4.8.1.

Other theoretical uncertainties have minimal effect on the unfolding, although their effect is larger on the particle-level predictions that the data is compared against. Generator choice aside, the dominant source is from the factorization and renormalization scale variations, with smaller contributions from PDF uncertainties, parton shower uncertainties, next-to-leading order $k-$factor reweighting uncertainties. Overall, this indicates that a good level of model-independence is achieved.

4.10. Results

This section presents the results of the inclusive four-lepton analysis published in Reference [67] by the ATLAS collaboration. The measured fiducial cross-sections are presented in Table 4.13. The first column shows the cross-section measured in the full fiducial phase space, while the subsequent columns quote the cross-section in the four

	Region				
	Full	$Z \to 4\ell$	$H \to 4\ell$	Off-shell ZZ	On-shell ZZ
Measured fiducial XS [fb]	88.9 ± 1.1 (stat.) ± 2.3 (syst.) ± 1.5 (lumi.) ± 3.0 (total)	22.1 ± 0.7 (stat.) ± 1.1 (syst.) ± 0.4 (lumi.) ± 1.3 (total)	4.76 ± 0.29 (stat.) ± 0.18 (syst.) ± 0.08 (lumi.) ± 0.35 (total)	12.4 ± 0.5 (stat.) ± 0.6 (syst.) ± 0.2 (lumi.) ± 0.8 (total)	49.3 ± 0.8 (stat.) ± 0.8 (syst.) ± 0.8 (lumi.) ± 1.3 (total)
SHERPA	86 ± 5	23.6 ± 1.5	4.57 ± 0.21	11.5 ± 0.7	46.0 ± 2.9
POWHEG + PYTHIA8	83 ± 5	21.2 ± 1.3	4.38 ± 0.20	10.7 ± 0.7	46.4 ± 3.0

Table 4.13.: Fiducial cross-sections in the full fiducial phase space and in the $Z \to 4\ell$, $H \to 4\ell$, on-shell ZZ, and off-shell ZZ dominated regions in femtobarns. They are compared with two particle-level predictions and their uncertainties where the $q\bar{q} \to 4\ell$ process is simulated with either SHERPA or with POWHEG + PYTHIA8.

$m_{4\ell}$ regions dominated by $Z \to 4\ell$, $H \to 4\ell$, on-shell ZZ, or off-shell ZZ production. The theoretical predictions for the cross-sections in these regions are also provided in the bottom two rows. The two predictions differ in the choice of generator used to simulate the dominant $q\bar{q} \to 4\ell$ process; one uses SHERPA at NLO accuracy in QCD and the other uses POWHEG interfaced to PYTHIA8 normalized to a NNLO prediction. Details of the theoretical predictions can be found in Section 4.5.2.

The associated uncertainties are also presented. For the measured cross-sections, the total combined uncertainty as well as the uncertainties split into three categories (statistical, systematic, or luminosity) are given. For more on the uncertainty breakdown and how they are estimated, see Section 4.9. The data are slightly higher than both predictions in all but the $Z \to 4\ell$ region, where it lies between the SHERPA and POWHEG + PYTHIA8 predicted values. In general, the SHERPA predictions are higher than the POWHEG + PYTHIA8 predictions, with the on-shell ZZ region being an exception. Overall, the measured data are in good agreement with both predictions within the quoted uncertainties. The largest differences comes from the on-shell ZZ region where the data is around one sigma higher than the predicted SHERPA value.

Figure 4.13 presents the differential cross-section as a function of $m_{4\ell}$, as well as two predicted SM cross-sections where either SHERPA or POWHEG is used to model the $q\bar{q} \to 4\ell$ contribution. The breakdown of the SM processes in the predictions are plotted in colour and stacked. Various features corresponding the different physics processes are visible in this plot. At $m_{4\ell}$=$m_Z \simeq 91.19$ GeV [9] there is the single resonant Z peak, and similarly for the $m_{4\ell}$=$m_H \simeq 125.10$ [9] for the Higgs. An enhancement is visible at $m_{4\ell}$=$2m_Z \simeq 182$ GeV when the on-shell production of two Z bosons becomes possible. Overall, the SM predictions are in agreement with the measurement within the quoted uncertainties for the entire distribution.

A p-value quantifies the probability of finding the data at least as extreme as the data observed [138], with n degrees of freedom equal to the number of bins. There are two p-values shown (one for each SM prediction using either SHERPA or POWHEG to model $q\bar{q} \rightarrow 4\ell$) for the inclusive $m_{4\ell}$ of Figure 4.13 and all other distributions. The p-value is derived from the χ^2, which is defined as:

$$\chi^2 = \left[\vec{\sigma}^{\text{meas}} - \vec{\sigma}^{\text{pred}}\right]^T C^{-1} \left[\vec{\sigma}^{\text{meas}} - \vec{\sigma}^{\text{pred}}\right] \tag{4.12}$$

where $\vec{\sigma}^{\text{meas}}$ and $\vec{\sigma}^{\text{pred}}$ are n-dimensional vectors representing the binned measured and predicted differential cross-sections, and C is the $n \times n$ summed total covariance matrix which accounts for the combination of statistical and systematic uncertainties. For the inclusive $m_{4\ell}$ distribution, the calculated p-value for the data is $p = 0.22$ for the SHERPA prediction and $p = 0.09$ for the POWHEG prediction, echoing the results in Table 4.13 where the SHERPA prediction is the higher of the two and the data are higher than both predictions.

Figure 4.14 shows the differential cross-section as a function of $m_{4\ell}$ in five slices of the four-lepton transverse momentum, $p_{\text{T},4\ell}$. Likewise in Figure 4.15 the $m_{4\ell}$ spectrum is plotted in five slices of $|y_{4\ell}|$, the absolute rapidity of the four-lepton system. Figure 4.16 contains three subplots of the differential cross-section as a function of $m_{4\ell}$ in the $4e, 4\mu$ and $2e2\mu$ flavour channels. There is good agreement between the data and the SM predictions overall for these distributions, however, the POWHEG+PYTHIA8 prediction in the $100 < p_{\text{T},4\ell} < 600$ GeV slice and the $0.9 < y_{4\ell} < 1.2$ slice are below the data, resulting in low p-values ($p = 0.008$ and $p = 0.003$ respectively). These features reflect the results presented in Table 4.13. The third mass bin of Figure 4.14 (b) displays a large discrepancy between data and prediction, where both the SHERPA and POWHEG prediction are over two times larger. This feature is also present in the reconstruction level results, and therefore is not a by product of the unfolding process.

The cross-section as a function of the dilepton mass of the primary and the secondary lepton pair, m_{12} and m_{34}, are presented in Figures 4.17 and 4.18 in the different $m_{4\ell}$ regions. In the region dominated by Higgs production, the Higgs contribution is drawn separately in blue. For m_{12}, a peak is visible at m_Z in all but the $Z \rightarrow 4\ell$ region. m_{34}

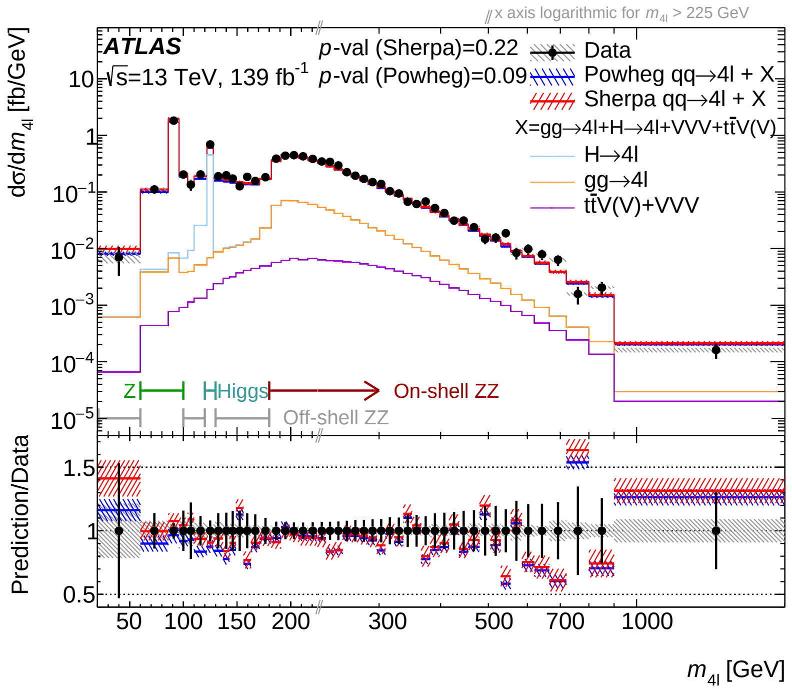

Figure 4.13.: Differential cross-section as a function of the four-lepton invariant mass $m_{4\ell}$as measured in data in black. The error bars on the data points give the total uncertainty and the grey hashed band illustrates the contribution from the systematic uncertainty. The SM predictions use either SHERPA or POWHEG + PYTHIA8 to model the $q\bar{q} \to 4\ell$ contribution, plotted in red and blue respectively. The uncertainties on the SM predictions are represented by the red and blue hash. The coloured stacked histograms represent the per-process breakdown of the SM prediction. In the lower left corner of the figure, boundary lines are drawn to indicate the four different $m_{4\ell}$ regions, each dominated by a different process. The p-value is the probability for the χ^2 to have at least the observed value, assuming the SM prediction. The number of degrees of freedom is the number of bins in the histogram. The ratio of the SHERPA and POWHEG prediction to the data is shown in the lower panel. The x-axis is on a linear scale until $m_{4\ell} = 216$ GeV, where it switches to a logarithmic scale.

on the other hand has the m_Z enhancement only in the on-shell ZZ region where it is kinematically allowed. The $Z \to 4\ell$ and off-shell ZZ regions of m_{34} are dominated by off-shell Z boson and photon exchange, while the $H \to 4\ell$ region is dominated by off-shell Z production. In the third mass bin of the Higgs slice of m_{34} shown in Figure A.5, the theoretical predictions are more than two times higher than the observed data. Once again, this feature is also present in the reconstruction level results. There are some low p-values for these observables, notably in the on-shell ZZ region of m_{12}, and the $H \to 4\ell$ and off-shell ZZ region of m_{34}. These are attributed to features discussed in Table 4.13, paired with statistical fluctuations in the data and differences in modelling between the two generators.

The transverse momentum of the leading and sub-leading lepton pair in the four $m_{4\ell}$ regions are presented in Figures 4.19 and 4.20. In the on-shell ZZ region for both the spectrum peaks at around 40 GeV. For the other three regions, the peak is approximately 20 GeV. The shapes of all slices for both $p_{\mathrm{T},12}$ and $p_{\mathrm{T},34}$ are similar, with a steady rise to the peak and a slow fall into the high p_T tail. There is a notable disagreement between observation and prediction in $p_{\mathrm{T},34}$. An under-prediction of the cross-section for low p_{T} in on-shell ZZ region is visible. This was already observed in prior ATLAS measurements of ZZ diboson production [65].

The variables $\cos\theta^*_{12}$ and $\cos\theta^*_{34}$ are sensitive to the polarization of the decaying bosons, and can serve as a probe for new physics [139]. For each lepton pair, θ^* is defined as the angle between the negative lepton in the Z rest frame and the Z boson in the lab frame. Figures 4.21 and 4.22 show the polarization variables leading and sub-leading lepton pair, $\cos\theta^*_{12}$ and $\cos\theta^*_{34}$, in the $m_{4\ell}$ regions. There is good agreement between data and prediction for all distributions.

The unfolded cross-section in the $m_{4\ell}$ regions for the azimuthal angle between the leading and sub-leading leptons of the quadruplet, $|\Delta\phi_{\ell\ell}|$, is shown in Figure 4.23. Studied in detail in Reference [140], this variable is sensitive to next-to-leading order electroweak corrections on four lepton production. The shape of the distributions in the four regions are largely similar, peaking at $|\Delta\phi_{\ell\ell}| \approx \pi$ when the leading and sub-leading leptons are in opposite hemispheres. Good agreement with the SM prediction is seen throughout.

Figures 4.24 and 4.25 show the azimuthal angle difference and the rapidity difference between the lepton pairs. In the off-shell ZZ and on-shell ZZ region of $|\Delta\phi_{\mathrm{pairs}}|$, the low p-values are mainly driven by statistical fluctuations in the data alongside low SM predictions for $|\Delta\phi_{\mathrm{pairs}}| < \frac{26}{64}\pi$. The $|\Delta y_{\mathrm{pairs}}|$ distributions peak at zero and with a gradual tail to five. In the on-shell ZZ region of $|\Delta y_{\mathrm{pairs}}|$, the SM prediction drops to be up to 50% lower than the data at high values, indicating mis-modelling by the MC generators.

4.11. Interpretations

As a demonstration of how the data may be re-interpreted, two well-motivated BSM scenarios are selected and the unfolded measurements of Section 4.10 are used to set exclusion limits on the parameter space of both. The first considers the Standard Model in an effective field theory (EFT) framework, and the second is a gauged $B - L$ model

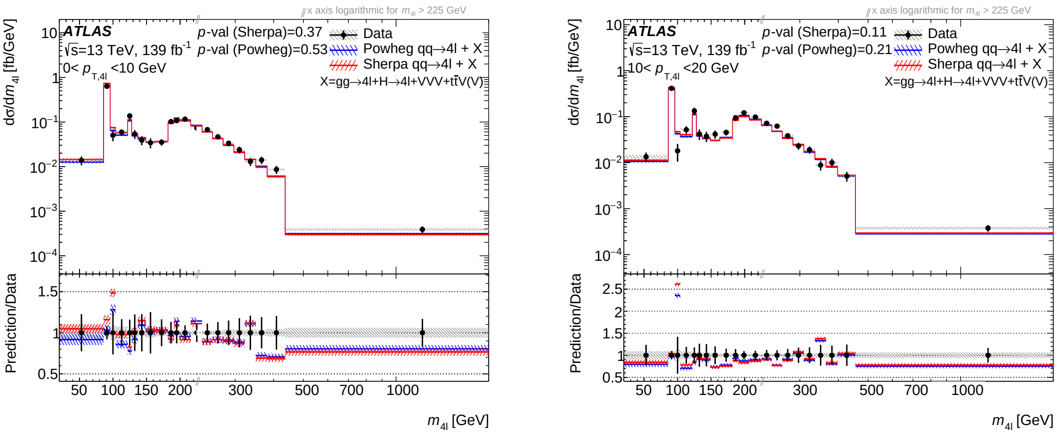

(a) 0 GeV $< p_{\mathrm{T},4\ell} <$ 10 GeV **(b)** 10 GeV $< p_{\mathrm{T},4\ell} <$ 20 GeV

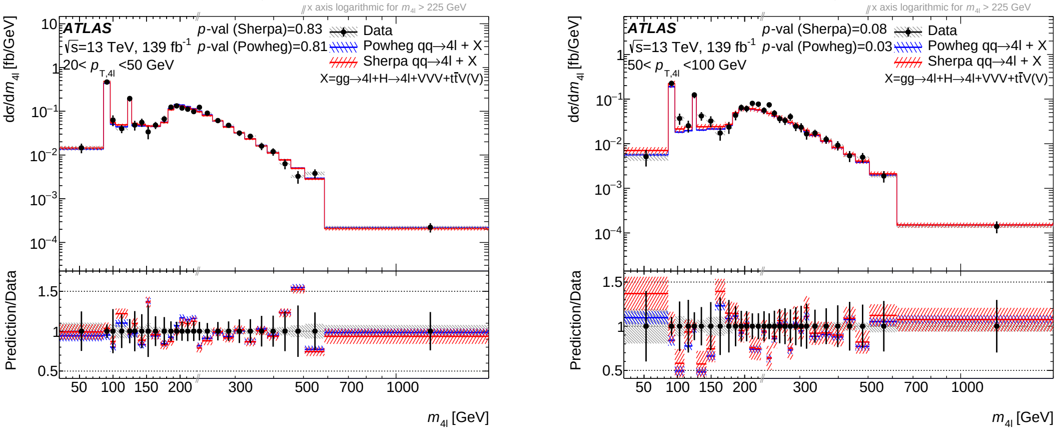

(c) 20 GeV $< p_{\mathrm{T},4\ell} <$ 50 GeV **(d)** 50 GeV $< p_{\mathrm{T},4\ell} <$ 100 GeV

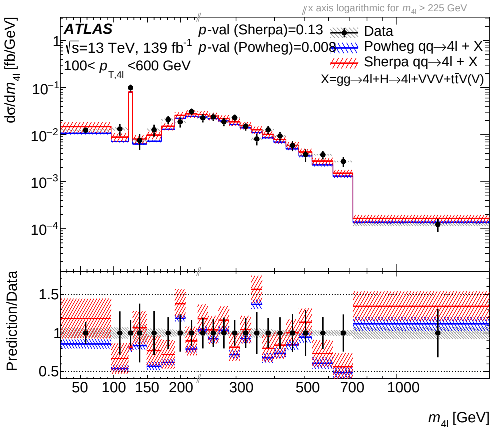

(e) 100 GeV $< p_{\mathrm{T},4\ell} <$ 60 0 GeV

Figure 4.14.: Differential cross-section as a function of $m_{4\ell}$ in slices of $p_{\mathrm{T},4\ell}$. The error bars on the data points give the total uncertainty and the grey hashed band illustrates the contribution from the systematic uncertainty. The SM predictions use either SHERPA or POWHEG + PYTHIA8 to model the $q\bar{q} \to 4\ell$ contribution, plotted in red and blue respectively. The uncertainties on the SM predictions are represented by the red and blue hash. The p-value is the probability for the χ^2 to have at least the observed value, assuming the SM prediction. The number of degrees of freedom is the number of bins in the histogram. The ratio of the SHERPA prediction to the data is shown in the lower panel.

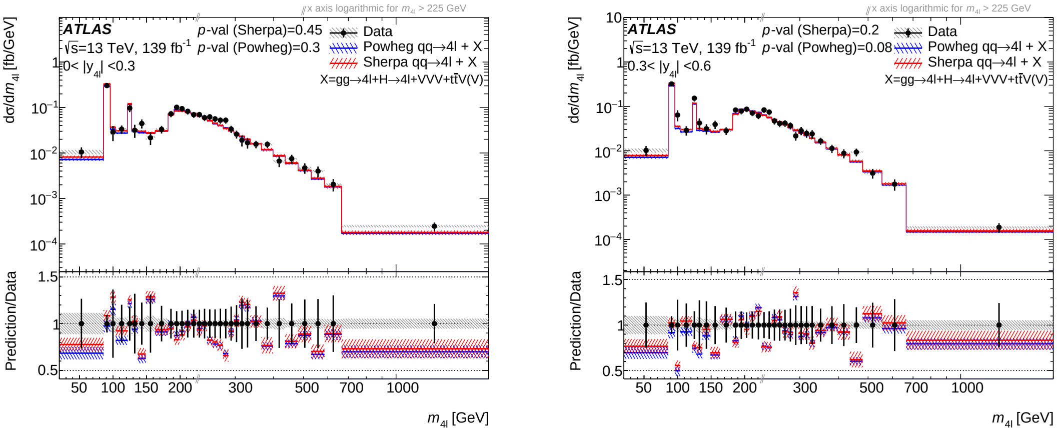

(a) $0 < y_{4\ell} < 0.3$

(b) $0.3 < y_{4\ell} < 0.6$

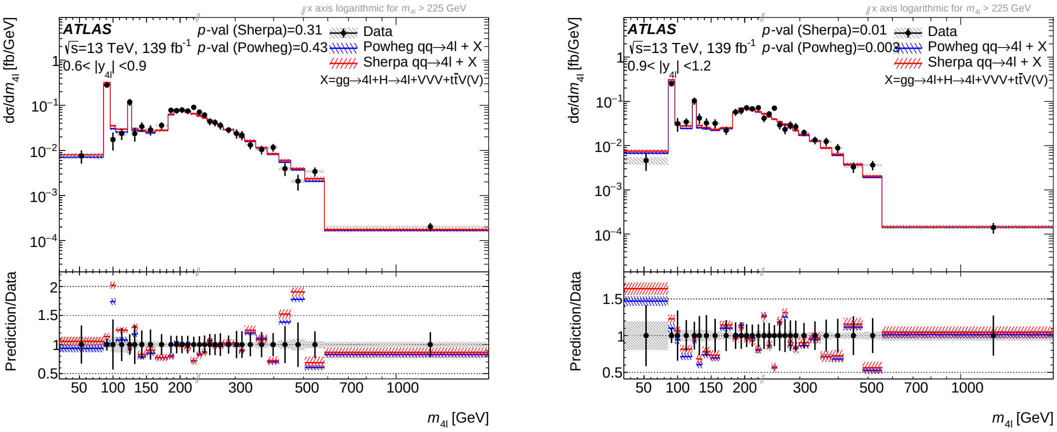

(c) $0.6 < y_{4\ell} < 0.9$

(d) $0.9 < y_{4\ell} < 1.2$

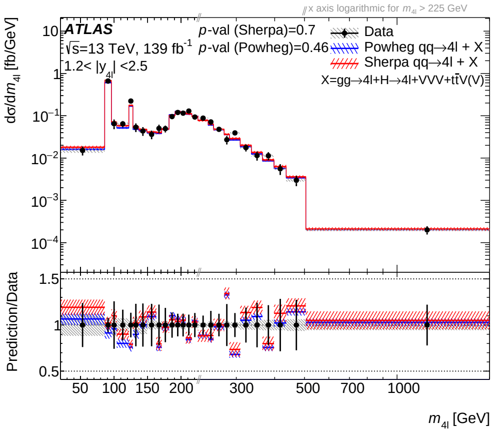

(e) $1.2 < y_{4\ell} < 2.5$

Figure 4.15.: Differential cross-section as a function of $m_{4\ell}$ in slices of $y_{4\ell}$. The error bars on the data points give the total uncertainty and the grey hashed band illustrates the contribution from the systematic uncertainty. The SM predictions use either SHERPA or POWHEG + PYTHIA8 to model the $q\bar{q} \to 4\ell$ contribution, plotted in red and blue respectively. The uncertainties on the SM predictions are represented by the red and blue hash. The p-value is the probability for the χ^2 to have at least the observed value, assuming the SM prediction. The number of degrees of freedom is the number of bins in the histogram. The ratio of the SHERPA prediction to the data is shown in the lower panel.

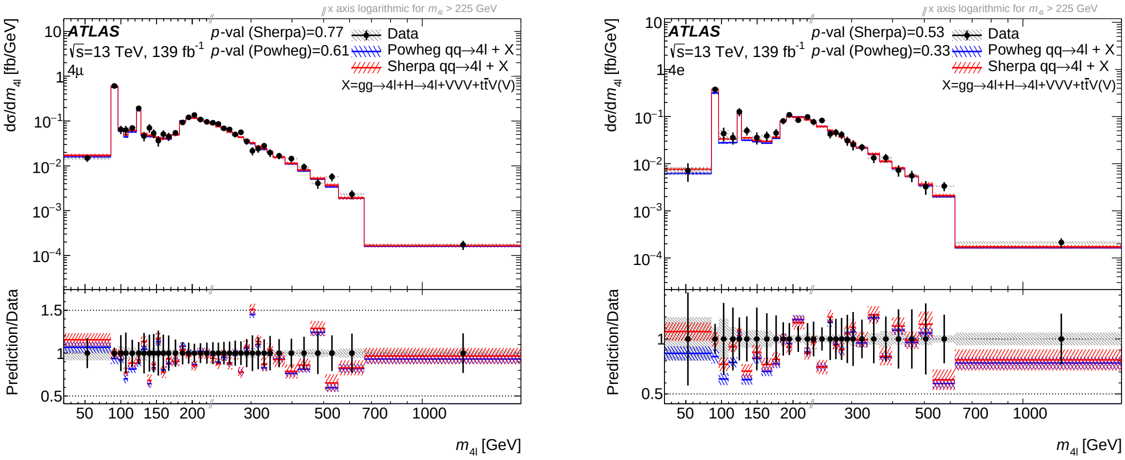

(a) 4μ channel

(b) $4e$ channel

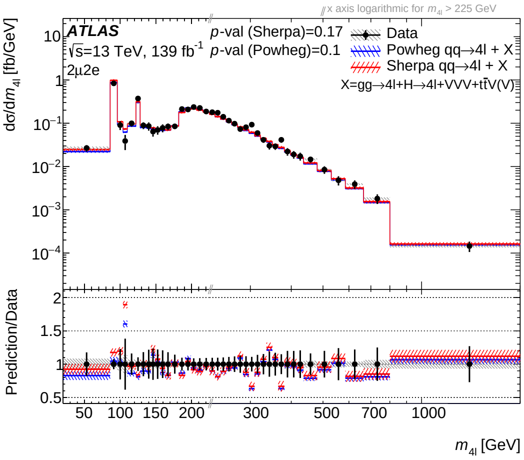

(c) $2e2\mu$ channel

Figure 4.16.: Differential cross-section as a function of $m_{4\ell}$ for each lepton flavour channel. The error bars on the data points give the total uncertainty and the grey hashed band illustrates the contribution from the systematic uncertainty. The SM predictions use either SHERPA or POWHEG + PYTHIA8 to model the $q\bar{q} \to 4\ell$ contribution, plotted in red and blue respectively. The uncertainties on the SM predictions are represented by the red and blue hash. The p-value is the probability for the χ^2 to have at least the observed value, assuming the SM prediction. The number of degrees of freedom is the number of bins in the histogram. The ratio of the SHERPA prediction to the data is shown in the lower panel. The x-axis is on a linear scale until $m_{4\ell} = 225$ GeV, where it switches to a logarithmic scale.

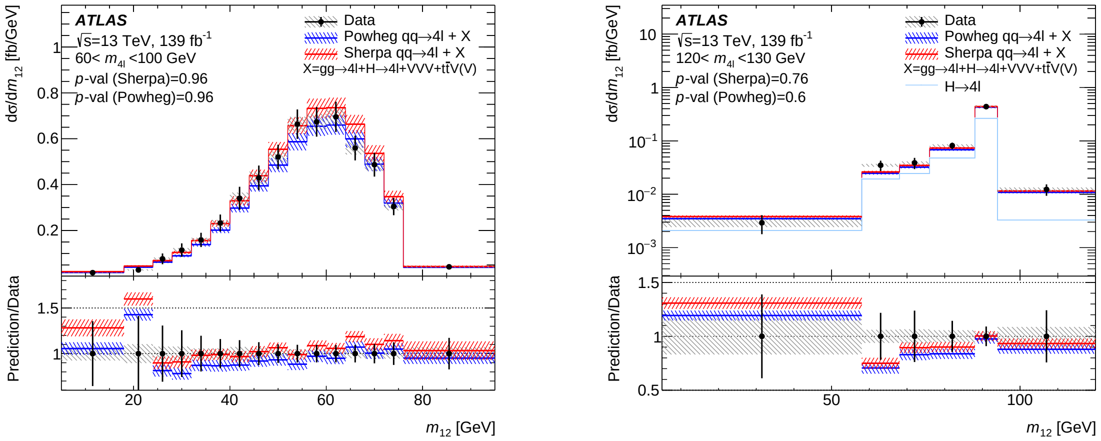

(a) $Z \to 4\ell$ region

(b) $H \to 4\ell$ region

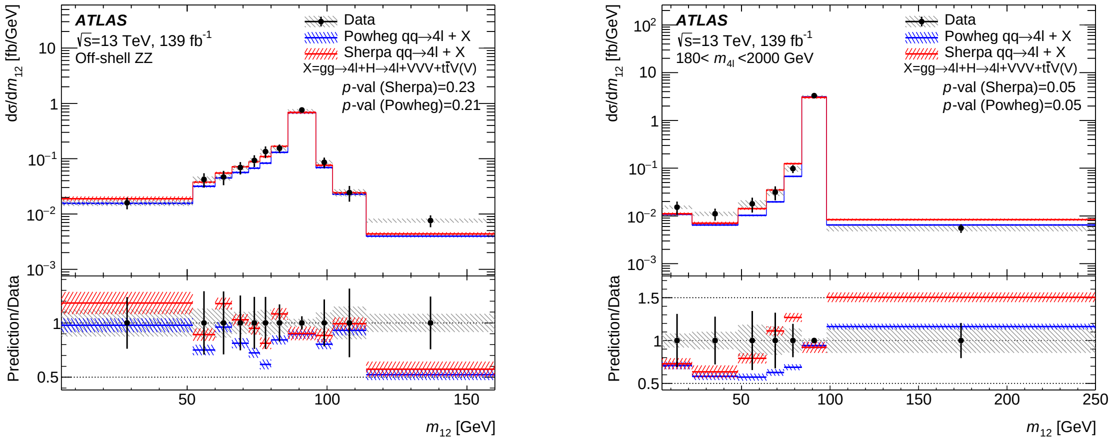

(c) Off-shell ZZ region

(d) On-shell ZZ region

Figure 4.17.: Differential cross-section as a function of m_{12} in the four $m_{4\ell}$ regions. The error bars on the data points give the total uncertainty and the grey hashed band illustrates the contribution from the systematic uncertainty. The SM predictions use either SHERPA or POWHEG + PYTHIA8 to model the $q\bar{q} \to 4\ell$ contribution, plotted in red and blue respectively. The uncertainties on the SM predictions are represented by the red and blue hash. The p-value is the probability for the χ^2 to have at least the observed value, assuming the SM prediction. The number of degrees of freedom is the number of bins in the histogram. The ratio of the SHERPA prediction to the data is shown in the lower panel. In (b) the contribution from Higgs production is shown in addition to the total SM prediction.

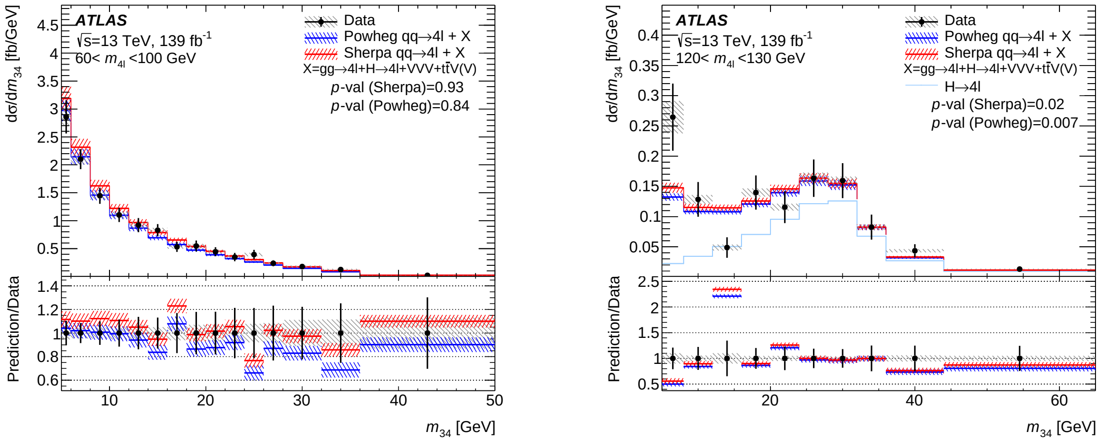

(a) $Z \to 4\ell$ region **(b)** $H \to 4\ell$ region

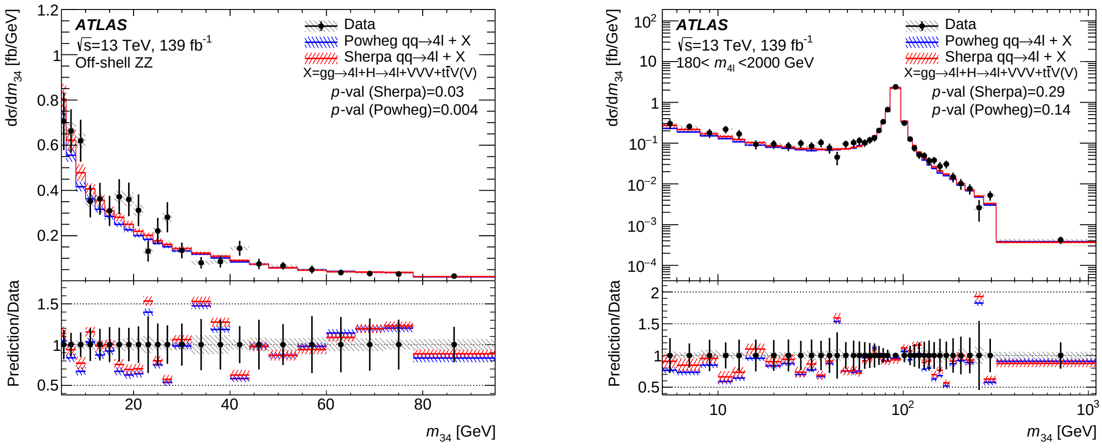

(c) Off-shell ZZ region **(d)** On-shell ZZ region

Figure 4.18.: Differential cross-section as a function of m_{34} in the four $m_{4\ell}$ regions. The measured data (black points) are compared with the SM prediction using either SHERPA (red, with red hashed band for the uncertainty) or POWHEG + PYTHIA8 (blue, with blue hashed band for the uncertainty) to model the $q\bar{q} \to 4\ell$ contribution. In (b) the contribution from Higgs production is shown in addition to the total SM prediction. The error bars on the data points give the total uncertainty and the grey hashed band gives the systematic uncertainty. The p-value is the probability for the χ^2 to have at least the observed value, assuming the SM prediction. The number of degrees of freedom is the number of bins in the histogram. The lower panel shows the ratio of the SM predictions to the data.

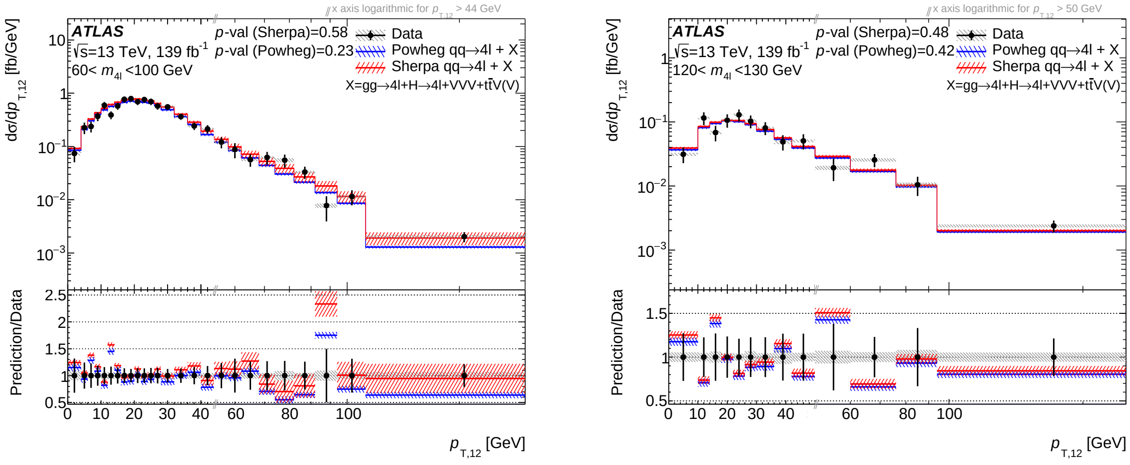

(a) $Z \to 4\ell$ region

(b) $H \to 4\ell$ region

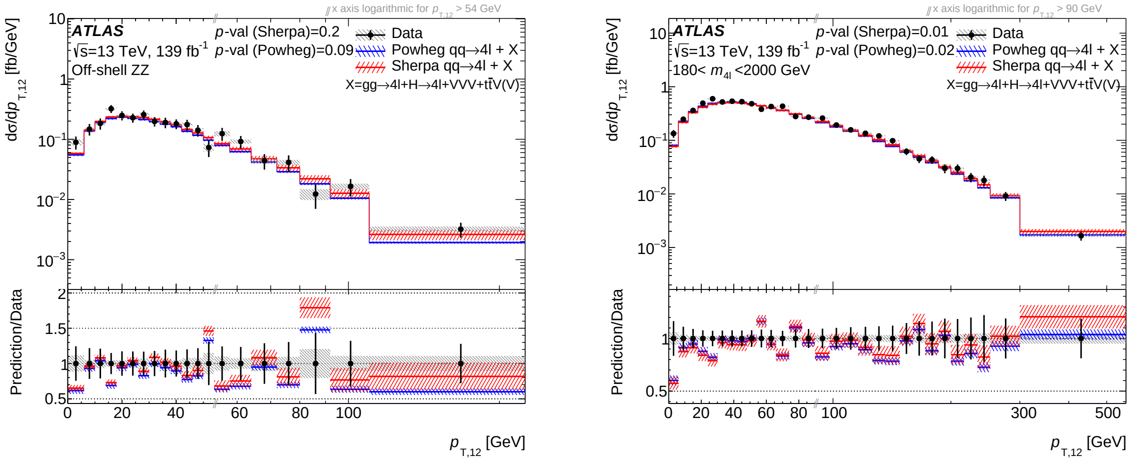

(c) Off-shell ZZ region

(d) On-shell ZZ region

Figure 4.19.: Differential cross-section as a function of $p_{\mathrm{T},12}$ in the four $m_{4\ell}$ regions. The measured data (black points) are compared with the SM prediction using either SHERPA (red, with red hashed band for the uncertainty) or POWHEG + PYTHIA8 (blue, with blue hashed band for the uncertainty) to model the $q\bar{q} \to 4\ell$ contribution. In (b) the contribution from Higgs production is shown in addition to the total SM prediction. The error bars on the data points give the total uncertainty and the grey hashed band gives the systematic uncertainty. The p-value is the probability for the χ^2 to have at least the observed value, assuming the SM prediction. The number of degrees of freedom is the number of bins in the histogram. The lower panel shows the ratio of the SM predictions to the data.

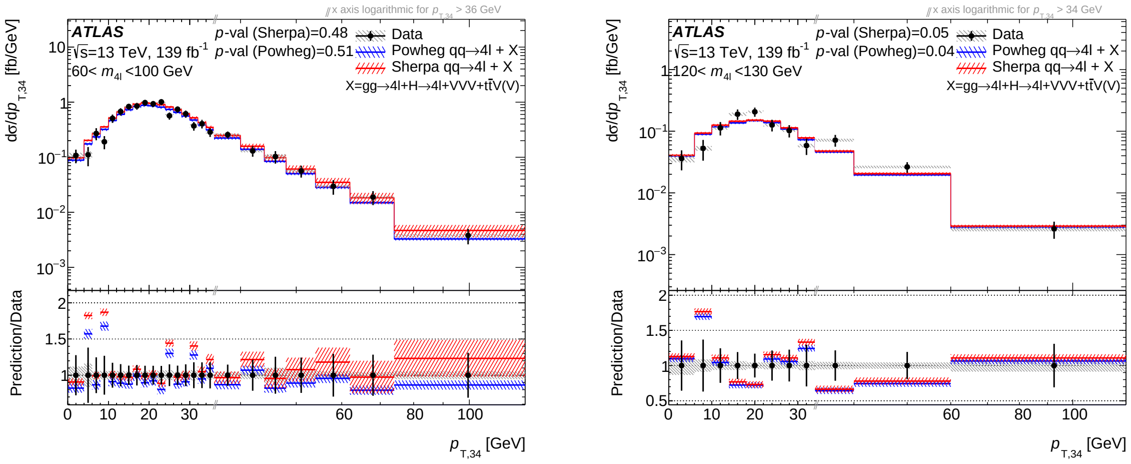

(a) $Z \to 4\ell$ region **(b)** $H \to 4\ell$ region

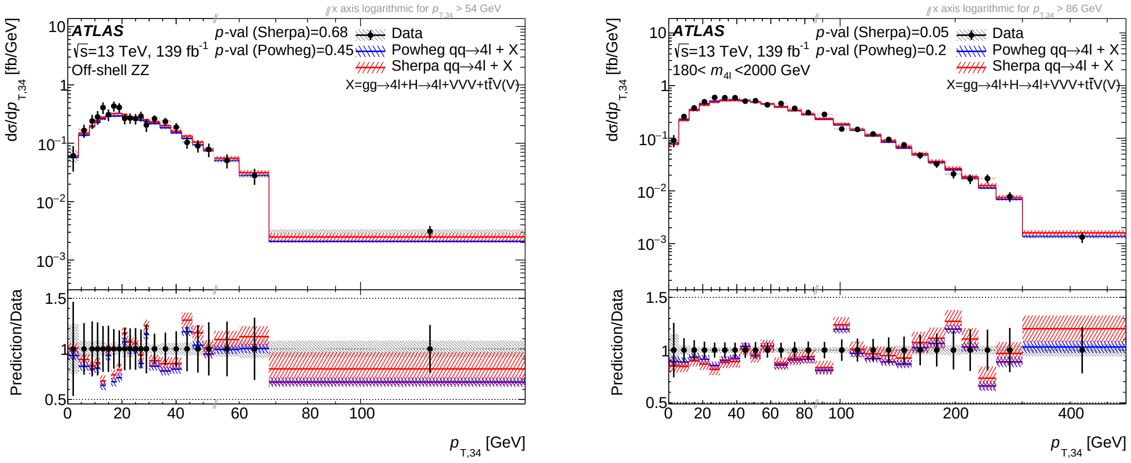

(c) Off-shell ZZ region **(d)** On-shell ZZ region

Figure 4.20.: Differential cross-section as a function of $p_{\mathrm{T},34}$ in the four $m_{4\ell}$ regions. The measured data (black points) are compared with the SM prediction using either SHERPA (red, with red hashed band for the uncertainty) or POWHEG + PYTHIA8 (blue, with blue hashed band for the uncertainty) to model the $q\bar{q} \to 4\ell$ contribution. The error bars on the data points give the total uncertainty and the grey hashed band gives the systematic uncertainty. The p-value is the probability for the χ^2 to have at least the observed value, assuming the SM prediction. The number of degrees of freedom is the number of bins in the histogram. The lower panel shows the ratio of the SM predictions to the data.

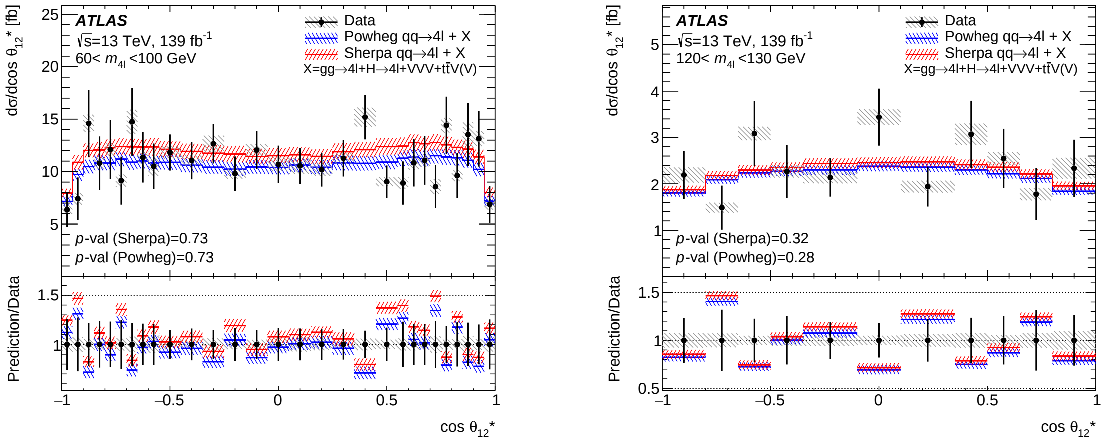

(a) $Z \to 4\ell$ region **(b)** $H \to 4\ell$ region

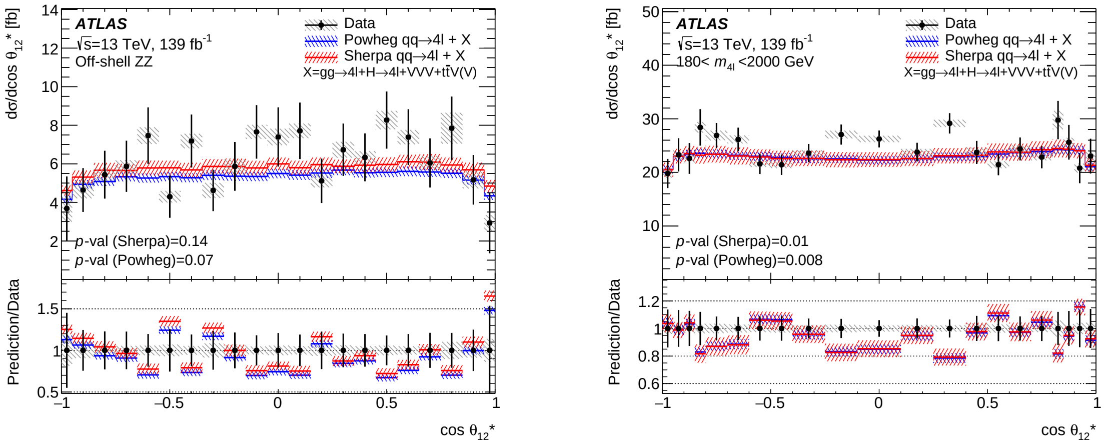

(c) Off-shell ZZ region **(d)** On-shell ZZ region

Figure 4.21.: Differential cross-section as a function of $\cos\theta^*_{12}$ in the four $m_{4\ell}$ regions. The measured data (black points) are compared with the SM prediction using either SHERPA (red, with red hashed band for the uncertainty) or POWHEG + PYTHIA8 (blue, with blue hashed band for the uncertainty) to model the $q\bar{q} \to 4\ell$ contribution. The error bars on the data points give the total uncertainty and the grey hashed band gives the systematic uncertainty. The p-value is the probability for the χ^2 to have at least the observed value, assuming the SM prediction. The number of degrees of freedom is the number of bins in the histogram. The lower panel shows the ratio of the SM predictions to the data.

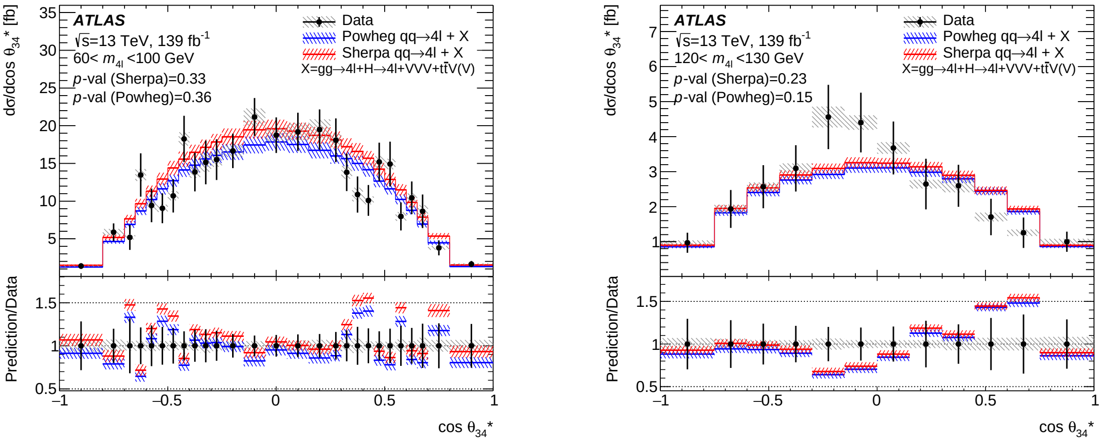

(a) $Z \to 4\ell$ region

(b) $H \to 4\ell$ region

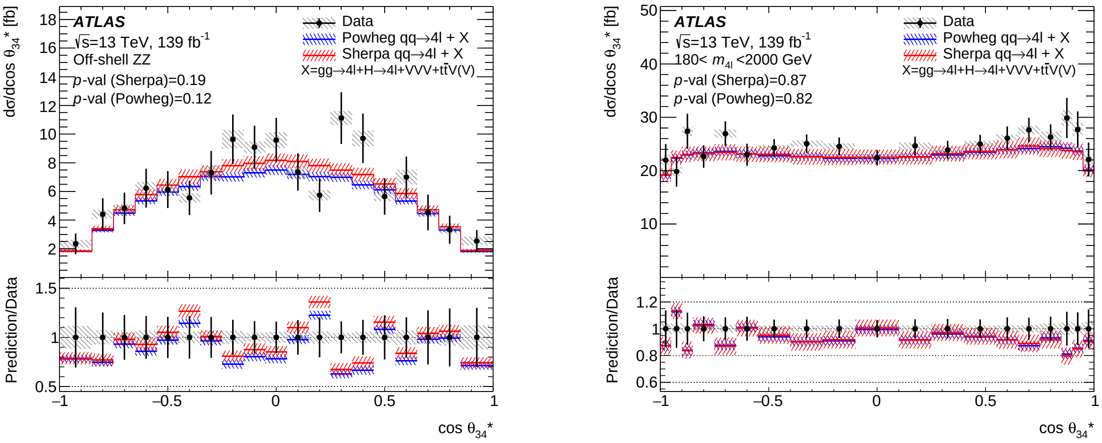

(c) Off-shell ZZ region

(d) On-shell ZZ region

Figure 4.22.: Differential cross-section as a function of $\cos\theta^*_{34}$ in the four $m_{4\ell}$ regions. The measured data (black points) are compared with the SM prediction using either SHERPA (red, with red hashed band for the uncertainty) or POWHEG + PYTHIA8 (blue, with blue hashed band for the uncertainty) to model the $q\bar{q} \to 4\ell$ contribution. The error bars on the data points give the total uncertainty and the grey hashed band gives the systematic uncertainty. The p-value is the probability for the χ^2 to have at least the observed value, assuming the SM prediction. The number of degrees of freedom is the number of bins in the histogram. The lower panel shows the ratio of the SM predictions to the data.

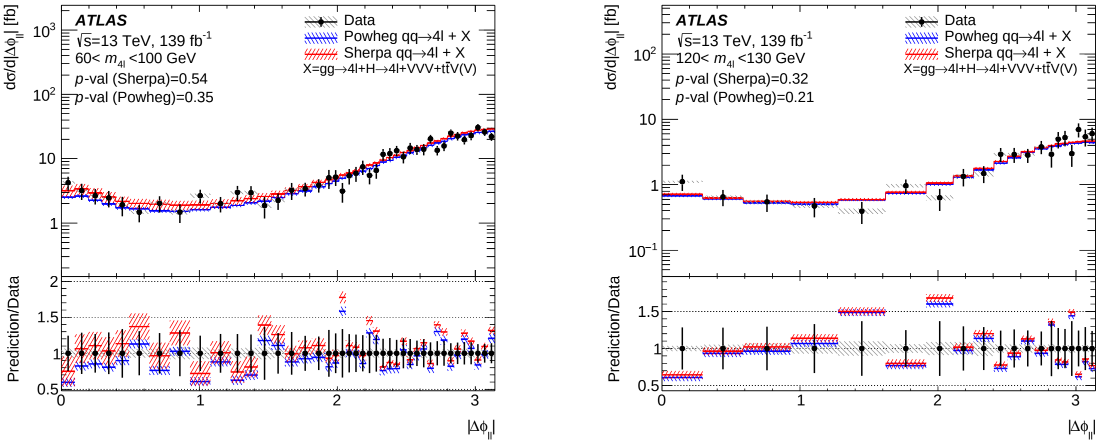

(a) $Z \to 4\ell$ region **(b)** $H \to 4\ell$ region

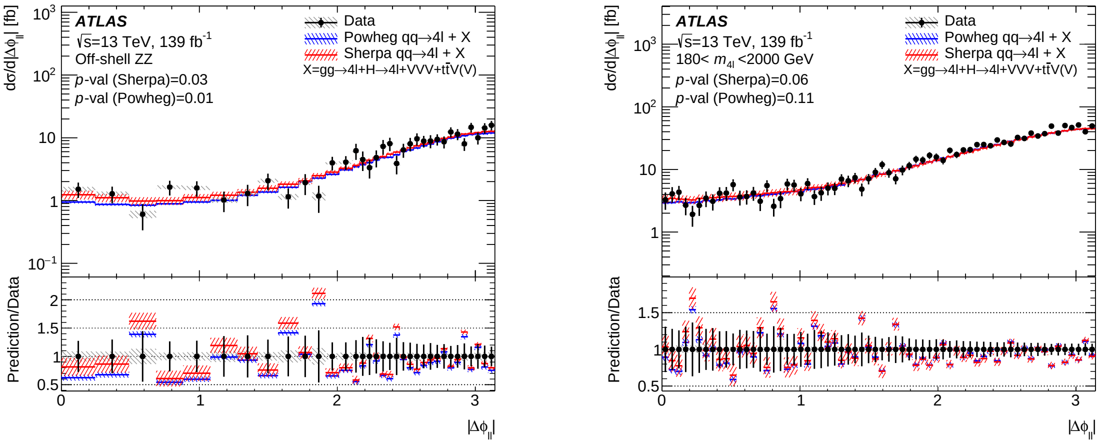

(c) Off-shell ZZ region **(d)** On-shell ZZ region

Figure 4.23.: Differential cross-section as a function of $|\Delta\phi_{\ell\ell}|$ in the four $m_{4\ell}$ regions. The measured data (black points) are compared with the SM prediction using either SHERPA (red, with red hashed band for the uncertainty) or POWHEG + PYTHIA8 (blue, with blue hashed band for the uncertainty) to model the $q\bar{q} \to 4\ell$ contribution. The error bars on the data points give the total uncertainty and the grey hashed band gives the systematic uncertainty. The p-value is the probability for the χ^2 to have at least the observed value, assuming the SM prediction. The number of degrees of freedom is the number of bins in the histogram. The lower panel shows the ratio of the SM predictions to the data.

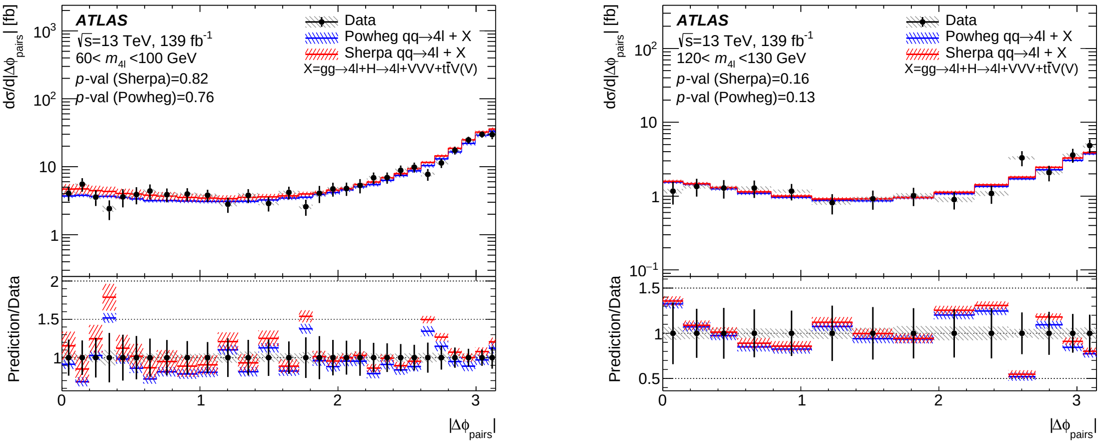

(a) $Z \to 4\ell$ region

(b) $H \to 4\ell$ region

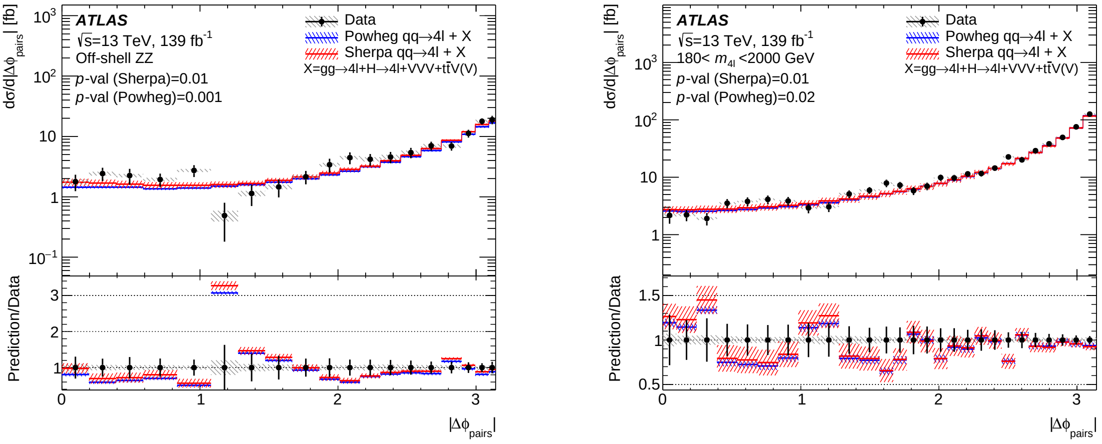

(c) Off-shell ZZ region

(d) On-shell ZZ region

Figure 4.24.: Differential cross-section as a function of $|\Delta\phi_{\text{pairs}}|$ in the four $m_{4\ell}$ regions. The measured data (black points) are compared with the SM prediction using either SHERPA (red, with red hashed band for the uncertainty) or POWHEG + PYTHIA8 (blue, with blue hashed band for the uncertainty) to model the $q\bar{q} \to 4\ell$ contribution. The error bars on the data points give the total uncertainty and the grey hashed band gives the systematic uncertainty. The p-value is the probability for the χ^2 to have at least the observed value, assuming the SM prediction. The number of degrees of freedom is the number of bins in the histogram. The lower panel shows the ratio of the SM predictions to the data.

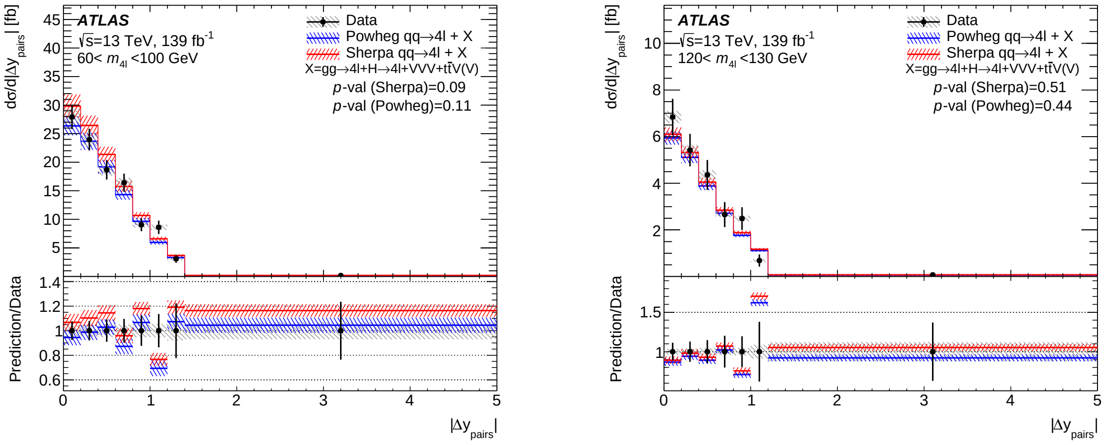

(a) $Z \to 4\ell$ region **(b)** $H \to 4\ell$ region

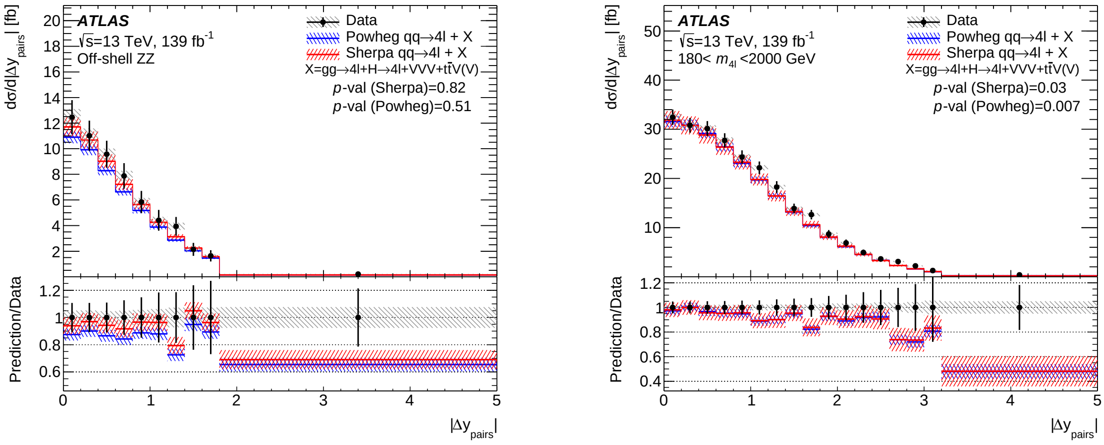

(c) Off-shell ZZ region **(d)** On-shell ZZ region

Figure 4.25.: Differential cross-section as a function of $|\Delta y_{\text{pairs}}|$ in the four $m_{4\ell}$ regions. The measured data (black points) are compared with the SM prediction using either SHERPA (red, with red hashed band for the uncertainty) or POWHEG + PYTHIA8 (blue, with blue hashed band for the uncertainty) to model the $q\bar{q} \to 4\ell$ contribution. The error bars on the data points give the total uncertainty and the grey hashed band gives the systematic uncertainty. The p-value is the probability for the χ^2 to have at least the observed value, assuming the SM prediction. The number of degrees of freedom is the number of bins in the histogram. The lower panel shows the ratio of the SM predictions to the data.

that introduces a heavy Higgs and a new gauge boson. The EFT limits are presented in this section, while the $B-L$ limits are presented in Section 5.3.2 of Chapter 5, in conjunction with limits set by the CONTUR reinterpretation tool. Note that the author did not explicitly work on the interpretation studies within this section - all results are credited to relevant members of the analysis team. This section is discussed in detail due to its relevance to the re-interpretation theme.

Each model has multiple variants which differ in value for some adjustable parameter. This could be, for example, the mass of a new particle or the strength of a new coupling constant. These variants can be compared as explanations for the same observed data, and the probability of the variant being true can be calculated. The probability to obtain the exact data observations given the parameters is known as the likelihood of that variant of the model. The maximum likelihood (ML) estimate is defined as the parameter value at which the likelihood at a maximum. Accordingly, a maximum likelihood estimator (MLE) returns the value of the parameter which, given the data, is most likely.

A likelihood function is constructed using only the published results of the measurement and is used to set limits on the BSM models. It has the form

$$\mathcal{L} = \frac{1}{\sqrt{(2\pi)^k |C|}} \exp\left(-\frac{1}{2}\left(\vec{\sigma}^{\text{meas}} - \vec{\sigma}^{\text{pred}}(\vec{\theta})\right)^T C^{-1} \left(\vec{\sigma}^{\text{meas}} - \vec{\sigma}^{\text{pred}}(\vec{\theta})\right)\right) \times \prod_i \mathcal{G}\left(\theta_i, 0, 1\right), \tag{4.13}$$

where C is the measurement covariance matrix, and $\vec{\sigma}^{\text{meas}}$ and $\vec{\sigma}^{\text{pred}}$ k-dimensional vectors of the measured and predicted cross-sections respectively. The uncertainties in the BSM prediction are included as Gaussian constrained nuisance parameters θ; meaning the uncertainties come from imperfect knowledge of the model parameters. The total covariance matrix is C is the sum of the statistical and systematics uncertainty matrices and the Standard Model theory uncertainty matrix. For the statistical uncertainty, the predicted uncertainty from the expected Standard Model yield is used instead of what is observed in data. This was the result of a study which showed that the data's downward fluctuations in bins with lower statistics resulted in a biased best fit value as well as non-optimal intervals, and a non-asymptotic test statistic [66].

For any given point in the BSM parameter space, there may be different effects on various distributions. In order to obtain the most stringent limit, it is necessary to examine the effect on each of the unfolded kinematic observables presented in section 4.10. There are a total of twelve observables - those that are measured in slices of another count as one observable with the slices combined. Due to the lack of statistical correlation between the observables, the one providing the best expected sensitivity is used to set the limit [67].

4.11.1. $Z \rightarrow 4\ell$ branching fraction

The measured cross-section in the single Z region from table 4.13 is used to extract the single resonant $Z \rightarrow 4\ell$ decay branching fraction and the result is compared to previous LHC measurements. For ease of comparison, phase space corrections are applied the branching fraction so it matches that of previous analyses.

First, the predicted contribution from sources other than $q\bar{q} \rightarrow 4\ell$ ($\sigma^{\text{pred}}_{\text{non-}qq\rightarrow 4\ell} = 0.22 \pm 0.04$) are subtracted from the measured cross-section (σ_{meas}) in the $Z \rightarrow 4\ell$ enriched region. Next, contributions originating from $t-$channel ZZ production rather than single Z production are accounted for with $f_Z = 0.952 \pm 0.005$. A tau correction factor of $f_\tau = 0.99186 \pm 0.00014$ is also applied; this is the fraction of events where no leptons originate from tau decays. In the denominator, σ_Z is the total production cross-section for single Z as quoted in the ATLAS measurement of Reference [141]. Finally, the fiducial correction factor $A_{\text{fid}} 0.935 \pm 0.001$ accounts for the difference in the Z mass window definition. This calculation is written as

$$\mathcal{B}_{Z\rightarrow 4\ell} = \frac{\left(\sigma^{\text{meas}} - \sigma^{\text{pred}}_{\text{non-}qq\rightarrow 4\ell}\right) \times f_{\text{non-}\tau} \times (1 - f_{\text{qqZZ, non-res}})}{\sigma_Z \times A_{\text{fid}}},$$

where

$$\sigma_{\text{unfolded}} = (22.1 \pm 0.7(\text{stat}) \pm 1.1(\text{sys}) \pm 0.4(\text{lumi}))\,\text{fb}$$

is the unfolded cross-section in the single Z region (see Section 4.10) and

$$\sigma_{\text{pred, non-qqZZ}} = (0.222 \pm 0.036(\text{sys}) \pm 0.001(\text{stat}) \pm 0.004(\text{lumi}))\text{fb} = (0.22 \pm 0.04)\,\text{fb}$$

is the predicted contribution in the same region from sources other than $qq \rightarrow ZZ$. It is estimated using the respective theoretical predictions at particle-level.

The resulting $Z \rightarrow 4\ell$ branching fraction is measured to be

$$\begin{aligned}\mathcal{B}_{Z\rightarrow 4\ell} &= (4.41 \pm 0.13\,[\text{stat}] \pm 0.23\,[\text{exp. sys}] \pm 0.09\,[\text{theory}] \pm 0.12\,[\text{lumi}]) \times 10^{-6} \\ &= (4.41 \pm 0.30) \times 10^{-6}\end{aligned}$$

with the quoted statistical, systematic, theoretical, luminosity, and combined uncertainties. This result is compatible with the previous measurements from CMS and ATLAS [63, 64, 142], and is the highest precision measurement of the $Z \to 4\ell$ branching fraction achieved at the LHC to date.

4.11.2. EFT couplings

A simple example of an effective field theory (EFT) is the Fermi theory of beta decay. In this theory postulated in 1933, the neutron decay occurs in a point-like manner to an electron, a proton, and a neutrino. In the underlying model (the SM), the "point" is characterized by the emission of a W boson by a down quark which then transforms into an up quark. The W boson decays to an electron and a neutrino. The Fermi theory effective Lagrangian describing this interaction contains G_F, the Fermi constant. G_F is proportional to the ratio of the weak coupling constant to the mass of the W boson. This was only discovered later on, however, and at the time knowing only the Fermi constant was a sufficient way to model the process. The W boson has a mass that is an order of magnitude higher than the typical energy of β decays, and has been integrated out in the Fermi theory. This is said to be an effective field theory calculation, which is consistent way to describe a higher-order process so long as the energy scale E of the process is small compared to the energy scale Λ of the mediating heavy state [143]. The scale hierarchy $E \ll \Lambda$ is a fundamental property of an EFT [144].

The Standard Model in the Effective Field Theory approach, often abbreviated as SMEFT, is an expansion of the Standard Model Lagrangian that introduces higher dimension operators suppressed by powers of Λ. The suppression increases by Λ^1 for each successive increase in dimension. Λ represents the mass scale of BSM particles, and for the EFT to hold its validity the processes probed should be lower than Λ. The theory is required to contain the Standard Model gauge groups, and at low energies it must reduce to the Standard Model. The Standard Model Lagrangian contains operators of dimension-four, so the expansion for the SMEFT Lagrangian starts at dimension-five and is written as

$$\mathcal{L}_\mathrm{SMEFT} = \mathcal{L}_\mathrm{SM} + \sum_i \frac{c_i^5}{\Lambda}\mathcal{O}_i^5 + \sum_i \frac{c_i^6}{\Lambda^2}\mathcal{O}_i^6 + \sum_i \frac{c_i^7}{\Lambda^3}\mathcal{O}_i^7 + \sum_i \frac{c_i^8}{\Lambda^4}\mathcal{O}_i^8 + \cdots \tag{4.14}$$

where Λ is the energy scale at which new physics appears, $\mathcal{O}_i^d$ are operators of dimension-d, and c_i^d are the coupling constants for the operators, also called the Wilson coefficients.

For each dimension, a complete set of operators must be computed for the expansion. Starting with dimension-five operators, S. Weinberg showed in reference [145] that it violates lepton number. Some decades later, reference [146] demonstrated that there are no $\mathrm{SU}(3) \times \mathrm{SU}(2) \times \mathrm{U}(1)$ gauge-invariant odd-dimensional operators that preserve both baryon and lepton number [147]. Even higher dimensions are very suppressed by factors of Λ. It is for these reasons that in the SMEFT framework considered for the four lepton analysis only dimension-six operators are considered. The effective Lagrangian is therefore defined as

$$\mathcal{L}_{\text{SMEFT}} = \mathcal{L}_{\text{SM}} + \sum_i \frac{C_i^6}{\Lambda^2}\mathcal{O}_i^6. \tag{4.15}$$

A common notation is to absorb the Λ^2 into the Wilson coefficient, thus redefining them as $c_i = \frac{C_i}{\Lambda^2}$. A complete and non-redundant basis for the fifty-nine independent dimension-six operators can be found in reference [148].

Following the Lagrangian of equation 4.15, the amplitude is computed as

$$\mathcal{M}_{Mix} = \mathcal{M}_{SM} + c_i\mathcal{M}_{\text{EFT, }d=6} \tag{4.16}$$

where c_i represent any Wilson coefficient. The matrix element squared reads

$$|\mathcal{M}_{Mix}|^2 = |\mathcal{M}_{SM}|^2 + c_i 2\mathcal{R}\left(M_{SM}^* M_{\text{EFT, }d=6}\right) + c_i^2\left|\mathcal{M}_{\text{EFT, }d=6}\right|^2. \tag{4.17}$$

Here the first term represents the Standard Model contribution, the third term is the pure BSM component, and the second term describes the interference effect between the Standard Model and the effective field theory.

If the effective field theory framework is assessed in context of dimension-six and higher dimension operators, the square of the matrix element is written as

$$\begin{aligned}
|\mathcal{M}|^2 &= \left|\mathcal{M}_{SM} + \frac{C_{i,6}}{\Lambda^2}\mathcal{M}_{\text{EFT, dim6,}i} + \frac{C_{i,8}}{\Lambda^4}\mathcal{M}_{\text{EFT, dim8,}i} + \dots\right|^2 \\
|\mathcal{M}|^2 &= \underbrace{|\mathcal{M}_{SM}|^2}_{\mathcal{O}(1)} + \underbrace{2\frac{C_{i,6}}{\Lambda^2}\mathcal{R}\left(\mathcal{M}_{\text{EFT, dim6,}i}^*\mathcal{M}_{SM}\right)}_{\mathcal{O}(\Lambda^{-2})} \\
&\quad + \underbrace{\frac{C_{i,6}^2}{\Lambda^4}\left|\mathcal{M}_{\text{EFT, dim6,}i}\right|^2 + 2\frac{C_{i,8}}{\Lambda^4}\mathcal{R}\left(\mathcal{M}_{\text{EFT, dim8,}i}^*\mathcal{M}_{SM}\right)}_{\mathcal{O}(\Lambda^{-4})} + \dots.
\end{aligned} \tag{4.18}$$

The Wilson coefficients here are written in their raw form with the power of Λ included in the denominator. It is interesting to note that the quadratic term of the dimension-six operators are suppressed by the same Λ^{-4} as the interference term of the dimension-eight operators with the Standard Model contribution. This motivates the construction of a linear-only model alongside the full model, where terms higher than order Λ^{-2} are ignored. For the dimension-six model, the linear-only limit sets the third term of equation 4.19 to zero.

Considering the resulting limits set for the linear-only and the full EFT model, should the limits be largely compatible with one another then the implication is that the impact of possible higher-dimension operators is expected to be small. A difference in the two, however, indicates that sensitivity to the possibly neglected contributions could exist.

The new physics component considered in this section for SMEFT is described using only dimension-six operators. The energy cutoff scale for new physics is taken to be 1 TeV. Following equation 4.17, the cross-section prediction can also be decomposed into a Standard Model term, an interference term, and a BSM term.

$$\sigma(c_i) = \sigma_{\text{SM}} + \frac{\sigma_{\text{SM}}}{\sigma_{\text{SM(LO)}}}(c_i\sigma_{\text{INT}} + c_i^2\sigma_{d=6}). \tag{4.19}$$

The SM prediction σ_{SM} is the same one described in section 4.5.2 using SHERPA to simulate the $q\bar{q} \to 4\ell$ process. The predictions for the interaction and BSM term are obtained using the SMEFTSIM package [149]. There is an additional factor multiplied: the ratio of the best SM prediction to the leading order SM prediction. This corrects the BSM prediction for higher order effects, under the assumption that said effects are the same for BSM contributions as they are for SM contributions. The limits on the Wilson coefficients are set using a profile likelihood method as described at the beginning of this section 4.11.

To test a hypothesized value of c, it is useful to write the the profile likelihood ratio:

$$\lambda(c) = \frac{\mathcal{L}(\vec{c}, \hat{\hat{\vec{\theta}}}(\vec{c}))}{\mathcal{L}(\hat{\vec{c}}, \hat{\vec{\theta}})} \tag{4.20}$$

where the numerator is the conditional maximum likelihood estimator for specified $\vec{c}$ while the denominator is the unconditional maximum likelihood estimator. From the definition of $\lambda(c)$ in, it is evident that that $\lambda(c)$ must lie between 0 and 1, where λ near 1 implies good agreement between the data and the hypothesized value of c.

Equivalently it is convenient to use the statistic

$$q = -2 \ln \lambda(c), \tag{4.21}$$

where higher values of q correspond to a stronger incompatibility between the data and c [150].

A screening procedure is used to identify the subset of the EFT parameters which contribute non-negligibly to the four-lepton final state. These twenty-two parameters are:

- c_{HG}, $\tilde{c}_{HG}$, c_{HD} affecting the Higgs couplings[2];
- c_{HWB} affecting the gauge boson couplings;
- c_{Hd}, c_{Hu}, c_{He}, $c_{Hl}^{(1)}$, $c_{Hl}^{(3)}$, $c_{Hq}^{(1)}$, $c_{Hq}^{(3)}$ affecting the $Z \to \ell\ell$ vertex;
- c_{ed}, c_{ee}, c_{eu}, c_{ld}, c_{le}, c_{ll}, $c_{ll}^{(1)}$, $c_{lq}^{(1)}$, $c_{lq}^{(3)}$, c_{lu}, c_{qe} from four-fermion interactions (contact terms).

Limits

Figure 4.26 and Table 4.15 present the limits using the linear-only model, and Figure 4.27 and Table 4.14 show the limits using the full model. Also shown in the tables is the most sensitive observable that is used to set the limit.

With the two sets of results, a comparison is made to interpret the similarities and differences. Overall, the coefficients can be grouped into four categories:

1. c_{HD}, c_{HWB}, c_{He}, $c_{Hl}^{(1)}$, $c_{Hq}^{(3)}$, $c_{Hl}^{(3)}$ and $c_{ll}^{(1)}$ have very similar limits in the linear and full model. There is a negligible contribution from the quadratic term, and whether or not it's included does not affect the end result.
2. $c_{Hq}^{(1)}$ and $c_{lq}^{(3)}$ which have slightly lower upper and lower limits due to the small positive contributions from the quadratic term which enhances the linear contribution at positive values of the coefficient, and lessens at negative values.

---

[2] The tilde indicates a CP-violating term.

Coefficient	Observable	95% CL Expected [TeV^{-2}]	95% CL Observed [TeV^{-2}]
c_{HG}	m_{34} vs. $m_{4\ell}$	$[-0.18, -0.027]$ $\cup[-0.014, 0.011]$	$[-0.20, -0.029]$ $\cup[-0.010, 0.012]$
$\tilde{c}_{HG}$	m_{34} vs. $m_{4\ell}$	$[-0.031, 0.031]$	$[-0.033, 0.033]$
c_{HD}	m_{34} vs. $m_{4\ell}$	$[-0.45, 0.44]$	$[-0.60, 0.29]$
c_{HWB}	m_{34} vs. $m_{4\ell}$	$[-0.20, 0.21]$	$[-0.29, 0.13]$
c_{Hd}	$p_{\mathrm{T},12}$ vs. $m_{4\ell}$	$[-4.9, 9.8]$	$[-2.6, 8.3]$
c_{Hu}	$\lvert\Delta\phi_{\ell\ell}\rvert$ vs. $m_{4\ell}$	$[-11, 2.8]$	$[-13, -6.9] \cup [-1.5, 4.4]$
c_{He}	$\lvert\Delta\phi_{\mathrm{pairs}}\rvert$ vs. $m_{4\ell}$	$[-0.46, 0.49]$	$[-0.70, 0.21]$
$c_{Hl}^{(1)}$	$\lvert\Delta\phi_{\mathrm{pairs}}\rvert$ vs. $m_{4\ell}$	$[-0.39, 0.37]$	$[-0.19, 0.55]$
$c_{Hl}^{(3)}$	$\lvert\Delta\phi_{\ell\ell}\rvert$ vs. $m_{4\ell}$	$[-0.28, 0.29]$	$[-0.47, 0.12]$
$c_{Hq}^{(1)}$	m_{34} vs. $m_{4\ell}$	$[-0.93, 0.69]$	$[-1.6, 0.43]$
$c_{Hq}^{(3)}$	$\lvert\Delta\phi_{\mathrm{pairs}}\rvert$ vs. $m_{4\ell}$	$[-0.34, 0.33]$	$[-0.15, 0.52]$
c_{ed}	m_{34} vs. $m_{4\ell}$	$[-0.49, 0.39]$	$[-0.51, 0.41]$
c_{ee}	m_{34} vs. $m_{4\ell}$	$[-38, 35]$	$[-33, 42]$
c_{eu}	$m_{4\ell}$	$[-0.21, 0.35]$	$[-0.14, 0.21]$
c_{ld}	m_{34} vs. $m_{4\ell}$	$[-0.40, 0.34]$	$[-0.41, 0.36]$
c_{le}	m_{34} vs. $m_{4\ell}$	$[-23, 22]$	$[-21, 26]$
c_{ll}	m_{34} vs. $m_{4\ell}$	$[-23, 21]$	$[-20, 25]$
$c_{ll}^{(1)}$	$\lvert\Delta\phi_{\mathrm{pairs}}\rvert$ vs. $m_{4\ell}$	$[-0.34, 0.33]$	$[-0.17, 0.50]$
$c_{lq}^{(1)}$	$m_{4\ell}$	$[-0.14, 0.28]$	$[-0.086, 0.17]$
$c_{lq}^{(3)}$	m_{34} vs. $m_{4\ell}$	$[-0.083, 0.071]$	$[-0.064, 0.081]$
c_{lu}	$m_{4\ell}$	$[-0.24, 0.32]$	$[-0.16, 0.20]$
c_{qe}	$m_{4\ell}$	$[-0.17, 0.21]$	$[-0.11, 0.14]$

Table 4.14.: The expected and observed confidence intervals at 95% CL for the SMEFT Wilson coefficients, including both the linear and quadratic terms. The most sensitive observable indicated for each coefficient is used for the constraints. Only one coefficient is fitted at a time, with all others set to zero. This table is from Ref. [66].

3. c_{HG} and c_{Hu} have a double maxima in the likelihood scan when using the full model with the quadratic term, thus resulting in a less stringent limit than the linear-only model.

4. the remaining eleven coefficients receive non-negligible contributions from the quadratic term, and therefore have more stringent limits when using the full-model. In particular, $\tilde{c}_{HG}$ receives zero contribution from the linear term.

Coefficient	Observable	95% CL Expected [TeV^{-2}]	95% CL Observed [TeV^{-2}]
c_{HG}	m_{34} vs. $m_{4\ell}$	$[-0.011, 0.013]$	$[-0.0090, 0.015]$
$\tilde{c}_{HG}$	m_{34} vs. $m_{4\ell}$	–	–
c_{HD}	m_{34} vs. $m_{4\ell}$	$[-0.46, 0.45]$	$[-0.63, 0.28]$
c_{HWB}	m_{34} vs. $m_{4\ell}$	$[-0.21, 0.20]$	$[-0.29, 0.13]$
c_{Hd}	$p_{\mathrm{T},12}$ vs. $m_{4\ell}$	$[-10, 10]$	$[-3.0, 18]$
c_{Hu}	$\lvert\Delta\phi_{\ell\ell}\rvert$ vs. $m_{4\ell}$	$[-3.5, 3.7]$	$[-1.6, 6.1]$
c_{He}	$\lvert\Delta\phi_{\mathrm{pairs}}\rvert$ vs. $m_{4\ell}$	$[-0.47, 0.46]$	$[-0.75, 0.21]$
$c_{Hl}^{(1)}$	$\lvert\Delta\phi_{\mathrm{pairs}}\rvert$ vs. $m_{4\ell}$	$[-0.37, 0.38]$	$[-0.19, 0.57]$
$c_{Hl}^{(3)}$	$\lvert\Delta\phi_{\ell\ell}\rvert$ vs. $m_{4\ell}$	$[-0.29, 0.29]$	$[-0.51, 0.12]$
$c_{Hq}^{(1)}$	m_{34} vs. $m_{4\ell}$	$[-0.81, 0.78]$	$[-1.1, 0.47]$
$c_{Hq}^{(3)}$	$\lvert\Delta\phi_{\mathrm{pairs}}\rvert$ vs. $m_{4\ell}$	$[-0.34, 0.35]$	$[-0.15, 0.53]$
c_{ed}	m_{34} vs. $m_{4\ell}$	$[-1.3, 1.8]$	$[-1.0, 2.3]$
c_{ee}	m_{34} vs. $m_{4\ell}$	$[-59, 65]$	$[-25, 100]$
c_{eu}	$m_{4\ell}$	$[-0.62, 0.45]$	$[-0.36, 0.63]$
c_{ld}	m_{34} vs. $m_{4\ell}$	$[-1.8, 2.5]$	$[-1.3, 3.0]$
c_{le}	m_{34} vs. $m_{4\ell}$	$[-63, 68]$	$[-18, 130]$
c_{ll}	m_{34} vs. $m_{4\ell}$	$[-39, 43]$	$[-17, 70]$
$c_{ll}^{(1)}$	$\lvert\Delta\phi_{\mathrm{pairs}}\rvert$ vs. $m_{4\ell}$	$[-0.34, 0.34]$	$[-0.18, 0.50]$
$c_{lq}^{(1)}$	$m_{4\ell}$	$[-0.76, 0.40]$	$[-4.1, 0.53]$
$c_{lq}^{(3)}$	m_{34} vs. $m_{4\ell}$	$[-0.059, 0.083]$	$[-0.050, 0.098]$
c_{lu}	$m_{4\ell}$	$[-1.4, 0.99]$	$[-0.78, 1.4]$
c_{qe}	$m_{4\ell}$	$[-1.1, 0.83]$	$[-0.72, 1.2]$

Table 4.15.: The expected and observed confidence intervals at 95% CL for the SMEFT Wilson coefficients, including only linear terms. The most sensitive observable indicated for each coefficient is used for the constraints. Only one coefficient is fitted at a time, with all others set to zero. This table is from Ref. [66].

The improvement seen in the limits in the last category when using the full-model including quadratic terms of order Λ^{-4} indicate that dimension-eight terms may have non-negligible effects.

Overall the expected limits and observed limits are compatible, with the exception of the lower limit of $c_{lq}^{(1)}$ in the linear-only case. The observed lower limit is significantly

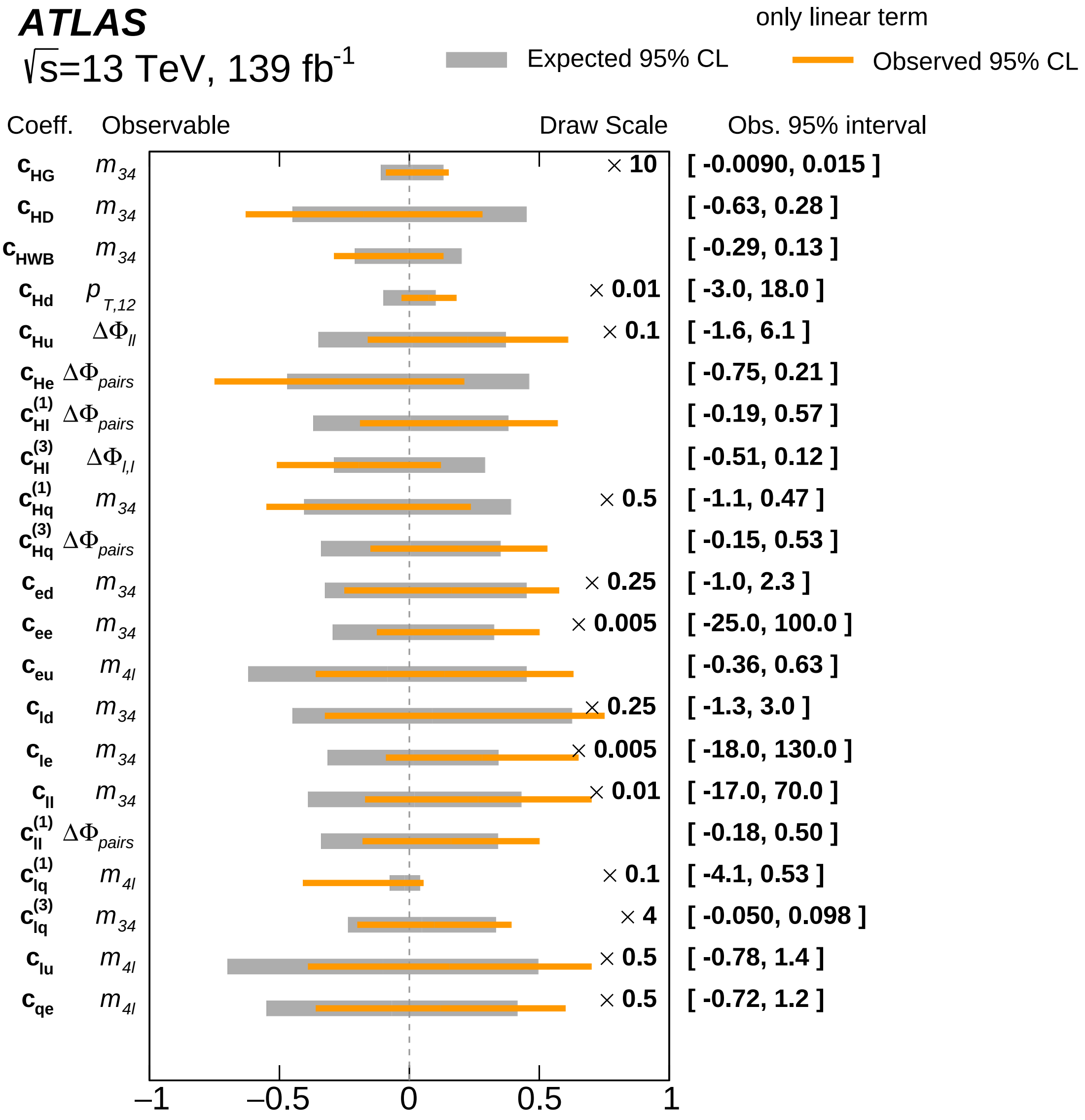

Figure 4.26.: The expected and observed confidence intervals at 95% CL for the SMEFT Wilson coefficients, which are in units of TeV^2 for only the linear terms. The multiplicative number shown to the right of plotted points indicates a scaling factor that is applied to the limit for the purpose of the plot, in order to show all coefficients on the same scale. The most sensitive observable indicated for each coefficient is used for the constraints. Only one coefficient is fitted at a time, with all others set to zero. This figure is from Ref. [67]

less stringent that the expected lower limit. This is thought to be an artifact of the simple model where the scale uncertainty is affecting the EFT prediction [67][3].

---

[3] The paper explains that for a large EFT signal that is incompatible with the data, the EFT scale uncertainty's nuisance parameter is pulled in order to bring the prediction closer to the observation. The nuisance parameter's constraint term penalizes this behaviour in the likelihood. However, for large negative values of $c_{lq}^{(1)}$ the size and shape of the scale uncertainty's effect on the signal prediction are related in a way that produces a prediction precisely imitating the statistical fluctuations in the

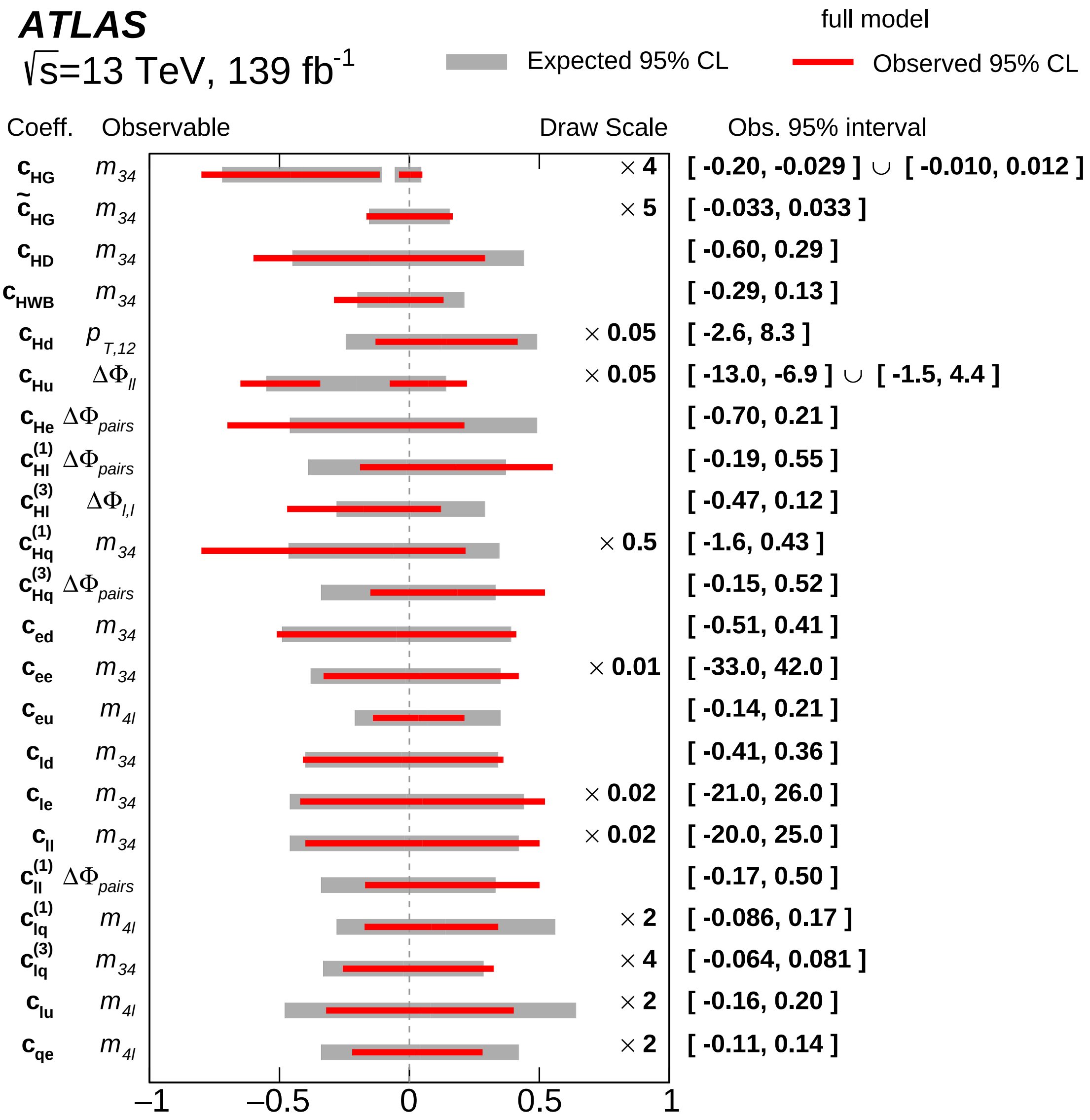

Figure 4.27.: The expected and observed confidence intervals at 95% CL for the SMEFT Wilson coefficients, which are in units of TeV^2 for the full model. The multiplicative number shown to the right of plotted points indicates a scaling factor that is applied to the limit for the purpose of the plot, in order to show all coefficients on the same scale. The most sensitive observable indicated for each coefficient is used for the constraints. Only one coefficient is fitted at a time, with all others set to zero. . This figure is from Ref. [67]

Limits have previously been placed on c_{HG}, $\tilde{c}_{HG}$ and c_{HWB}, in a measurement of the $H \rightarrow 4\ell$ cross-section [151]. The $H \rightarrow 4\ell$ cross-section analysis has more stringent limits for c_{HG}, but for $\tilde{c}_{HG}$ the limits are very similar, with the $m_{4\ell}$ analysis providing slightly tighter constraints. For c_{HWB} the constraints of this analysis are significantly more stringent with $[-0.20, 0.21]$ expected and $[-0.29, 0.13]$ observed compared to $[-1.09, 0.99]$ expected and $[-1.06, 0.99]$ observed in the $H \rightarrow 4\ell$ analysis. The improvement can be understood as being due to the fact that changes in c_{HWB} affect the entire $m_{4\ell}$ spectrum, not just the region close to m_H [67]. Limits on the coefficients affecting the $Z \rightarrow \ell\ell$ vertex have been obtained previously from a global fit to LEP and LHC data [152], and are generally one or two orders of magnitude more stringent than the limits presented from Reference [67].

---

measured cross-section, increasing the likelihood. This leads to a larger than expected observed lower limit on $c_{lq}^{(1)}$ [67]

Chapter 5.

Re-interpreting results from LHC measurements

In general, analyses at the LHC fall under one of two broad categories: they are either measurements (which, to this day, have shown to agree with the Standard Model), or direct searches for beyond the Standard Model physics. Although direct searches are precise and sensitive to the targeted new physics signals, they tend to very model dependent and cover only a small subset of all possible theories and parameter space. Furthermore, an LHC search can take from months to years from inception to publication. There is simply not enough person- or computing-power to conduct a direct search for every BSM model on the market. A solution to this well-known problem lies in the former category of LHC results: the measurements. The idea is that the addition of a new particle or new interaction would affect observables that have already been precisely measured. Therefore a good handful of models may already be excluded, given that so far, no excesses have been observed.

This idea is a bottom-up, data-driven approach at probing BSM models. In the particle physics community, the reuse of data after its publication is called re-interpretation. Re-interpretation allows a much larger breadth of BSM models to be tested outside of the experimental collaborations by theorists and experimentalists alike. Given how time consuming it is to do physics analyses, it is in the interest of the particle physics community to maximize the scientific impact of published data by ensuring reinterpretability. Although it is not a tool for discovery, reinterpretation studies are often useful in helping experiments identify plausible BSM scenarios that direct searches should target. Since they make use of existing results, they do not require any reprocessing of the data, event selection, or background and systematics estimates. It is considered good practice for analysis teams to publish, along with their measurement, material for reinterpretation. The latest report from the LHC reinterpretation forum can be found in Reference [153], which details the recommendations that analysis teams can take to ensure reinterpretability.

In this Chapter, an overview of the philosophy and workflow behind the CONTUR reinterpretation package is given. Two reinterpretation studies are presented where existing LHC measurements are used to set limits in previously unexplored regions of BSM model space. The ATLAS four-lepton measurement of Chapter 4 plays a particularly important role in both, and is studied in detail. First, section 5.1 introduces CONTUR, from which the results are derived for the rest of this Chapter. Section 5.2 is adapted from Reference [1], where limits are set by LHC measurements on a BSM particles vector-like quarks. Finally, section 5.3 shows the results of a brief study on a model with a gauged $B-L$ symmetry. Limits are additionally set on this model as part of the ATLAS $m_{4\ell}$ measurement, which are also presented.

5.1. CONTUR and related software tools

This section provides a brief summary of the CONTUR method, adapted from key paragraphs of the manual. For more comprehensive explanations, please refer to the relevant sections of the manual.

The backbone of the CONTUR method lies in the fact that many differential cross-sections are precisely measured and well understood, and that any modifications to the SM Lagrangian would inevitably introduce changes to these cross-sections. If the change induced by adding in a new particle or a new field is well beyond the data's uncertainties, then (quoting the manual) "we'd already have seen it". In other words, if one can predict the changes to the hundreds of LHC measured distributions that a BSM model would make, then one can already determine what regions of the model's parameter space are already excluded. This is the philosophy upon which CONTUR was built.

A couple of ingredients are necessary for running CONTUR. First, the BSM model must be interfaced to a Monte Carlo event generator in order to simulate events. Facilitating this procedure is the FeynRules package [154]. At its core, FeynRules is a mathematica package used to develop BSM models. Upon the input of a Lagrangian, it derives the Feynman rules. An important feature is the export to the Universal FeynRules Object [155] (UFO) format, compatible with a range of event generators. UFO files hold the basic information about new particles and parameters which are directly used to generate events for new physics signals. The MC event generator used for studies in this thesis is Herwig [156], the default MC event generator used by CONTUR. It is important to note here another pillar in the CONTUR philosophy: to use inclusive event generation wherever possible. The advantage of doing so is the coverage of all allowed final states which would be affected if that BSM model were to exist in nature. Generating events inclusively rather than exclusively allows CONTUR to paint a comprehensive picture of the exclusion across all manner of final states instead of focusing on the most spectacular signatures of a new model [157].

Second, a platform to compare the simulated BSM events to the plethora of LHC measurements is needed. This job is done by RIVET [158], a general-purpose tool used to reproduce analysis procedures on simulated events. Since its inception, the RIVET system has been used to validate and tune Monte Carlo event generators with minimal effort and maximum portability [158]. For example, it has been used extensively in tuning in Minimum Bias (MB) and Underlying Event (UE) observables for the LHC using Tevatron data [159]. It hosts a wealth of measurements from various high energy physics experiments. Each measurement is written into a RIVET routine which preserves the workflow of the analysis. Included are crucial information such as the fiducial region selection cuts and observable binnings. With this information, RIVET is able to transform the output from Monte Carlo event generators into histograms of cross-sections in the scope of the measurement. In general, it is considered good practice for LHC measurements to publish their data on HEPData [160] and to provide the analysis code as a RIVET routine. RIVET's growing library of available analyses and it's ability to make fast and easy to comparisons between raw generator output and particle-level data is the foundation upon which CONTUR is built.

The CONTUR workflow is summarized in Figure 5.1 in four steps, taken from Reference [157]. Each step is written in bold, with the tool used to achieve it in smaller font. First in the workflow is to call upon an event generator (e.g. Herwig) to simulate new physics events for a specified BSM model. The free paramters of the BSM model should be defined manually by the user. Herwig is interfaced to RIVET directly so the events are directly piped into the observables' histograms. The RIVET output corresponds to the excess BSM contribution in any of the measured distributions made at the LHC which would be present should the model hold true. The next step is to evaluate the likelihood for the BSM model given the size of the measurement uncertainty. The heap of measurements are grouped into orthogonal pools based on their final state signature, and CONTUR uses the best constraint from each pool to form a global exclusion measure for a given model at a given set of parameter values [157]. This is CONTUR's main

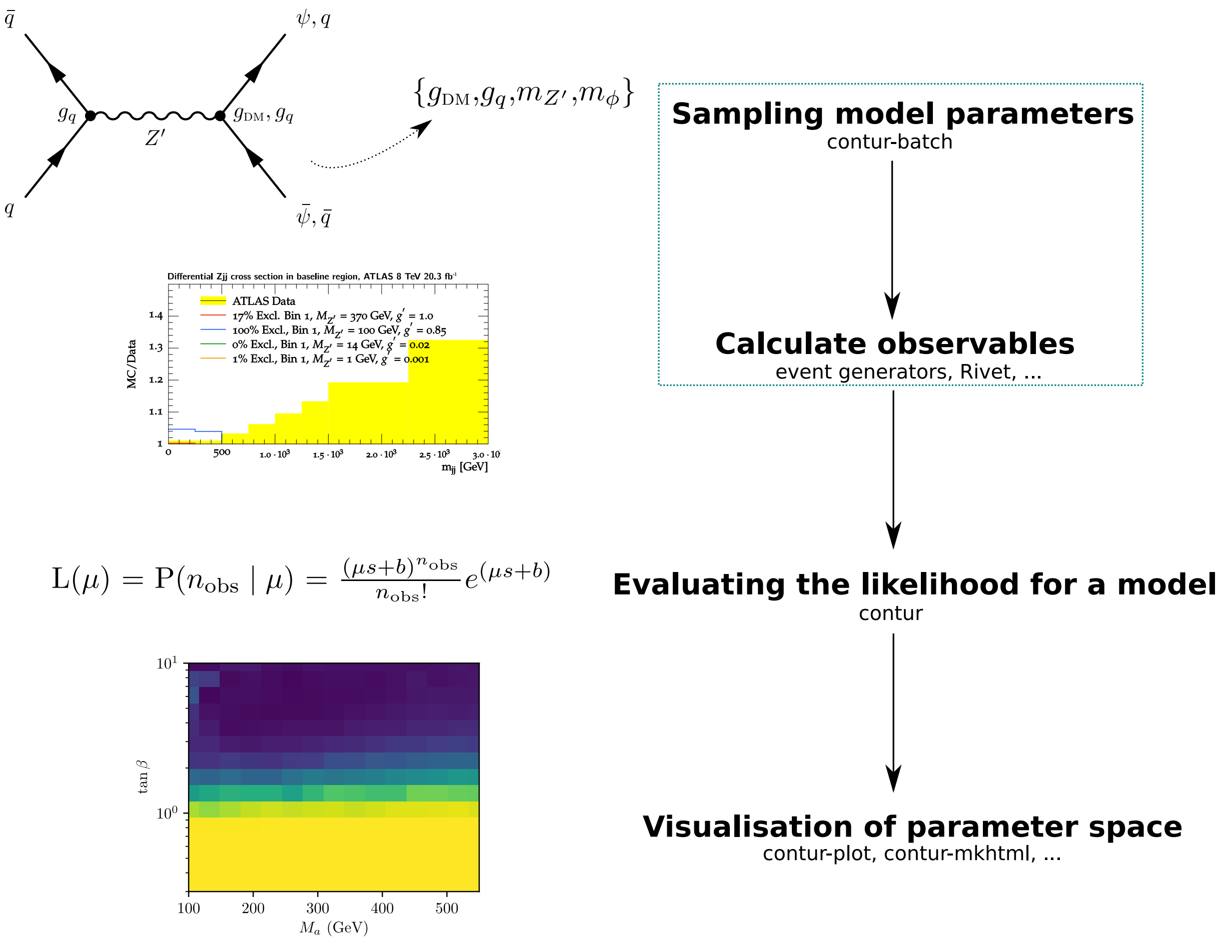
$\bar{q}$
ψ, q
g_q
g_{DM}, g_q
Z'
q
$\bar{\psi}, \bar{q}$
$\{g_{\mathrm{DM}}, g_q, m_{Z'}, m_\phi\}$
Sampling model parameters
contur-batch
Calculate observables
event generators, Rivet, ...
Differential Zjj cross section in baseline region, ATLAS 8 TeV 20.3 fb⁻¹
ATLAS Data
17% Excl. Bin 1, $M_{Z'}$ = 370 GeV, g' = 1.0
100% Excl. Bin 1, $M_{Z'}$ = 100 GeV, g' = 0.85
0% Excl., Bin 1, $M_{Z'}$ = 14 GeV, g' = 0.02
1% Excl., Bin 1, $M_{Z'}$ = 1 GeV, g' = 0.001
MC/Data
m_{jj} [GeV]
$\mathrm{L}(\mu) = \mathrm{P}(n_{\mathrm{obs}} \mid \mu) = \frac{(\mu s+b)^{n_{\mathrm{obs}}}}{n_{\mathrm{obs}}!} e^{(\mu s+b)}$
Evaluating the likelihood for a model
contur
$\tan\beta$
M_a (GeV)
Visualisation of parameter space
contur-plot, contur-mkhtml, ...

Figure 5.1.: An simplified schematic of the CONTUR workflow. The dotted box denotes the portion of the workflow that makes extensive use of external packages, affording multiple options, such as the choice of MC event generator. The next stage is the taking of physics observables as inputs to a statistical analysis (i.e. evaluating the likelihood for the model). Finally the last stage involves using tools to visualize the output of the likelihood analysis. Figure taken from Reference [157]

.

functionality, and takes around one hour to complete for a single model parameter point. The same process is repeated for many points in a two-dimensional grid of the BSM model's parameter values. With the help of a computing farm with multiple nodes, this can be done in less than one workday. Finally, CONTUR's plotting functions allow the user to visualize the likelihood evaluation of their scanned parameter space. Like so, CONTUR is able to tell the user whether wide regions of the BSM model's parameter is already excluded by LHC previous measurements. An in depth description of each step can be found in Reference [157].

5.2. Sensitivity of LHC measurements to Vector-like Quarks

Vector-like quarks belong to a separate family from the SM quarks. They are non-chiral, and thus both the left- and right-handed components transform the same way under the SM symmetries. This enables them to have a bare mass term and obtain mass without interacting with the Higgs boson. Consequently, they are not constrained by Higgs measurements, unlike a fourth generation in the SM quark family. In short, VLQs are simplest example of coloured fermions still allowed by experimental data [161].

Vector-like quarks arise in many classes of BSM theories, such as composite Higgs that assume electroweak symmetry breaking is due to a a new strongly interacting sector [162], or little Higgs models that introduce extended global symmetries, or models with extra dimensional symmetries. As with most models extending the SM, many of these introduce new sources of CP violation.

5.2.1. Phenomenology of VLQs

For the material presented in this section, vector-like quarks are studied in a model-independent fashion involving relatively few free parameters. The framework is developed in Reference [163], which presents an effective Lagrangian description for vector-like quarks that is easily translated to experimental observables. The Lagrangian is written in equation 3.2 of Reference [163] as:

$$
\begin{aligned}
\mathcal{L} =& \kappa_B \left[\sqrt{\frac{\zeta_i \xi_W^B}{\Gamma_W^0}} \frac{g}{\sqrt{2}} [\bar{B}_{L/R} W_\mu^- \gamma^\mu u_{L/R}^i] + \sqrt{\frac{\zeta_i \xi_Z^B}{\Gamma_Z^0}} \frac{g}{2c_W} [\bar{B}_{L/R} Z_\mu \gamma^\mu d_{L/R}^i] - \sqrt{\frac{\zeta_i \xi_H^B}{\Gamma_H^0}} \frac{M_B}{v} [\bar{B}_{R/L} H d_{L/R}^i] \right] \\
&+ \kappa_T \left[\sqrt{\frac{\zeta_i \xi_W^T}{\Gamma_W^0}} \frac{g}{\sqrt{2}} [\bar{T}_{L/R} W_\mu^+ \gamma^\mu d_{L/R}^i] + \sqrt{\frac{\zeta_i \xi_Z^T}{\Gamma_Z^0}} \frac{g}{2c_W} [\bar{T}_{L/R} Z_\mu \gamma^\mu u_{L/R}^i] - \sqrt{\frac{\zeta_i \xi_H^T}{\Gamma_H^0}} \frac{M_T}{v} [\bar{T}_{R/L} H u_{L/R}^i] \right] \\
&+ \kappa_X \left[\sqrt{\frac{\zeta_i}{\Gamma_W^0}} \frac{g}{\sqrt{2}} [\bar{X}_{L/R} W_\mu^+ \gamma^\mu u_{L/R}^i] \right] + \kappa_Y \left[\sqrt{\frac{\zeta_i}{\Gamma_W^0}} \frac{g}{\sqrt{2}} [\bar{Y}_{L/R} W_\mu^- \gamma^\mu d_{L/R}^i] \right] + \text{h.c.},
\end{aligned}
\tag{5.1}
$$

where B, T, X, and Y are the four types of vector-like quarks with triplet colour charges, and electromagnetic charges $-\frac{1}{3}$, $\frac{2}{3}$, $\frac{5}{3}$ and $-\frac{4}{3}$ respectively. The couplings with the photon and gluon are derived via the standard gauge invariance route. The overall coupling strength of the vector-like quarks Q is governed by the parameters κ_Q. ζ_i

represents the coupling of the vector-like quarks to the i^{th} generation SM quark. ξ_V^B and ξ_V^T govern the couplings of the B and T quarks to Z, W, and Higgs bosons via new QqV vertices. Another free parameter is the mass of the new quarks, denoted as M_Q. Under the assumption that $\sum_V \xi_V^B = 1$ and $\sum_V \xi_V^T = 1$, and $\sum_i \zeta_i = 1$, the branching ratio of any vector-like quark to an SM quark and gauge boson is written as

$$\text{BR}(Q \to Vq_i) = \zeta_i \xi^V. \tag{5.2}$$

At the LHC, vector-like quarks can be either pair- or singly-produced. Pair-production occurs via the strong and electromagnetic interaction, and via the weak interaction through the t-channel exchange of an SM weak boson. Single production in association with a quark or with an SM boson occurs via the weak interaction only. Examples of leading-order Feynman diagrams for VLQ production are shown in Figure 5.2. Vector-like quarks can only decay via the weak interaction into an SM weak boson and an SM quark. Given the charge assignments, the possible decay channels of the vector-like quarks are:

$$\begin{aligned} B^{-\frac{1}{3}} &\to W^- + q_u, \quad Z + q_d, \quad H + q_d && (5.3)\\ T^{+\frac{2}{3}} &\to W^+ + q_d, \quad Z + q_u, \quad H + q_u && (5.4)\\ X^{+\frac{5}{3}} &\to W^+ + q_u && (5.5)\\ Y^{-\frac{4}{3}} &\to W^- + q_d. && (5.6) \end{aligned}$$

The B and T quark decays to the W, Z, or Higgs boson plus an up- or down-type quark, depending on the values of the ξ^V and ζ_i parameters. The X and Y quarks, however, can only decay via the W decay channel due to electromagnetic charge conservation, and are unaffected by the values of ξ^V[1]. The production rates of the vector-like quarks depend on the mass m_Q, especially for the QCD-dominated pair production [163]. The coupling strength factors κ_Q drive the electroweak production cross-sections, which are therefore sensitive to the overall strength of the coupling.

The phenomenology of vector-like quark production and decay can be inferred from the Lagrangian of Equation 5.1. In particular, the production cross-sections are dependent on M_Q and κ. For this section, it is assumed that the $B, T, X,$ and$Y$ quarks all have the same mass and coupling strength (i.e. $M_B = M_T = M_X = M_Y$ and $\kappa_B = \kappa_T = \kappa_X = \kappa_Y$).

---

[1] Since ξ^W=1 and $\xi^Z = \xi^H = 0$ are constants for X and Y.

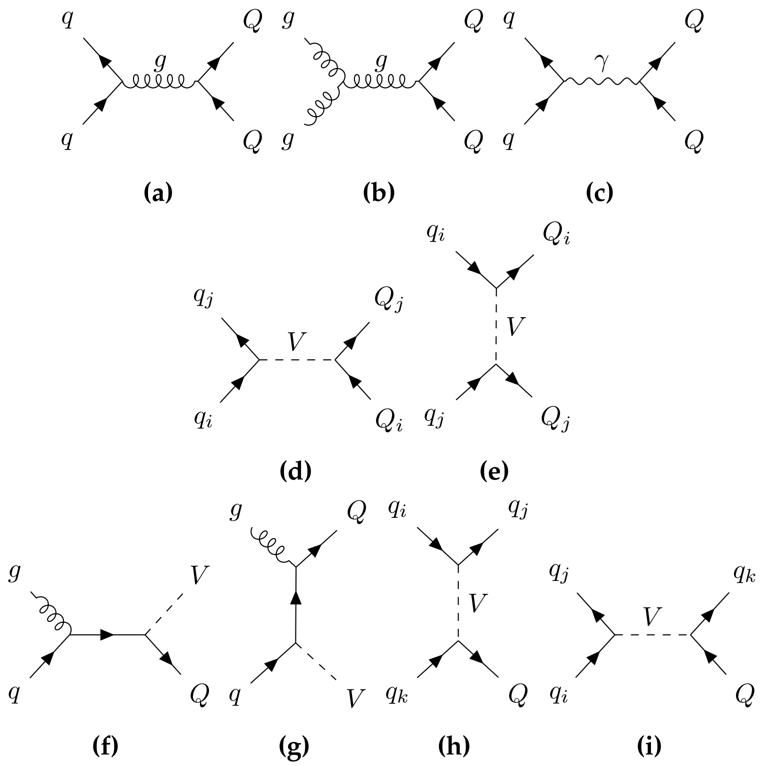

(a) (b) (c)

(d) (e)

(f) (g) (h) (i)

Figure 5.2.: Leading-order Feynman diagrams for production of VLQs Q. The top row (a–c) shows VLQ pair-production diagrams via strong and EM interactions, which do not depend on κ. The second row (d–e) shows pair-production of VLQs via a weak boson $V \in \{W, Z, H\}$, which may lead to different-flavoured VLQs in the final state. The third row (f–i) shows single-production of Q in association with a weak boson or SM quark q. All Feynman diagrams are from Reference [1].

.

Pair production

Figures 5.2(a–c) show the pair production of VLQs via the strong and electromagnetic interaction. These three diagrams are not dependent on any of the coupling parameters κ, ξ or ζ. For a VLQ of mass $\sim$1.3 TeV at the LHC, the cross-section is of the order of 10 fb [1]. In the second row, Figures 5.2(d–e) show the s- and t-channel pair-production of VLQs through the exchange of a weak boson. These diagrams are dependent on κ, and may have a non-negligible contribution to the production cross-section. In fact, when the VLQs couple only to first generation SM quarks, Figure 5.2e can become the dominant production mechanism. Since the up and down quarks are the constituents of the proton, Figure 5.2e is the only possible diagram with two incoming valence quarks. All other diagrams require at least one anti-quark or gluon. If the VLQs couple to the second or third generation SM quarks, however, Figure 5.2e is no longer dominant. This effect is illustrated in Figure 5.3 for TT pair-production. For VLQs coupling to the first

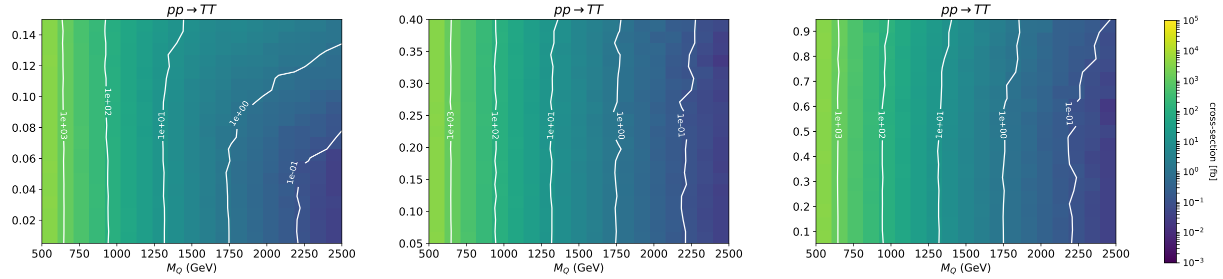

(a) T coupling to u, d only **(b)** T coupling to c, s only **(c)** T coupling to t, b only

Figure 5.3.: Leading-order cross-sections extracted from Herwig for production of a TT pair as a function of M_Q and κ, for 13 TeV pp collisions, in the $W{:}Z{:}H = \frac{1}{2}{:}\frac{1}{4}{:}\frac{1}{4}$ scenario, assuming couplings to individual generations of quarks. The white lines indicate the contours for production cross-sections in multiples of 10. The first-generation cross-sections acquire a dependence on κ since pair-production initiated by proton valence quarks becomes possible. The situation is analogous for other VLQ flavours, although somewhat attenuated for X and Y since they still require at least one antiquark from the sea to be produced via W exchange in the t-channel. These figures are from Reference [1].

generation, a dependence on κ becomes visible as the mass of the VLQs increase. This feature is not visible for couplings to the second and third generation. The VLQs are produced in pairs of different flavours when mediated by a W boson. For the X and Y, this is always the case since they do not couple to the Z or the Higgs.

Single production

Single production is illustrated in the last row of Figure 5.2. It can occur in association with a weak boson V, or with a Standard Model quark q. In both cases a strong κ dependence is present since single production always takes place via the weak interaction.

Looking first at VLQ production alongside a weak boson, it is important to note the dependence of the production cross-section on the flavour of the incoming quark. Consider VLQs that couple only to first generation SM quarks. Using Figures 5.2(f–g) one can deduced that $g + u \to T + H/Z$ production is roughly two times $g + d \to B + H/Z$ production, due to the composition of the proton's valence quarks, uud. Similarly, $g + u \to B + W$ production is twice as frequent as $g + d \to T + W$, and the $g + u \to X + W$ production cross-section surpasses that of $g + u \to Y + W$. Factoring in the weak boson couple ratio of $W{:}Z{:}H = \frac{1}{2}{:}\frac{1}{4}{:}\frac{1}{4}$, the dominant production process is $X + V$. The $B + V$ and $T + V$ production rates are 25% less frequent, and $Y + V$ is 50% less frequent. When VLQs couple to the second or third generation SM quarks, the valence quark effect disappears and single-production is suppressed compared to pair-production. In the case of third-generation coupling, diagrams that include a top

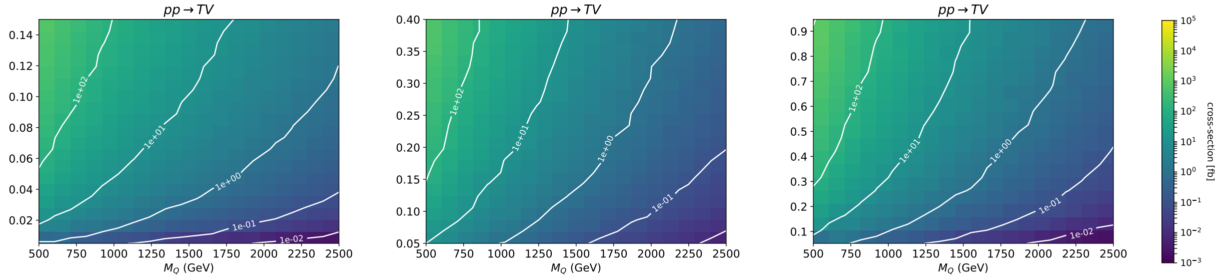

(a) T coupling to u, d only **(b)** T coupling to c, s only **(c)** T coupling to t, b only

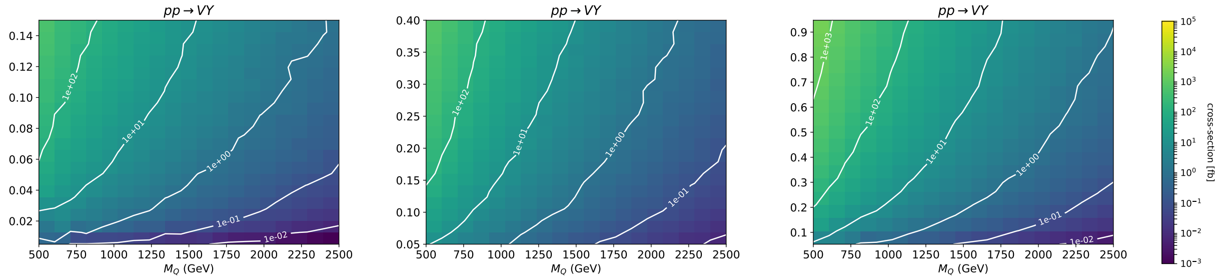

(d) Y coupling to u, d only **(e)** Y coupling to c, s only **(f)** Y coupling to t, b only

Figure 5.4.: Leading-order cross-sections extracted from Herwig for production of a T and Y with a weak boson as a function of M_Q and κ, for 13 TeV pp collisions, in the $W{:}Z{:}H = \frac{1}{2}{:}\frac{1}{4}{:}\frac{1}{4}$ scenario, assuming couplings to individual generations of quarks. The white lines indicate the contours for production cross-sections in multiples of 10. First-generation couplings lead to higher production cross-sections, as a result of valence-quark-induced diagrams, while second and third-generation couplings lead to suppressed production rates, according to the relevant quark PDFs. This figure is from Reference [1].

quark are nearly vanish. $X + W$, $T + H/Z$, and $B + W$ production becomes largely impossible. These effects are illustrated in Figure 3 of Reference [1] and reproduced in Figure 5.4. Shown is the production cross-sections for $T + V$ and $Y + V$ for VLQs coupling to first-, second- or third-generation SM quarks.

Figures 5.2(h–i) show the single-production of VLQs in association with a quark, mediated by a weak boson. Considering the case where VLQs couple to first-generation quarks, the dominant production mechanism is the $t-$channel diagram where both the incoming quarks can be valence quarks. Valence quarks, on average, carry a larger portion of the proton's momentum than sea quarks. Diagrams with dd induced VLQ production have the lowest cross-section, and ud or uu induced cross-sections are four times higher [2]. Consequently, the dominant production process is $u + u \to X + q$, which is four times as frequent as the dd induced $Y + q$. Both are mediated by a W boson. For $B + q$ and $T + q$ production there is a further suppression from the small coupling of the Higgs boson to light SM quarks. When the VLQs couple to the second-generation

---

[2] Since the proton composition is uud, the possible incoming quark pairs are: $uu, uu, ud,;$ $uu, uu, ud,;$ $du, du,$ and dd.

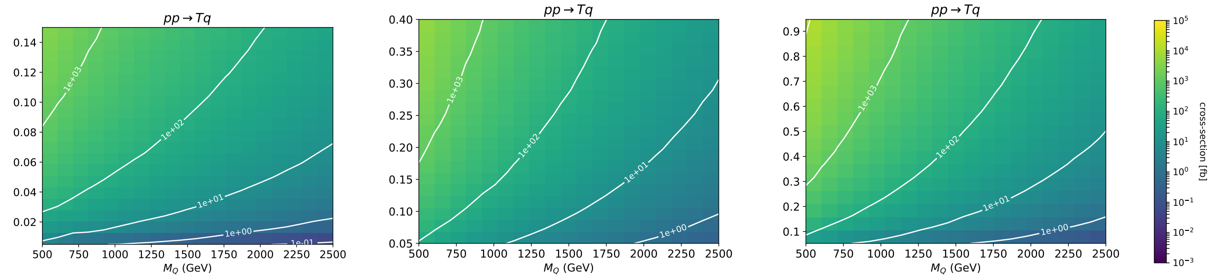

(a) T coupling to u, d only **(b)** T coupling to c, s only **(c)** T coupling to t, b only

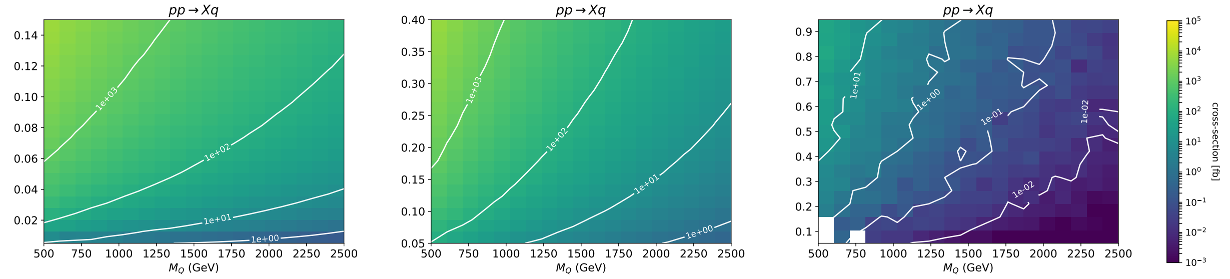

(d) X coupling to u, d only **(e)** X coupling to c, s only **(f)** X coupling to t, b only

Figure 5.5.: Leading-order cross-sections extracted from Herwig for production of a T and X with a SM quark as a function of M_Q and κ, for 13 TeV pp collisions, in the $W{:}Z{:}H = \frac{1}{2}{:}\frac{1}{4}{:}\frac{1}{4}$ scenario, assuming couplings to individual generations of quarks. The white lines indicate the contours for production cross-sections in multiples of 10. First-generation couplings lead to higher production cross-sections, as a result of valence-quark-induced diagrams, while second and third-generation couplings lead to suppressed production rates, according to the relevant quark PDFs. $X + q$ production goes from being the dominant production process at the LHC if X couples to first-generation quarks only, to vanishing if X couples to third-generation quarks only. White cells indicate corners of phase-space where the process in question is highly subdominant, and therefore where the cross-section was not sampled during the Herwig run. This figure is from Reference [1].

quarks, the production cross-sections are dependent on the quark PDFs. For coupling to the third-generation, some production modes are inaccessible if they involve an incoming top quark. This effect is illustrated in Figure 4 of Reference [1] and reproduced in Figure 5.5, where the production cross-sections for T and X in association with a quark are illustrated.

5.2.2. Comparison to ATLAS searches

Typically, searches conducted by the ATLAS and CMS experiments focus on the T and B vector-like quarks that couple only with the third generation SM quarks. In this sub-section the same assumption are made in order to compare the exclusions from LHC results to exclusions computed by CONTUR. The B and T quarks are studied separately with all other VLQs decoupled from the SM. The possible decay channels

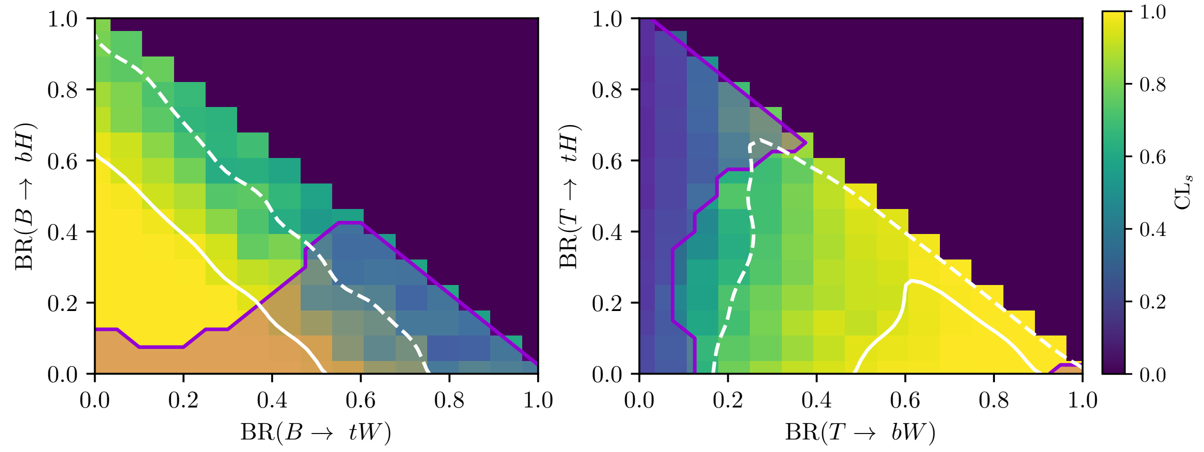

(a) **(b)**

Figure 5.6.: Sensitivity of LHC measurements to a B-production for $M_B = 1200$ GeV and b T-production for $M_T = 1350$ GeV. The CONTUR exclusion is shown in the bins in which it is evaluated, graduated from yellow through green to black on a linear scale, with the 95% CL (solid white) and 68% CL (dashed white) exclusion contours superimposed. The mauve region is excluded at 95% CL by the ATLAS combination [166]. This figure is from Reference [1].

are $b + Z$, $b + H$ and $t + W$ for the B quark, and similarly $t + Z$, $t + H$ and $b = W$ for the T. Both ATLAS and CMS have conducted searches targeting specific final states . ATLAS published a combination limit from multiple searches of pair-produced VLQs in Reference [164], and similarly from CMS in Reference [165]. The ATLAS results presents the exclusion limits in a two-dimensional parameter space of the VLQ branching ratios which is easily mimicked by CONTUR.

Figures 5.6a and 5.6b show the results of the CONTUR scan in the triangular plane of the branching ratios to the weak bosons, for $M_B = 1200$ GeV and $M_T = 1350$ GeV respectively. It is assumed that the sum of the branching ratios to the W, Z, and Higgs bosons is equal to one. On the x-axis is the branching ratio to W's, ξ^W, and on the y-axis is the branching ratio to Higgs, ξ^H. The branching ratio to Z bosons, therefore, is $1 - \xi^W - \xi^H$. The shaded purple region shows the excluded phase-space at 95% confidence level (CL) by ATLAS.

Looking first at Figure 5.6a for the VLB, the excluded region from CONTUR is in the Z corner of the branching ratio triangle and comes mainly from Z+jet measurements [167–170]. The ATLAS limit in mauve, on the other hand, receives contributions from four main searches: one each targeting the Z and H decay channels [171, 172], and the remaining two target B-decay to Wt [173, 174]. As a result, the sensitivity for $BR(B \to tW)$ is high, thus leading to a strong exclusion at the bottom-right corner of the triangle. The excluded regions from CONTUR and ATLAS are somewhat complementary.

Show in Figure 5.6b is the excluded region from CONTUR for $M_T = 1350$ GeV, and the ATLAS search exclusion for this mass value in mauve. Here there are three analyses going into to the ATLAS combination limit which target T-decay to Ht [172, 174, 175], two that target T-decay to Zt [171, 176], and only one sensitive in the W channel [177]. The ATLAS sensitivity is mainly in the Higgs corner of the branching ratio half-plane. In contrast, the CONTUR exclusion comes mainly from top quark and W boson measurements [178–182], giving sensitivity in the W corner. The complementarity between CONTUR and direct searches is nicely demonstrated.

5.2.3. All quark generations

Although most searches at ATLAS and CMS assume that VLQs couple only to the third-generation quarks, it is not at all the case that mixing with the first- and second-generation quarks are forbidden. They do, however, receive more stringent lower bounds on the overall coupling κ from flavour physics [163]. These bounds come from the LEP measurements of the Z boson's couplings to light quarks, and from other low energy experiments such as the measurement of the weak charge of the Cesium atom (Atom Parity Violation) [183]. These measurements are proportional to the branching fraction to the specific generation, and therefore from it an absolute bound on κ can be extracted. For VLQs that couple only to one SM quark generation at a time, these bounds are estimated to be$\kappa < 0.07$ and $\kappa = 0.2$ for coupling to the first- and second-generation only. Although scenarios with VLQ couplings to all generations is allowed, they suffer from an extra order of magnitude suppression on κ [163].

At low VLQ masses, the QCD induced pair production mode is dominant. As previously discussed, this is independent of the overall coupling κ. However, pair production sees a suppression at high VLQ masses, therefore when M_Q is large enough, single production becomes dominant [184]. This feature is of particular interest when the VLQs couple to first-generation quarks. Since the proton's valence quarks are of the first-generation, production diagrams that involve two incoming initial state quarks will see an enhancement. In particular, the $t-$channel VLQ pair production via the weak interaction (Figure 5.2e) becomes dominant, and a dependence on κ comes into play. The rest of this subsection explores the VLQs coupling to each of the SM quark generations independently, in four ξ_V branching fraction scenario indicated by ratios:

- $W : H : Z = 0 : 0 : 1$ coupling only to the Z boson
- $W : H : Z = 0 : 1 : 0$ coupling only to the Higgs boson

- $W:H:Z = 1:0:0$ coupling only to the W boson
- $W:H:Z = \frac{1}{2}:\frac{1}{4}:\frac{1}{4}$ an admixture of the three bosons.

The results are presented as two-dimensional exclusion maps in the plane of M_Q and κ. Each square on the map represents a scan point for a specific (M_Q, κ) combination where a CLs value is calculated by CONTUR. The colour of the square indicates the dominant analyses pool contributing towards the exclusion. The final state of the ATLAS analysis present in Section 4 is four-leptons, and therefore belongs to the four-lepton pool in pink. The solid white line is the exclusion at 95% CLs, and the dashed at 68%.

Coupling to first-generation quarks

The exclusion maps for VLQs coupling to first-generation SM quarks in the four WHZ branching fraction scenarios are show in Figure 5.7. The range in κ values is from $\kappa = 0$ to $\kappa = 0.15$. The bound from flavour physics at $\kappa = 0.07$ is drawn in pink. In the Higgs only and the mixture scenarios, the $M_Q < 1000$ GeV region is largely excluded at 95% CL. For the W only and Z only configurations, this goes up to $M_Q < 1125$ GeV and $M_Q < 1250$ GeV respectively. Below these masses the white contour lines are relatively vertical and therefore independent of κ. This is credited to the fact that the VLQs are mainly pair-produced via the strong and electromagnetic interaction. Above these masses the contour lines become nearly horizontal, indicating that a strong dependence on κ has developed as dominant production mode switches to single production via the weak interaction. Overall the limits at high mass oscillate around $\kappa \sim 0.07$. They are most stringent for the $Z-$only ξ configuration.

The colouring of the plot indicates the dominant analyses contributing to the exclusion. For all but the Z configuration where Z+jets measurements hold the most exclusion power, it is the ATLAS $\ell_1\ell_2 + E_{\mathrm{T}}^{\mathrm{miss}} + jet$ pool in light blue that prevails. This pool contains final state signatures typical of a leptonic WW decay; with two leptons (either e or μ), missing energy E_T, and sometimes jets. The sensitivity in the Higgs only corner occurs as a result of the the $H \to WW$ decay channel. In the middle region of of the Higgs only and W only configuration, there is a strong presence from ATLAS lepton+$E_{\mathrm{T}}^{\mathrm{miss}}$+jet analyses. This signature is sensitive to the weakly and singly produced VLQ, thus introducing a reliance on κ and driving the exclusion contour horizontally. Multiple measurements contribute to each analyses pool. An investigation into the appearance of the lepton+$E_{\mathrm{T}}^{\mathrm{miss}}$+jet pool reveals that it is dominated by measurements of leading jet p_{T} in the detector-corrected control regions of the 8 TeV ATLAS vector-boson fusion (VBF) Wjj analysis [178]. In the 1 TeV-2 TeV range, the VLQ decays shows up as

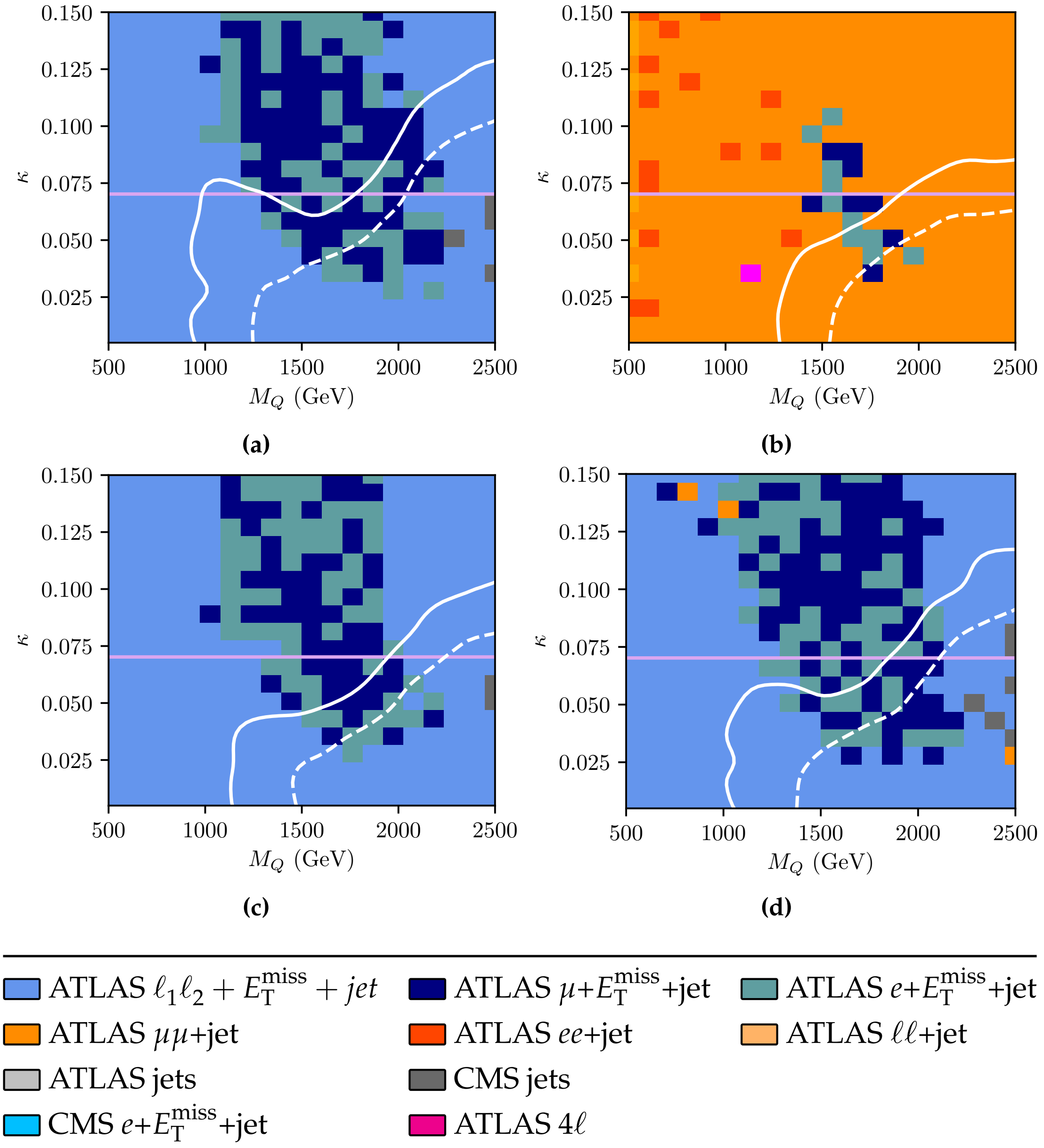

(a) **(b)** **(c)** **(d)**

Figure 5.7.: Dominant LHC analysis pools contributing to VLQ limit-setting in the κ vs VLQ mass plane, where κ is the coupling to first-generation SM quarks. All VLQ (B, T, X, Y) masses are set to be degenerate. The disfavoured regions are located above and to the left of the dashed (68% CL) and solid (95% CL) white contours respectively. The lower bounds in κ from non-LHC flavour physics are indicated with the pink horizontal contour. The VLQ branching fractions to W:Z:H are a 0:0:1 b 0:1:0 c 1:0:0 and d $\frac{1}{2}$:$\frac{1}{4}$:$\frac{1}{4}$. This figure is from Reference [1].

an excess in the highest leading jet p_T bin. This is illustrated in Figure 5.8 for the W only configuration at $M_Q = 1000$ GeV, 1750 GeV, and 2250 GeV. These are excluded at 28%, 91%, and 41% respectively. For higher masses the enhancement is out of bin range, and the cross-section also drops.

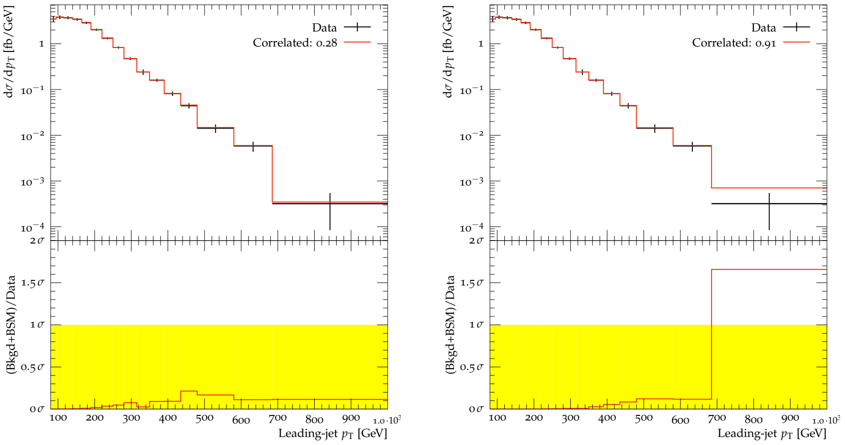

(a) **(b)** **(c)**

Figure 5.8.: ATLAS 8TeV Wjj forward-lepton control region leading-jet p_T distributions at three points on the 95% exclusion contour for W:Z:H = 1:0:0, respectively at M_Q values of a 1000 GeV, b 1750 GeV, and c 2250 GeV. The rise and subsidence of a 90% CL_s exclusion from a single Wjj bin is seen as the contour passes from below 1 TeV to above 2 TeV. The black points are data, the red histogram is the VLQ contribution stacked on top of the data. In the lower insets, the ratio is shown and the yellow band indicates the significance, taking into account the statistical and systematic uncertainties on the data. The legend gives the exclusion (i.e. one minus the p-value) for that histogram after fitting nuisance parameters for the correlated systematic uncertainties. This figure is from Reference [1].

Coupling to second-generation quarks

The results for VLQs coupling to second-generation quarks for the four branching fraction scenarios is presented in Figure 5.9. These exclusion maps scan between $\kappa = 0$ and $\kappa = 0.4$. The bound on the coupling is at $\kappa = 0.2$ and comes from measurements of the $Z \to q\bar{q}$ couplings at LEP [185, 186]. Since the VLQs couple to second-generation quarks, access to valence quarks are forbidden, and the weak production diagrams of Figure 5.2e and Figure 5.2h no longer play a dominant role. It is pair-production via the strong and electromagnetic interaction that dominates the excluded regions. In contrast to the first-generation case, only a hint of κ dependence is visible at high M_Q.

The Z+jets analyses are driving the exclusion in the Z configuration, and the similarly the ATLAS $\ell_1\ell_2 + E_T^{\text{miss}} + jet$ analyses for the W and Higgs configuration. In the $WHZ = \frac{1}{2}\frac{1}{4}\frac{1}{4}$ mixture both make an appearance. In the M_Q region between 1 TeV and 2 TeV, the

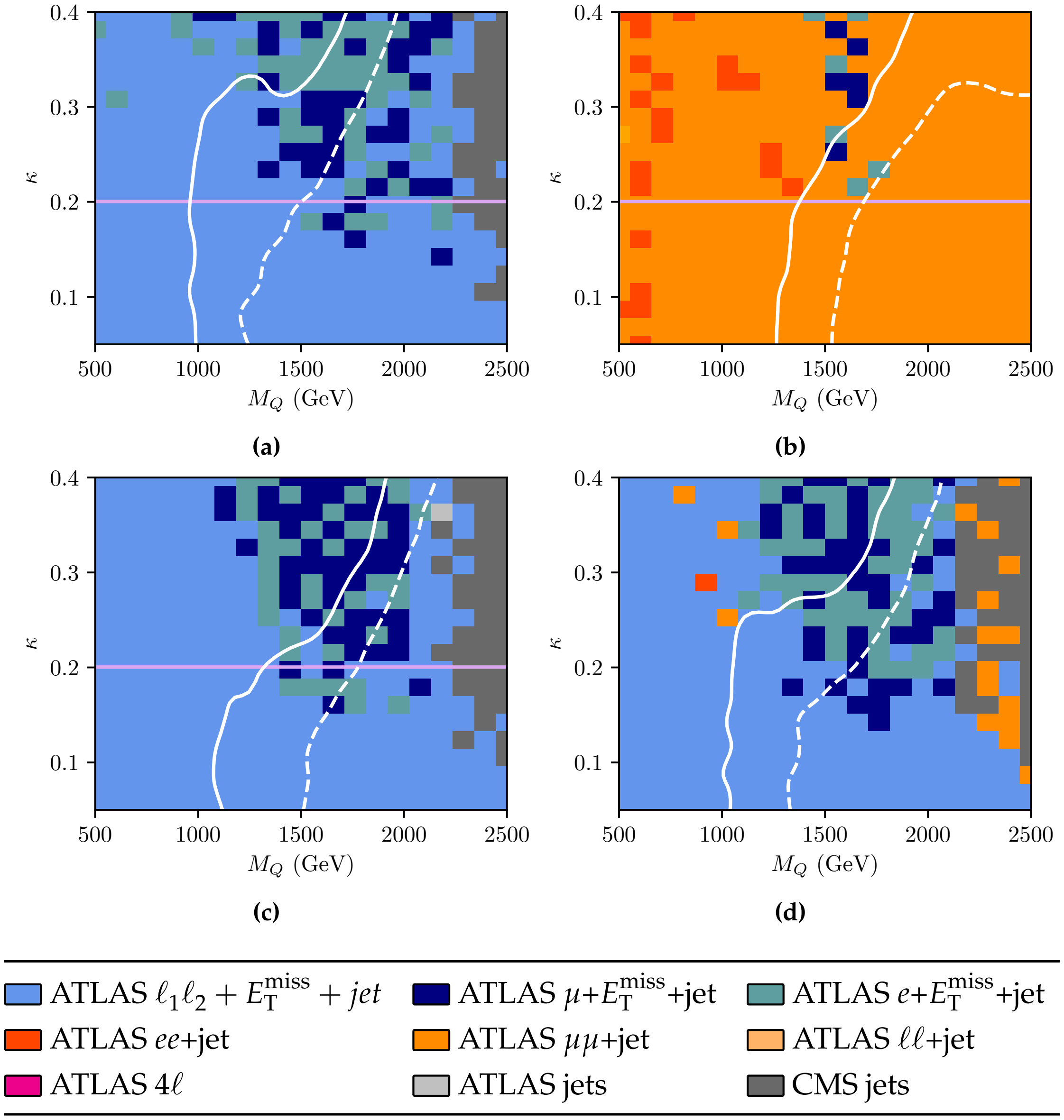

Figure 5.9.: Dominant LHC analysis pools contributing to VLQ limit-setting in the κ vs VLQ mass plane, where κ is the coupling to second-generation SM quarks. All VLQ (B, T, X, Y) masses are set to be degenerate. The disfavoured regions are located above and to the left of the dashed (68% CL) and solid (95% CL) white contours respectively. The lower bounds in κ from non-LHC flavour physics are indicated with the pink horizontal contour. The VLQ branching fractions to W:Z:H are a 0:0:1 b 0:1:0 c 1:0:0 and d $\frac{1}{2}$:$\frac{1}{4}$:$\frac{1}{4}$. This figure is from Reference [1].

same emergence of the lepton+E_T^{miss}+jet pool is present. The sensitivity is driven by the same ATLAS VBF Wjj analysis. New in the coupling to the second generation is the sensitivity coming from the 13 TeV CMS jet mass analysis [187] (and less so from the ATLAS 13 TeV dijet and inclusive jet analysis [188]) beyond M_Q =2 TeV.

Coupling to third-generation quarks

Finally Figure 5.10 shows the exclusion in the $M_Q - \kappa$ plane for VLQs that couple only to the third-generation SM quarks. Unlike the lighter generations, no constraint exists on κ and therefore it is scanned in the full range from $0 - 1$. The results are once again presented for the four WHZ scenarios. Overall, pair-production dominates and κ has little effect on the shape of the white contour. Single-production via the weak interaction is sees a further suppression in comparison to the first- and second-generation. At a high enough κ, however, the lepton+$E_{\mathrm{T}}^{\mathrm{miss}}$+jet analyses sensitive to single production bring a little horizontal momentum to the white contour.

Comparing the set of plots for the third-generation with that of the lighter generations, the biggest difference is in the Z only ξ configuration. For the former this region's exclusion is driven by the ATLAS $\ell_1\ell_2 + E_{\mathrm{T}}^{\mathrm{miss}} + jet$ pool, with minor contributions from dilepton and four-lepton measurements, while for the latter it is driven by dilepton+jets measurements. This is a result of the allowed production and decay modes when the VLQs only couple to the top and bottom quark. For $X + q$ and $T + q$ production, there is a suppression due to the lack of top quarks in the proton sea. At high masses, $Y + q$ production dominates. Recalling from Equation 5.1 that the X and Y only couple to W bosons, therefore even in the Z only configuration they will decay to W's. Furthermore, Y and T will decay to top quarks, which then decays very quickly to a W boson and (usually) a bottom quark. As a result, when VLQs couple to the third-generation, there are lepton+$E_{\mathrm{T}}^{\mathrm{miss}}$ +jet signatures that are not present for the lighter generations.

It is important to highlight here the impact of analyses publishing bin-correlation information in data. The results of this section make use of correlation information where available. Correlation information allowed CONTUR to use multiple bins in the WW analysis pool. Without it, the (statistically limited) ATLAS four-lepton pool would dominate a larger region of κ–M_Q plane in the Z only configuration, and the CMS ℓ+$E_{\mathrm{T}}^{\mathrm{miss}}$+jet analyses [180–182, 189–191] would dominate the low M_Q regions in the other three configurations.

5.2.4. Role of the ATLAS $m_{4\ell}$ measurement

Assuming a $\xi_Z = 1$ branching fraction, the production of a vector-like B or T quark at the LHC is characterized by final states with high p_{T} Z bosons. In the case where there are two Z bosons involved that both decay into charged leptons, the result is a four-lepton final state made up of two same flavour, opposite sign, lepton pairs. All pair

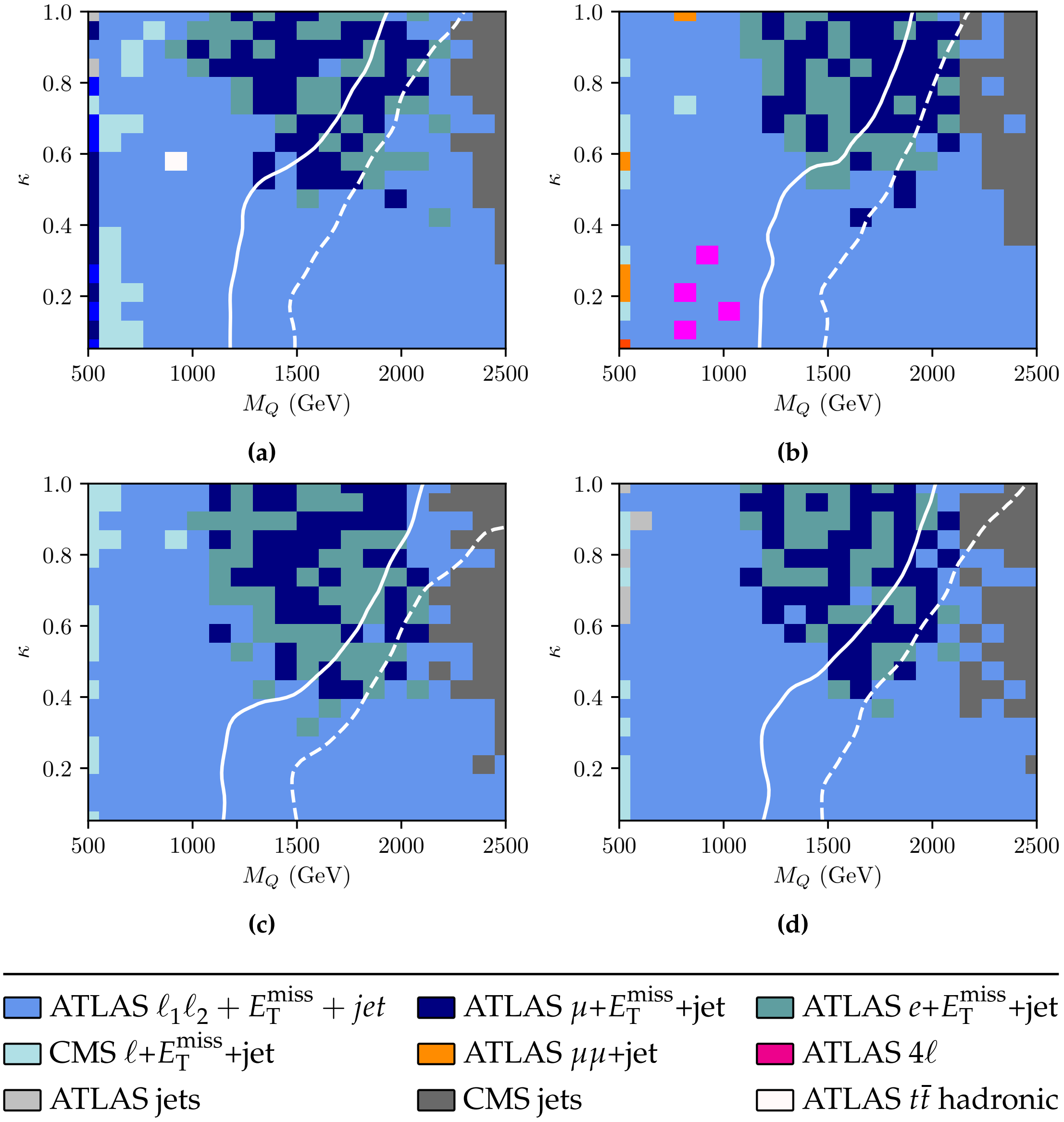

Figure 5.10.: Dominant LHC analysis pools contributing to VLQ limit-setting in the κ vs VLQ mass plane, where κ is the coupling to third-generation SM quarks. All VLQ (B, T, X, Y) masses are set to be degenerate. The disfavoured regions are located above and to the left of the dashed (68% CL) and solid (95% CL) white contours respectively. The VLQ branching fractions to W:Z:H are a 0:0:1 b 0:1:0 c 1:0:0 and d $\frac{1}{2}$:$\frac{1}{4}$:$\frac{1}{4}$. This figure is from Reference [1].

production modes can contribute to the four-lepton signature since BB and TT decay to $ZtZt$ and $ZbZb$ respectively. Single production can also result in a four-lepton final state, if the VLQ is produced in association with a Z boson (Figure 5.2f and 5.2g). The ATLAS $m_{4\ell}$measurement presented in Chapter 4 falls into this final state and therefore is sensitive to the production of VLQs in the Z only scenario. This section explores the role that the full Run II $m_{4\ell}$ measurement plays in constraining VLQs. The results presented in the previous sections were made with CONTUR version 1.2.2 and RIVET 3.1.1 prior to the publication of the four-lepton analysis. In this section the Z only configuration scans are remade using CONTUR 2.1.x and RIVET 3.1.4 , which includes the newly published four-lepton measurement [67].

Figure 5.11 shows the new CONTUR scans in the $\xi_Z = 1$ Z only configuration for VLQs coupling to the first-, second-, and third-generation SM quarks. These scans are replicated in the same model parameter space as that of Figure 5.7b, Figure 5.9b and Figure 5.10b, and uses the ATLAS full Run II $m_{4\ell}$ measurement (and other new measurements) in calculating the excluded region. Looking at Figure 5.11a for coupling to the first-generation quarks, the limits as well as the most sensitivity analyses pools are similar to that of Figure 5.7b, with some minor differences. First, the white exclusion contour at 95% is more stringent, extending to lower values of κ. Second, there is the appearance of the sand-coloured CMS ee+jet and CMS $\mu\mu$+jet at high mass.

For the second-generation quarks shown in Figure 5.11b it is a similar story, although the effects are more prominent. Beyond M_Q =1500 GeV, it is the CMS Z+jets pool that dominates rather than the ATLAS Z+jet, this is due to the addition of two CMS Z boson cross-section measurements [192, 193]. The four-lepton pool, which was not visible in the CONTUR 1.2.2 scan of Figure 5.9b, now makes an appearance at low κ between 1000 GeV-1250 GeV. Overall, the CONTUR limit is more stringent. In the high mass region in particular, the increased sensitivity results in a visible dependence on κ, which was not present earlier.

Lastly, Figure 5.11c is for VLQs that interact only with third-generation quarks. Here the dominant final state pool for the majority of scan points is still ATLAS $\ell_1\ell_2 + E_{\mathrm{T}}^{\mathrm{miss}} + jet$ [3]. At VLQ masses between 650 GeV-1100 GeV, there is a notable pink patch that was not visible prior. This is due to the addition of the four-lepton measurement presented in Chapter 4, whose increase statistics and widened acceptance has boosted the four-lepton pool to be the one providing the most sensitivity at those points.

---

[3] Due to plotting script modifications, ATLAS $\ell_1\ell_2 + E_{\mathrm{T}}^{\mathrm{miss}} + jet$ is turquoise in this plot, and sky blue in Figure 5.9b

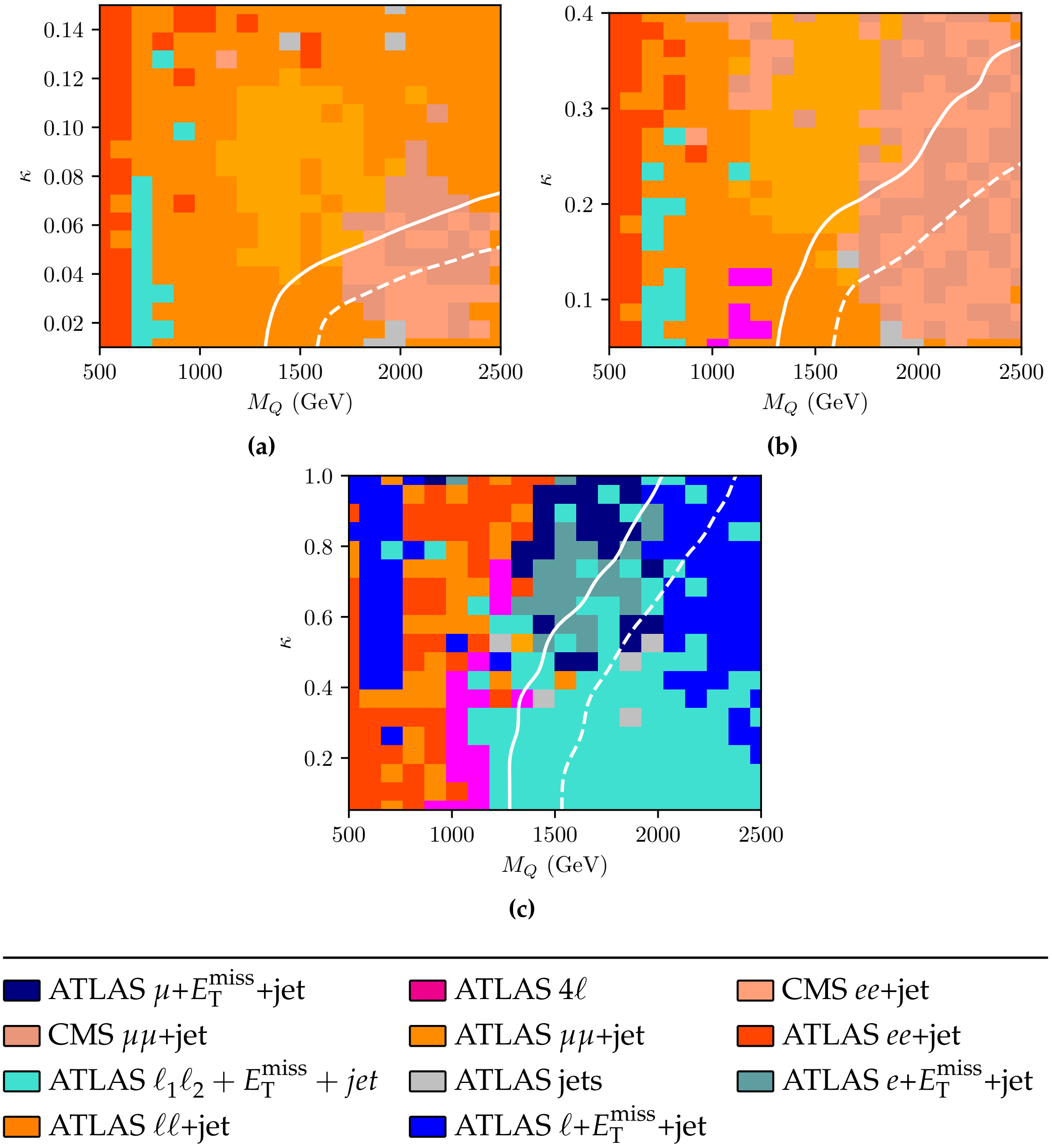

(a) **(b)**

(c)

Figure 5.11.: Dominant LHC analysis pools contributing to VLQ limit-setting in the κ vs VLQ mass plane, where κ is the coupling to third-generation SM quarks. All VLQ (B, T, X, Y) masses are set to be degenerate. The disfavoured regions are located above and to the left of the dashed (68% CL) and solid (95% CL) white contours respectively. The VLQ branching fraction to W:Z:H is 0:1:0. Plots are made with CONTUR 2.1.x and RIVET 3.1.4.

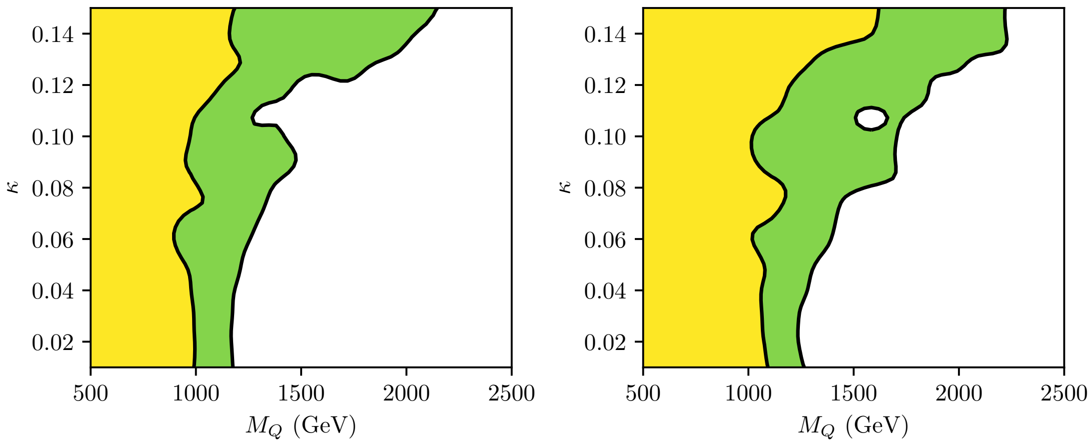

(a) **(b)**

Figure 5.12.: CONTUR exclusion (a) without and (b) with new four-lepton measurement. The disfavoured regions at 95% CL and 68% CL are shaded in yellow and green respectively.

Figure 5.12 shows the CONTUR excluded region by the four-lepton final state pool alone in the $M_Q - \kappa$ plane for VLQs coupling to first generation quarks. The yellow and green regions are disfavoured at 95% CL and 68% CL respectively. The left and right plots correspond to the limit set by the pool while omitting and including the full Run II $m_{4\ell}$ measurement, respectively. In other words, the improvement in the limit seen in Figure 5.12b compared to Figure 5.12a is attributed solely to the addition of the new $m_{4\ell}$ measurement. The upper limit on VLQ mass increases from 1000 GeV to 1100 GeVat low κ, and from 1200 GeV to over 1500 GeV at high κ. Without the new $m_{4\ell}$ measurement, the 95% CL exclusion reaches $\sim$1 TeV, any higher and there are not enough events. Below this mass, the exclusion in Figure 5.12a is driven by pair production via the strong and EM interaction, which is independent of κ. The κ dependence in the green 68% CL excluded region of Figure 5.12a is an early sign for the 95% CL excluded region of Figure 5.12b. The inclusion of the 139 fb^{-1} four-lepton measurement allows probing into higher M_Q, where a κ dependence comes into play as VLQs are pair produced via the weak interaction.

A closer look into what drives the improved limit is illustrated in Figure 5.12 at the $M_Q = 1237$ GeV and $\kappa = 0.05$ scan point. The left and right plot shows the $m_{4\ell}$ distribution in the $2e2\mu$ channel, for the previous iteration of the four-lepton analysis (36.1 fb^{-1}) and the most recent iteration (139 fb^{-1}), respectively. The latter has widened acceptance cuts, improved statistics, and a higher upper mass limit. It is the fine binned high mass tail of Figure 5.13b that drives the 89% CL given by the $2e2\mu$ channel. Without it, Figure 5.13a provides only a 30% CL. In general, it is the high mass tails of $m_{4\ell}$ related variables, and variables in the on-shell ZZ region (see Section 4.2) that provide the highest sensitivity.

The same conclusions are drawn when the VLQs couple to second- and third-generation quarks. The addition of the new four-lepton measurement expands the upper mass limit of the excluded region by the four-lepton pool by a few hundred GeV, thanks for the finer binning and extended range in the high mass tail. Due to the lack of access to valence quarks, however, VLQ production via the weak interaction is highly suppressed and the exclusion contours from the four-lepton pool are independent of κ.

5.3. Sensitivity of LHC measurements to a gauged $B - L$ model

The focus of this section is on the limits set on a gauged $B - L$ model. This model is interpreted by the ATLAS $m_{4\ell}$ measurement of Chapter 4. As a complementary further studies are conducted to investigate how the $m_{4\ell}$ measurement may be easily re-interpreted using the CONTUR machinery. Both sets of limits (ATLAS and CONTUR) are presented, with a particular focus on the role the $m_{4\ell}$ measurement plays.

5.3.1. About the model

Since gauge symmetry has been a huge success in describing the SM, a way of incorporating new physics can be through the extension of its gauge symmetry. In the theoretical community, several new physics scenarios have been postulated in which the gauge symmetry of the Standard Model are extended via $\mathrm{U}(1)$ gauge symmetries beyond $\mathrm{U}(1)_Y$ [194,195] . This class of models is strongly reinforced by the observation of neutrino oscillations, evidence that neutrinos have non-zero mass. They predict three additional SM singlet fermions which are accounted for by right-handed neutrinos, thus enabling the seesaw mechanism of neutrino mass generation.

In this section, the model is based on the gauge group where an additional $\mathrm{U}(1)_{B-L}$ symmetry group representing the global Baryon-number-minus-Lepton-number symmetry: $\mathrm{SU}(3)_C \times \mathrm{SU}(2)_L \times \mathrm{U}(1)_Y \times \mathrm{U}(1)_{B-L}$. The symmetry is spontaneously broken by an extra SM singlet scalar (the heavy Higgs h_2). Three SM singlet fermions are also introduced (the right-handed neutrinos) for the cancellation of gauge anomalies, along with an extra gauge boson Z'. The Z' couples to the SM via g', and the heavy Higgs h_2

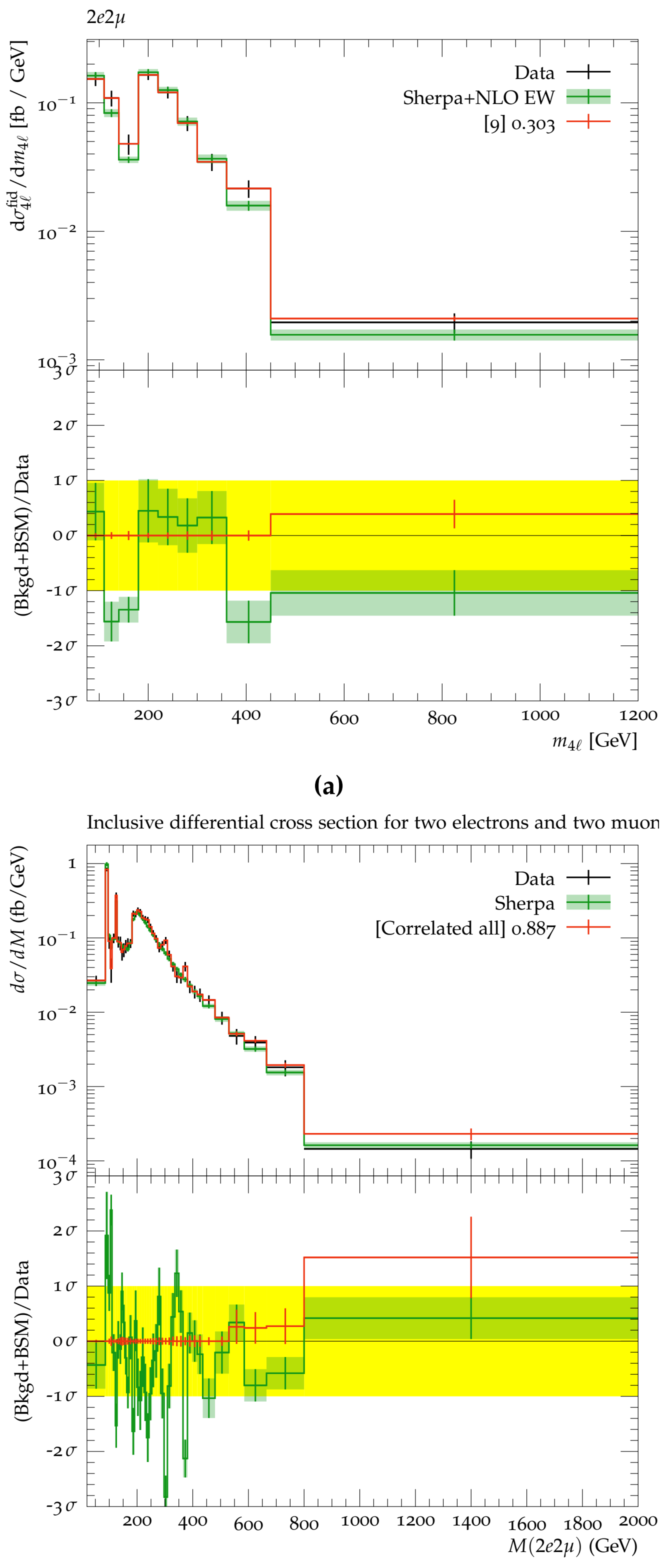

(a)

(b)

Figure 5.13.: ATLAS 13 TeV four-lepton measurement at (a) 36.1 fb^{-1} and (b) 139 fb^{-1} at $M_Q = 1237$ GeVand $\kappa = 0.05$. The black points are data, the red histogram is the VLQ contribution stacked on top of the data, and the green histogram is the SM prediction. In the lower insets, the ratio is shown and the yellow band indicates the significance, taking into account the statistical and systematic uncertainties on the data. The legend gives the exclusion (i.e. one minus the p-value) for that histogram.

	$M_{Z'}$	g_1'	M_{N_i}	M_{h_2}	$\sin\alpha$
Scenario C	$[1, 10^4]$ GeV	$[3\times 10^{-5}, 0.6]$	$M_{Z'}/5$	200 GeV	0.2
Scenario E	35 GeV	10^{-3}	$M_{Z'}/5$	$[0, 800]$ GeV	[0,0.7]

Table 5.1.: B-L model parameters set for scenario C of the gauge sector and scenario E of the scalar sector, as defined in Reference [2].

mixes with the SM Higgs with mixing angle α. The introduction of these new particles may have a non-negligible impact on the phenomenology of the SM, and may manifest themselves in measurements taken at the LHC.

The constraints from LHC measurements on this model are studied in detail using the CONTUR machinery in Reference [2]. The paper showed that ATLAS measurements with a four-lepton final state provided significant constraints on certain regions of parameter space. In context of the model, contributions to the spectrum may come from the production of multiple Z', the production of h_2 via gluon-gluon fusion which decays via $h_2 \to Z'Z'$ or $h_2 \to ZZ$, or the SM Higgs decaying to a pair of Z'. In the study, five well-motivated scenarios are considered: three target the vector boson sector, and two target the scalar sector. In all five, the sterile neutrino sector is set as identically. All scenarios are described in Section 3.4 of Reference [2]. The rest of this section will focus only on scenarios C and E, as they are found to contribute to a four-lepton final state in the studies of Reference [2]. In the former, M_{h_2}, $\sin\alpha$, and $M_{Z'}$ are set to be constants while the scan is performed in the $M_{Z'}$ versus g_1' plane. In the latter, $M_{Z'}$, g_1', and M_{N_i} are set to be constants while the scan is performed in the $M_{h_2} - \sin\alpha$ plane. The parameters for both are summarized in Table 5.1.

5.3.2. ATLAS limit from the $m_{4\ell}$ analysis

One sensitivity scan published in Reference [2] is repeated as an interpretation example in the ATLAS $m_{4\ell}$ analysis, in the plane of the sine of the mixing angle α and the mass of the exotic Higgs boson m_{h_2}. The new gauge boson Z' is assumed to have a mass of 35 GeV, and weakly coupled to the SM with $g' = 10^{-3}$.

An alternate test statistic $\tilde{q}$ for upper limits is defined using the likelihood function of equation 4.13 as

$$\tilde{q} = \begin{cases} -2\ln\frac{\mathcal{L}(\mu,\hat{\hat{\vec{\theta}}}(\mu))}{\mathcal{L}(0,\hat{\hat{\vec{\theta}}}(0))} & \hat{\mu} < 0, \\ -2\ln\frac{\mathcal{L}(\mu,\hat{\hat{\vec{\theta}}}(\mu))}{\mathcal{L}(\hat{\mu},\hat{\vec{\theta}})} & 0 \leq \hat{\mu} \leq \mu, \\ 0 & \hat{\mu} > \mu. \end{cases} \tag{5.7}$$

Here the parameter μ dictates the strength of the BSM signal process. $\mu = 0$ and $\mu = 1$ correspond to the background-only hypothesis and the nominal signal hypothesis respectively [67]. The reason for setting $\tilde{q} = 0$ for $\hat{\mu} > \mu$ is that when setting an upper limit, an excess in data (corresponding to larger $\hat{\mu}$) should not be used to reject a signal model with lower yield (lower μ). $\tilde{q}$ is interpreted as an upper exclusion limit on the parameter of interest at a certain CL, usually set to 95%, based on the CLs prescription [196] .

The exclusion contour in the plane of $\sin\alpha - m_{h_2}$ is depicted in Figure 5.15, where the variable providing the best expected sensitivity to set the limit. An alternate version using only the inclusive $m_{4\ell}$ distribution to set the limit is shown in Figure 5.14. Corresponding to Figure 5.15, the colour map of Figure 5.16 shows the observable used to derive the limits at each point in the parameter space. It is clearly visible that there is a larger excluded region when using the most sensitive observable rather than the $m_{4\ell}$ distribution only. The event kinematics of the BSM model changes as the model parameters change. It is therefore advantageous to exploit various observables accordingly at each model point; ultimately enhancing the sensitivity significantly. This effect is most evident at high m_{h_2}, where the expected limit on $\sin\alpha$ strengthens from 0.46 to 0.28. Referring to Figure 5.16, the improvements at high m_{h_2} come mainly from the m_{12} distribution. These results demonstrate the power that comes with measuring more variables in regions of phase space.

5.3.3. Updated CONTUR limit with new $m_{4\ell}$ measurement

Figure 5.17b shows the exclusion contours from Reference [2] for Scenario E in the $M_{h_2} - \sin\alpha$ plane. In this scenario, the Z' is light enough such that $h_2 \to Z'Z'$ is an allowed decay channel. The excluded regions at 95% CL and 68% CL are indicated by the yellow-shaded and green-shaded areas respectively. The upper right portion of the plot is excluded by the perturbativity requirement that the model must be stable

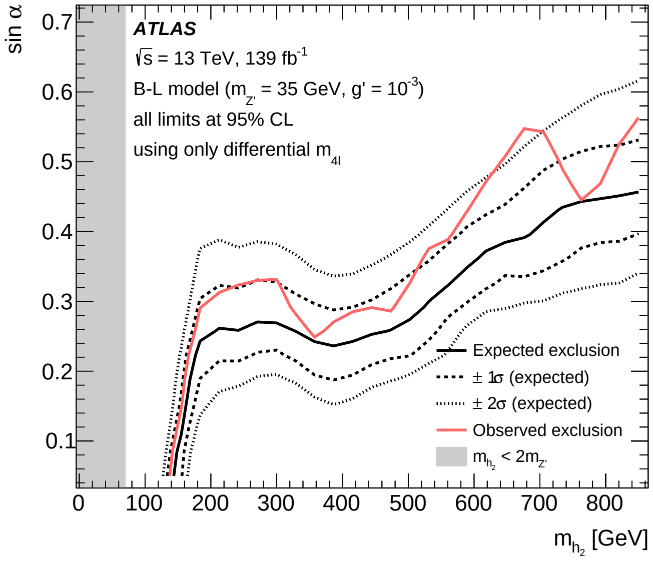

Figure 5.14.: ATLAS result from the $m_{4\ell}$ measurement. Limits set on the B-L model using only the inclusive $m_{4\ell}$ variable. The red line shows the observed exclusion and the solid black line shows the expected exclusion, with the dashed black lines indicating the $\pm 1\sigma$ and $\pm 2\sigma$ uncertainty bands. The region above and to the left of the lines is excluded, up to the grey band, which shows the region $m_{h_2} < 2m_{Z'}$, where the four-lepton final state has no sensitivity. This figure is from Reference [67].

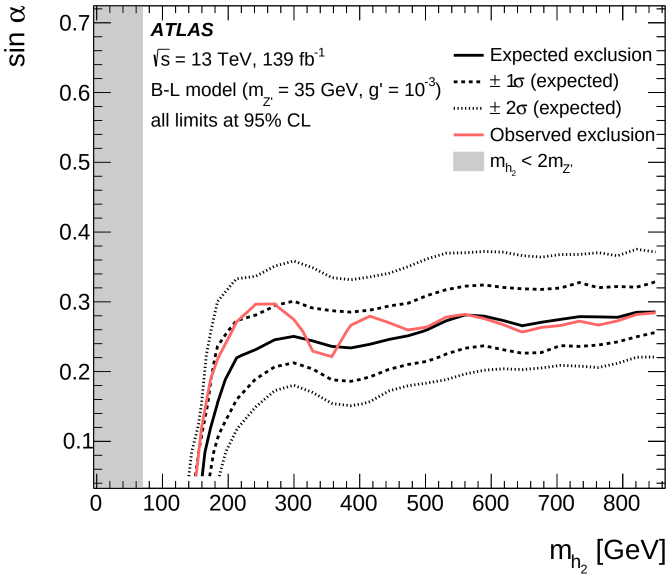

Figure 5.15.: ATLAS result from the $m_{4\ell}$ measurement. Limits set on the B-L model using the most sensitive variable. The red line shows the observed exclusion and the solid black line shows the expected exclusion, with the dashed black lines indicating the $\pm 1\sigma$ and $\pm 2\sigma$ uncertainty bands. The region above and to the left of the lines is excluded, up to the grey band, which shows the region $m_{h_2} < 2m_{Z'}$, where the four-lepton final state has no sensitivity. This figure is from Reference [67].

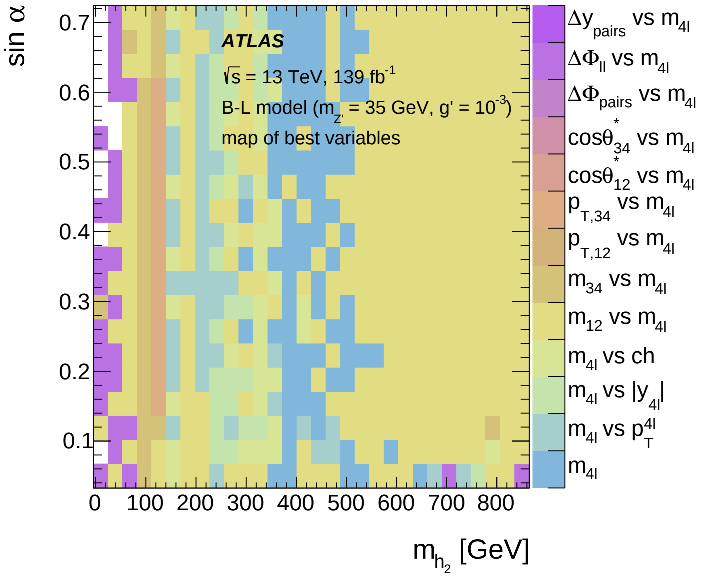

Figure 5.16.: ATLAS result from the $m_{4\ell}$ measurement. This colour map shows the B-L model space and the most sensitive variable at each point used to set the limit. This figure is from Reference [67].

up to at least 10 TeV, and to a greater extent, by precise measurements of the W boson mass [2]. The CONTUR excluded region provides some additional sensitivity in the low M_{h_2} region. The 7 TeV and 8 TeV four-lepton measurements have shown to be important in constraining the the small $M_{Z'}$, $g' > 10^{-3}$ region, where the h_2 decays dominantly to Z' pairs, and the branching fractions for $Z' \to \mu^+\mu^-$ and $Z' \to e^+e^-$ are both $\sim$20% [2]. Bearing all this in mind, it is sensible to expect that new measurements in the four-lepton final state should affect the exclusion in the region.

Figure 5.17a is a replica of the scan in the same parameter space performed by the author using a newer version of CONTUR (and RIVET), which includes the 139 fb^{-1} four-lepton measurement presented in Chapter 4 and published in Reference [67]. The excluded region in this plot is to the right and above the solid white line at 95% (dashed white line is 68%). The improvement in the limit in comparison to Figure 5.17b is clearly visible. The $\sin\alpha > 0.3$ region is largely excluded in the high mass range at 95%, and nearly the entire plane is disfavoured at 68%. At around $M_{h_2} = 200$ GeV, CONTUR is able to rule out a new region of phase space that was previously not excluded. This drastic improvement is attributed nearly single-handedly to the addition of the of the new $m_{4\ell}$ measurement in RIVET. This is illustrated in Figure 5.18, where the 3σ excluded region (yellow) in the four-lepton pool alone is plotted without (left), and with (right), the new measurement.

The driving force behind the improved sensitivity in the new $m_{4\ell}$ analysis, particularly at high M_{h_2}, is higher event statistics, finer binning, and the addition of new observables (see Section 4.2). Looking only at the new $m_{4\ell}$ analysis, the breakdown of the distribution giving the highest exclusion at each scan point is shown in Figure **??**. At low masses, the $|\Delta\phi_{\ell\ell}|$, $m_{4\ell}$ vs flavour, $m_{4\ell}$ vs $y_{4\ell}$, and $p_{\mathrm{T},12}$ distributions share the role of being the most dominant. At higher M_{h_2}, it is the mass of the first lepton pair m_{12} that is dominant for most parameters.

As presented in Section 4.11 of Chapter 4, CONTUR studies for this model motivated a complete study in context of the ATLAS four-lepton measurement. The ATLAS limits obtained, shown in Figure 5.15, are comparable to those of Figure 5.17a. Similarly, the ATLAS colour map of Figure 5.16 which shows the most sensitive observable used to derive the limits is comparable to plot to Figure 5.19, which shows the most sensitive observable used for the CONTUR limit. In both, there is the dominance of m_{12} in the high M_{h_2} region. In terms of the 95% CL excluded region, at low masses the ATLAS and CONTUR results are largely similar. At higher masses the CONTUR limits are slightly weaker. The ATLAS limit excludes the entire $\sin\alpha > 0.3$ region at high M_{h_2}, whereas for CONTUR it is only up to $\sin\alpha > 0.4$. These results are a good demonstration of how useful CONTUR can be in performing broad scans that cover large regions of parameter space. Although slightly less sensitive than a dedicated ATLAS limit, the CONTUR scan takes just a few hours, rather than weeks, to complete.

In Scenario C, the effects of the Higgs mixing and the second Higgs mass eigenstates are switched on by setting $\sin\alpha = 0.2$ and $M_{h_2} = 200$ GeV. Figure 5.20b is the excluded model space from Reference [2] for Scenario C in the $M_{Z'}$ - g_1' plane. There is an experimental constraint arising from electron-neutrino scattering that is shaded in red on the scan, as well as the excluded region from the perturbativity requirement. Figure 5.20a shows the new exclusion obtained using CONTUR version 2.0.x, which includes the 13 TeV $m_{4\ell}$ analysis. At low $M_{Z'}$, there is an order of magnitude improvement in the 95% CL excluded region. At higher masses, the improvement is more subtle but still present. Even more prominent is the improvement in the 68% CL exclusion. Prior to the addition of the 13 TeV $m_{4\ell}$ measurement, the 68% CL exclusion of Figure 5.20b in green covers only a little more area than the yellow. In Figure 5.20a, however, nearly the entire scanned parameter space is excluded at 68% CL (the only allowed area is to the left of the dashed white line). This change is attributed mainly to the $m_{4\ell}$ measurement, which dominates the high mass and low g_1' regions.

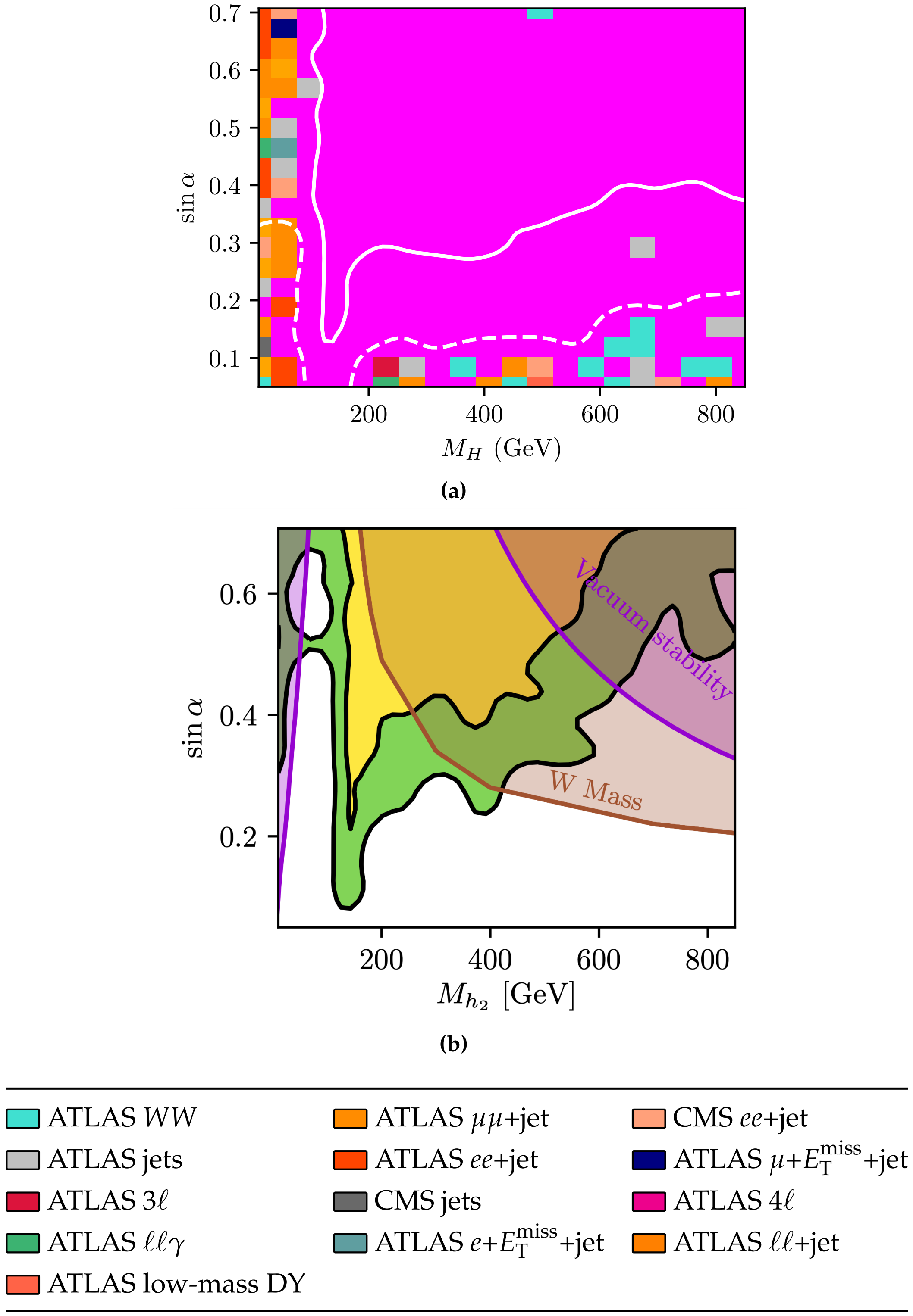

(a)

(b)

Figure 5.17.: (a) Dominant LHC analysis pools contributing to the exclusion limit set for the gauged $B-L$ model in M_{h_2} vs $\sin\alpha$ plane, where $g_1' = 0.001$ and $M_{Z'} = 35\,\text{GeV}$. The disfavoured regions are located above and to the left of the dashed (68% CL) and solid (95% CL) white contours respectively. Plot is made with CONTUR 2.1.x and RIVET 3.1.4. (b) The corresponding heatmap from Figure 6b of Reference [2]. The disfavoured regions at 95% CL and 68% CL are shaded in yellow and green respectively. The constraints from perturbativity up to a scale of at least 10 TeV, and from W mass measurements are also shown.

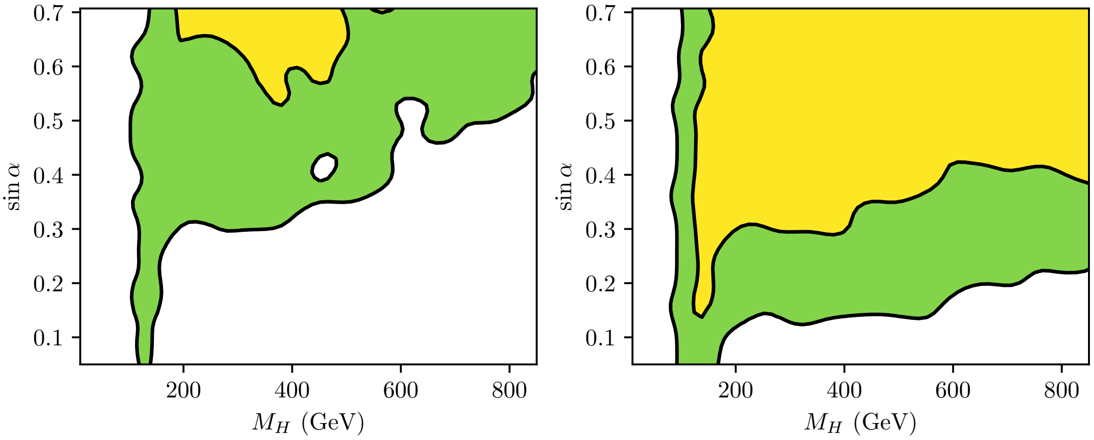

(a) **(b)**

Figure 5.18.: CONTUR exclusion (a) without and (b) with the new four-lepton measurement. The disfavoured regions at 95% CL and 68% CL are shaded in yellow and green respectively.

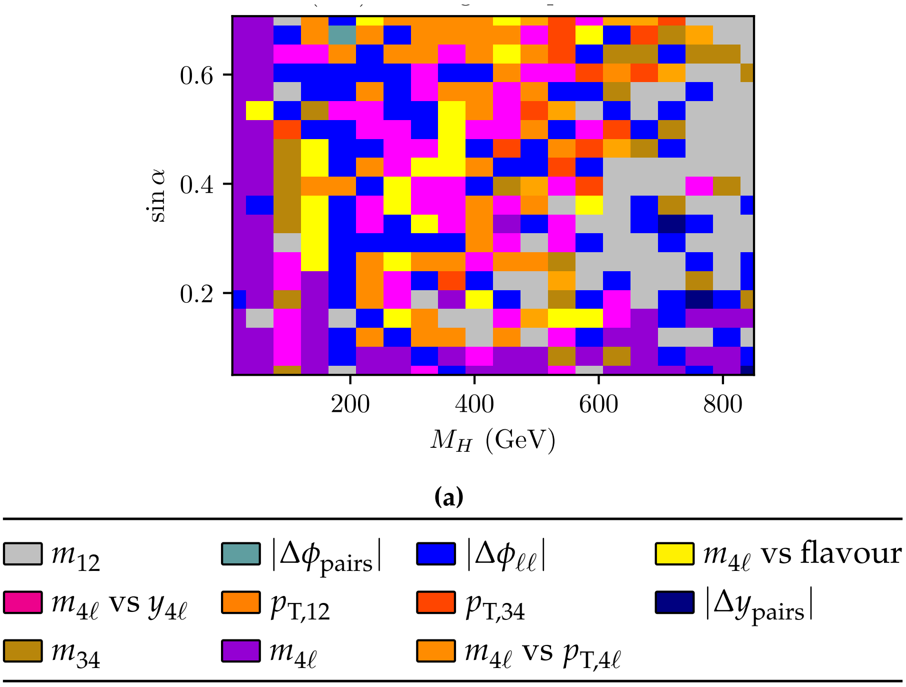

(a)

Figure 5.19.: The most sensitive distribution from the ATLAS four-lepton measurement contributing to the limit is indicated in colour for the gauged $B-L$ model in M_{h_2} vs $\sin\alpha$ plane, where $g_1' = 0.001$ and $M_{Z'} = 35$ GeV.

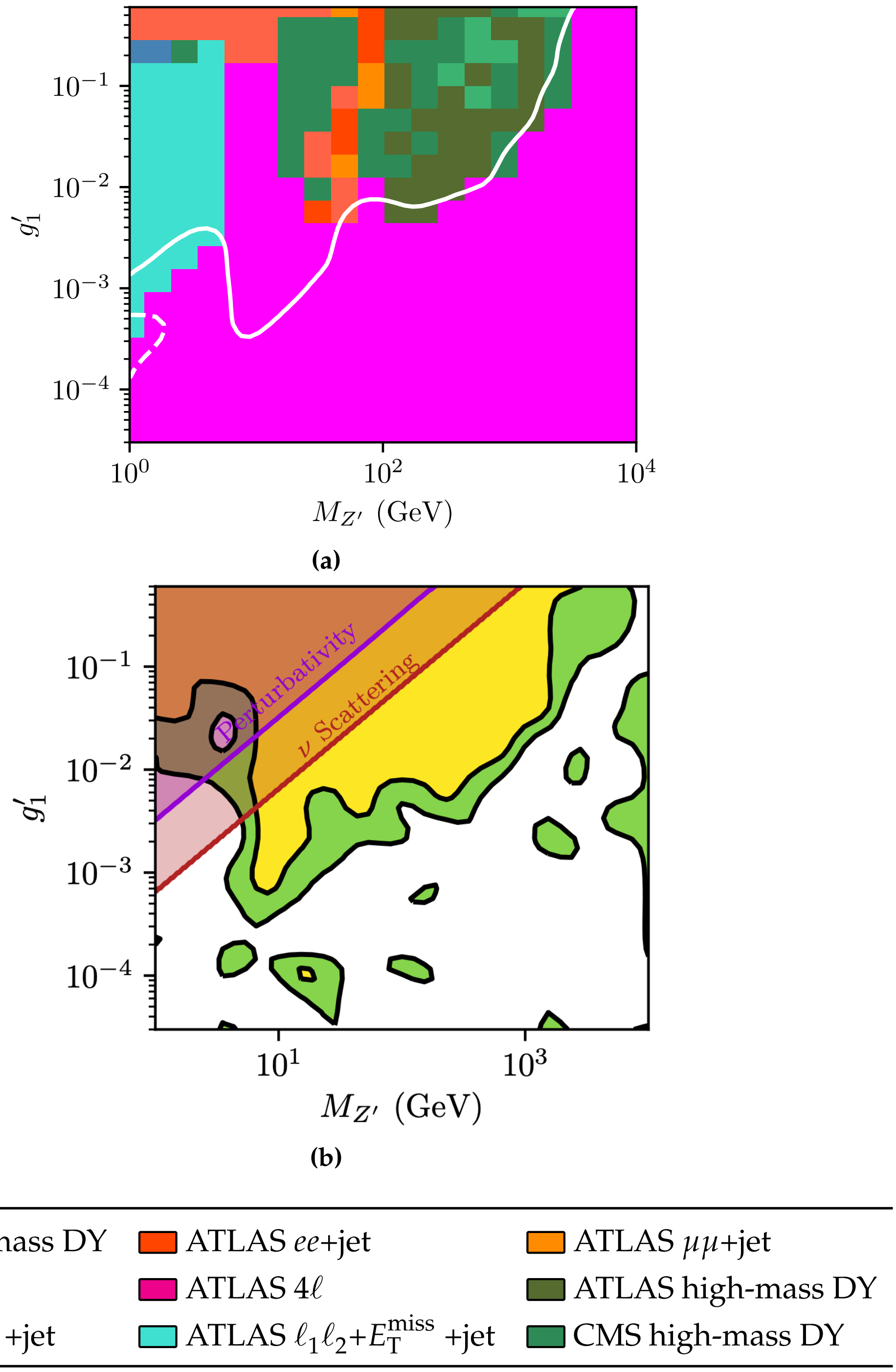

(a)

(b)

Figure 5.20.: (a) Dominant LHC analysis pools contributing to the exclusion limit set for the gauged $B-L$ model in $M_{Z'}$ vs g'_1 plane, where $\sin\alpha = 0.2$ and $M_{h_2} = 200$ GeV. The disfavoured regions are located above and to the left of the dashed (68% CL) and solid (95% CL) white contours respectively. Plot is made with CONTUR 2.1.x and RIVET 3.1.4. (b) The corresponding heatmap from Figure 5c of Reference [2]. The disfavoured regions at 95% CL and 68% CL are shaded in yellow and green respectively. The constraints from perturbativity up to a scale of at least 10 TeV, and from electron-neutrino scattering, are also indicated.

Chapter 6.

Conclusion

The Run-2 of the LHC at an unprecedented centre-of-mass energy of 13 TeV is now finished, and 139 fb^{-1} of data has been successfully collected. The ATLAS collaboration made great efforts in analyzing the data in both making and refining cross-section measurements and conducting direct searches for new physics. As the latter continues to be unfruitful, the focus shifts to a complementary approach in the hunt for BSM physics - the reinterpretation of the precision measurements which are compatible with the Standard Model. This approach is sensitive to potential new signatures that may be "hidden" in the data, appearing as subtle changes to a spectrum rather than a visible peak.

Cross-sections measured in terms of final state particles have a high degree of model independence, facilitating its reuse in constraining BSM physics. One such precision measurement targets processes that have at least four leptons in the final state. Chapter 4 presented the ATLAS four-lepton cross-section measurements using 139 fb^{-1} of data. Four-lepton production has been measured inclusively, and differentially in the fiducial phase space, along with measurements of the dilepton mass, and kinematic and angular variables in four regions of $m_{4\ell}$ dominated by difference physics processes. All results are presented at the particle-level, meaning they are corrected for detector effects. The procedure used for the unfolding process was optimized and found to have minimal bias in the presence of physics beyond the SM. Overall, the measured distributions are found to be consistent with the leading SM predictions. A few interpretation examples are conducted by the analysis team. The most precise $Z \rightarrow 4\ell$ branching fraction to date was extracted and has a value of, consistent with previous measurements and predictions. Limits on coefficients in a SMEFT framework and parameters governing a model based on a spontaneously broken $B - L$ gauge symmetry were set using the data. To facilitate future re-interpretability, the data are made public and the analysis workflow documented. In doing so, the analysis team hopes that the measurement can be used to further probe BSM models in the years to come.

In Chapter 5, two re-interpretation studies using re-interpretation software CONTUR are presented. The first focuses on a generic class of VLQ models, and the second is the $B-L$ model that was also interpreted within the ATLAS $m_{4\ell}$ analysis. For these studies, a large bank of LHC differential cross-section measurements were used. Although these measurements were not specifically tailored to be sensitive to the BSM models, they nonetheless were able to exclude significant regions of the model parameter space. For the case of the VLQs, the fast-paced CONTUR machinery was able to survey previously unexplored model scenarios. The study of the $B-L$ model yielded competitive limits to that of the ATLAS $m_{4\ell}$ analysis, and improves upon the limits of a previous paper with limits derived using the same toolkit [2], thanks to the addition of new measurements. For both models, the role that the new ATLAS $m_{4\ell}$ measurement plays was investigated. In certain scenarios, the addition of this new measurement resulted in a significantly larger excluded region.

Overall, the work in this thesis demonstrated how a model-independent measurement is made, and how powerful they can be, if well preserved, in constraining new physics. What takes a dedicated search team years accomplish, takes the CONTUR framework one day. Undeniably, this toolkit can be beneficial if used in complement by searches when designing analyses and deciding what parameter space to target. Furthermore, given how resource-intensive it is to publish an analysis, it is in the best interest of the particle physics community to maximize its usefulness. From an overarching collaborative perspective, ensuring an analysis' re-interpretability is highly desirable. It signifies a longer legacy for the published data well beyond the lifetime of the experiment.

Appendix A.

Unfolding inputs and studies

Figures A.1-A.12 show the predicted detector-level and particle-level yields, as well as the reconstruction efficiency, the fiducial purity (equivalent to the diagonal elements of the migration matrices) and the fiducial fraction for each bin of each distribution, after the pre-unfolding weights are applied. Note, that the yields are normalized by bin width to show clearly that the number of events per bin satisfy the criteria we required, but this can lead to the distributions looking jumpy.

Figures A.14-A.25 show the migration matrices for each slice of all 2D distributions, and also the migration matrices across the slices in each distribution. They are separated purely for legibility, and the elements are normalized across the entire matrix in all cases.

Figure **??** shows the migration between the $m_{4\ell}$mass slices with the current definition and with the Higgs-enriched slice altered from 120-130 GeV to 115-130 GeV. Migrations between the Higgs-enriched bin and neighbouring off-shell bin do decrease minimally, but we are not convinced this is sufficient to motivate altering the binning at this stage.

Figures **??**-**??** show the results of unfolding the MC and comparing it to the particle-level MC as a cross-check for the method. All distributions close completely.

Figures **??**-**??** show the results of splitting the MC randomly into two subsets, unfolding one and validating it against the other. The bins of all distributions generally close within the uncertainties, which are produced by bootstrapping on both halves of the MC.

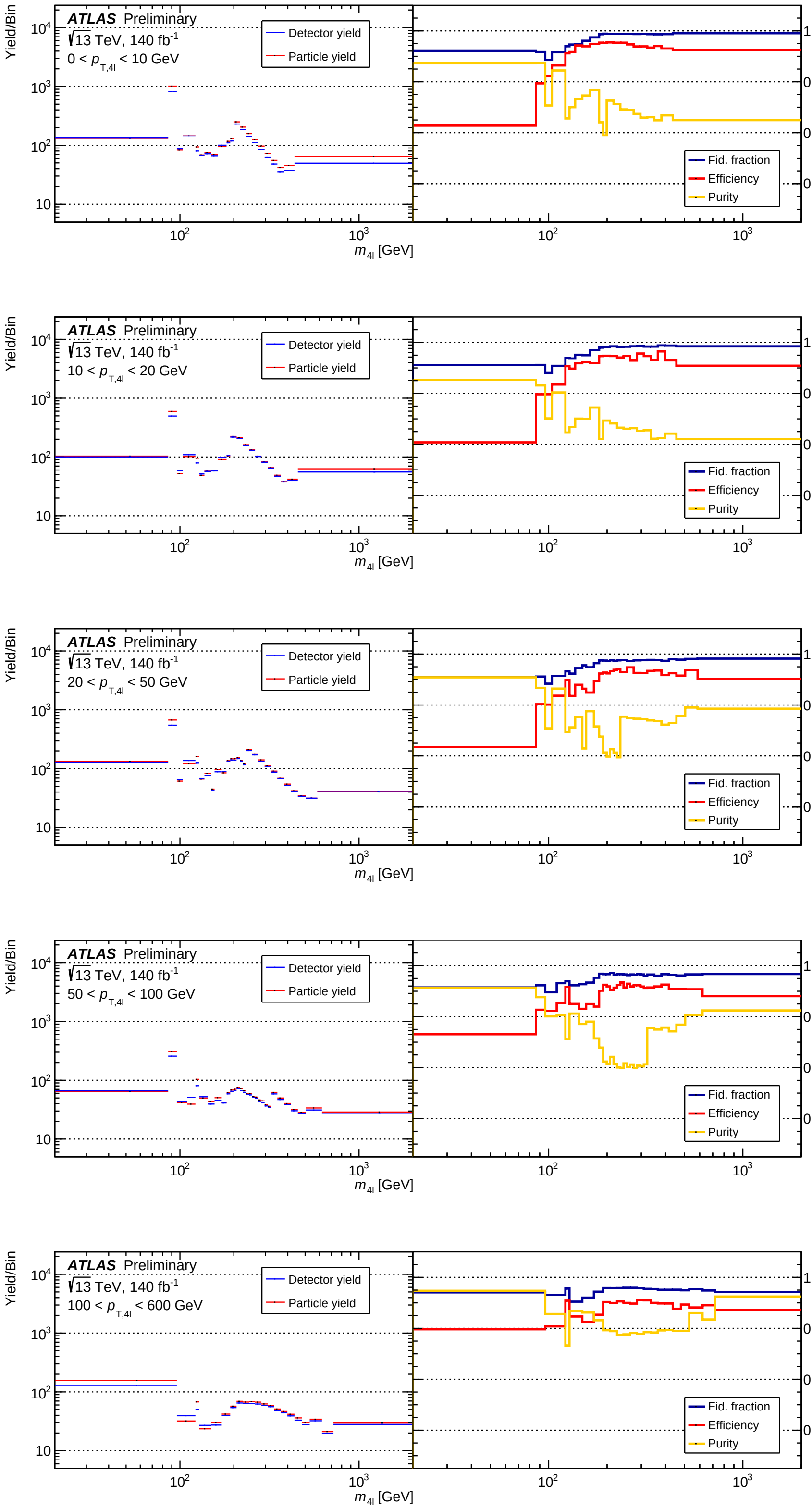

Figure A.1.: In the left-hand panels, the number of predicted events passing the reconstruction- and fiducial- level selections are displayed as the detector yield and particle yield, respectively. The right-hand panel shows the efficiency, fiducial purity and fiducial fraction. All variables are plotted as a function of the $m_{4\ell}$bins, in slices of the $p_{\mathrm{T},4\ell}$variable which are stacked and labelled with the included $p_{\mathrm{T},4\ell}$range.

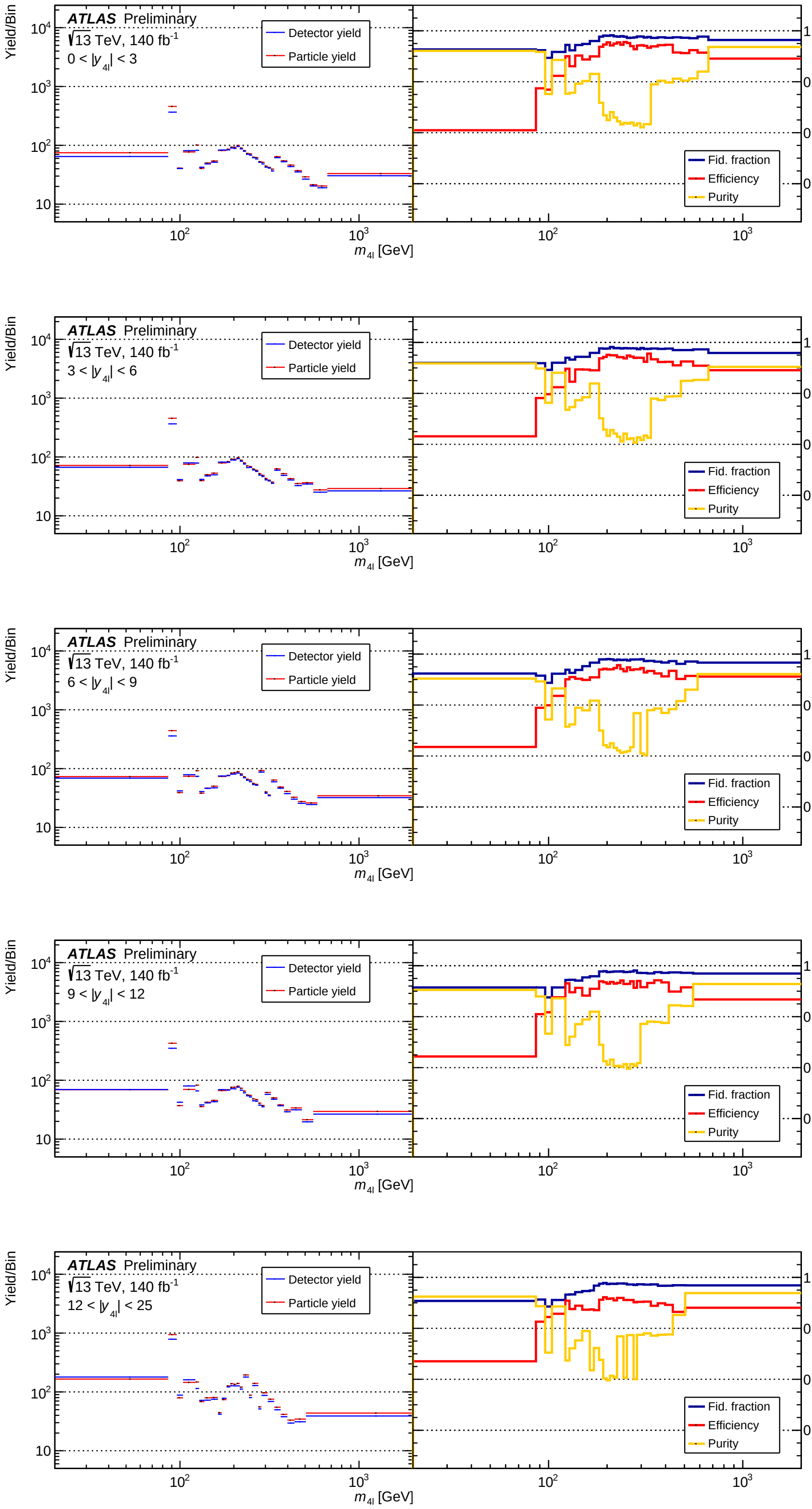

Figure A.2.: In the left-hand panels, the number of predicted events passing the reconstruction- and fiducial- level selections are displayed as the detector yield and particle yield, respectively. The right-hand panel shows the efficiency, fiducial purity and fiducial fraction. All variables are plotted as a function of the $m_{4\ell}$bins, in slices of the $y_{4\ell}$variable which are stacked and labelled with the included $y_{4\ell}$range.

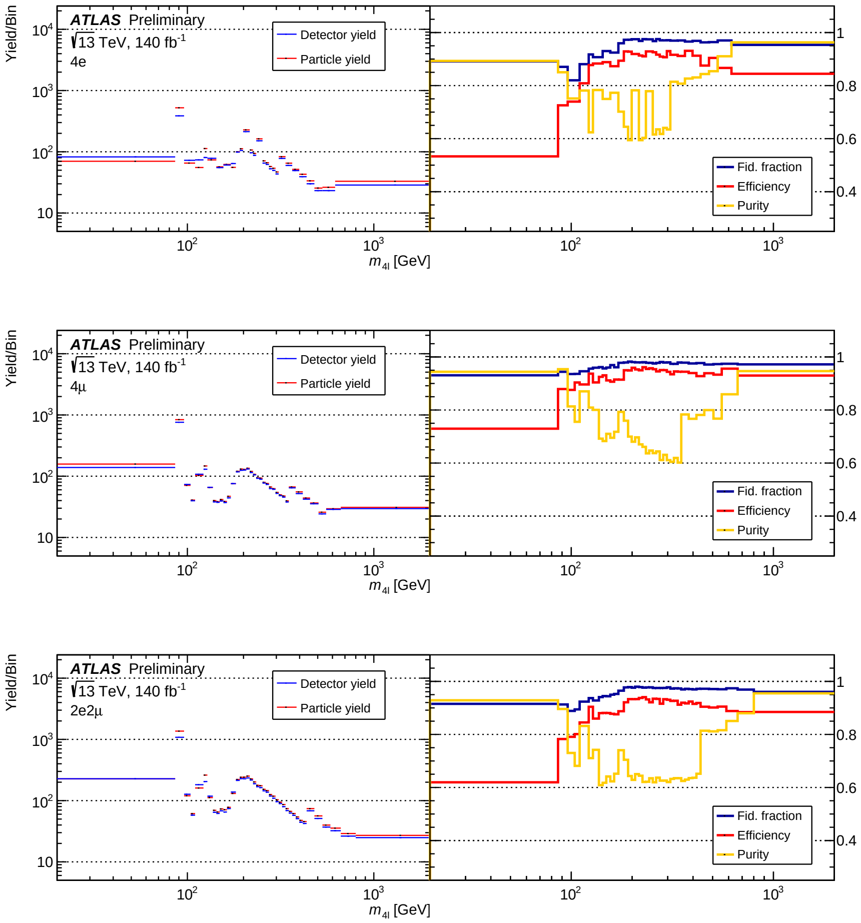

Figure A.3.: In the left-hand panels, the number of predicted events passing the reconstruction- and fiducial- level selections are displayed as the detector yield and particle yield, respectively. The right-hand panel shows the efficiency, fiducial purity and fiducial fraction. All variables are plotted as a function of the $m_{4\ell}$bins, in the $4e$, 4μ and $2e2\mu$ flavour channels from top to bottom.

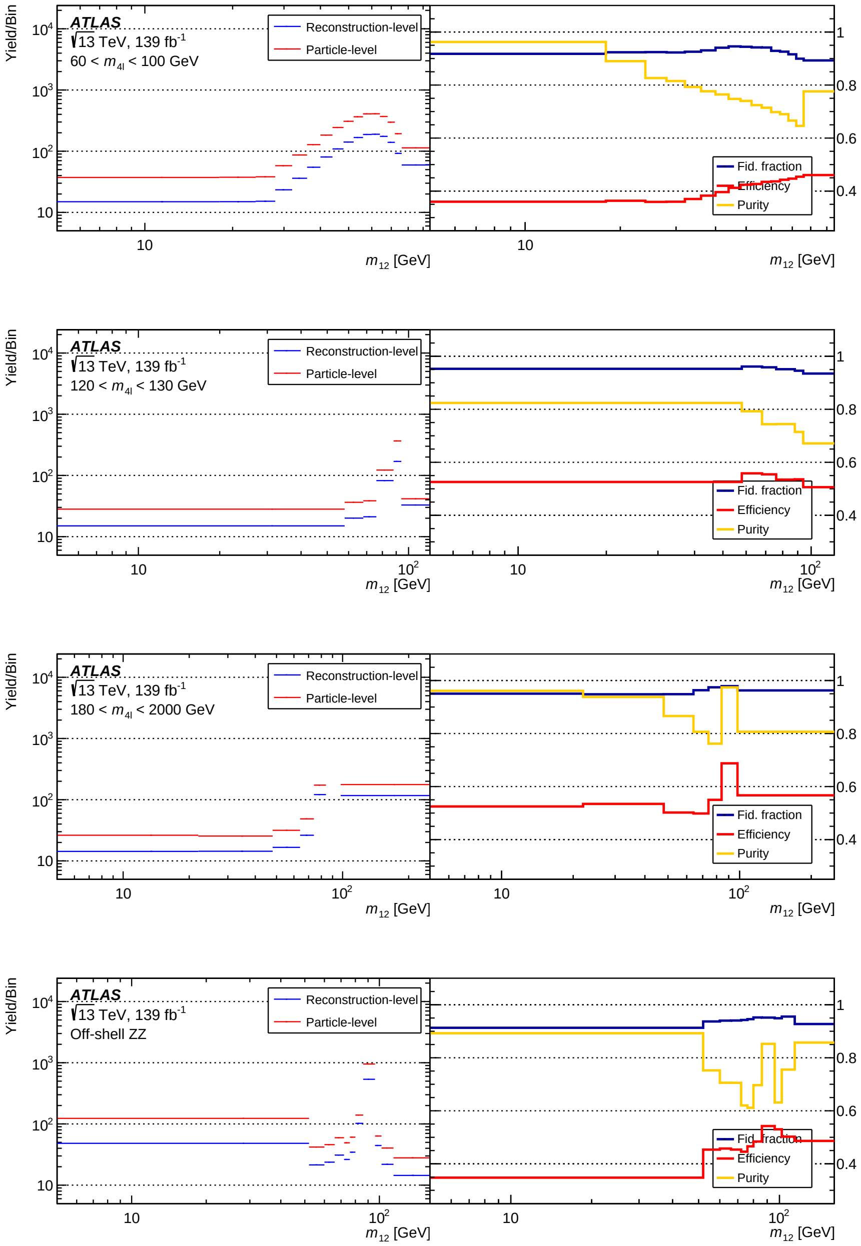

Figure A.4.: In the left-hand panels, the number of predicted events passing the reconstruction- and fiducial- level selections are displayed as the detector yield and particle yield, respectively. The right-hand panel shows the efficiency, fiducial purity and fiducial fraction. All variables are plotted as a function of the m_{12} bins, in slices of the $m_{4\ell}$variable which are stacked and labelled with the included $m_{4\ell}$range.

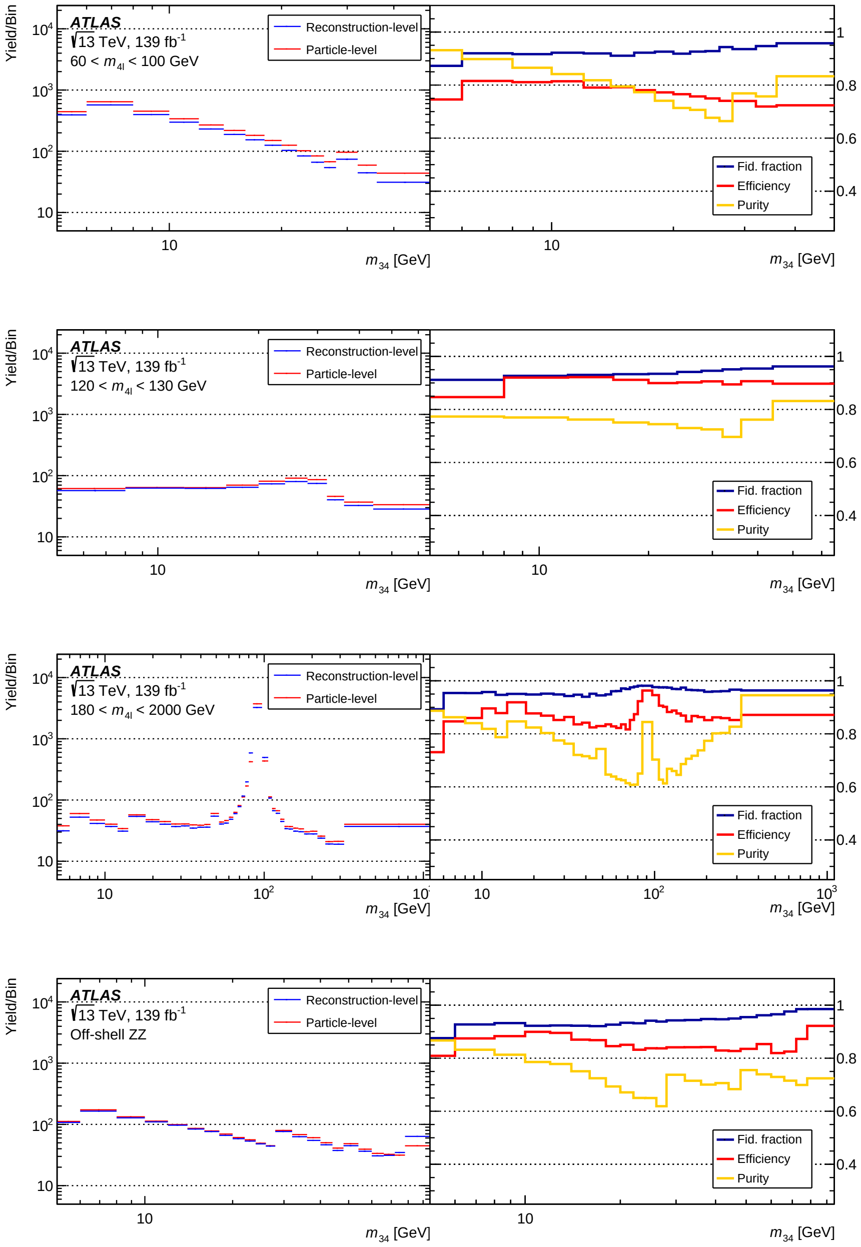

Figure A.5.: In the left-hand panels, the number of predicted events passing the reconstruction- and fiducial- level selections are displayed as the detector yield and particle yield, respectively. The right-hand panel shows the efficiency, fiducial purity and fiducial fraction. All variables are plotted as a function of the m_{34} bins, in slices of the $m_{4\ell}$variable which are stacked and labelled with the included $m_{4\ell}$range.

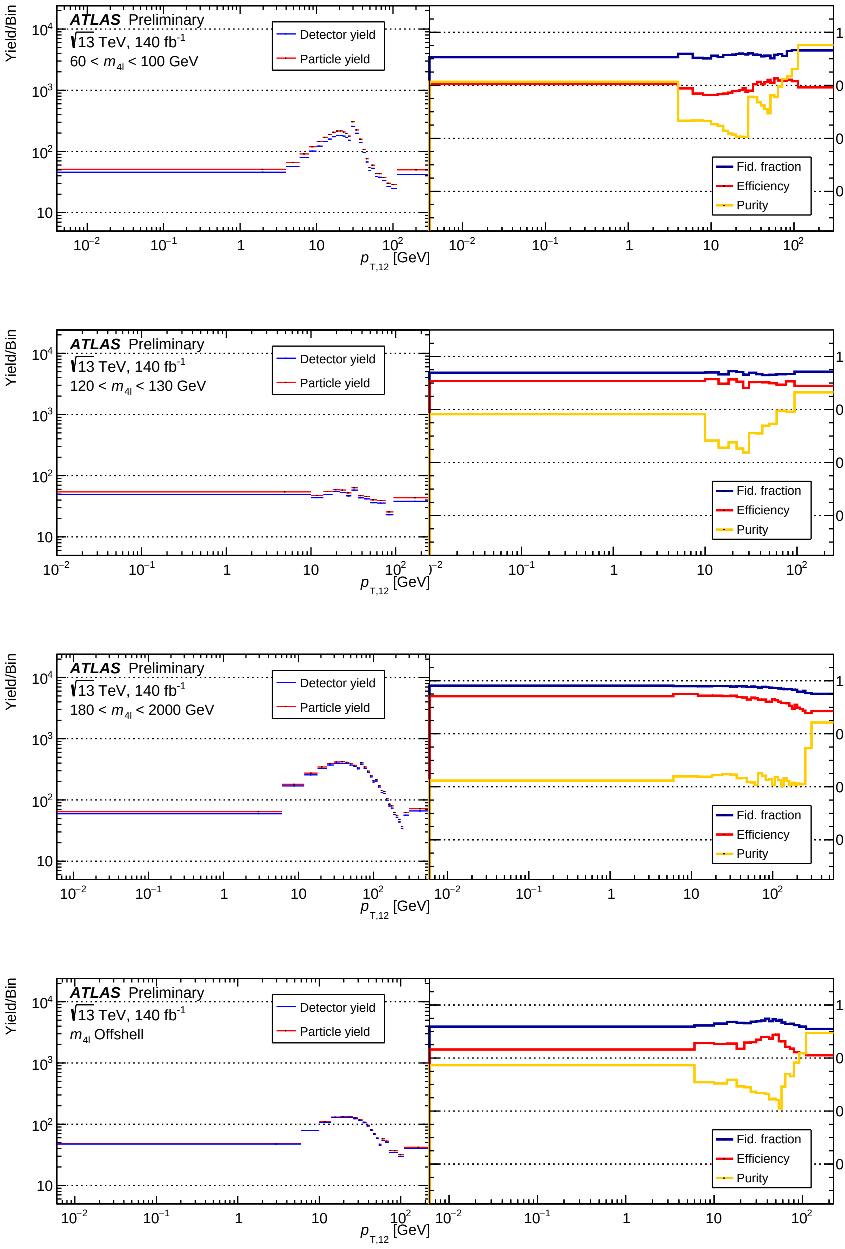

Figure A.6.: In the left-hand panels, the number of predicted events passing the reconstruction- and fiducial- level selections are displayed as the detector yield and particle yield, respectively. The right-hand panel shows the efficiency, fiducial purity and fiducial fraction. All variables are plotted as a function of the $p_{T,12}$bins, in slices of the $m_{4\ell}$variable which are stacked and labelled with the included $m_{4\ell}$range.

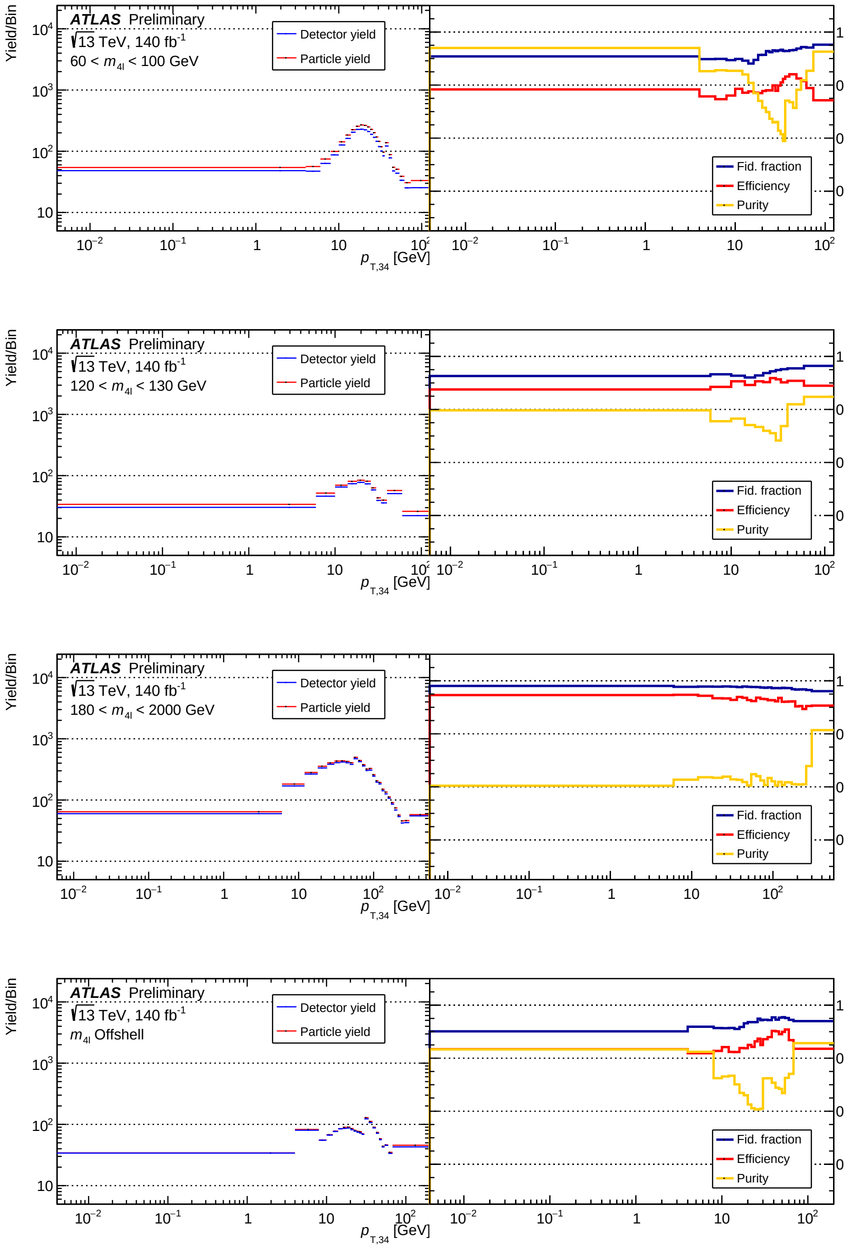

Figure A.7.: In the left-hand panels, the number of predicted events passing the reconstruction- and fiducial- level selections are displayed as the detector yield and particle yield, respectively. The right-hand panel shows the efficiency, fiducial purity and fiducial fraction. All variables are plotted as a function of the $p_{T,34}$bins, in slices of the $m_{4\ell}$variable which are stacked and labelled with the included $m_{4\ell}$range.

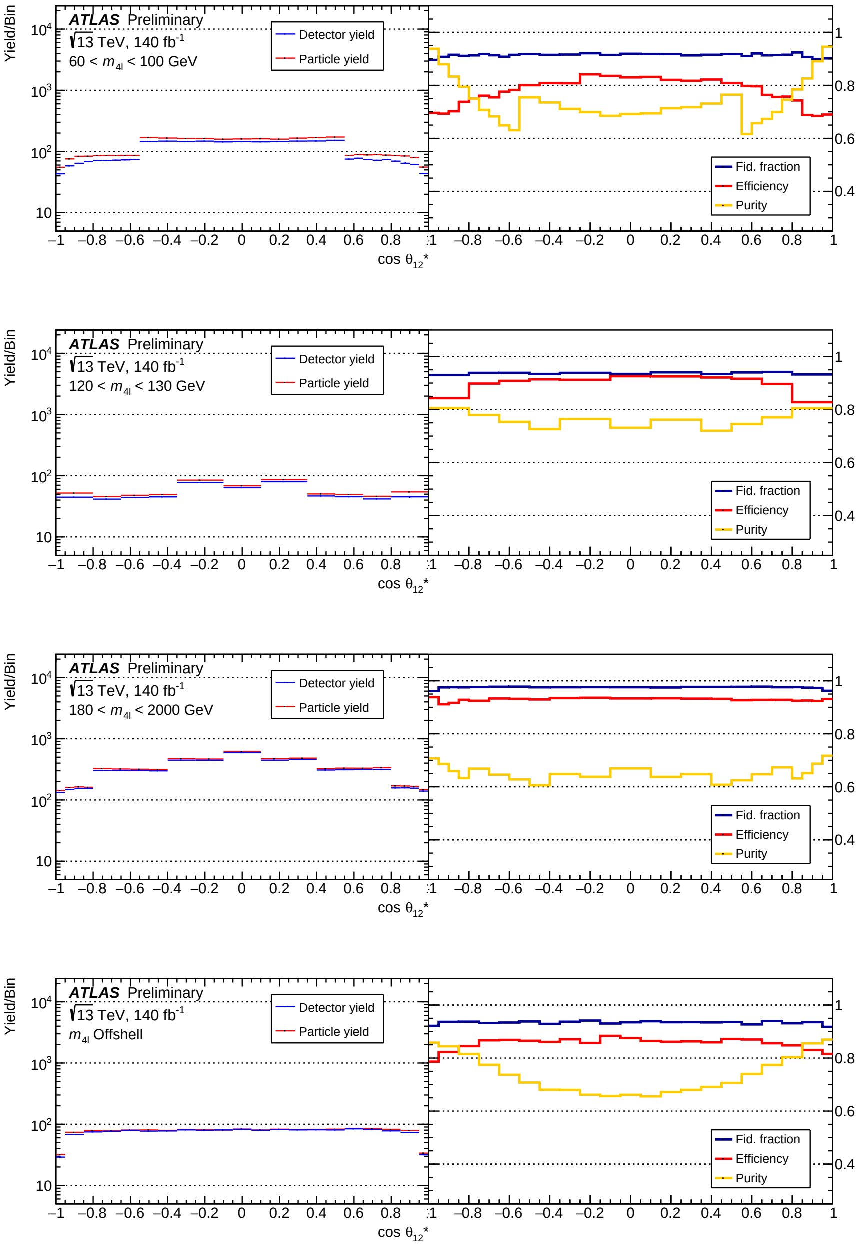

Figure A.8.: In the left-hand panels, the number of predicted events passing the reconstruction- and fiducial- level selections are displayed as the detector yield and particle yield, respectively. The right-hand panel shows the efficiency, fiducial purity and fiducial fraction. All variables are plotted as a function of the $\cos\theta^*$bins, in slices of the $m_{4\ell}$variable which are stacked and labelled with the included $m_{4\ell}$range.

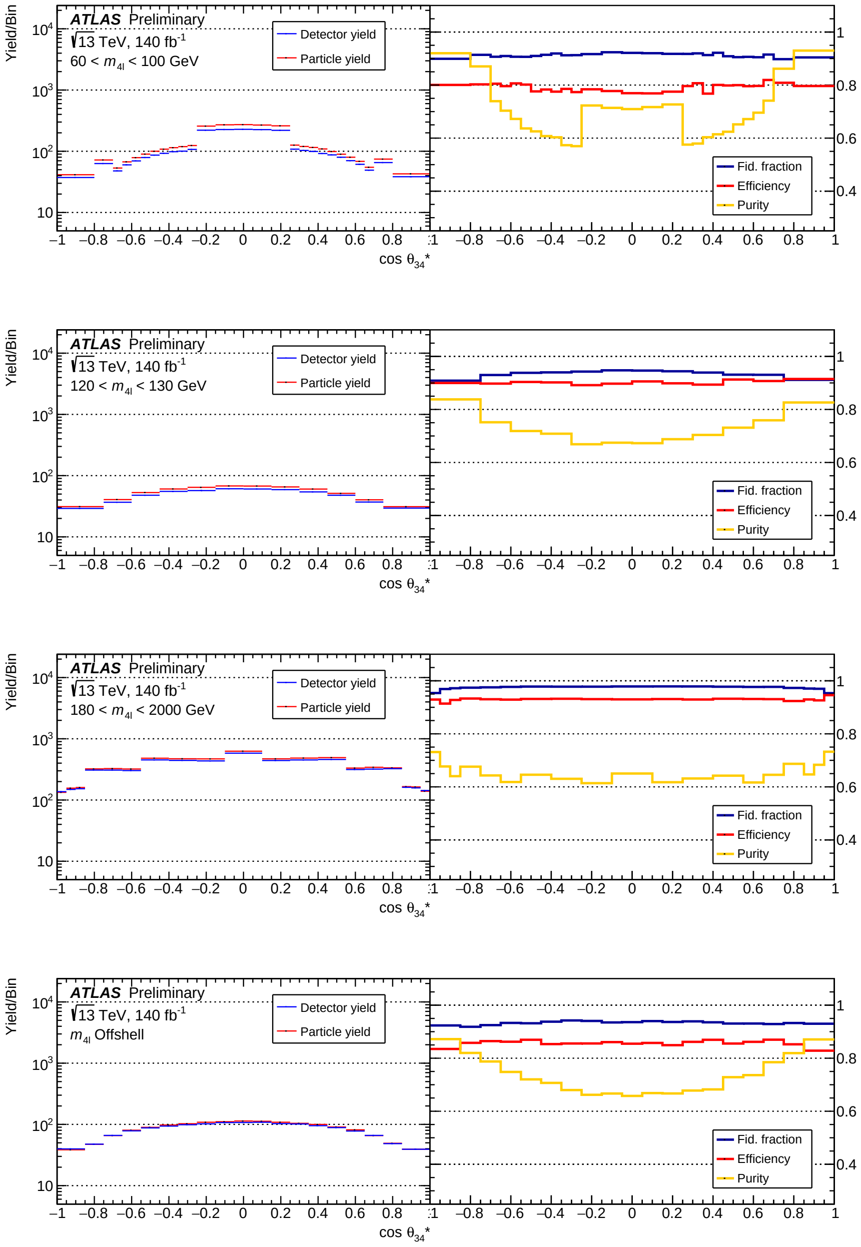

Figure A.9.: In the left-hand panels, the number of predicted events passing the reconstruction- and fiducial- level selections are displayed as the detector yield and particle yield, respectively. The right-hand panel shows the efficiency, fiducial purity and fiducial fraction. All variables are plotted as a function of the $\cos\theta^*$bins, in slices of the $m_{4\ell}$variable which are stacked and labelled with the included $m_{4\ell}$range.

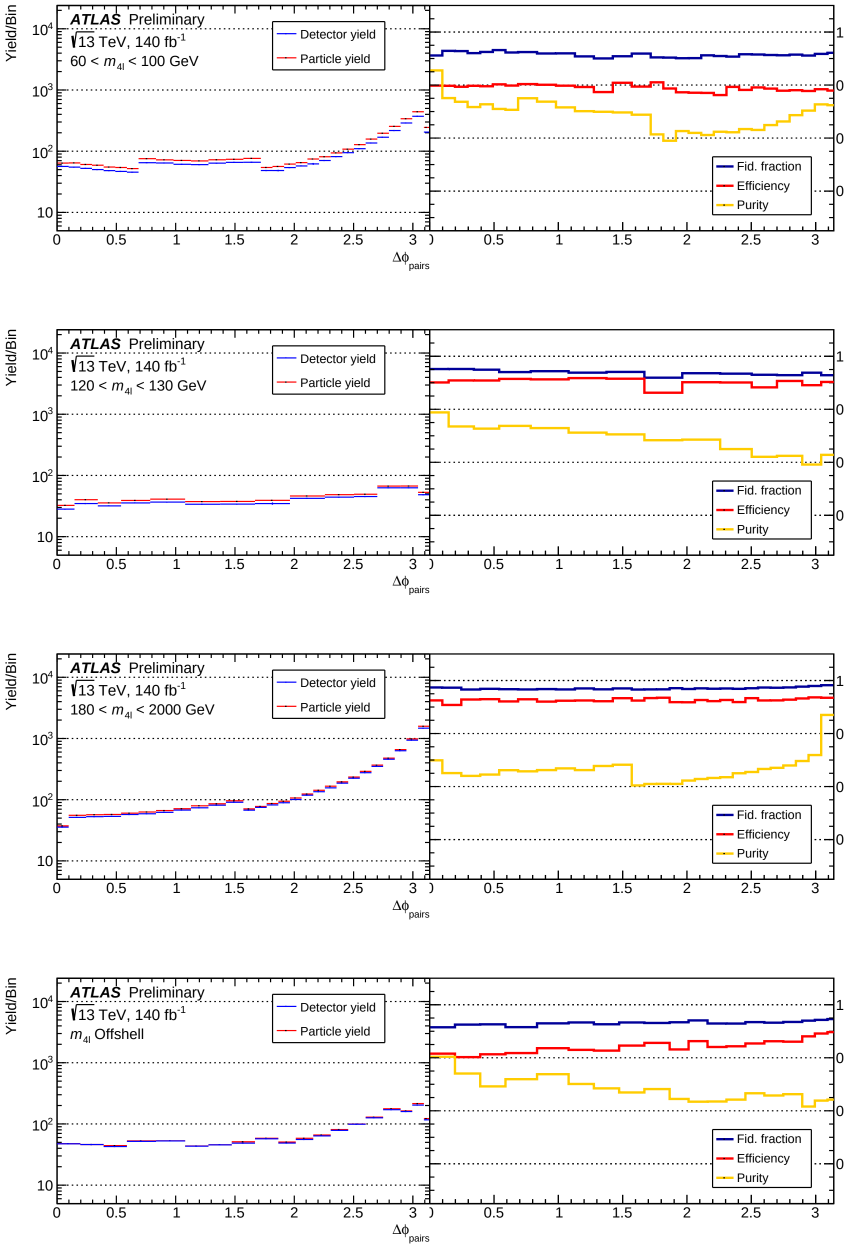

Figure A.10.: In the left-hand panels, the number of predicted events passing the reconstruction- and fiducial- level selections are displayed as the detector yield and particle yield, respectively. The right-hand panel shows the efficiency, fiducial purity and fiducial fraction. All variables are plotted as a function of the $|\Delta\phi_{\text{pairs}}|$ bins, in slices of the $m_{4\ell}$variable which are stacked and labelled with the included $m_{4\ell}$range.

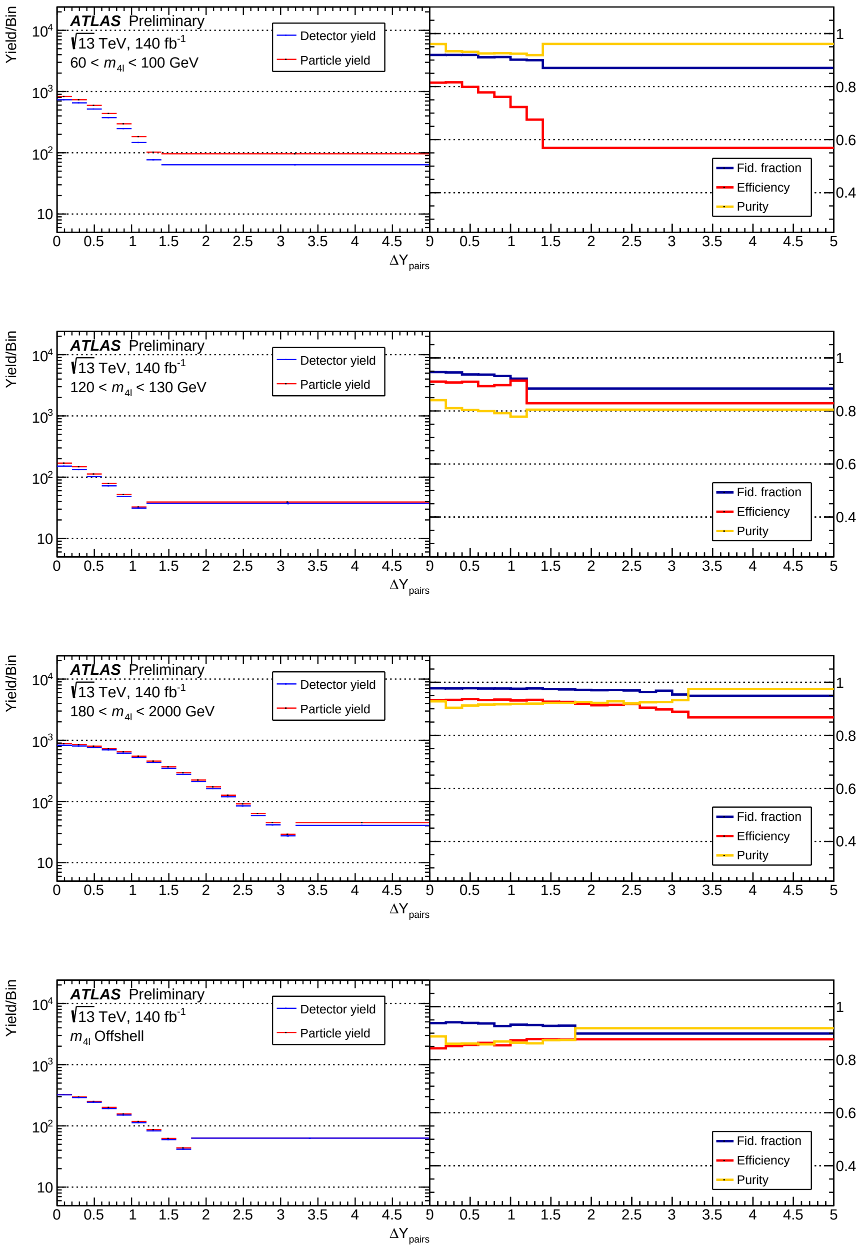

Figure A.11.: In the left-hand panels, the number of predicted events passing the reconstruction- and fiducial- level selections are displayed as the detector yield and particle yield, respectively. The right-hand panel shows the efficiency, fiducial purity and fiducial fraction. All variables are plotted as a function of the $|\Delta y_{\mathrm{pairs}}|$bins, in slices of the $m_{4\ell}$variable which are stacked and labelled with the included $m_{4\ell}$range.

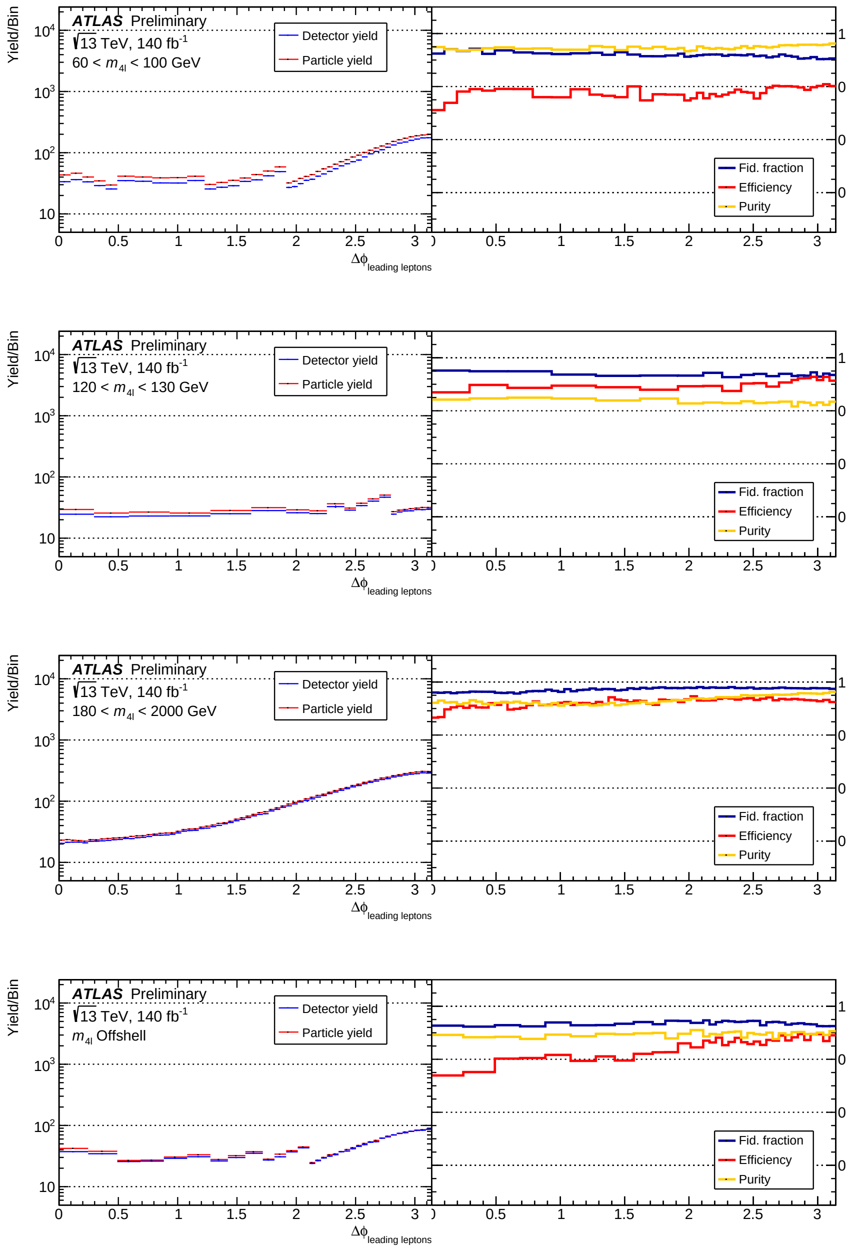

Figure A.12.: In the left-hand panels, the number of predicted events passing the reconstruction- and fiducial- level selections are displayed as the detector yield and particle yield, respectively. The right-hand panel shows the efficiency, fiducial purity and fiducial fraction. All variables are plotted as a function of the $|\Delta\phi_{\ell\ell}|$ bins, in slices of the $m_{4\ell}$variable which are stacked and labelled with the included $m_{4\ell}$range.

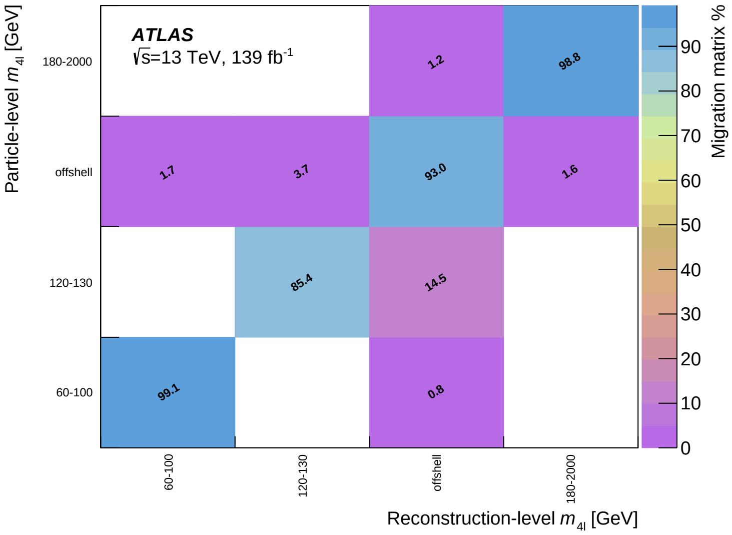

Figure A.13.: Migration matrices for the four $m_{4\ell}$regions between the slices.

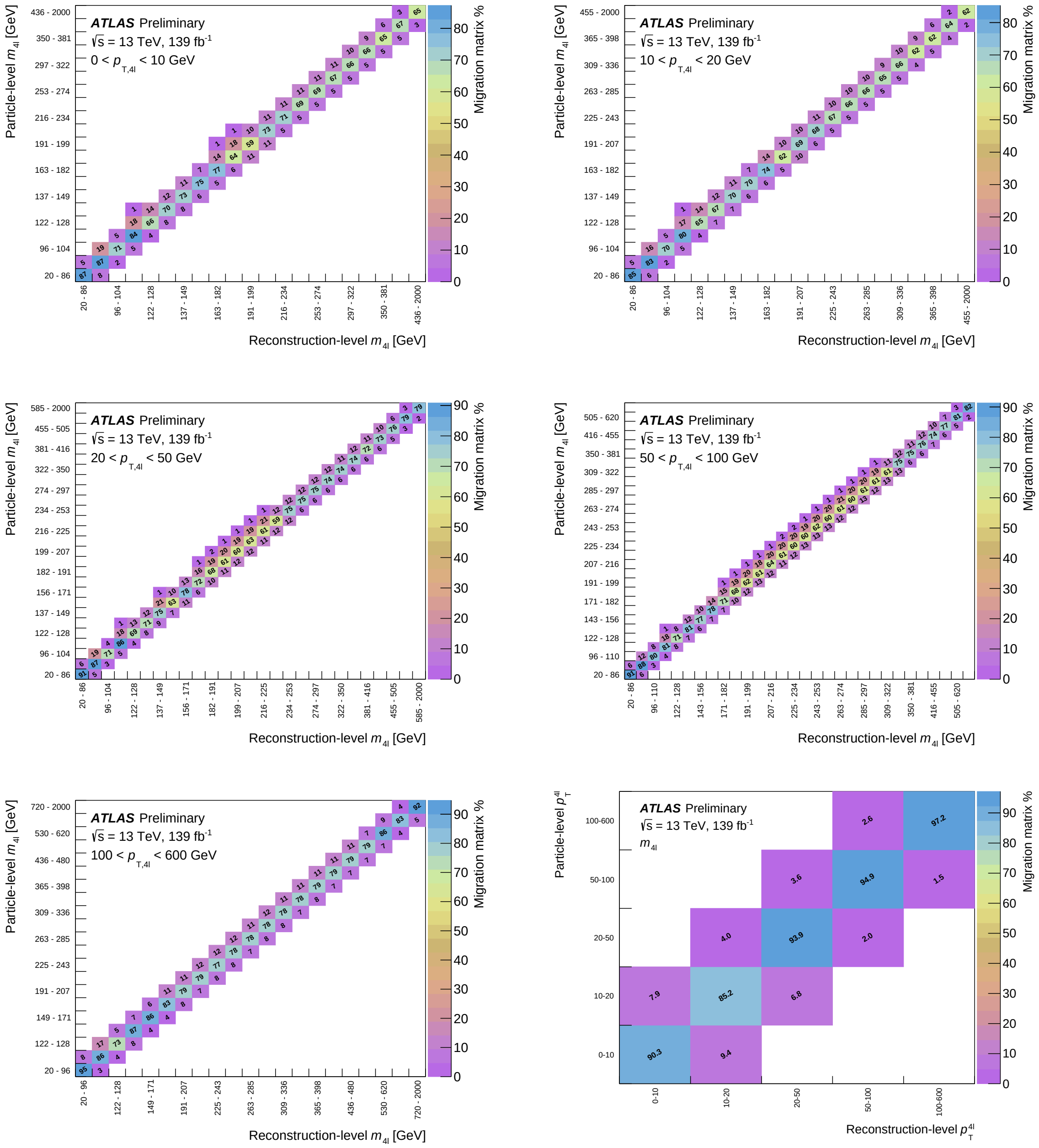

Figure A.14.: Migration matrices for the $m_{4\ell}$bins in each $p_{\mathrm{T},4\ell}$slice of the $m_{4\ell}$-$p_{\mathrm{T},4\ell}$distribution and between the slices.

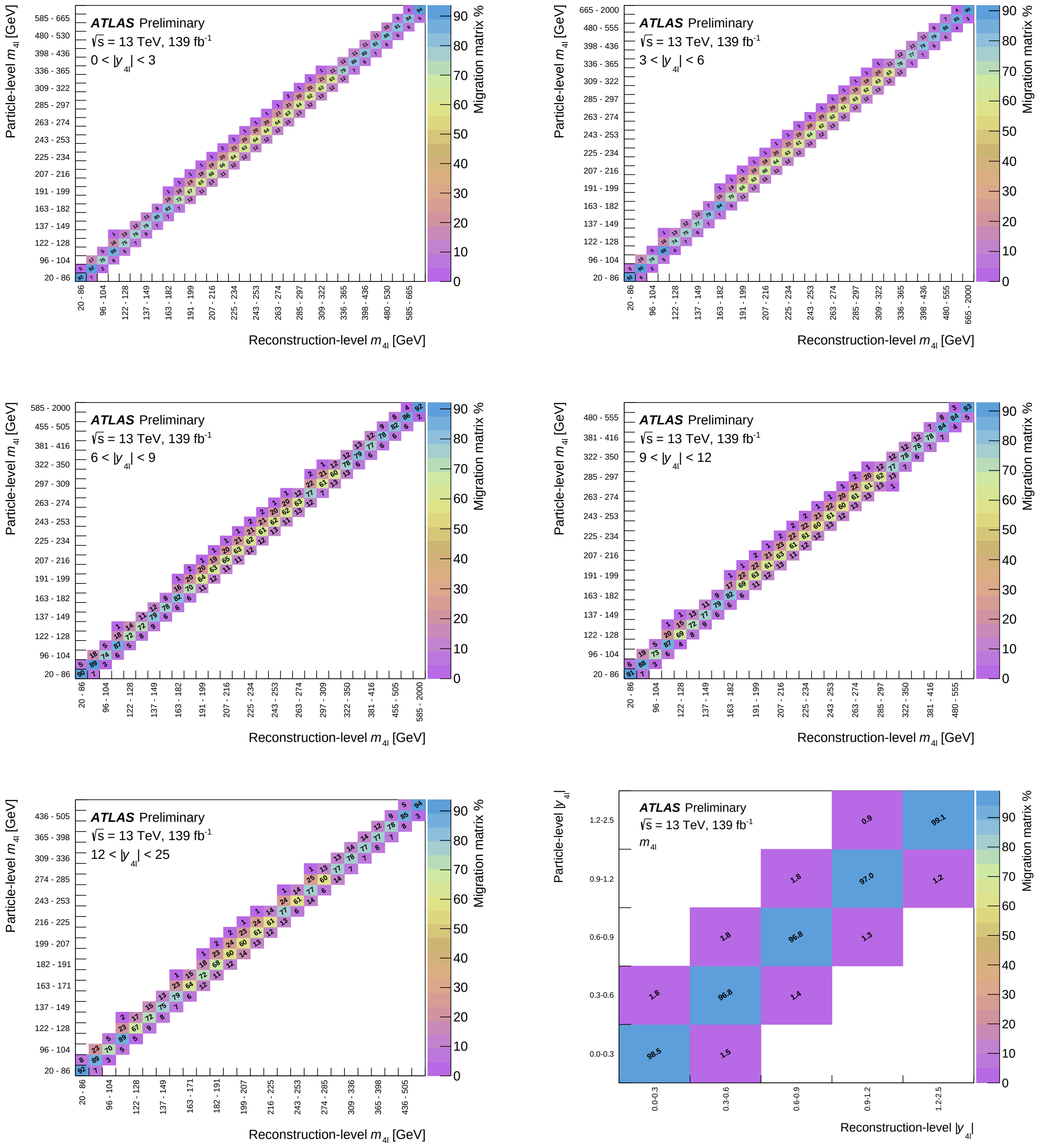

Figure A.15.: Migration matrices for the $m_{4\ell}$bins in each $y_{4\ell}$slice of the $m_{4\ell}$-$y_{4\ell}$distribution and between the slices.

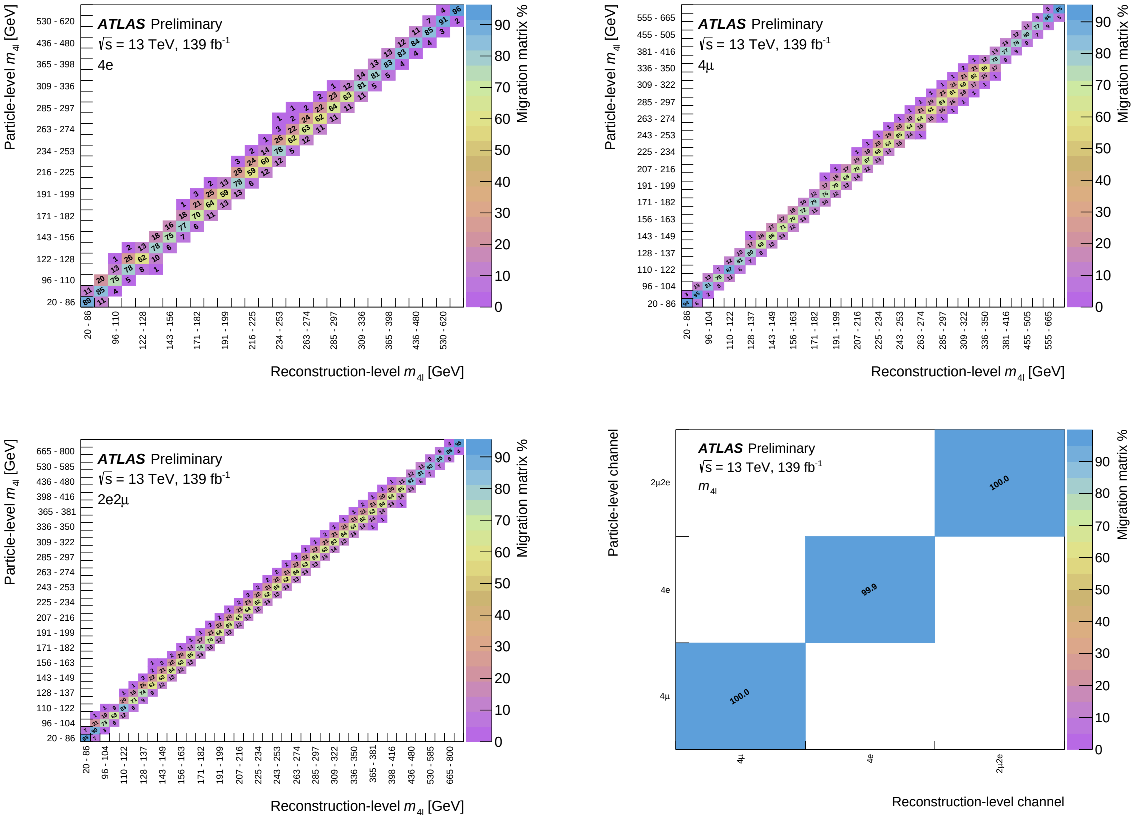

Figure A.16.: Migration matrices for the $m_{4\ell}$bins in each flavour slice and between the flavour slices of the $m_{4\ell}$-lepton flavour distribution (where no migration is seen, as expected).

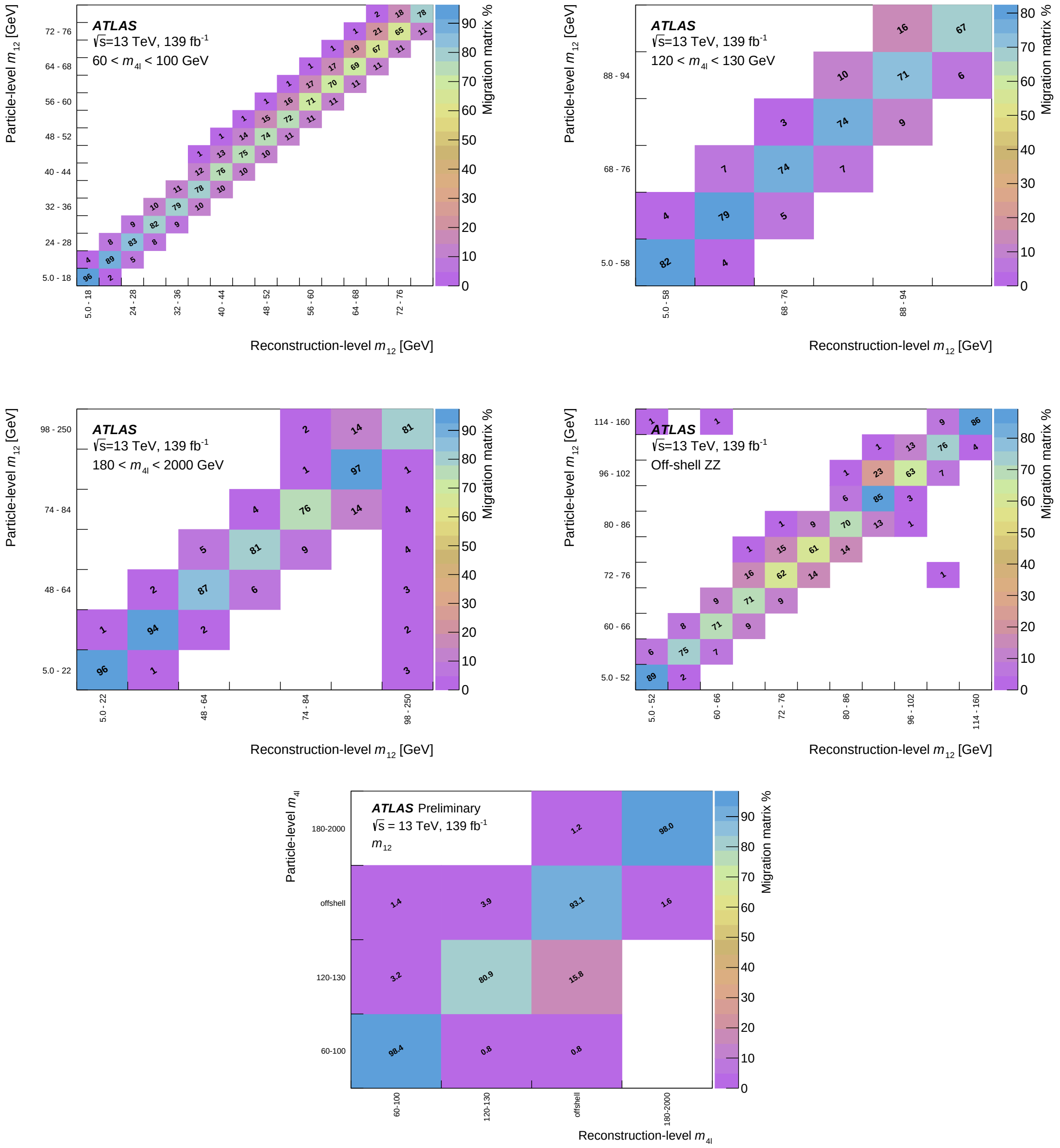

Figure A.17.: Migration matrices for the m_{12} bins in each of the $m_{4\ell}$slices of the m_{12}-$m_{4\ell}$distribution and between the slices.

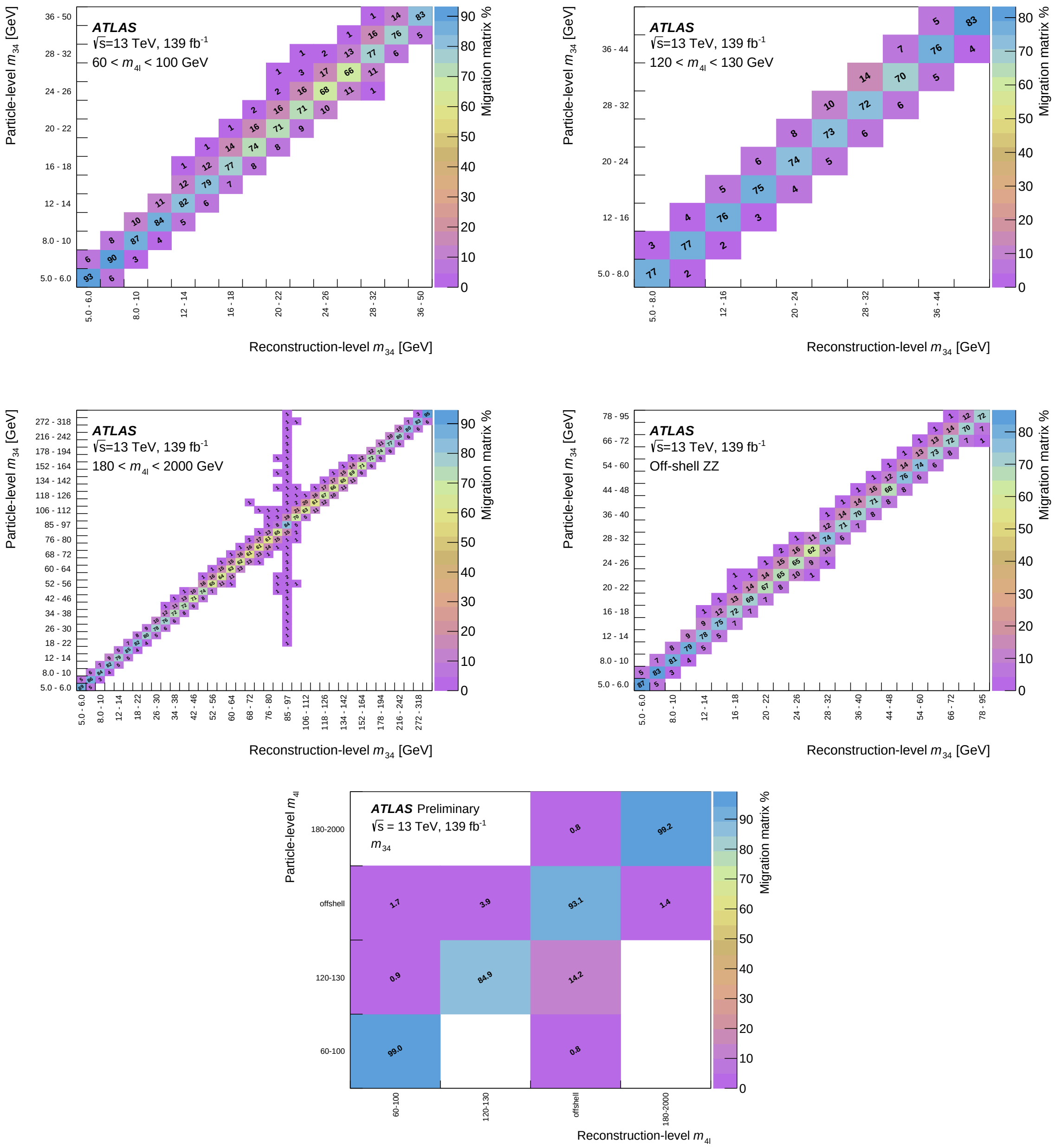

Figure A.18.: Migration matrices for the m_{34} bins in each of the $m_{4\ell}$slices of the m_{34}-$m_{4\ell}$distribution and between the slices.

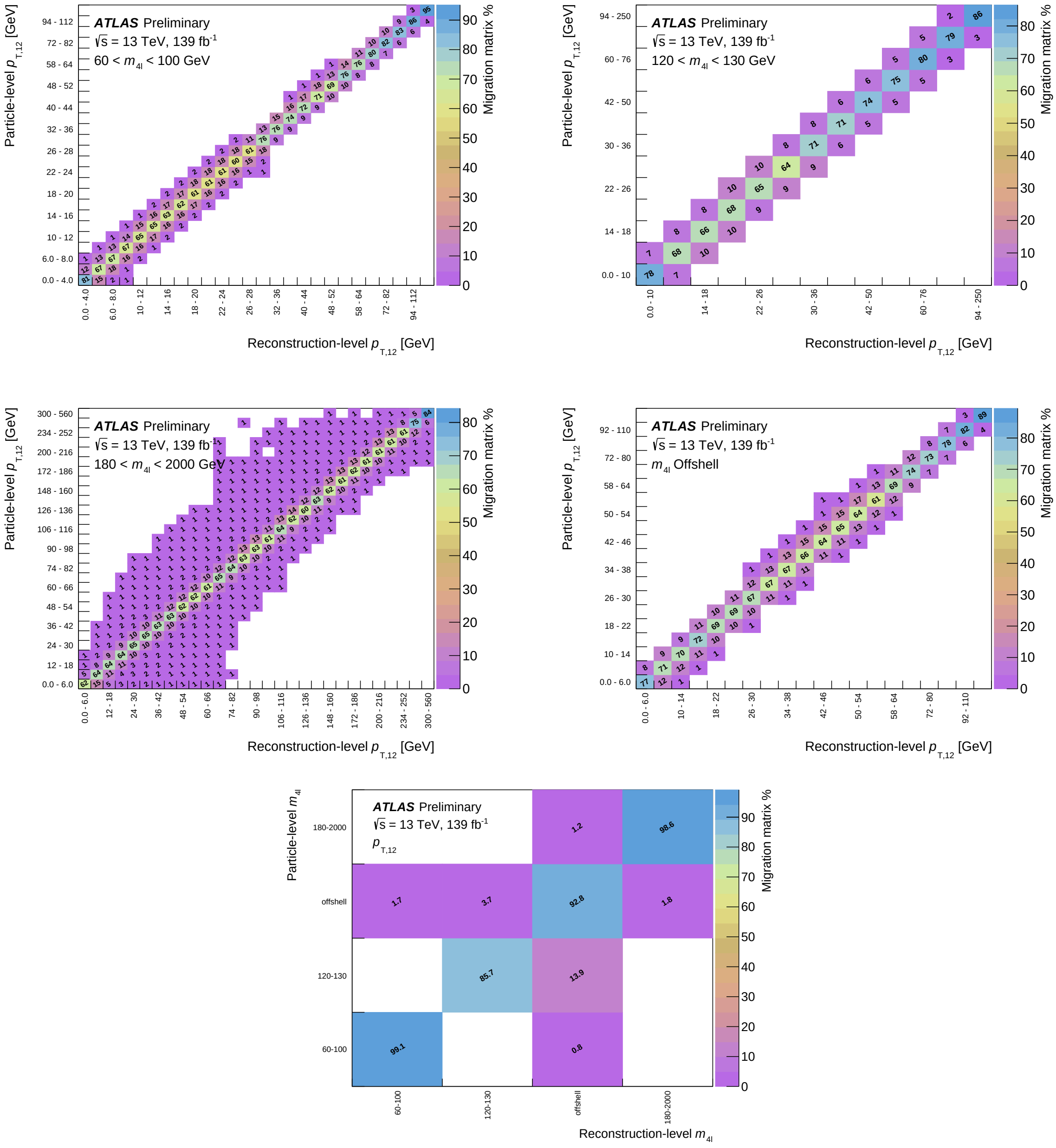

Figure A.19.: Migration matrices for the $p_{\mathrm{T},12}$ bins in each of the $m_{4\ell}$ slices of the $p_{\mathrm{T},12}$-$m_{4\ell}$ distribution and between the slices.

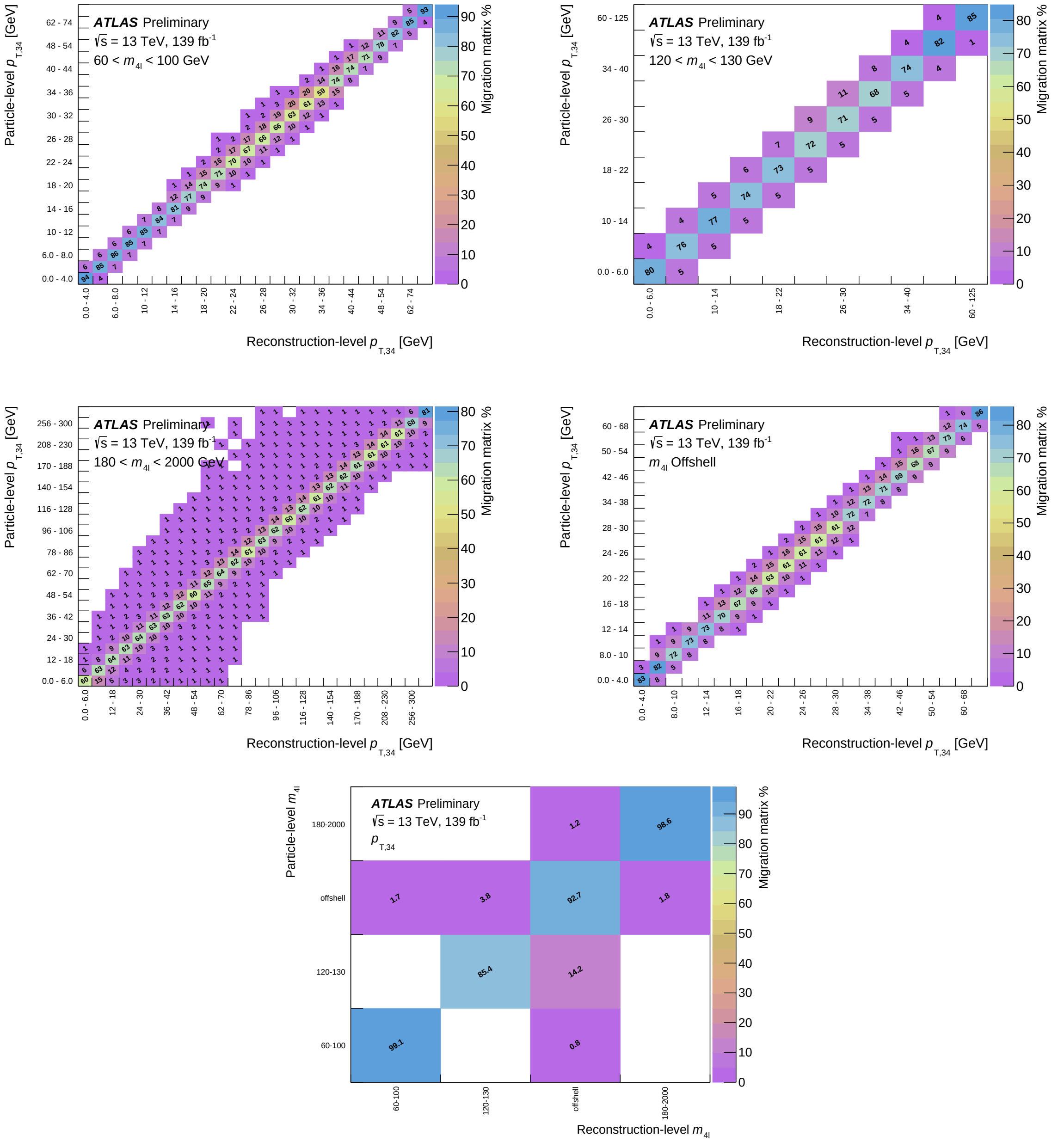

Figure A.20.: Migration matrices of the $p_{\mathrm{T},34}$bins in each of the $m_{4\ell}$slices of the $p_{\mathrm{T},34}$-$m_{4\ell}$distribution and between the slices.

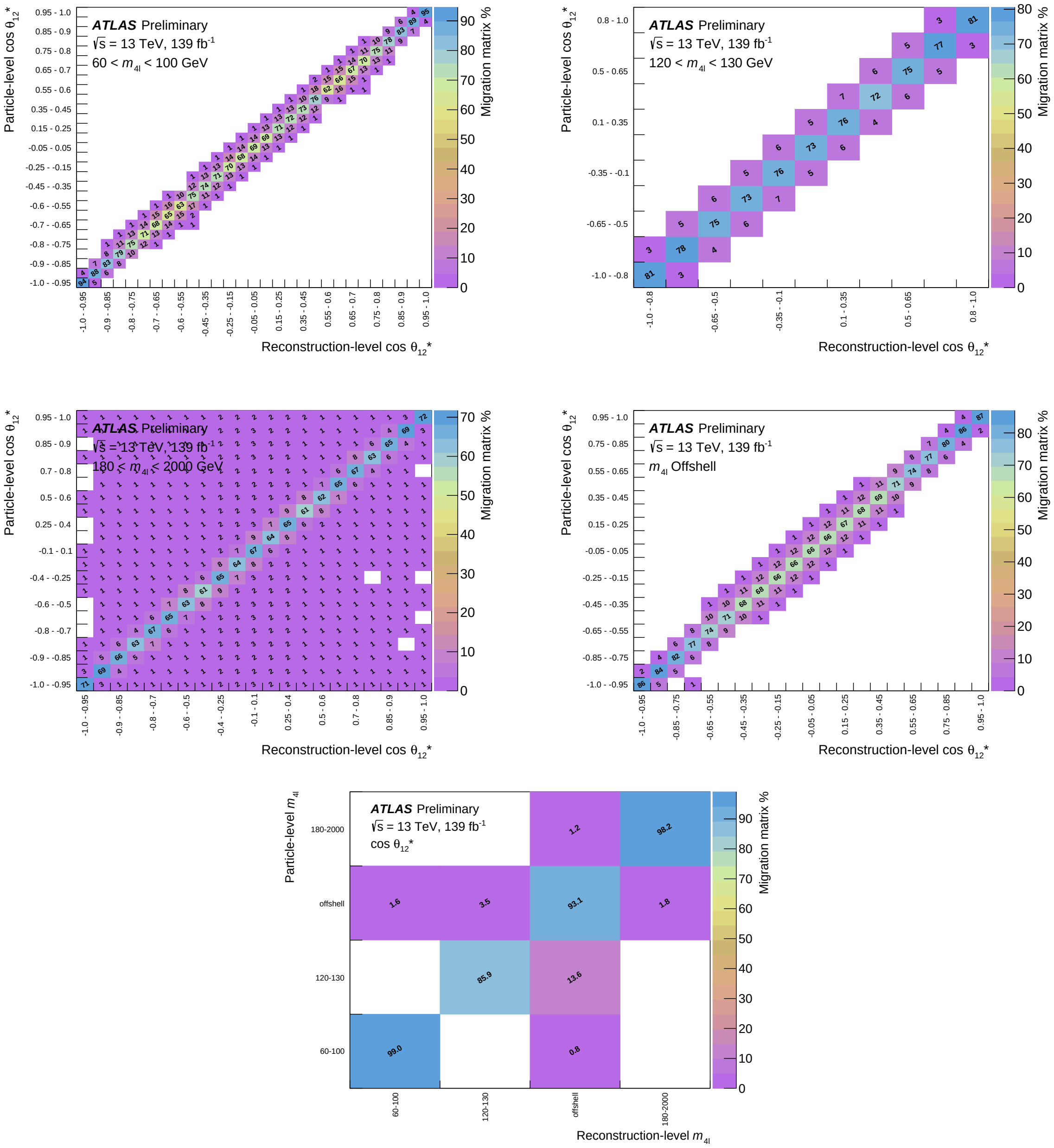

Figure A.21.: Migration matrices for the θ_1^* bins in each of the $m_{4\ell}$slices of the θ_1^*-$m_{4\ell}$distribution and between the slices.

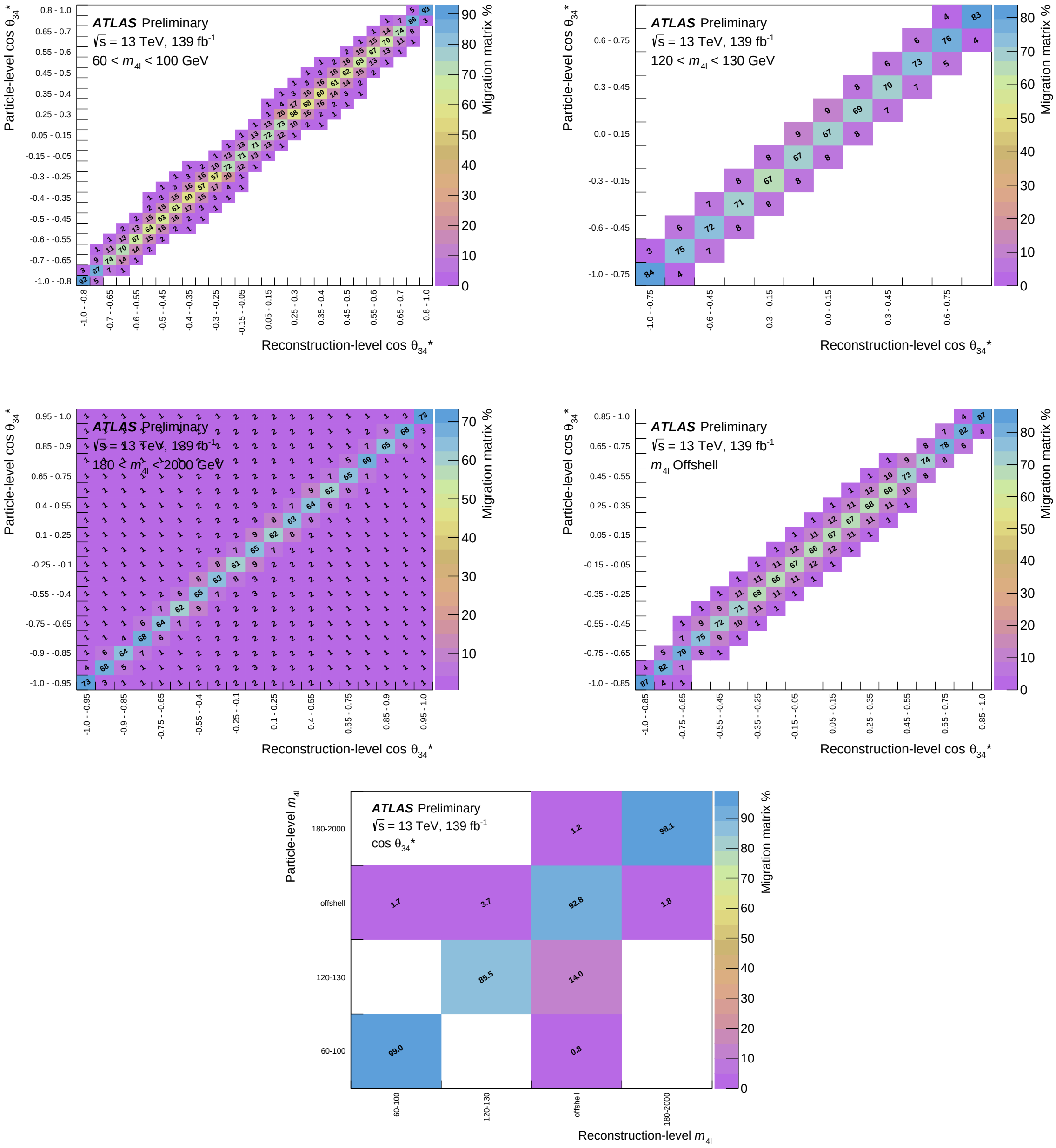

Figure A.22.: Migration matrices for the θ_2^* bins in each of the $m_{4\ell}$slices of the θ_2^*-$m_{4\ell}$distribution and between the slices.

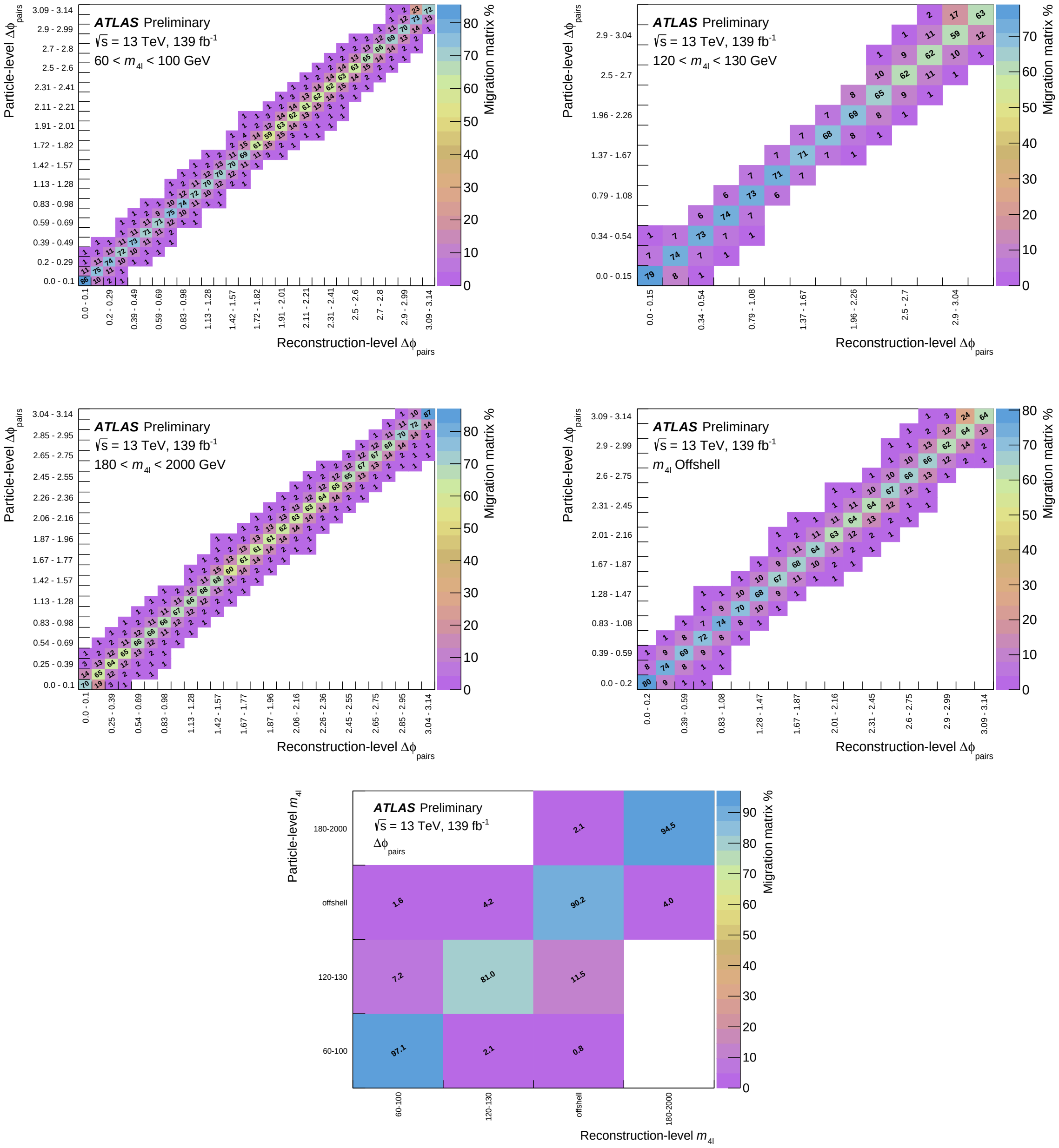

Figure A.23.: Migration matrix for the $|\Delta\phi_{\text{pairs}}|$ bins in each of the $m_{4\ell}$slices of the $|\Delta\phi_{\text{pairs}}|$-$m_{4\ell}$distribution and between the slices.

This appendix includes unfolded systematics for all observables not included in Section 4.9. In some bins, the reducible background systematic uncertainty drops to zero as a result of the prediction being truncated to zero during the background smoothing procedure.

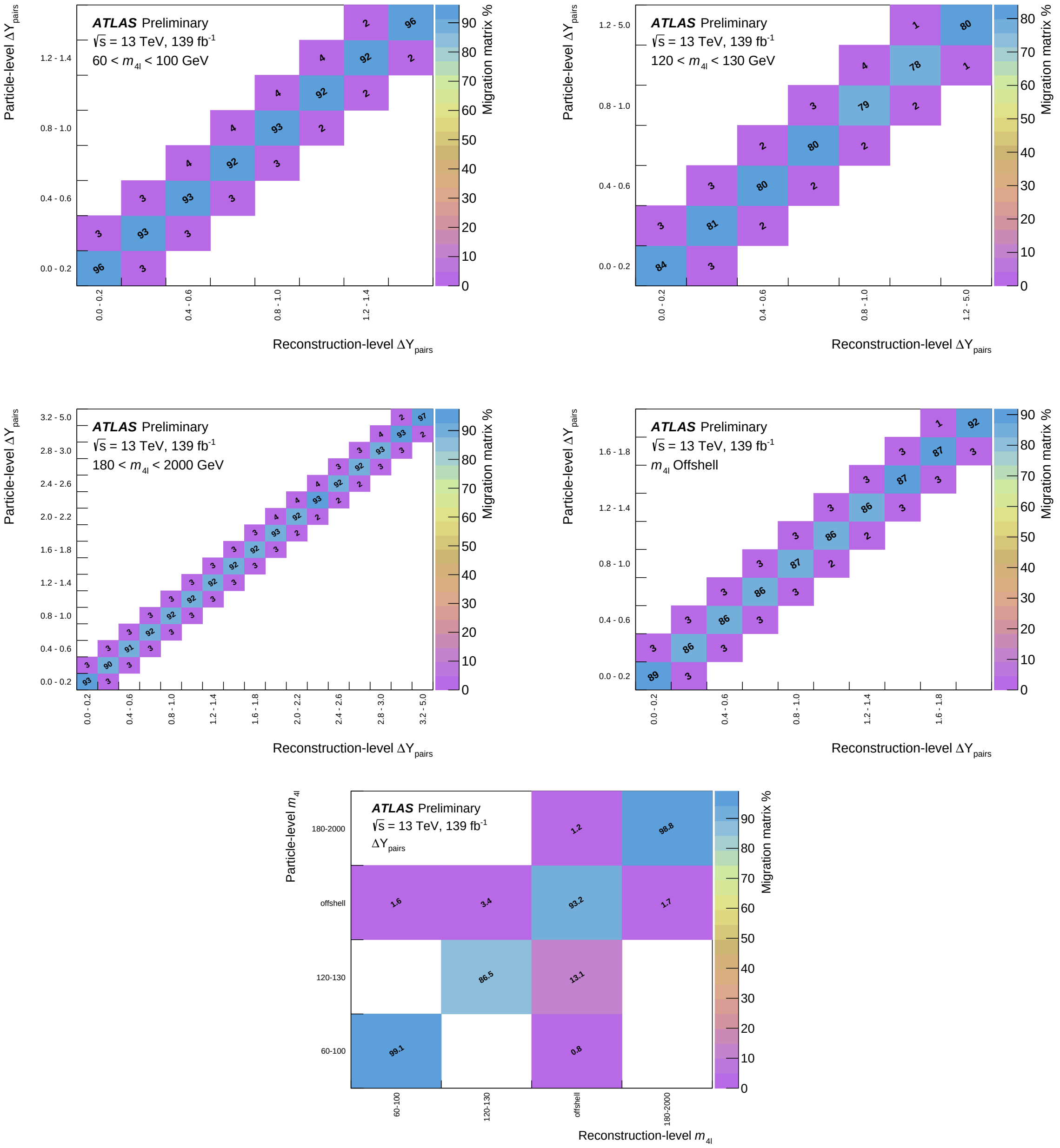

Figure A.24.: Migration matrices for the $|\Delta y_{\text{pairs}}|$bins in each of the $m_{4\ell}$slices of the $|\Delta y_{\text{pairs}}|$-$m_{4\ell}$distribution and between the slices.

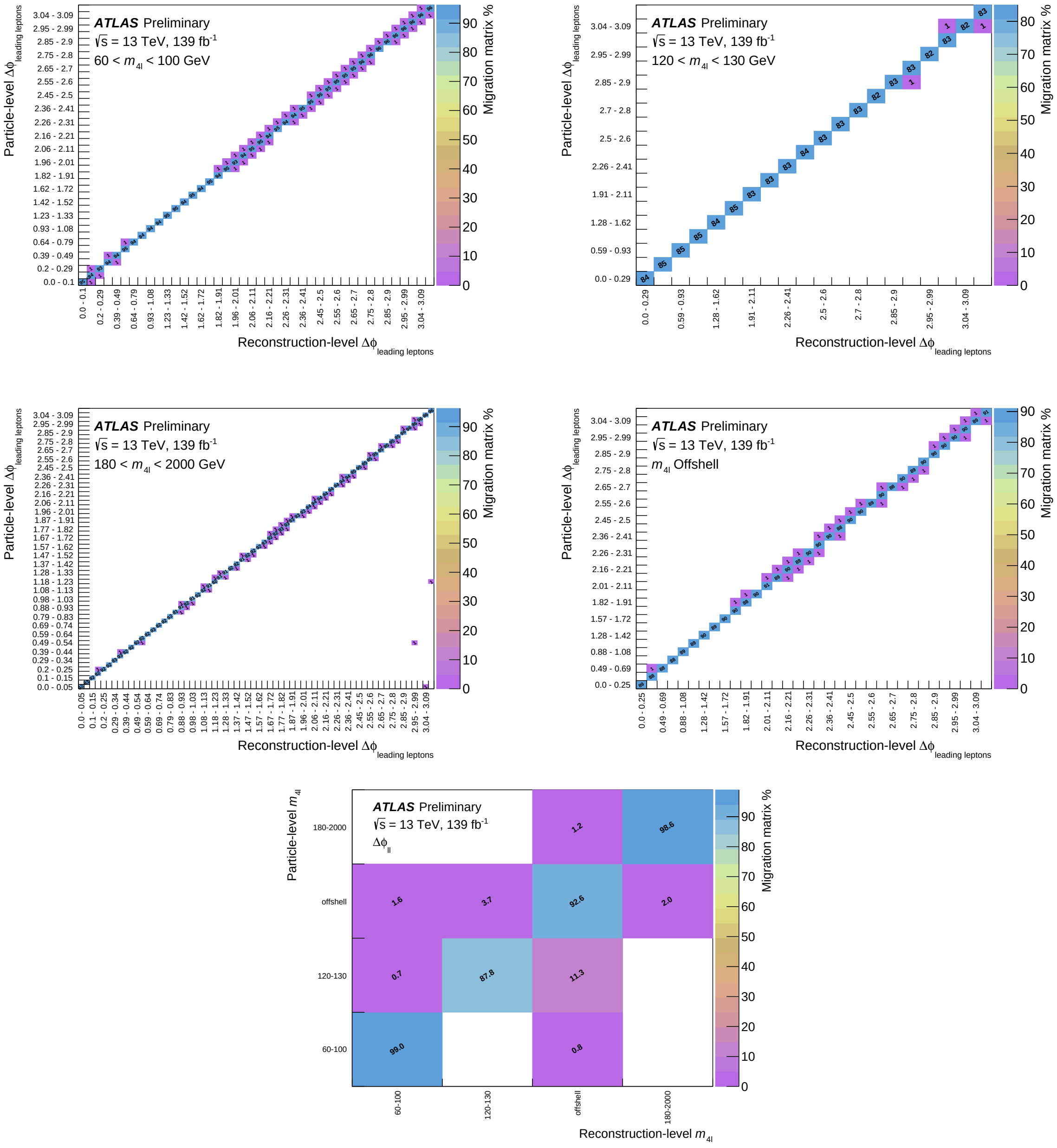

Figure A.25.: Migration matrices for the $|\Delta\phi_{\ell\ell}|$ bins in each of the $m_{4\ell}$slices of the $|\Delta\phi_{\ell\ell}|$-$m_{4\ell}$distribution and between the slices.

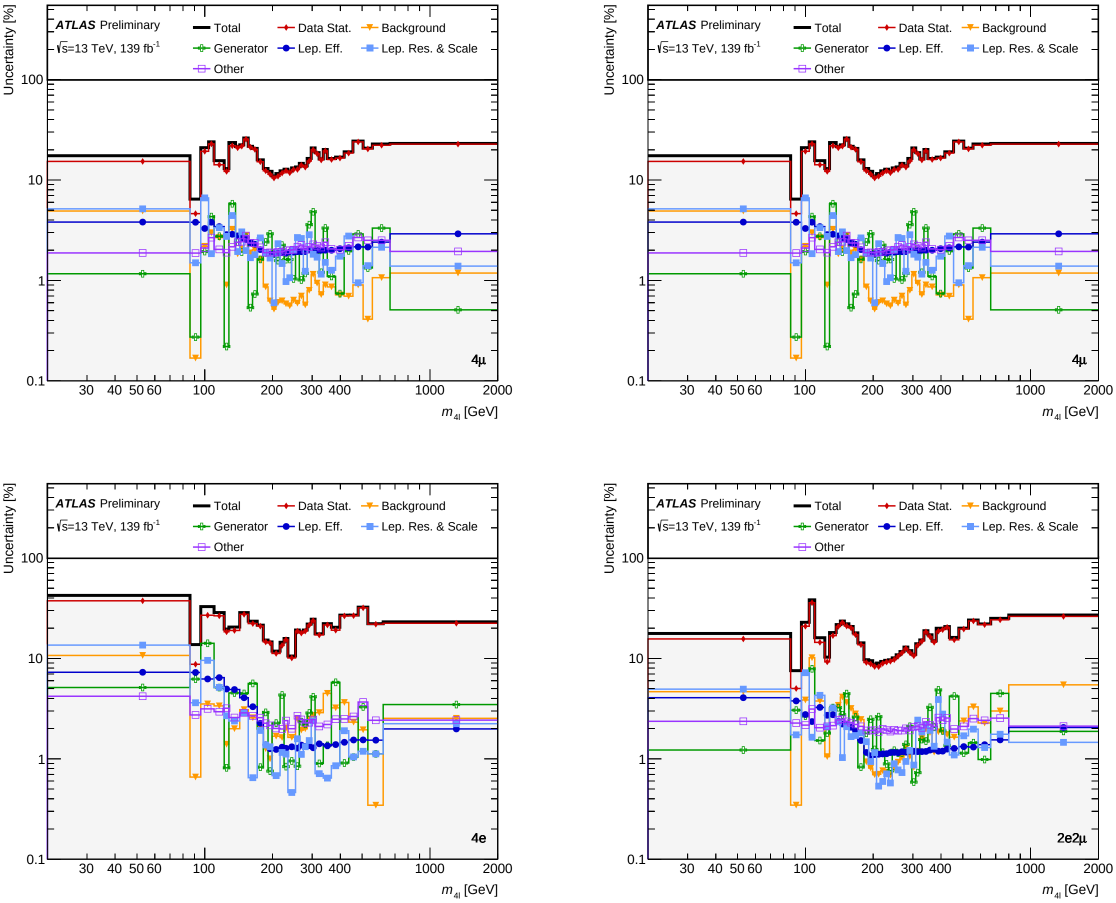

Figure A.26.: Unfolded systematics versus $m_{4\ell}$, in slices of the final-state channel.

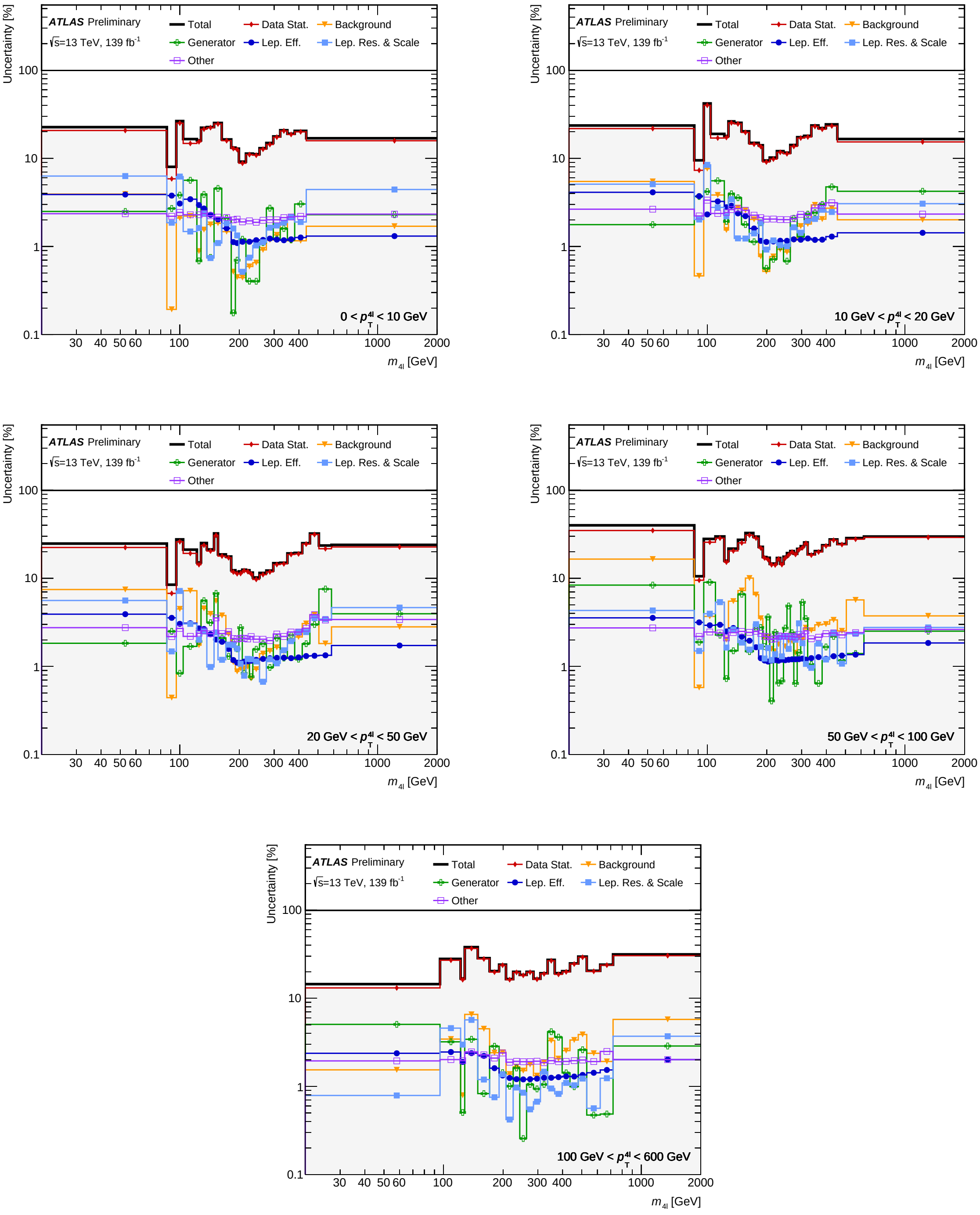

Figure A.27.: Unfolded systematics versus $m_{4\ell}$, in slices of $p_{\mathrm{T},4\ell}$.

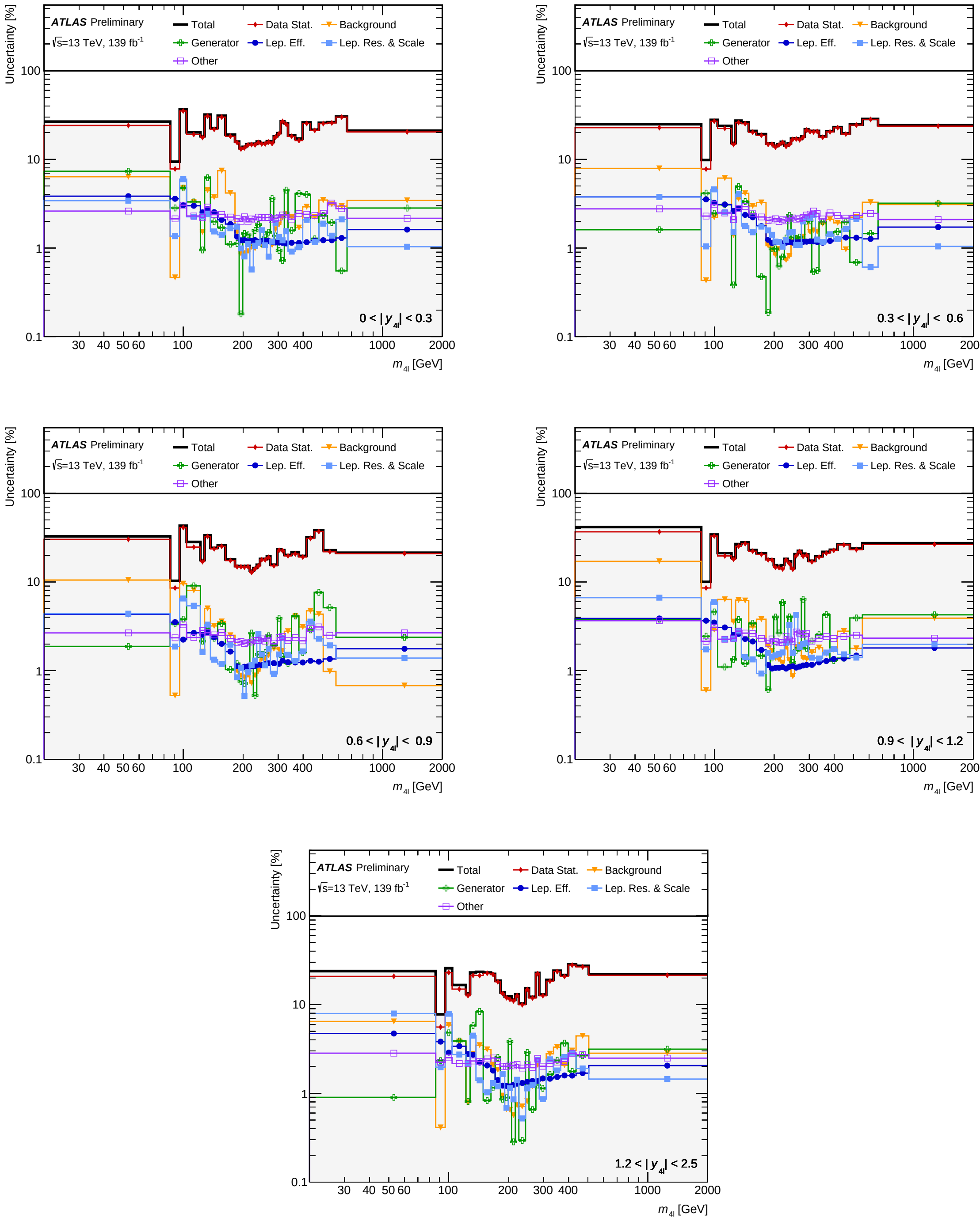

Figure A.28.: Unfolded systematics versus $m_{4\ell}$, in slices of $y_{4\ell}$.

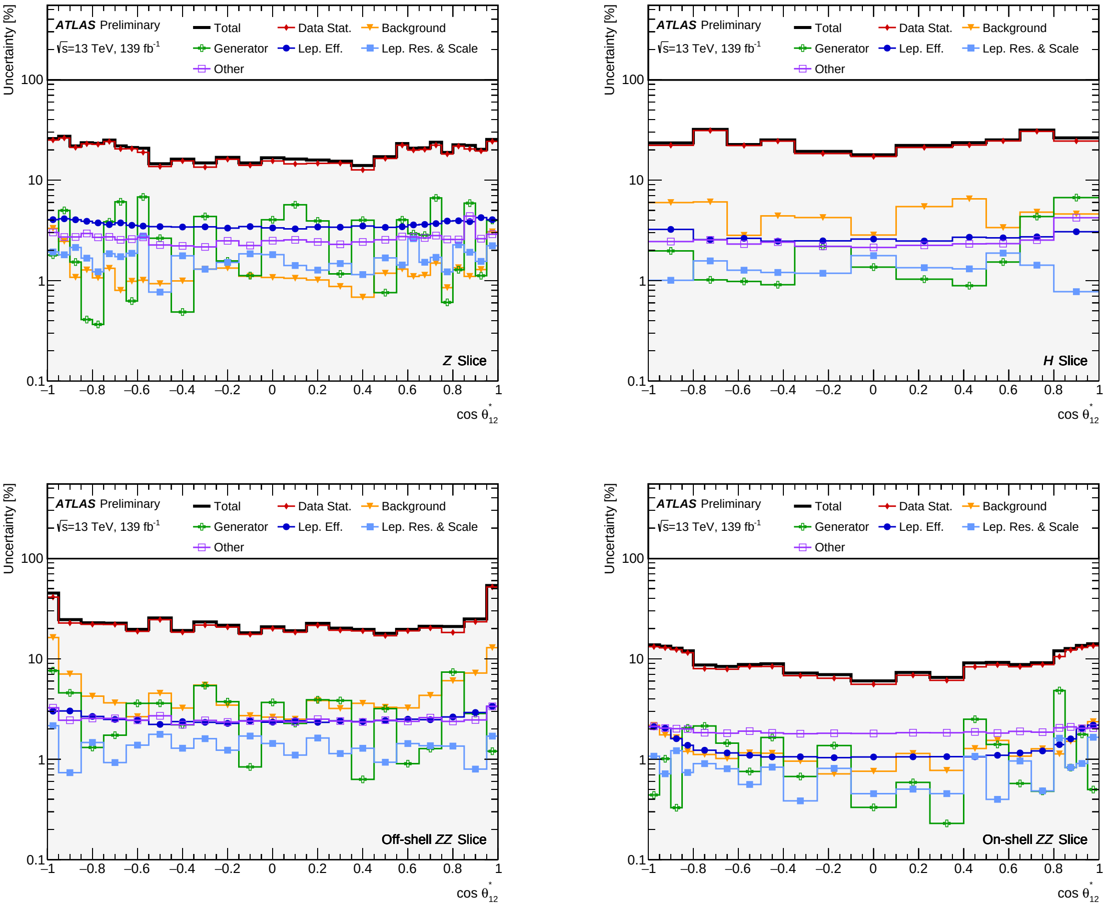

Figure A.29.: Unfolded systematics versus cos θ_1^*, in slices of $m_{4\ell}$.

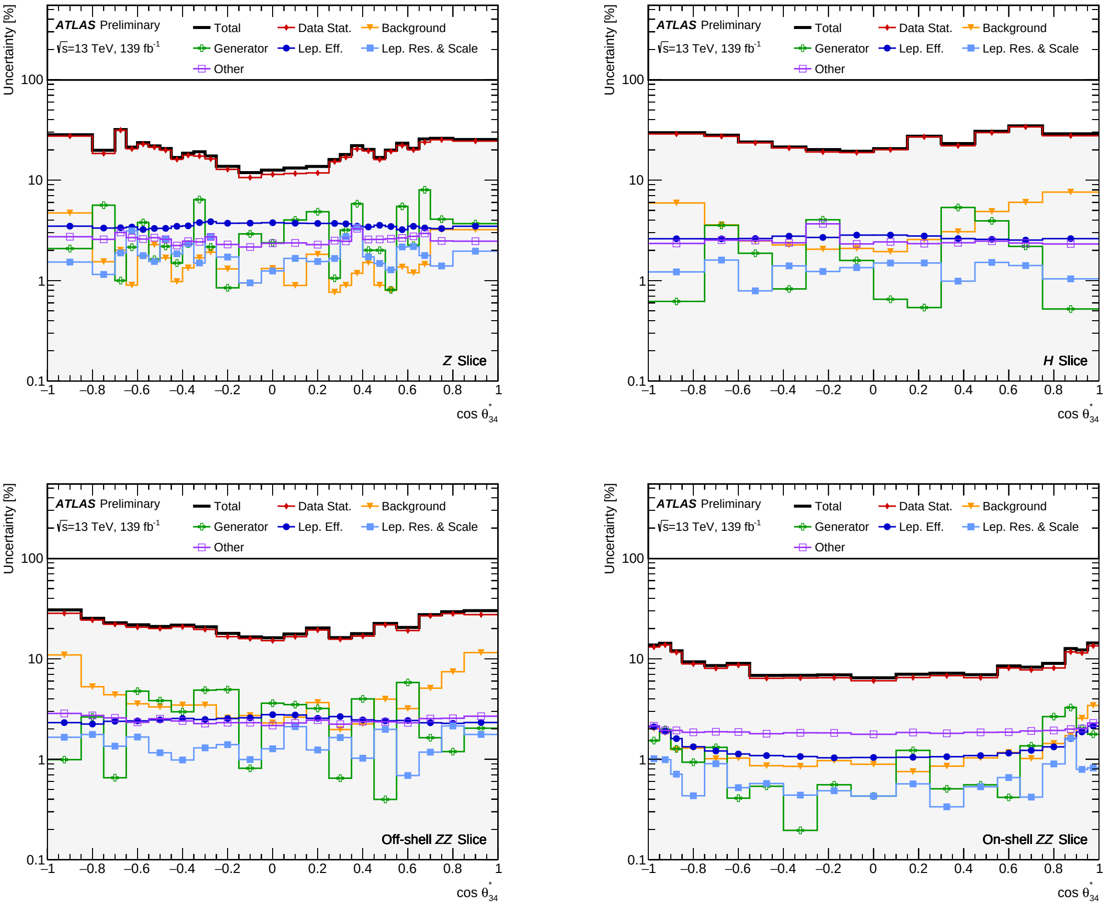

Figure A.30.: Unfolded systematics versus $\cos\theta_2^*$, in slices of $m_{4\ell}$.

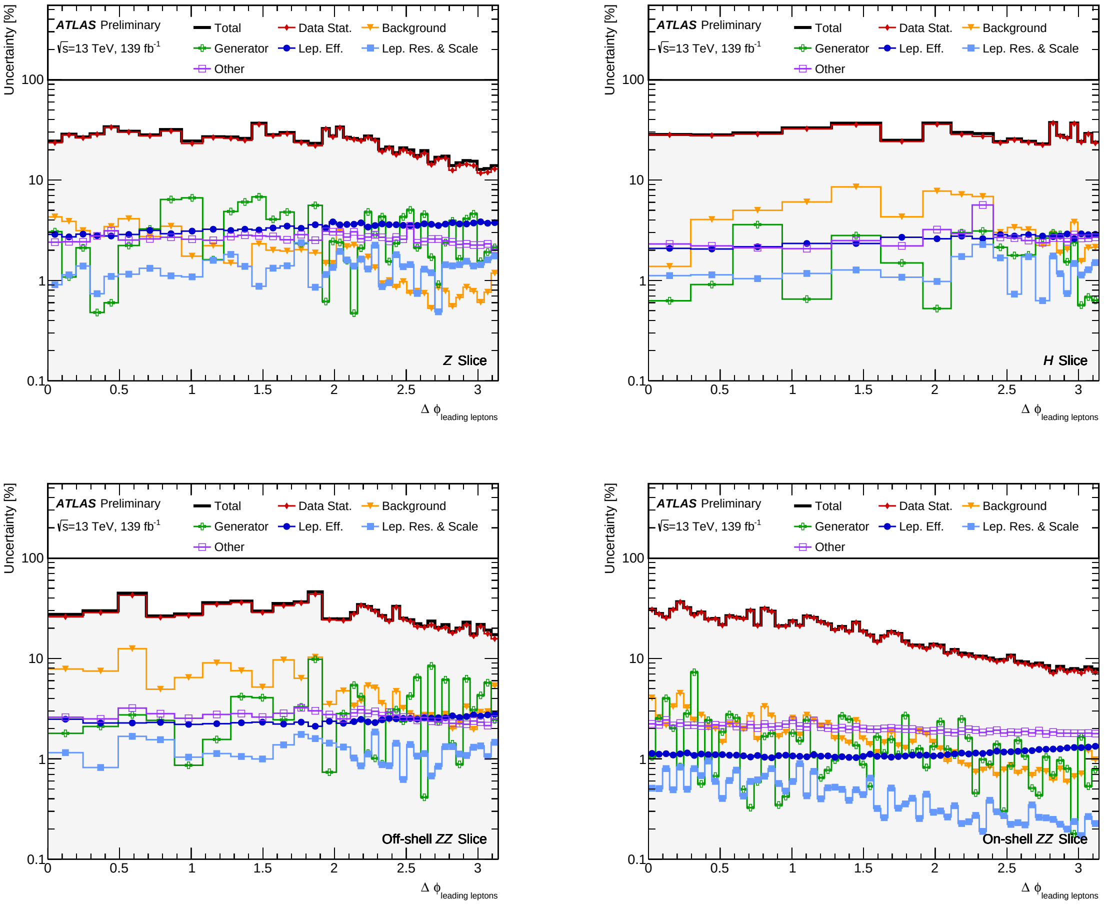

Figure A.31.: Unfolded systematics versus $|\Delta\phi_{\ell\ell}|$, in slices of $m_{4\ell}$.

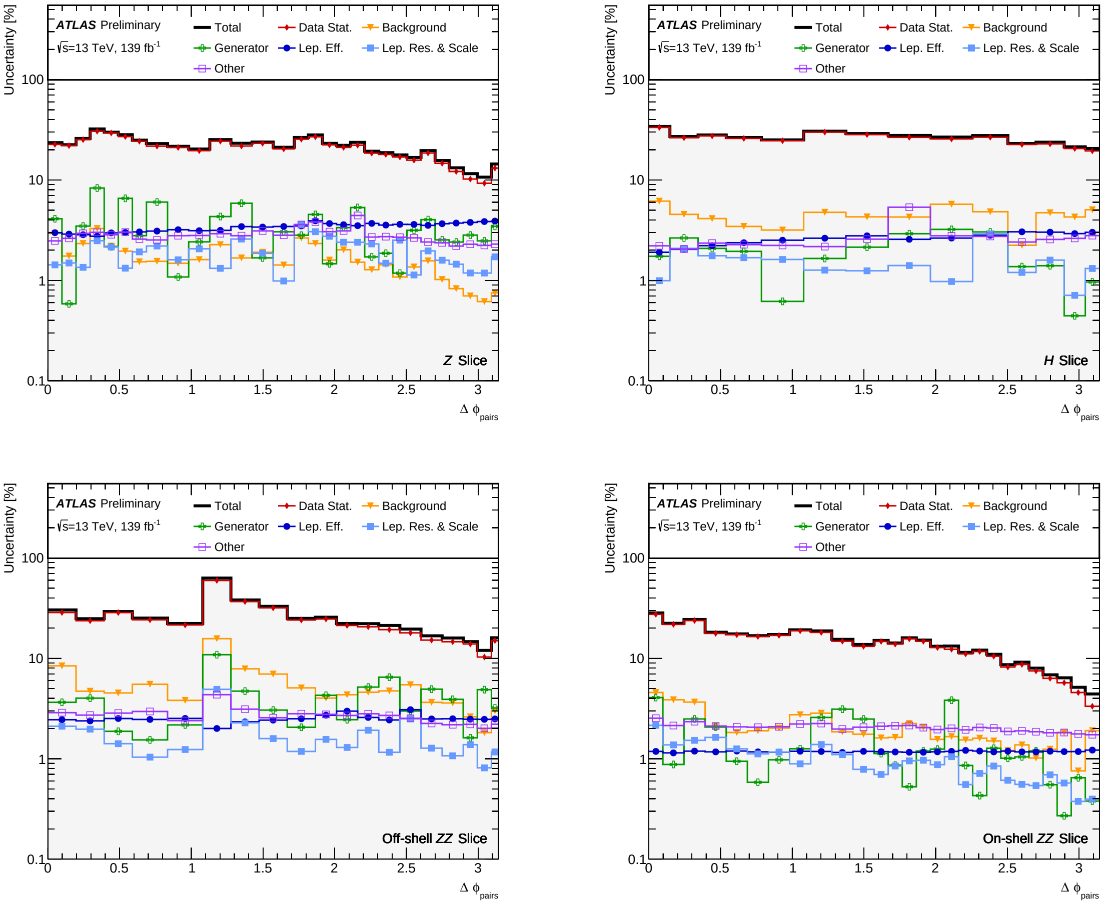

Figure A.32.: Unfolded systematics versus $|\Delta\phi_{\text{pairs}}|$, in slices of $m_{4\ell}$.

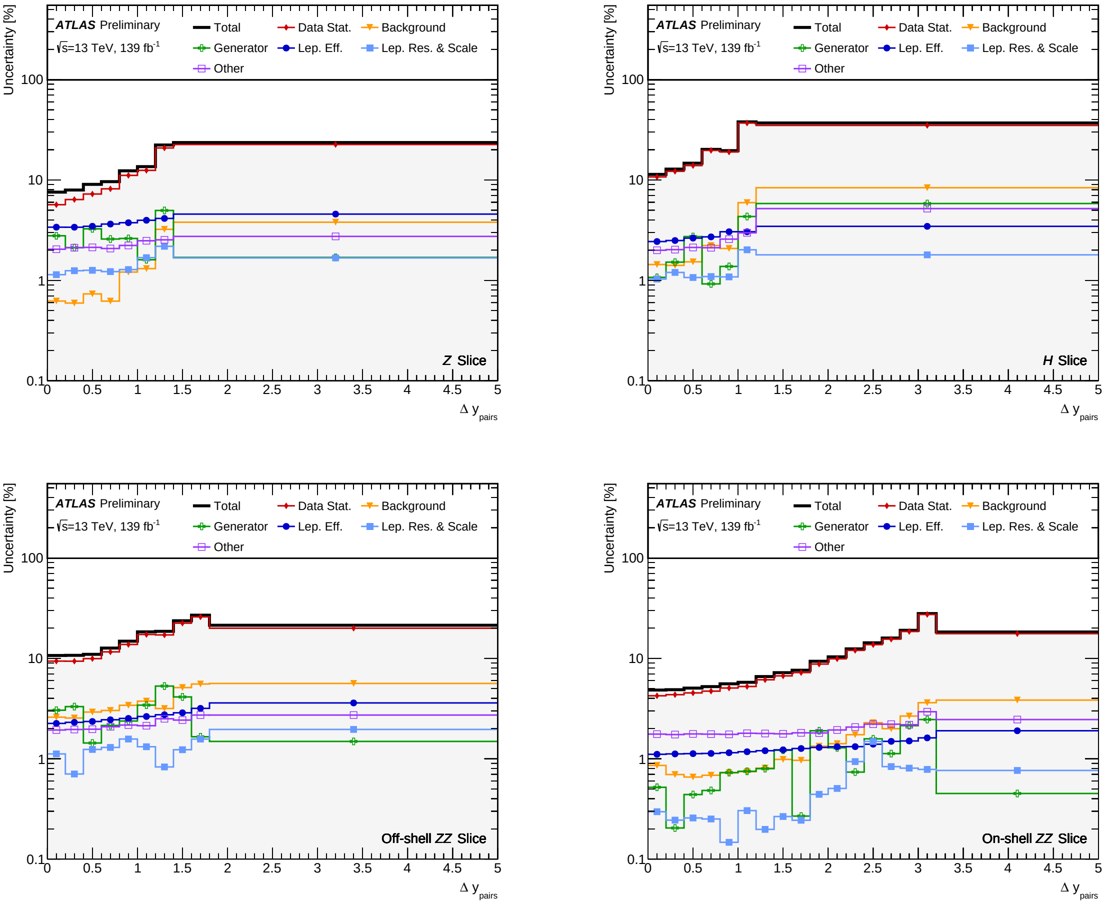

Figure A.33.: Unfolded systematics versus $|\Delta y_{\text{pairs}}|$, in slices of $m_{4\ell}$.

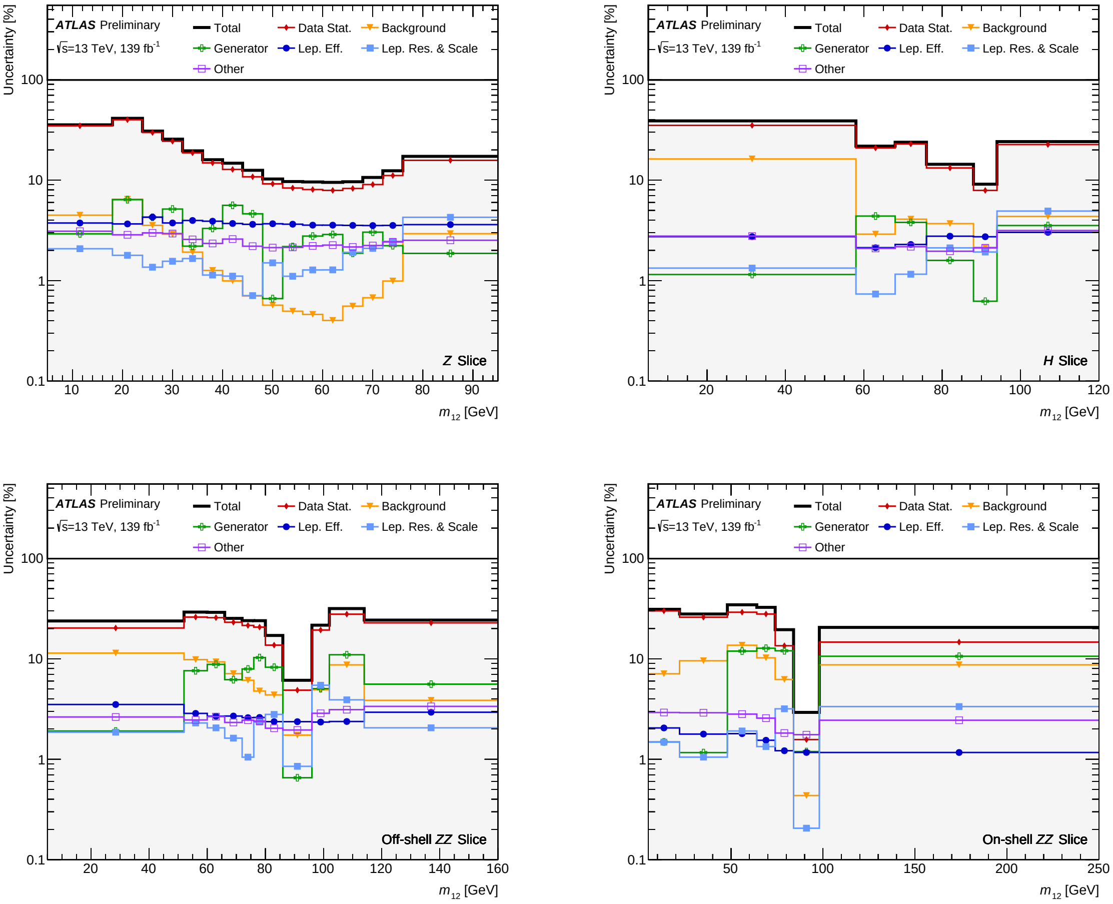

Figure A.34.: Unfolded systematics versus m_{12}, in slices of $m_{4\ell}$.

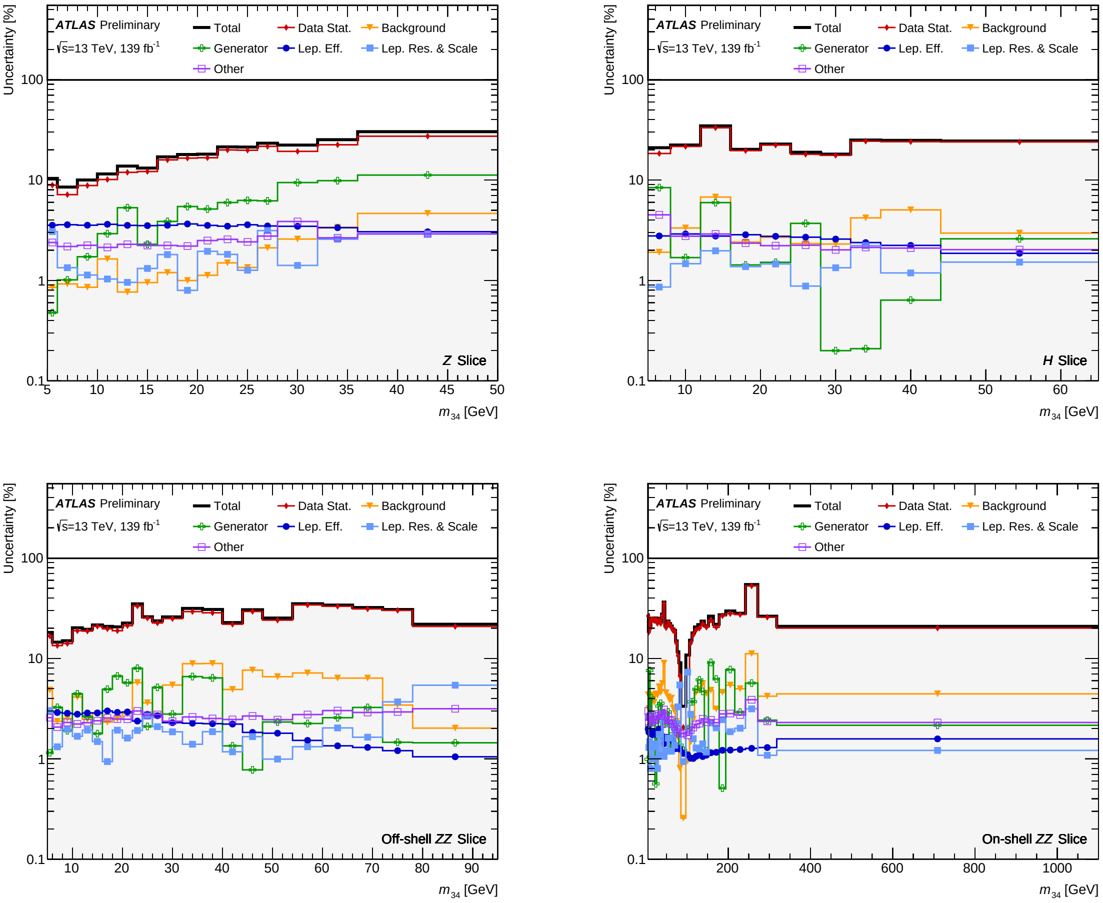

Figure A.35.: Unfolded systematics versus m_{34}, in slices of $m_{4\ell}$.

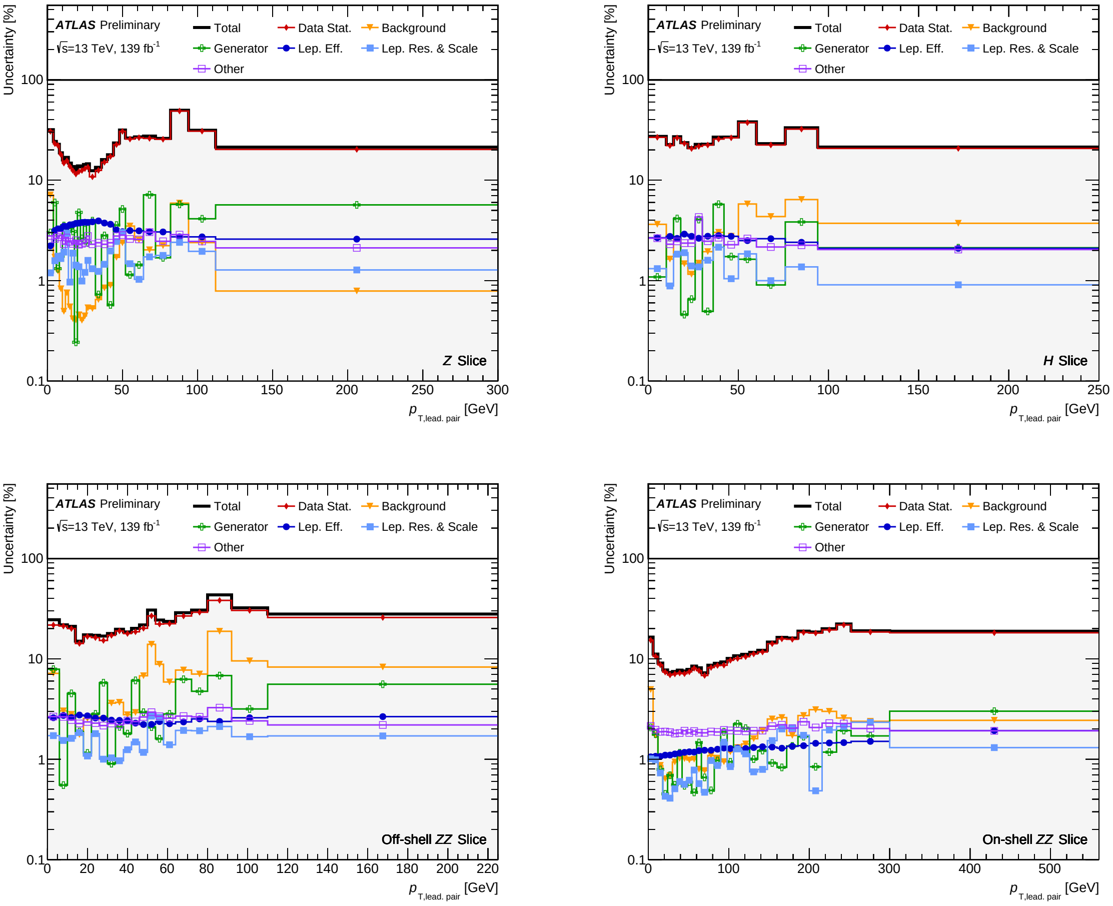

Figure A.36.: Unfolded systematics versus $p_{\mathrm{T},12}$, in slices of $m_{4\ell}$.

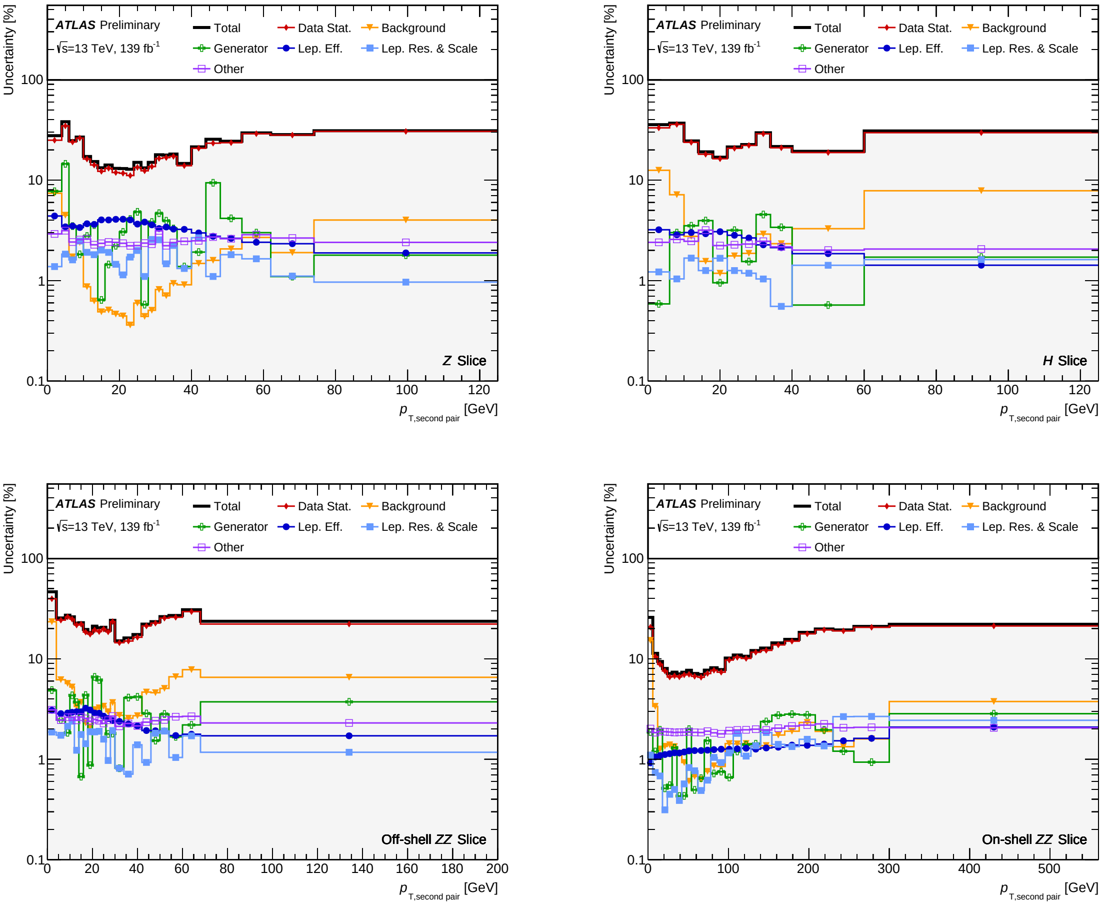

Figure A.37.: Unfolded systematics versus $p_{\mathrm{T},34}$, in slices of $m_{4\ell}$.

Colophon

This thesis was made in $\LaTeX\,2_{\varepsilon}$ using the “hepthesis” class [197]. The bibliography was processed by Biblatex.

Bibliography

[1] Andy Buckley, Jonathan Butterworth, Louie Corpe, Danping Huang, and Puwen Sun. New sensitivity of current LHC measurements to vector-like quarks. *SciPost Physics*, 9(5), Nov 2020.

[2] S. Amrith, J. M. Butterworth, F. F. Deppisch, W. Liu, A. Varma, and D. Yallup. LHC constraints on a $B - L$ gauge model using Contur. *Journal of High Energy Physics*, 2019(5), May 2019.

[3] Dan Ping Huang. Validation of V+jets production in Herwig7 with NLO multi-jet merging. Technical report, CERN, Geneva, Mar 2019. `https://cds.cern.ch/record/2676143`.

[4] David Griffiths. *Introduction to elementary particles*. 2008.

[5] David Galbraith. Standard Model tikz diagram. `http://davidgalbraith.org/portfolio/ux-standard-model-of-the-standard-model/`, 2021.

[6] James T. Wheeler. Noether's theorem. `http://www.physics.usu.edu/Wheeler/ClassicalMechanics/CMNoetherTheorem.pdf`, 2014.

[7] Antonio Pich. The Standard model of electroweak interactions. In *2006 European School of High-Energy Physics*, pages 1–49, 2007.

[8] S. Raby. Family mixing and the origin of mass: The difference between weak eigenstates and mass eigenstates. *Los Alamos Sci.*, 25:72–77, 1997.

[9] P.A. Zyla et al. Review of Particle Physics. *PTEP*, 2020(8):083C01, 2020.

[10] Janosh. The Higgs potential tikz diagram. `https://phoenix.yizimg.com/321HG/tikz/blob/main/assets/higgs-potential`.

[11] Lyndon Evans and Philip Bryant. LHC machine. *Journal of Instrumentation*, 3(08):S08001–S08001, aug 2008.

[12] Esma Mobs. The CERN accelerator complex - 2019. Jul 2019. `https://cds.cern.`

ch/record/2684277.

[13] M. Vretenar. Radio frequency for particle accelerators: evolution and anatomy of a technology. https://arxiv.org/abs/1201.2345, 2012.

[14] ATLAS Collaboration. The new LUCID-2 detector for luminosity measurement and monitoring in ATLAS. *JINST*, 13:P07017. 33 p, 2018.

[15] J. T. Boyd. Lhc run-2 and future prospects, 2020.

[16] ATLAS Collaboration. Luminosity public results run 2. https://twiki.cern.ch/twiki/bin/view/AtlasPublic/LuminosityPublicResultsRun2, 2020.

[17] E. Daw. Rapidity and pseudorapidity. http://www.hep.shef.ac.uk/edaw/PHY206/Site/2012_course_files/phy206rlec7.pdf, 2012.

[18] ETH Zurich. How to draw diagrams in LaTeX with TikZ. http://davidgalbraith.org/portfolio/ux-standard-model-of-the-standard-model/, 2021.

[19] Robert Reed. The Upgrade of the ATLAS Tile Calorimeter Readout Electronics for Phase II. *Journal of Physics Conference Series 1742-6588*, 623, 12 2014.

[20] A. Yamamoto, T. Kondo, Y. Doi, Y. Makida, K. Tanaka, Y. Haruyama, H. Yamaoka, H. Kate, L. Bjorset, K. Wada, S. Meguro, J.S.H. Ross, and K.D. Smith. Design and development of the ATLAS central solenoid magnet. *Applied Superconductivity, IEEE Transactions on*, 9:852 – 855, 07 1999.

[21] M. Capeans, G. Darbo, K. Einsweiller, M. Elsing, T. Flick, M. Garcia-Sciveres, C. Gemme, H. Pernegger, O. Rohne, and R. Vuillermet. ATLAS Insertable B-Layer Technical Design Report. Technical report.

[22] A. Ahmad and Z. Albrechtskirchinger et al. The silicon microstrip sensors of the ATLAS semiconductor tracker. *Nuclear Instruments and Methods in Physics Research Section A: Accelerators, Spectrometers, Detectors and Associated Equipment*, 578(1):98 – 118, 2007.

[23] ATLAS Collaboration. Technical Design Report for the ATLAS Inner Tracker Strip Detector. Technical Report CERN-LHCC-2017-005. ATLAS-TDR-025, CERN, Geneva, Apr 2017. https://cds.cern.ch/record/2257755.

[24] A. Abdesselam and T. Akimoto. The Barrel Modules of the ATLAS Semi-Conductor Tracker. Technical report, CERN, Geneva, Jul 2006. https://cds.cern.ch/record/974073.

[25] A Vogel. ATLAS Transition Radiation Tracker (TRT): Straw Tube Gaseous Detectors at High Rates. Technical report, CERN, Geneva, Apr 2013.

[26] Vitalii L. Ginzburg. Radiation by uniformly moving sources (Vavilov–Cherenkov effect, transition radiation, and other phenomena). *Physics-Uspekhi*, 39(10):973–982, Oct 1996.

[27] W. Lampl. Optimizing the Energy Measurement of the ATLAS Electromagnetic Calorimeter, 2006. `http://cds.cern.ch/record/923625`.

[28] Huaqiao Zhang. The ATLAS liquid argon calorimeter: Overview and performance. *Journal of Physics: Conference Series*, 293:012044, Apr 2011. `https://doi.org/10.1088/1742-6596/293/1/012044`.

[29] Morad Aaboud et al. Operation and performance of the ATLAS Tile Calorimeter in Run 1. *Eur. Phys. J. C*, 78(12):987, 2018.

[30] Sandro Palestini. The muon spectrometer of the ATLAS experiment. *Nuclear Physics B - Proceedings Supplements*, 125:337 – 345, 2003.

[31] S. Levin, N. Amram, R. Ball, and et al. Drift time spectrum and gas monitoring in the atlas muon spectrometer precision chambers. *Nuclear Instruments and Methods in Physics Research Section A: Accelerators, Spectrometers, Detectors and Associated Equipment*, 588(3):347 – 358, 2008.

[32] E. Etzion, Y. Benhammou, J. Ginzburg, M. Ishino, L. Levinson, G. Mikenberg, N. Panikashvili, D. Primor, and V. Smakhtin. The certification of ATLAS thin gap chambers produced in Israel and China. *IEEE Symposium Conference Record Nuclear Science 2004*. `http://dx.doi.org/10.1109/NSSMIC.2004.1462188`.

[33] Koichi Nagai. Thin gap chambers in ATLAS. *Nuclear Instruments and Methods in Physics Research Section A: Accelerators, Spectrometers, Detectors and Associated Equipment*, 384(1):219 – 221, 1996. BEAUTY '96.

[34] Diagram of the ATLAS Muon Spectrometer. `https://mediaarchive.cern.ch/MediaArchive/Photo/Public/2008/0803017/0803017_01/0803017_01-A4-at-144-dpi.jpg`, 2021.

[35] H. J. Herman. The superconducting magnet system for the ATLAS Detector at CERN. *IEEE Transactions on Applied Superconductivity*, 10(1):347–352, 2000.

[36] Quantum diaries. Atlas magnets. `https://www.quantumdiaries.org/wp-content/uploads/2011/05/exp-magnets.png`, 2021.

[37] Martin zur Nedden. The Run-2 ATLAS Trigger System: Design, Performance and Plan. Technical report, CERN, Geneva, Dec 2016.

[38] ATLAS collaboration. Performance of the ATLAS muon triggers in Run 2. *JINST*, 15:60, Apr 2020.

[39] F. Winklmeier. Real-time configuration changes of the atlas high level trigger. In *2010 17th IEEE-NPSS Real Time Conference*, pages 1–5, 2010.

[40] ATLAS Collaboration. Performance of the ATLAS Inner Detector Track and Vertex Reconstruction in the High Pile-Up LHC Environment. Technical Report ATLAS-CONF-2012-042, CERN, Geneva, Mar 2012. `https://cds.cern.ch/record/1435196`.

[41] P. F. Åkesson, T. Atkinson, and M. J. Costa et al. ATLAS Tracking Event Data Model. Technical report, CERN, Geneva, Jul 2006. `https://cds.cern.ch/record/973401`.

[42] ATLAS Collaboration. Reconstruction of primary vertices at the ATLAS experiment in Run 1 proton–proton collisions at the LHC. *The European Physical Journal C*, 77(5), May 2017.

[43] G Piacquadio, K Prokofiev, and A Wildauer. Primary vertex reconstruction in the ATLAS experiment at LHC. *Journal of Physics: Conference Series*, 119(3):032033, jul 2008.

[44] ATLAS Collaboration. Topological cell clustering in the ATLAS calorimeters and its performance in LHC Run 1. *The European Physical Journal C*, 77(7), Jul 2017.

[45] W Lampl, S Laplace, D Lelas, P Loch, H Ma, S Menke, S Rajagopalan, D Rousseau, S Snyder, and G Unal. Calorimeter Clustering Algorithms: Description and Performance. Technical Report ATL-LARG-PUB-2008-002. ATL-COM-LARG-2008-003, CERN, Geneva, Apr 2008.

[46] ATLAS Collaboration. Electron and photon reconstruction and performance in ATLAS using a dynamical, topological cell clustering-based approach. Technical report, CERN, Geneva, Dec 2017. `https://cds.cern.ch/record/2298955`.

[47] ATLAS Collaboration. Electron reconstruction and identification in the ATLAS experiment using the 2015 and 2016 LHC proton–proton collision data at $\sqrt{s} = 13$ TeV. *The European Physical Journal C*, 79(8), Aug 2019.

[48] ATLAS Collaboration. Improved electron reconstruction in ATLAS using the

Gaussian Sum Filter-based model for bremsstrahlung. Technical Report ATLAS-CONF-2012-047, CERN, Geneva, May 2012. `https://cds.cern.ch/record/1449796`.

[49] ATLAS Collaboration. Electron and photon performance measurements with the ATLAS detector using the 2015–2017 LHC proton-proton collision data. *Journal of Instrumentation*, 14(12):P12006–P12006, Dec 2019.

[50] ATLAS Collaboration. Measurements of Higgs boson production and couplings in the four-lepton channel inppcollisions at center-of-mass energies of 7 and 8 TeV with the ATLAS detector. *Physical Review D*, 91(1), Jan 2015.

[51] ATLAS Collaboration. Measurement of the muon reconstruction performance of the ATLAS detector using 2011 and 2012 LHC proton–proton collision data. *The European Physical Journal C*, 74(11), Nov 2014.

[52] ATLAS Collaboration. Performance of electron and photon triggers in ATLAS during LHC Run 2. *The European Physical Journal C*, 80(1), Jan 2020.

[53] ATLAS Collaboration. Muon reconstruction performance of the atlas detector in proton–proton collision data at $\sqrt{s}$ =13 tev. *The European Physical Journal C*, 76(5), May 2016.

[54] John Ottersbach. *Muons in early ATLAS Data: from first collisions to W^+W^- production*. PhD thesis, U. Amsterdam, IHEF, 2012.

[55] ATLAS Collaboration. Muon reconstruction efficiency and momentum resolution of the ATLAS experiment in proton–proton collisions at $\sqrt{s} = 7$ TeV in 2010. *The European Physical Journal C*, 74(9), Sep 2014.

[56] ATLAS Collaboration. Muon reconstruction performance of the ATLAS detector in proton–proton collision data at $\sqrt{s}$ = 13 TeV. *The European Physical Journal C*, 76(5), May 2016.

[57] Nikolay P. Zotov. Small x physics and hard QCD processes at LHC, 2012. `https://arxiv.org/abs/1201.4144`.

[58] E W Nigel Glover and Jochum J Van der Bij. Z-boson pair production via gluon fusion. *Nucl. Phys. B*, 321(CERN-TH-5248-88):561–590. 44 p, Dec 1988.

[59] M. Becker, W. Buttinger, C. Geng, E. Nurse, O. Penc, S. Richter, J. Rosten, E. Skorda, K. Kordas, A. Leisos, and B. Zhou. Differential $ZZ \to 4\ell$ cross section measurements and aTGC search in 13 TeV proton-proton collisions with the AT-

LAS detector. Technical Report ATL-COM-PHYS-2016-1584, CERN, Geneva, Nov 2016. https://cds.cern.ch/record/2230817.

[60] John M. Campbell, R. Keith Ellis, Michal Czakon, and Sebastian Kirchner. Two loop correction to interference in gg $\to$ zz. *Journal of High Energy Physics*, 2016(8), Aug 2016.

[61] G. Cacciapaglia, A. Deandrea, G. D. La Rochelle, and J. B. Flament. Higgs Couplings: Disentangling New Physics with Off-Shell Measurements. *Physical Review Letters*, 113(20), Nov 2014.

[62] Fabrizio Caola and Kirill Melnikov. Constraining the Higgs boson width with ZZ production at the LHC. *Physical Review D*, 88(5), Sep 2013.

[63] ATLAS Collaboration. Measurement of the four-lepton invariant mass spectrum in 13 TeV proton-proton collisions with the ATLAS detector. Technical report, CERN, 2019. https://cds.cern.ch/record/2659410?ln=en.

[64] CMS Collaboration. Measurements of the $pp \to ZZ$ production cross section and the Z $\to 4\ell$ branching fraction, and constraints on anomalous triple gauge couplings at $\sqrt{s} = 13$ TeV. *The European Physical Journal C*, 78(2), Feb 2018.

[65] ATLAS Collaboration. $ZZ \to 4\ell$ cross-section measurements and search for anomalous triple gauge couplings in $\sqrt{s} = 13$ TeV pp collisions with the ATLAS detector. *Physical Review D*, 97(3), Feb 2018.

[66] Z. J. Grout, M. Goblirsch-Kolb, P. Bhattarai, J. Butterworth, L. D. Corpe, D. P. Huang, X. Liu, E. Nurse, A. Pilkington, Z. Michael Schillaci, M. Vozak, R. Wang, Y. Wu, L. Xu, J. J. Junggeburth, Z. Zhao, and B. Zhou. Unfolded four lepton mass and angular distributions. Technical report, CERN, Geneva, Dec 2019. https://cds.cern.ch/record/2704274.

[67] ATLAS Collaboration. Measurements of differential cross-sections in four-lepton events in 13 tev proton-proton collisions with the atlas detector. *Journal of High Energy Physics*, 2021(5), Jul 2021.

[68] Deepak Kar. *Experimental Particle Physics*. 2053-2563. IOP Publishing, 2019. http://dx.doi.org/10.1088/2053-2563/ab1be6.

[69] ATLAS Collaboration. Fiducial and differential cross sections of Higgs boson production measured in the four-lepton decay channel in pp collisions at $\sqrt{s}$=8 TeV with the ATLAS detector. *Phys. Lett.*, B738:234–253, 2014.

[70] ATLAS Collaboration. Measurements of four-lepton production in pp collisions at $\sqrt{s} = 8$ TeV with the ATLAS detector. *Phys. Lett.*, B753:552–572, 2016.

[71] Johannes Bellm et al. Herwig 7.1 Release Note. Technical report, 2017. https://arxiv.org/abs/1705.06919.

[72] Torbjorn Sjöstrand, Stephen Mrenna, and Peter Z. Skands. PYTHIA 6.4 physics and manual. *Journal of High Energy Physics*, 05:026, 2006.

[73] T. Gleisberg, Stefan. Hoeche, F. Krauss, M. Schonherr, S. Schumann, F. Siegert, and J. Winter. Event generation with SHERPA 1.1. *Journal of High Energy Physics*, 02:007, 2009.

[74] Michael H. Seymour and Marilyn Marx. Monte Carlo Event Generators, 2013. https://arxiv.org/abs/1304.6677.

[75] Stefan Höche. Introduction to parton-shower event generators, 2015. https://arxiv.org/abs/1411.4085.

[76] P.A. Zyla et al. Review of Particle Physics. *PTEP*, 2020(8):083C01, 2020.

[77] Michiel Botje. Lecture notes Particle Physics II, Quantum Chromo Dynamics, The QCD improved Parton Model, Dec 2013. https://www.nikhef.nl/~h24/qcdcourse/section-9.pdf.

[78] Ringaile Placakyte. Parton distribution functions, 2011. https://arxiv.org/abs/1111.5452.

[79] Christian Gütschow. Monte Carlo for the LHC. https://www.hep.ucl.ac.uk/postgrad/teaching/lhc/MC_2017.pdf, 2017.

[80] Zoltán Nagy and Davison E. Soper. What is a parton shower? *Phys. Rev. D*, 98:014034, Jul 2018.

[81] Grazia Cabras. Measurement of the $ZH(H \to b\bar{b})$ associated production with $Z \to \ell^+\ell^-$ in pp collisions at $\sqrt{s} = 13$ TeV with the ATLAS Experiment, 2019. https://cds.cern.ch/record/2743914.

[82] Johannes Bellm et al. Herwig 7.2 Release Note. 2019.

[83] Enrico Bothmann et al. Event generation with Sherpa 2.2. *SciPost Phys.*, 7(3):034, 2019.

[84] Richard D. Ball et al. Parton distributions for the LHC run II. *Journal of High Energy Physics*, 04:040, 2015.

[85] Tanju Gleisberg and Stefan Höche. Comix, a new matrix element generator. *Journal of High Energy Physics*, 12:039, 2008.

[86] Stefan Hoeche, Frank Krauss, Marek Schonherr, and Frank Siegert. A critical appraisal of NLO+PS matching methods. *JHEP*, 09:049, 2012.

[87] S. Catani, F. Krauss, R. Kuhn, and B. R. Webber. QCD Matrix Elements + Parton Showers. *Journal of High Energy Physics*, 11:063, 2001.

[88] Stefan Hoeche, Frank Krauss, Steffen Schumann, and Frank Siegert. QCD matrix elements and truncated showers. *Journal of High Energy Physics*, 05:053, 2009.

[89] Simone Alioli, Paolo Nason, Carlo Oleari, and Emanuele Re. A general framework for implementing NLO calculations in shower Monte Carlo programs: the POWHEG BOX. *Journal of High Energy Physics*, 06:043, 2010.

[90] Tom Melia, Paolo Nason, Raoul Röntsch, and Giulia Zanderighi. W^+W^- , WZ and ZZ production in the POWHEG BOX. *Journal of High Energy Physics*, 11:078, 2011.

[91] Paolo Nason and Giulia Zanderighi. W^+W^- , WZ and ZZ production in the POWHEG-BOX-V2. *Eur. Phys. J. C*, 74(1):2702, 2014.

[92] ATLAS Collaboration. Measurement of the Z/γ boson transverse momentum distribution in pp collisions at $\sqrt{s} = 7$ TeV with the ATLAS detector. *Journal of High Energy Physics*, 2014(9), Sep 2014.

[93] F. Cascioli, T. Gehrmann, M. Grazzini, S. Kallweit, P. Maierhöfer, A. von Manteuffel, S. Pozzorini, D. Rathlev, L. Tancredi, and E. Weihs. ZZ production at hadron colliders in NNLO QCD. *Phys. Lett. B*, 735:311–313, 2014.

[94] Massimiliano Grazzini, Stefan Kallweit, and Dirk Rathlev. ZZ production at the LHC: Fiducial cross sections and distributions in NNLO QCD. *Phys. Lett. B*, 750:407–410, 2015.

[95] Massimiliano Grazzini, Stefan Kallweit, and Marius Wiesemann. Fully differential NNLO computations with MATRIX. *Eur. Phys. J. C*, 78(7):537, 2018.

[96] Stefan Kallweit and Marius Wiesemann. ZZ production at the LHC: NNLO predictions for $2\ell 2\nu$ and 4ℓ signatures. *Phys. Lett. B*, 786:382–389, 2018.

[97] John M. Campbell, R. Keith Ellis, and Ciaran Williams. Vector boson pair production at the LHC. *Journal of High Energy Physics*, 07:018, 2011.

[98] Giampiero Passarino. Higgs CAT. *Eur. Phys. J. C*, 74:2866, 2014.

[99] D. de Florian et al. Handbook of LHC Higgs Cross Sections: 4. Deciphering the Nature of the Higgs Sector. 2016. `https://inspirehep.net/literature/1494411`.

[100] Jon Butterworth and Stefano et al. Carrazza. PDF4LHC recommendations for LHC Run II. *Journal of Physics G: Nuclear and Particle Physics*, 43(2):023001, Jan 2016.

[101] Keith Hamilton, Paolo Nason, Emanuele Re, and Giulia Zanderighi. NNLOPS simulation of Higgs boson production. *Journal of High Energy Physics*, 10:222, 2013.

[102] Keith Hamilton, Paolo Nason, and Giulia Zanderighi. Finite quark-mass effects in the NNLOPS POWHEG+MiNLO Higgs generator. *Journal of High Energy Physics*, 05:140, 2015.

[103] Paolo Nason. A new method for combining NLO QCD with shower Monte Carlo algorithms. *Journal of High Energy Physics*, 11:040, 2004.

[104] Stefano Frixione, Paolo Nason, and Carlo Oleari. Matching NLO QCD computations with Parton Shower simulations: the POWHEG method. *Journal of High Energy Physics*, 11:070, 2007.

[105] Torbjörn Sjöstrand, Stefan Ask, Jesper R. Christiansen, Richard Corke, Nishita Desai, Philip Ilten, Stephen Mrenna, Stefan Prestel, Christine O. Rasmussen, and Peter Z. Skands. An introduction to PYTHIA 8.2. *Comput. Phys. Commun.*, 191:159–177, 2015.

[106] C. Anastasiou, C. Duhr, et al. High precision determination of the gluon fusion Higgs boson cross-section at the LHC. *Journal of High Energy Physics*, 05:058, 2016.

[107] Charalampos Anastasiou, Claude Duhr, Falko Dulat, Franz Herzog, and Bernhard Mistlberger. Higgs Boson Gluon-Fusion Production in QCD at Three Loops. *Phys. Rev. Lett.*, 114:212001, 2015.

[108] Falko Dulat, Achilleas Lazopoulos, and Bernhard Mistlberger. iHixs 2 – Inclusive Higgs cross sections. *Comput. Phys. Commun.*, 233:243–260, 2018.

[109] Robert V. Harlander and Kemal J. Ozeren. Finite top mass effects for hadronic Higgs production at next-to-next-to-leading order. *Journal of High Energy Physics*, 11:088, 2009.

[110] Robert V. Harlander and Kemal J. Ozeren. Top mass effects in Higgs production at

next-to-next-to-leading order QCD: Virtual corrections. *Phys. Lett. B*, 679:467–472, 2009.

[111] Robert V. Harlander, Hendrik Mantler, Simone Marzani, and Kemal J. Ozeren. Higgs production in gluon fusion at next-to-next-to-leading order QCD for finite top mass. *Eur. Phys. J. C*, 66:359–372, 2010.

[112] Alexey Pak, Mikhail Rogal, and Matthias Steinhauser. Finite top quark mass effects in NNLO Higgs boson production at LHC. *Journal of High Energy Physics*, 02:025, 2010.

[113] Stefano Actis, Giampiero Passarino, Christian Sturm, and Sandro Uccirati. NLO electroweak corrections to Higgs boson production at hadron colliders. *Phys. Lett. B*, 670:12–17, 2008.

[114] Stefano Actis, Giampiero Passarino, Christian Sturm, and Sandro Uccirati. NNLO computational techniques: The cases $H \to \gamma\gamma$ and $H \to gg$. *Nucl. Phys. B*, 811:182–273, 2009.

[115] Marco Bonetti, Kirill Melnikov, and Lorenzo Tancredi. Higher order corrections to mixed QCD-EW contributions to Higgs boson production in gluon fusion. *Phys. Rev. D*, 97(5):056017, 2018.

[116] Paolo Nason and Carlo Oleari. NLO Higgs boson production via vector-boson fusion matched with shower in POWHEG. *Journal of High Energy Physics*, 02:037, 2010.

[117] M. Ciccolini, Ansgar Denner, and S. Dittmaier. Strong and Electroweak Corrections to the Production of Higgs + 2 Jets via Weak Interactions at the Large Hadron Collider. *Phys. Rev. Lett.*, 99:161803, 2007.

[118] Mariano Ciccolini, Ansgar Denner, and Stefan Dittmaier. Electroweak and QCD corrections to Higgs production via vector-boson fusion at the CERN LHC. *Phys. Rev. D*, 77:013002, 2008.

[119] Paolo Bolzoni, Fabio Maltoni, Sven-Olaf Moch, and Marco Zaro. Higgs Boson Production via Vector-Boson Fusion at Next-to-Next-to-Leading Order in QCD. *Phys. Rev. Lett.*, 105:011801, 2010.

[120] M. L. Ciccolini, S. Dittmaier, and M. Krämer. Electroweak radiative corrections to associated WH and ZH production at hadron colliders. *Phys. Rev. D*, 68:073003, 2003.

[121] Oliver Brein, Abdelhak Djouadi, and Robert Harlander. NNLO QCD corrections to the Higgs-strahlung processes at hadron colliders. *Phys. Lett. B*, 579:149–156, 2004.

[122] Oliver Brein, Robert Harlander, Marius Wiesemann, and Tom Zirke. Top-quark mediated effects in hadronic Higgs-Strahlung. *Eur. Phys. J. C*, 72:1868, 2012.

[123] Ansgar Denner, Stefan Dittmaier, Stefan Kallweit, and Alexander Mück. HAWK 2.0: A Monte Carlo program for Higgs production in vector-boson fusion and Higgs strahlung at hadron colliders. *Comput. Phys. Commun.*, 195:161–171, 2015.

[124] Oliver Brein, Robert V. Harlander, and Tom J. E. Zirke. VH@NNLO – Higgs Strahlung at hadron colliders. *Comput. Phys. Commun.*, 184:998–1003, 2013.

[125] ATLAS Collaboration. Search for Higgs boson pair production in the $b\bar{b}$ final state with 13 TeV pp collision data collected by the ATLAS experiment. *Journal of High Energy Physics*, 2018(11), Nov 2018.

[126] J. Alwall, R. Frederix, S. Frixione, V. Hirschi, F. Maltoni, O. Mattelaer, H. S. Shao, T. Stelzer, P. Torrielli, and M. Zaro. The automated computation of tree-level and next-to-leading order differential cross sections, and their matching to parton shower simulations. *Journal of High Energy Physics*, 07:079, 2014.

[127] S Agostinelli. Geant4–a simulation toolkit. *Nuclear Instruments and Methods in Physics Research Section A: Accelerators, Spectrometers, Detectors and Associated Equipment*, 506(3):250–303, 2003.

[128] Erich W. Varnes. A poisson likelihood approach to fake lepton estimation with the matrix method, 2016. https://arxiv.org/abs/1606.06817v1.

[129] ATLAS collaboration. Estimation of non-prompt and fake lepton backgrounds in final states with top quarks produced in proton-proton collisions at $\sqrt{s} = 8$ TeV with the ATLAS detector. Technical report, CERN, Geneva, Oct 2014. https://cds.cern.ch/record/1951336.

[130] G. D'Agostini. A multidimensional unfolding method based on bayes' theorem. *Nuclear Instruments and Methods in Physics Research Section A: Accelerators, Spectrometers, Detectors and Associated Equipment*, 362(2):487–498, 1995.

[131] Evaluating statistical uncertainties and correlations using the bootstrap method. Technical report, CERN, Geneva, Apr 2021. https://cds.cern.ch/record/2759945.

[132] Jay Orear. Notes on statistics for physicists, revised. http://ned.ipac.caltech.edu/level5/Sept01/Orear/frames.html.

[133] Klaus Reygers and Sebastian Neubert. Statistical methods in particle physics. https://www.physi.uni-heidelberg.de/~reygers/lectures/2017/smipp/stat_methods_ss2017_03_uncertainties.pdf, 2017.

[134] Roger Barlow. Systematic errors: facts and fictions, 2002. https://arxiv.org/abs/hep-ex/0207026.

[135] Luminosity determination in pp collisions at $\sqrt{s} = 13$ TeV using the ATLAS detector at the LHC. Technical report, CERN, Geneva, Jun 2019.

[136] G Avoni, M Bruschi, et al. The new LUCID-2 detector for luminosity measurement and monitoring in ATLAS. *JINST*, 13:P07017. 33 p, 2018.

[137] The ATLAS Collaboration. Measurement of the cross section for inclusive isolated-photon production in pp collisions at $\sqrt{s} = 13$ TeV using the ATLAS detector. *Physics Letters B*, 770:473–493, 2017.

[138] Glenn Cowan. Some statistical tools for particle physics. https://www.pp.rhul.ac.uk/~cowan/stat/cowan_munich16.pdf, 2016.

[139] Ansgar Denner and Giovanni Pelliccioli. Polarized electroweak bosons in W^+W production at the LHC including NLO QCD effects. *Journal of High Energy Physics*, 2020(9), Sep 2020.

[140] Christian Gütschow and Marek Schönherr. Four lepton production and the accuracy of QED FSR. *The European Physical Journal C*, 81(1), Jan 2021.

[141] ATLAS Collaboration. Measurement of $W^\pm$ and Z-boson production cross sections in pp collisions at $\sqrt{s} = 13$ TeV with the ATLAS detector. *Physics Letters B*, 759:601–621, Aug 2016.

[142] ATLAS Collaboration. Measurements of four-lepton production at the z resonance in pp collisions $\sqrt{s} = 7$ and 8 tev with atlas. *Physical Review Letters*, 112(23), Jun 2014.

[143] Andrea De Simone and Thomas Jacques. Simplified models vs. effective field theory approaches in dark matter searches. *The European Physical Journal C*, 76(7), Jul 2016.

[144] Johann Brehmer. Higgs effective field theory lecture notes, January 2016. https://www.thphys.uni-heidelberg.de/~gk_ppbsm/lib/exe/fetch.

php?media=students:lectures:student_lecture_eft.pdf.

[145] S Weinberg. Baryon- and lepton-nonconserving processes. *Phys. Rev. Lett. (United States)*, 11 1979.

[146] André de Gouvêa, Juan Herrero-García, and Andrew Kobach. Neutrino masses, grand unification, and baryon number violation. *Physical Review D*, 90(1), Jul 2014.

[147] Andrew Kobach. Baryon number, lepton number, and operator dimension in the standard model. *Physics Letters B*, 758:455–457, Jul 2016.

[148] B. Grzadkowski, M. Iskrzyński, M. Misiak, and J. Rosiek. Dimension-six terms in the Standard Model Lagrangian. *Journal of High Energy Physics*, 2010(10), Oct 2010.

[149] Ilaria Brivio, Yun Jiang, and Michael Trott. The SMEFTsim package, theory and tools. *Journal of High Energy Physics*, 2017(12), Dec 2017.

[150] Glen Cowan, Kyle Cranmer, Eilam Gross, and Ofer Vitells. Asymptotic formulae for likelihood-based tests of new physics. *The European Physical Journal C*, 71(2), Feb 2011.

[151] ATLAS Collaboration. Higgs boson production cross-section measurements and their EFT interpretation in the 4ℓ decay channel at $\sqrt{s} = 13$ TeV with the ATLAS detector. *Eur. Phys. J. C*, 80(10):957, 2020.

[152] John Ellis, Christopher W. Murphy, Verónica Sanz, and Tevong You. Updated global SMEFT fit to Higgs, diboson and electroweak data. *Journal of High Energy Physics*, 06:146, 2018.

[153] Waleed Abdallah et al. Reinterpretation of LHC Results for New Physics: Status and Recommendations after Run 2. 3 2020. https://arxiv.org/abs/2003.07868.

[154] Adam Alloul, Neil D. Christensen, Céline Degrande, Claude Duhr, and Benjamin Fuks. FeynRules 2.0 - A complete toolbox for tree-level phenomenology. *Comput. Phys. Commun.*, 185:2250–2300, 2014.

[155] Celine Degrande, Claude Duhr, Benjamin Fuks, David Grellscheid, Olivier Mattelaer, and Thomas Reiter. UFO - The Universal FeynRules Output. *Comput. Phys. Commun.*, 183:1201–1214, 2012.

[156] M. Bahr et al. Herwig++ Physics and Manual. *Eur. Phys. J.*, C58:639–707, 2008.

[157] A. Buckley, J. M. Butterworth, L. Corpe, M. Habedank, D. Huang, D. Yallup, M. Altakach, G. Bassman, I. Lagwankar, J. Rocamonde, H. Saunders, B. Waugh, and G. Zilgalvis. Testing new-physics models with global comparisons to collider measurements: the Contur toolkit. *SciPost Phys. Core*, 4:13, 2021.

[158] Andy Buckley, Jonathan Butterworth, Leif Lonnblad, David Grellscheid, Hendrik Hoeth, et al. Rivet user manual. *Comput.Phys.Commun.*, 184:2803–2819, 2013.

[159] Jon Butterworth. Personal communication.

[160] Eamonn Maguire, Lukas Heinrich, and Graeme Watt. HEPData: a repository for high energy physics data. *J. Phys. Conf. Ser.*, 898(10):102006, 2017.

[161] J. A. Aguilar-Saavedra, R. Benbrik, S. Heinemeyer, and M. Pérez-Victoria. Handbook of vectorlike quarks: Mixing and single production. *Physical Review D*, 88(9), Nov 2013.

[162] Oliver Witzel. Review on composite higgs models, 2019. `https://arxiv.org/abs/1901.08216`.

[163] Mathieu Buchkremer, Giacomo Cacciapaglia, Aldo Deandrea, and Luca Panizzi. Model-independent framework for searches of top partners. *Nuclear Physics B*, 876(2):376–417, Nov 2013.

[164] ATLAS Collaboration. Combination of the Searches for Pair-Produced Vectorlike Partners of the Third-Generation Quarks at $\sqrt{s} = 13$ TeV with the ATLAS Detector. *Physical Review Letters*, 121(21), Nov 2018.

[165] CMS Collaboration. Search for vector-like T and B quark pairs in final states with leptons at $\sqrt{s} = 13$ TeV. *Journal of High Energy Physics*, 2018(8), Aug 2018.

[166] ATLAS Collaboration. Combination of the searches for pair-produced vector-like partners of the third-generation quarks at $\sqrt{s} = 13$ TeV with the ATLAS detector. *Phys. Rev. Lett.*, 121(21):211801, 2018.

[167] ATLAS Collaboration. Measurement of the transverse momentum and ϕ^*_η distributions of Drell–Yan lepton pairs in proton–proton collisions at $\sqrt{s} = 8$ TeV with the ATLAS detector. *Eur. Phys. J.*, C76(5):291, 2016.

[168] ATLAS Collaboration. Measurement of the k_t splitting scales in $Z \to \ell\ell$ events in pp collisions at $\sqrt{s} = 8$ TeV with the ATLAS detector. *Journal of High Energy Physics*, 08:026, 2017.

[169] ATLAS Collaboration. Measurements of the production cross section of a Z boson

in association with jets in pp collisions at $\sqrt{s} = 13$ TeV with the ATLAS detector. *Eur. Phys. J.*, C77(6):361, 2017.

[170] ATLAS Collaboration. Searches for scalar leptoquarks and differential cross-section measurements in dilepton-dijet events in proton-proton collisions at a centre-of-mass energy of $\sqrt{s}$ = 13 TeV with the ATLAS experiment. *Eur. Phys. J.*, C79(9):733, 2019.

[171] ATLAS Collaboration. Search for pair production of vector-like quarks in final states with at least one Z boson decaying into a pair of electrons or muons in pp-collision data collected with the ATLAS detector at $\sqrt{s}$ = 13 TeV. *Physical Review D*, 98(11), Dec 2018.

[172] ATLAS Collaboration. Search for pair production of heavy vector-like quarks decaying into hadronic final states in pp collisions at $\sqrt{s}$ = 13 TeV with the ATLAS detector. *Physical Review D*, 98(9), Nov 2018.

[173] ATLAS Collaboration. Search for pair production of heavy vector-like quarks decaying into high-p_T W bosons and top quarks in the lepton-plus-jets final state in pp collisions at $\sqrt{s}$ = 13 TeV with the ATLAS detector. *Journal of High Energy Physics*, 2018(8), Aug 2018.

[174] ATLAS Collaboration. Search for new phenomena in events with same-charge leptons and b-jets in pp collisions at $\sqrt{s}$ = 13 TeV with the ATLAS detector. *Journal of High Energy Physics*, 2018(12), Dec 2018.

[175] ATLAS Collaboration. Search for pair production of up-type vector-like quarks and for four-top-quark events in final states with multiple b-jets with the ATLAS detector. *Journal of High Energy Physics*, 2018(7), Jul 2018.

[176] ATLAS Collaboration. Search for pair production of vector-like top quarks in events with one lepton, jets, and missing transverse momentum in $\sqrt{s}$ = 13 TeV TeV pp collisions with the ATLAS detector. *Journal of High Energy Physics*, 2017(8), Aug 2017.

[177] ATLAS Collaboration. Search for pair production of heavy vector-like quarks decaying to high-p_T W bosons and b quarks in the lepton-plus-jets final state in pp collisions at $\sqrt{s}$ = 13 TeV with the ATLAS detector. *Journal of High Energy Physics*, 2017(10), Oct 2017.

[178] ATLAS Collaboration. Measurements of electroweak Wjj production and constraints on anomalous gauge couplings with the ATLAS detector. *Eur. Phys. J.*,

C77(7):474, 2017.

[179] ATLAS Collaboration. Measurements of $t\bar{t}$ differential cross-sections of highly boosted top quarks decaying to all-hadronic final states in pp collisions at $\sqrt{s} = 13$ TeV using the ATLAS detector. *Phys. Rev.*, D98(1):012003, 2018.

[180] CMS Collaboration. Measurement of differential cross sections for the production of top quark pairs and of additional jets in lepton+jets events from pp collisions at $\sqrt{s} = 13$ TeV. *Phys. Rev.*, D97(11):112003, 2018.

[181] CMS Collaboration. Measurement of differential cross sections for top quark pair production using the lepton+jets final state in proton-proton collisions at 13 TeV. *Phys. Rev.*, D95(9):092001, 2017.

[182] CMS Collaboration. Measurements of differential cross sections of top quark pair production as a function of kinematic event variables in proton-proton collisions at $\sqrt{s} = 13$ TeV. *Journal of High Energy Physics*, 06:002, 2018.

[183] Yasuhiro Okada and Luca Panizzi. LHC signatures of vector-like quarks, 2012. `https://arxiv.org/abs/1207.5607`.

[184] L. Panizzi. Vector-like quarks: t' and partners. *Nuovo Cim. C*, 037(02):69–79, 2014.

[185] Mathieu Buchkremer, Giacomo Cacciapaglia, Aldo Deandrea, and Luca Panizzi. Model Independent Framework for Searches of Top Partners. *Nucl. Phys.*, B876:376–417, 2013.

[186] S. Schael et al. Precision electroweak measurements on the Z resonance. *Phys. Rept.*, 427:257–454, 2006.

[187] Albert M. Sirunyan et al. Measurements of the differential jet cross section as a function of the jet mass in dijet events from proton-proton collisions at $\sqrt{s} = 13$ TeV. *Journal of High Energy Physics*, 11:113, 2018.

[188] ATLAS Collaboration. Measurement of inclusive jet and dijet cross-sections in proton-proton collisions at $\sqrt{s} = 13$ TeV with the ATLAS detector. *Journal of High Energy Physics*, 05:195, 2018.

[189] ATLAS Collaboration. Measurements of differential cross sections of top quark pair production in association with jets in pp collisions at $\sqrt{s} = 13$ TeV using the ATLAS detector. *Journal of High Energy Physics*, 10:159, 2018.

[190] ATLAS Collaboration. Measurements of top-quark pair differential cross-sections in the lepton+jets channel in pp collisions at $\sqrt{s} = 13$ TeV using the ATLAS

detector. *Journal of High Energy Physics*, 11:191, 2017.

[191] ATLAS Collaboration. Measurements of inclusive and differential fiducial cross-sections of $t\bar{t}$ production with additional heavy-flavour jets in proton-proton collisions at $\sqrt{s} = 13$ TeV with the ATLAS detector. *Journal of High Energy Physics*, 04:046, 2019.

[192] CMS Collaboration. Measurements of differential Z boson production cross sections in proton-proton collisions at $\sqrt{s} = 13$ TeV. *Journal of High Energy Physics*, 2019(12), Dec 2019.

[193] A. M. Sirunyan, A. Tumasyan, W. Adam, F. Ambrogi, E. Asilar, T. Bergauer, J. Brandstetter, E. Brondolin, M. Dragicevic, and et al. Measurement of differential cross sections for z boson production in association with jets in proton-proton collisions at $\sqrt{s} = 13\,\mathrm{TeV}$. *The European Physical Journal C*, 78(11), Nov 2018.

[194] Nicholas Pollard. *B-L and Other U(1) Extensions of the Standard Model*. PhD thesis, UC, Riverside, 2017.

[195] Nobuchika Okada and Satomi Okada. Z'-portal right-handed neutrino dark matter in the minimal $\mathrm{U}(1)_X$ extended Standard Model. *Phys. Rev. D*, 95:035025, Feb 2017.

[196] Alexander L. Read. Presentation of search results: The CL(s) technique. *J. Phys. G*, 28:2693–2704, 2002.

[197] Andy Buckley. The hepthesis LaTeX class. `https://ctan.org/pkg/hepthesis?lang=en`.

List of figures

2.1. The particle content in the Standard Model. Included in the diagram is the graviton, however this is currently outside the scopes of the SM. This figure is from Ref. [5]. 5

2.2. Illustration of the Higgs potential. There is an infinite number of ground states. At point A, the global symmetry is unbroken. At point B, a local minimum is chosen and spontaneous symmetry breaking occurs. This figure is from Ref. [10]. 12

3.1. The CERN accelerator complex 22

3.2. Pile-up distributions. 25

3.3. The coordinate system used at the LHC in the perspective of the CMS experiment. Figure taken from [18]. 26

3.4. The ATLAS detector and its sub-components. This figure is from Ref. [19]. 27

3.5. Cross-sectional view of the calorimetry system in the ATLAS detector. This figure is from Ref. [27]. 30

3.6. A section view of the ATLAS Muon Spectrometer and its sub-components. This figure is from Ref. [34] 33

3.7. Schematic representation of the ATLAS magnet system. This Figure is from Ref. [36]. 34

3.8. Drawn in blue is the particle track, with the transverse and longitudinal impact parameters illustrated on the left and right graph respectively. The primary vertex (P.V.) is defined to be at the origin. 37

3.9. Simulated 4 lepton invariant mass distributions using the super-cluster (SC) and sliding window (SW) algorithms, in the $4e$ channel. This figure is from Ref. [46]. 39

3.10. Cross-sectional view of the ATLAS detector and how muon types are identified. The inner black lines represent the inner detector, the yellow is the calorimeter, and the outer blue lines are the muon spectrometer. This figure is adapted from [54]. 43

4.1. Breakdown of contributing processes in the $m_{4\ell}$ distribution as modelled by Monte Carlo simulation are shown in the solid coloured lines. The total of all processes is represented by the dotted black line. 47

4.2. Feynman diagrams for quark- and gluon-induced ZZ production. The processes shown are the main contributors. This figure is from Ref. [67]. 47

4.3. This is a diagram of a simulated proton-proton collision. The hard collision is shown in the centre in red. In purple is the secondary hard scattering event. The parton shower is drawn in blue. Hadronisation is sketched in light green, and the subsequent hadron decays and final state particles are shown in dark green. Finally, the electromagnetic radiation is presented in yellow. This figure is from Reference [75]. 56

4.4. Observed reconstruction-level $m_{4\ell}$ distribution compared with the SM prediction, using SHERPA for the $q\bar{q} \to 4\ell$ simulation. The statistical uncertainty of the data is displayed as error bars and systematic uncertainties in the prediction are shown as a grey hashed band. The ratio of the data to the prediction is shown in the lower panel. The x-axis is on a linear scale until $m_{4\ell} = 225$ GeV, where it switches to a logarithmic scale, as indicated by the double dashes on the axis. There is one additional data event reconstructed with $m_{4\ell} = 2.14$ TeV, while 0.4 events are expected from simulation for $m_{4\ell} > 2$ TeV. This figure is from Ref. [67]. 63

4.5. In the left-hand panel, the number of predicted events passing the reconstruction- and fiducial- level selections are displayed as the detector yield and particle yield, respectively. They are given as a function of inclusive $m_{4\ell}$ bins. The right-hand panel shows the efficiency, fiducial purity and fiducial fraction in each of the same $m_{4\ell}$ bins. 68

4.6. Migration matrix for the inclusive $m_{4\ell}$ distribution. 68

4.7. Migration matrices for the four $m_{4\ell}$ regions between the slices. 69

4.8. In the top panel is the effect of the pre-unfolding weights on the predicted detector level (also called reco level) yield, compared to the particle level yield. The bottom panel shows the reconstruction efficiency with and without application of the pre-unfolding weights. The pre-unfolding weights brings the detector yield closer to the particle yield, consequently the efficiency is much higher. 73

4.9. Monte Carlo closure tests performed on all bins in the inclusive $m_{4\ell}$ distribution. The top figure uses the full MC to unfold itself. The bottom figure splits the MC in half, and uses one set to unfold the other. The pink hash in 4.9b is the MC statistical uncertainty. Closure is achieved in all bins. 76

4.10. This figure shows the results of the BSM signal injection studies performed on the $m_{4\ell}$ distribution. Six BSM models are considered, with resonance masses at 300 GeV, 800 GeV, and 1400 GeV, and with narrow widths or a width 15% of the resonance mass. The cross-sections correspond to a 2σ signal significant with respect to the data uncertainty. Two unfolded distributions are shown with and without pre-unfolding (pre-UF) weights applied. The bottom panel shows the size of the bias. . 79

4.11. This figure shows the results of the enhanced $gg \to Z^{(*)}Z^{(*)}$ injection studies performed on the $m_{4\ell}$ distribution. The nominal $gg \to Z^{(*)}Z^{(*)}$ contribution is enhanced by 1.1–10 times. Two unfolded distributions are shown with and without pre-unfolding (pre-UF) weights applied. The bottom panel shows the size of the bias. 80

4.12. Unfolded systematics for the inclusive $m_{4\ell}$ spectrum. The data statistical uncertainty is the dominant source in all but the third bin. This figure is from Ref. [67] 82

4.13. Differential cross-section as a function of the four-lepton invariant mass $m_{4\ell}$as measured in data in black. The error bars on the data points give the total uncertainty and the grey hashed band illustrates the contribution from the systematic uncertainty. The SM predictions use either SHERPA or POWHEG + PYTHIA8 to model the $q\bar{q} \rightarrow 4\ell$ contribution, plotted in red and blue respectively. The uncertainties on the SM predictions are represented by the red and blue hash. The coloured stacked histograms represent the per-process breakdown of the SM prediction. In the lower left corner of the figure, boundary lines are drawn to indicate the four different $m_{4\ell}$ regions, each dominated by a different process. The p-value is the probability for the χ^2 to have at least the observed value, assuming the SM prediction. The number of degrees of freedom is the number of bins in the histogram. The ratio of the SHERPA and POWHEG prediction to the data is shown in the lower panel. The x-axis is on a linear scale until $m_{4\ell} = 216$ GeV, where it switches to a logarithmic scale. 88

4.14. Differential cross-section as a function of $m_{4\ell}$ in slices of $p_{\mathrm{T},4\ell}$. The error bars on the data points give the total uncertainty and the grey hashed band illustrates the contribution from the systematic uncertainty. The SM predictions use either SHERPA or POWHEG + PYTHIA8 to model the $q\bar{q} \rightarrow 4\ell$ contribution, plotted in red and blue respectively. The uncertainties on the SM predictions are represented by the red and blue hash. The p-value is the probability for the χ^2 to have at least the observed value, assuming the SM prediction. The number of degrees of freedom is the number of bins in the histogram. The ratio of the SHERPA prediction to the data is shown in the lower panel. 90

4.15. Differential cross-section as a function of $m_{4\ell}$ in slices of $y_{4\ell}$. The error bars on the data points give the total uncertainty and the grey hashed band illustrates the contribution from the systematic uncertainty. The SM predictions use either SHERPA or POWHEG + PYTHIA8 to model the $q\bar{q} \rightarrow 4\ell$ contribution, plotted in red and blue respectively. The uncertainties on the SM predictions are represented by the red and blue hash. The p-value is the probability for the χ^2 to have at least the observed value, assuming the SM prediction. The number of degrees of freedom is the number of bins in the histogram. The ratio of the SHERPA prediction to the data is shown in the lower panel. 91

4.16. Differential cross-section as a function of $m_{4\ell}$ for each lepton flavour channel. The error bars on the data points give the total uncertainty and the grey hashed band illustrates the contribution from the systematic uncertainty. The SM predictions use either SHERPA or POWHEG + PYTHIA8 to model the $q\bar{q} \to 4\ell$ contribution, plotted in red and blue respectively. The uncertainties on the SM predictions are represented by the red and blue hash. The p-value is the probability for the χ^2 to have at least the observed value, assuming the SM prediction. The number of degrees of freedom is the number of bins in the histogram. The ratio of the SHERPA prediction to the data is shown in the lower panel. The x-axis is on a linear scale until $m_{4\ell} = 225$ GeV, where it switches to a logarithmic scale. 92

4.17. Differential cross-section as a function of m_{12} in the four $m_{4\ell}$ regions. The error bars on the data points give the total uncertainty and the grey hashed band illustrates the contribution from the systematic uncertainty. The SM predictions use either SHERPA or POWHEG + PYTHIA8 to model the $q\bar{q} \to 4\ell$ contribution, plotted in red and blue respectively. The uncertainties on the SM predictions are represented by the red and blue hash. The p-value is the probability for the χ^2 to have at least the observed value, assuming the SM prediction. The number of degrees of freedom is the number of bins in the histogram. The ratio of the SHERPA prediction to the data is shown in the lower panel. In (b) the contribution from Higgs production is shown in addition to the total SM prediction. 93

4.18. Differential cross-section as a function of m_{34} in the four $m_{4\ell}$ regions. The measured data (black points) are compared with the SM prediction using either SHERPA (red, with red hashed band for the uncertainty) or POWHEG + PYTHIA8 (blue, with blue hashed band for the uncertainty) to model the $q\bar{q} \to 4\ell$ contribution. In (b) the contribution from Higgs production is shown in addition to the total SM prediction. The error bars on the data points give the total uncertainty and the grey hashed band gives the systematic uncertainty. The p-value is the probability for the χ^2 to have at least the observed value, assuming the SM prediction. The number of degrees of freedom is the number of bins in the histogram. The lower panel shows the ratio of the SM predictions to the data. 94

4.19. Differential cross-section as a function of $p_{\mathrm{T},12}$ in the four $m_{4\ell}$ regions. The measured data (black points) are compared with the SM prediction using either SHERPA (red, with red hashed band for the uncertainty) or POWHEG + PYTHIA8 (blue, with blue hashed band for the uncertainty) to model the $q\bar{q} \rightarrow 4\ell$ contribution. In (b) the contribution from Higgs production is shown in addition to the total SM prediction. The error bars on the data points give the total uncertainty and the grey hashed band gives the systematic uncertainty. The p-value is the probability for the χ^2 to have at least the observed value, assuming the SM prediction. The number of degrees of freedom is the number of bins in the histogram. The lower panel shows the ratio of the SM predictions to the data. 95

4.20. Differential cross-section as a function of $p_{\mathrm{T},34}$ in the four $m_{4\ell}$ regions. The measured data (black points) are compared with the SM prediction using either SHERPA (red, with red hashed band for the uncertainty) or POWHEG + PYTHIA8 (blue, with blue hashed band for the uncertainty) to model the $q\bar{q} \rightarrow 4\ell$ contribution. The error bars on the data points give the total uncertainty and the grey hashed band gives the systematic uncertainty. The p-value is the probability for the χ^2 to have at least the observed value, assuming the SM prediction. The number of degrees of freedom is the number of bins in the histogram. The lower panel shows the ratio of the SM predictions to the data. 96

4.21. Differential cross-section as a function of $\cos\theta^*_{12}$ in the four $m_{4\ell}$ regions. The measured data (black points) are compared with the SM prediction using either SHERPA (red, with red hashed band for the uncertainty) or POWHEG + PYTHIA8 (blue, with blue hashed band for the uncertainty) to model the $q\bar{q} \rightarrow 4\ell$ contribution. The error bars on the data points give the total uncertainty and the grey hashed band gives the systematic uncertainty. The p-value is the probability for the χ^2 to have at least the observed value, assuming the SM prediction. The number of degrees of freedom is the number of bins in the histogram. The lower panel shows the ratio of the SM predictions to the data. 97

4.22. Differential cross-section as a function of $\cos\theta^*_{34}$ in the four $m_{4\ell}$ regions. The measured data (black points) are compared with the SM prediction using either SHERPA (red, with red hashed band for the uncertainty) or POWHEG + PYTHIA8 (blue, with blue hashed band for the uncertainty) to model the $q\bar{q} \to 4\ell$ contribution. The error bars on the data points give the total uncertainty and the grey hashed band gives the systematic uncertainty. The p-value is the probability for the χ^2 to have at least the observed value, assuming the SM prediction. The number of degrees of freedom is the number of bins in the histogram. The lower panel shows the ratio of the SM predictions to the data. 98

4.23. Differential cross-section as a function of $|\Delta\phi_{\ell\ell}|$ in the four $m_{4\ell}$ regions. The measured data (black points) are compared with the SM prediction using either SHERPA (red, with red hashed band for the uncertainty) or POWHEG + PYTHIA8 (blue, with blue hashed band for the uncertainty) to model the $q\bar{q} \to 4\ell$ contribution. The error bars on the data points give the total uncertainty and the grey hashed band gives the systematic uncertainty. The p-value is the probability for the χ^2 to have at least the observed value, assuming the SM prediction. The number of degrees of freedom is the number of bins in the histogram. The lower panel shows the ratio of the SM predictions to the data. 99

4.24. Differential cross-section as a function of $|\Delta\phi_{\text{pairs}}|$ in the four $m_{4\ell}$ regions. The measured data (black points) are compared with the SM prediction using either SHERPA (red, with red hashed band for the uncertainty) or POWHEG + PYTHIA8 (blue, with blue hashed band for the uncertainty) to model the $q\bar{q} \to 4\ell$ contribution. The error bars on the data points give the total uncertainty and the grey hashed band gives the systematic uncertainty. The p-value is the probability for the χ^2 to have at least the observed value, assuming the SM prediction. The number of degrees of freedom is the number of bins in the histogram. The lower panel shows the ratio of the SM predictions to the data. 100

4.25. Differential cross-section as a function of $|\Delta y_{\text{pairs}}|$ in the four $m_{4\ell}$ regions. The measured data (black points) are compared with the SM prediction using either SHERPA (red, with red hashed band for the uncertainty) or POWHEG + PYTHIA8 (blue, with blue hashed band for the uncertainty) to model the $q\bar{q} \to 4\ell$ contribution. The error bars on the data points give the total uncertainty and the grey hashed band gives the systematic uncertainty. The p-value is the probability for the χ^2 to have at least the observed value, assuming the SM prediction. The number of degrees of freedom is the number of bins in the histogram. The lower panel shows the ratio of the SM predictions to the data. 101

4.26. The expected and observed confidence intervals at 95% CL for the SMEFT Wilson coefficients, which are in units of TeV^2 for only the linear terms. The multiplicative number shown to the right of plotted points indicates a scaling factor that is applied to the limit for the purpose of the plot, in order to show all coefficients on the same scale. The most sensitive observable indicated for each coefficient is used for the constraints. Only one coefficient is fitted at a time, with all others set to zero. This figure is from Ref. [67] 110

4.27. The expected and observed confidence intervals at 95% CL for the SMEFT Wilson coefficients, which are in units of TeV^2 for the full model. The multiplicative number shown to the right of plotted points indicates a scaling factor that is applied to the limit for the purpose of the plot, in order to show all coefficients on the same scale. The most sensitive observable indicated for each coefficient is used for the constraints. Only one coefficient is fitted at a time, with all others set to zero. . This figure is from Ref. [67] 111

5.1. An simplified schematic of the CONTUR workflow. The dotted box denotes the portion of the workflow that makes extensive use of external packages, affording multiple options, such as the choice of MC event generator. The next stage is the taking of physics observables as inputs to a statistical analysis (i.e. evaluating the likelihood for the model). Finally the last stage involves using tools to visualize the output of the likelihood analysis. Figure taken from Reference [157] 116

5.2. Leading-order Feynman diagrams for production of VLQs Q. The top row (a–c) shows VLQ pair-production diagrams via strong and EM interactions, which do not depend on κ. The second row (d–e) shows pair-production of VLQs via a weak boson $V \in \{W, Z, H\}$, which may lead to different-flavoured VLQs in the final state. The third row (f–i) shows single-production of Q in association with a weak boson or SM quark q. All Feynman diagrams are from Reference [1]. 119

5.3. Leading-order cross-sections extracted from Herwig for production of a TT pair as a function of M_Q and κ, for 13 TeV pp collisions, in the $W{:}Z{:}H = \frac{1}{2}{:}\frac{1}{4}{:}\frac{1}{4}$ scenario, assuming couplings to individual generations of quarks. The white lines indicate the contours for production cross-sections in multiples of 10. The first-generation cross-sections acquire a dependence on κ since pair-production initiated by proton valence quarks becomes possible. The situation is analogous for other VLQ flavours, although somewhat attenuated for X and Y since they still require at least one antiquark from the sea to be produced via W exchange in the t-channel. These figures are from Reference [1]. 120

5.4. Leading-order cross-sections extracted from Herwig for production of a T and Y with a weak boson as a function of M_Q and κ, for 13 TeV pp collisions, in the $W{:}Z{:}H = \frac{1}{2}{:}\frac{1}{4}{:}\frac{1}{4}$ scenario, assuming couplings to individual generations of quarks. The white lines indicate the contours for production cross-sections in multiples of 10. First-generation couplings lead to higher production cross-sections, as a result of valence-quark-induced diagrams, while second and third-generation couplings lead to suppressed production rates, according to the relevant quark PDFs. This figure is from Reference [1]. 121

5.5. Leading-order cross-sections extracted from Herwig for production of a T and X with a SM quark as a function of M_Q and κ, for 13 TeV pp collisions, in the W:Z:H $= \frac{1}{2}$:$\frac{1}{4}$:$\frac{1}{4}$ scenario, assuming couplings to individual generations of quarks. The white lines indicate the contours for production cross-sections in multiples of 10. First-generation couplings lead to higher production cross-sections, as a result of valence-quark-induced diagrams, while second and third-generation couplings lead to suppressed production rates, according to the relevant quark PDFs. $X + q$ production goes from being the dominant production process at the LHC if X couples to first-generation quarks only, to vanishing if X couples to third-generation quarks only. White cells indicate corners of phase-space where the process in question is highly subdominant, and therefore where the cross-section was not sampled during the Herwig run. This figure is from Reference [1]. 122

5.6. Sensitivity of LHC measurements to a B-production for $M_B = 1200$ GeV and b T-production for $M_T = 1350$ GeV. The CONTUR exclusion is shown in the bins in which it is evaluated, graduated from yellow through green to black on a linear scale, with the 95% CL (solid white) and 68% CL (dashed white) exclusion contours superimposed. The mauve region is excluded at 95% CL by the ATLAS combination [166]. This figure is from Reference [1]. 123

5.7. Dominant LHC analysis pools contributing to VLQ limit-setting in the κ vs VLQ mass plane, where κ is the coupling to first-generation SM quarks. All VLQ (B, T, X, Y) masses are set to be degenerate. The disfavoured regions are located above and to the left of the dashed (68% CL) and solid (95% CL) white contours respectively. The lower bounds in κ from non-LHC flavour physics are indicated with the pink horizontal contour. The VLQ branching fractions to W:Z:H are a 0:0:1 b 0:1:0 c 1:0:0 and d $\frac{1}{2}$:$\frac{1}{4}$:$\frac{1}{4}$. This figure is from Reference [1]. 126

5.8. ATLAS 8TeV Wjj forward-lepton control region leading-jet p_T distributions at three points on the 95% exclusion contour for W:Z:H $=$ 1:0:0, respectively at M_Q values of a 1000 GeV, b 1750 GeV, and c 2250 GeV. The rise and subsidence of a 90% $\mathrm{CL_s}$ exclusion from a single Wjj bin is seen as the contour passes from below 1 TeV to above 2 TeV. The black points are data, the red histogram is the VLQ contribution stacked on top of the data. In the lower insets, the ratio is shown and the yellow band indicates the significance, taking into account the statistical and systematic uncertainties on the data. The legend gives the exclusion (i.e. one minus the p-value) for that histogram after fitting nuisance parameters for the correlated systematic uncertainties. This figure is from Reference [1]. . . 127

5.9. Dominant LHC analysis pools contributing to VLQ limit-setting in the κ vs VLQ mass plane, where κ is the coupling to second-generation SM quarks. All VLQ (B, T, X, Y) masses are set to be degenerate. The disfavoured regions are located above and to the left of the dashed (68% CL) and solid (95% CL) white contours respectively. The lower bounds in κ from non-LHC flavour physics are indicated with the pink horizontal contour. The VLQ branching fractions to W:Z:H are a 0:0:1 b 0:1:0 c 1:0:0 and d $\frac{1}{2}$:$\frac{1}{4}$:$\frac{1}{4}$. This figure is from Reference [1]. 128

5.10. Dominant LHC analysis pools contributing to VLQ limit-setting in the κ vs VLQ mass plane, where κ is the coupling to third-generation SM quarks. All VLQ (B, T, X, Y) masses are set to be degenerate. The disfavoured regions are located above and to the left of the dashed (68% CL) and solid (95% CL) white contours respectively. The VLQ branching fractions to W:Z:H are a 0:0:1 b 0:1:0 c 1:0:0 and d $\frac{1}{2}$:$\frac{1}{4}$:$\frac{1}{4}$. This figure is from Reference [1]. 130

5.11. Dominant LHC analysis pools contributing to VLQ limit-setting in the κ vs VLQ mass plane, where κ is the coupling to third-generation SM quarks. All VLQ (B, T, X, Y) masses are set to be degenerate. The disfavoured regions are located above and to the left of the dashed (68% CL) and solid (95% CL) white contours respectively. The VLQ branching fraction to W:Z:H is 0:1:0. Plots are made with CONTUR 2.1.x and RIVET 3.1.4. 132

5.12. CONTUR exclusion (a) without and (b) with new four-lepton measurement. The disfavoured regions at 95% CL and 68% CL are shaded in yellow and green respectively. 133

5.13. ATLAS 13 TeV four-lepton measurement at (a) 36.1 fb^{-1} and (b) 139 fb^{-1} at $M_Q = 1237$ GeVand $\kappa = 0.05$. The black points are data, the red histogram is the VLQ contribution stacked on top of the data, and the green histogram is the SM prediction. In the lower insets, the ratio is shown and the yellow band indicates the significance, taking into account the statistical and systematic uncertainties on the data. The legend gives the exclusion (i.e. one minus the p-value) for that histogram. 135

5.14. ATLAS result from the $m_{4\ell}$ measurement. Limits set on the B-L model using only the inclusive $m_{4\ell}$ variable. The red line shows the observed exclusion and the solid black line shows the expected exclusion, with the dashed black lines indicating the $\pm 1\sigma$ and $\pm 2\sigma$ uncertainty bands. The region above and to the left of the lines is excluded, up to the grey band, which shows the region $m_{h_2} < 2m_{Z'}$, where the four-lepton final state has no sensitivity. This figure is from Reference [67]. 138

5.15. ATLAS result from the $m_{4\ell}$ measurement. Limits set on the B-L model using the most sensitive variable. The red line shows the observed exclusion and the solid black line shows the expected exclusion, with the dashed black lines indicating the $\pm 1\sigma$ and $\pm 2\sigma$ uncertainty bands. The region above and to the left of the lines is excluded, up to the grey band, which shows the region $m_{h_2} < 2m_{Z'}$, where the four-lepton final state has no sensitivity. This figure is from Reference [67]. 138

5.16. ATLAS result from the $m_{4\ell}$ measurement. This colour map shows the B-L model space and the most sensitive variable at each point used to set the limit. This figure is from Reference [67]. 139

5.17. (a) Dominant LHC analysis pools contributing to the exclusion limit set for the gauged $B-L$ model in M_{h_2} vs $\sin\alpha$ plane, where $g_1' = 0.001$ and $M_{Z'} = 35$ GeV. The disfavoured regions are located above and to the left of the dashed (68% CL) and solid (95% CL) white contours respectively. Plot is made with CONTUR 2.1.x and RIVET 3.1.4. (b) The corresponding heatmap from Figure 6b of Reference [2]. The disfavoured regions at 95% CL and 68% CL are shaded in yellow and green respectively. The constraints from perturbativity up to a scale of at least 10 TeV, and from W mass measurements are also shown. 141

5.18. CONTUR exclusion (a) without and (b) with the new four-lepton measurement. The disfavoured regions at 95% CL and 68% CL are shaded in yellow and green respectively. 142

5.19. The most sensitive distribution from the ATLAS four-lepton measurement contributing to the limit is indicated in colour for the gauged $B-L$ model in M_{h_2} vs $\sin\alpha$ plane, where $g_1' = 0.001$ and $M_{Z'} = 35$ GeV. 142

5.20. (a) Dominant LHC analysis pools contributing to the exclusion limit set for the gauged $B-L$ model in $M_{Z'}$ vs g_1' plane, where $\sin\alpha = 0.2$ and $M_{h_2} = 200$ GeV. The disfavoured regions are located above and to the left of the dashed (68% CL) and solid (95% CL) white contours respectively. Plot is made with CONTUR 2.1.x and RIVET 3.1.4. (b) The corresponding heatmap from Figure 5c of Reference [2]. The disfavoured regions at 95% CL and 68% CL are shaded in yellow and green respectively. The constraints from perturbativity up to a scale of at least 10 TeV, and from electron-neutrino scattering, are also indicated. 143

A.1. In the left-hand panels, the number of predicted events passing the reconstruction- and fiducial- level selections are displayed as the detector yield and particle yield, respectively. The right-hand panel shows the efficiency, fiducial purity and fiducial fraction. All variables are plotted as a function of the $m_{4\ell}$bins, in slices of the $p_{\mathrm{T},4\ell}$variable which are stacked and labelled with the included $p_{\mathrm{T},4\ell}$range. 148

A.2. In the left-hand panels, the number of predicted events passing the reconstruction- and fiducial- level selections are displayed as the detector yield and particle yield, respectively. The right-hand panel shows the efficiency, fiducial purity and fiducial fraction. All variables are plotted as a function of the $m_{4\ell}$bins, in slices of the $y_{4\ell}$variable which are stacked and labelled with the included $y_{4\ell}$range. 149

A.3. In the left-hand panels, the number of predicted events passing the reconstruction- and fiducial- level selections are displayed as the detector yield and particle yield, respectively. The right-hand panel shows the efficiency, fiducial purity and fiducial fraction. All variables are plotted as a function of the $m_{4\ell}$bins, in the $4e$, 4μ and $2e2\mu$ flavour channels from top to bottom. 150

A.4. In the left-hand panels, the number of predicted events passing the reconstruction- and fiducial- level selections are displayed as the detector yield and particle yield, respectively. The right-hand panel shows the efficiency, fiducial purity and fiducial fraction. All variables are plotted as a function of the m_{12} bins, in slices of the $m_{4\ell}$variable which are stacked and labelled with the included $m_{4\ell}$range. 151

A.5. In the left-hand panels, the number of predicted events passing the reconstruction- and fiducial- level selections are displayed as the detector yield and particle yield, respectively. The right-hand panel shows the efficiency, fiducial purity and fiducial fraction. All variables are plotted as a function of the m_{34} bins, in slices of the $m_{4\ell}$variable which are stacked and labelled with the included $m_{4\ell}$range. 152

A.6. In the left-hand panels, the number of predicted events passing the reconstruction- and fiducial- level selections are displayed as the detector yield and particle yield, respectively. The right-hand panel shows the efficiency, fiducial purity and fiducial fraction. All variables are plotted as a function of the $p_{\mathrm{T},12}$bins, in slices of the $m_{4\ell}$variable which are stacked and labelled with the included $m_{4\ell}$range. 153

A.7. In the left-hand panels, the number of predicted events passing the reconstruction- and fiducial- level selections are displayed as the detector yield and particle yield, respectively. The right-hand panel shows the efficiency, fiducial purity and fiducial fraction. All variables are plotted as a function of the $p_{\mathrm{T},34}$bins, in slices of the $m_{4\ell}$variable which are stacked and labelled with the included $m_{4\ell}$range. 154

A.8. In the left-hand panels, the number of predicted events passing the reconstruction- and fiducial- level selections are displayed as the detector yield and particle yield, respectively. The right-hand panel shows the efficiency, fiducial purity and fiducial fraction. All variables are plotted as a function of the $\cos\theta^*$bins, in slices of the $m_{4\ell}$variable which are stacked and labelled with the included $m_{4\ell}$range. 155

A.9. In the left-hand panels, the number of predicted events passing the reconstruction- and fiducial- level selections are displayed as the detector yield and particle yield, respectively. The right-hand panel shows the efficiency, fiducial purity and fiducial fraction. All variables are plotted as a function of the $\cos\theta^*$bins, in slices of the $m_{4\ell}$variable which are stacked and labelled with the included $m_{4\ell}$range. 156

A.10.In the left-hand panels, the number of predicted events passing the reconstruction- and fiducial- level selections are displayed as the detector yield and particle yield, respectively. The right-hand panel shows the efficiency, fiducial purity and fiducial fraction. All variables are plotted as a function of the $|\Delta\phi_{\mathrm{pairs}}|$ bins, in slices of the $m_{4\ell}$variable which are stacked and labelled with the included $m_{4\ell}$range. 157

A.11.In the left-hand panels, the number of predicted events passing the reconstruction- and fiducial- level selections are displayed as the detector yield and particle yield, respectively. The right-hand panel shows the efficiency, fiducial purity and fiducial fraction. All variables are plotted as a function of the $|\Delta y_{\mathrm{pairs}}|$bins, in slices of the $m_{4\ell}$variable which are stacked and labelled with the included $m_{4\ell}$range. 158

A.12.In the left-hand panels, the number of predicted events passing the reconstruction- and fiducial- level selections are displayed as the detector yield and particle yield, respectively. The right-hand panel shows the efficiency, fiducial purity and fiducial fraction. All variables are plotted as a function of the $|\Delta\phi_{\ell\ell}|$ bins, in slices of the $m_{4\ell}$variable which are stacked and labelled with the included $m_{4\ell}$range. 159

A.13.Migration matrices for the four $m_{4\ell}$regions between the slices. 160

A.14.Migration matrices for the $m_{4\ell}$bins in each $p_{\mathrm{T},4\ell}$slice of the $m_{4\ell}$-$p_{\mathrm{T},4\ell}$distribution and between the slices. 161

A.15.Migration matrices for the $m_{4\ell}$bins in each $y_{4\ell}$slice of the $m_{4\ell}$-$y_{4\ell}$distribution and between the slices. 162

A.16.Migration matrices for the $m_{4\ell}$bins in each flavour slice and between the flavour slices of the $m_{4\ell}$-lepton flavour distribution (where no migration is seen, as expected). 163

A.17.Migration matrices for the m_{12} bins in each of the $m_{4\ell}$slices of the m_{12}-$m_{4\ell}$distribution and between the slices. 164

A.18.Migration matrices for the m_{34} bins in each of the $m_{4\ell}$slices of the m_{34}-$m_{4\ell}$distribution and between the slices. 165

A.19.Migration matrices for the $p_{\mathrm{T},12}$bins in each of the $m_{4\ell}$slices of the $p_{\mathrm{T},12}$-$m_{4\ell}$distribution and between the slices. 166

A.20.Migration matrices of the $p_{\mathrm{T},34}$bins in each of the $m_{4\ell}$slices of the $p_{\mathrm{T},34}$-$m_{4\ell}$distribution and between the slices. 167

A.21.Migration matrices for the θ_1^* bins in each of the $m_{4\ell}$slices of the θ_1^*-$m_{4\ell}$distribution and between the slices. 168

A.22.Migration matrices for the θ_2^* bins in each of the $m_{4\ell}$slices of the θ_2^*-$m_{4\ell}$distribution and between the slices. 169

A.23.Migration matrix for the $|\Delta\phi_{\mathrm{pairs}}|$ bins in each of the $m_{4\ell}$slices of the $|\Delta\phi_{\mathrm{pairs}}|$-$m_{4\ell}$distribution and between the slices. 170

A.24.Migration matrices for the $|\Delta y_{\mathrm{pairs}}|$bins in each of the $m_{4\ell}$slices of the $|\Delta y_{\mathrm{pairs}}|$-$m_{4\ell}$distribution and between the slices. 171

A.25.Migration matrices for the $|\Delta\phi_{\ell\ell}|$ bins in each of the $m_{4\ell}$slices of the $|\Delta\phi_{\ell\ell}|$-$m_{4\ell}$distribution and between the slices. 172

A.26.Unfolded systematics versus $m_{4\ell}$, in slices of the final-state channel. . . . 173

A.27.Unfolded systematics versus $m_{4\ell}$, in slices of $p_{\mathrm{T},4\ell}$. 174

A.28.Unfolded systematics versus $m_{4\ell}$, in slices of $y_{4\ell}$. 175

A.29.Unfolded systematics versus $\cos\theta_1^*$, in slices of $m_{4\ell}$. 176

A.30.Unfolded systematics versus $\cos\theta_2^*$, in slices of $m_{4\ell}$. 177

A.31.Unfolded systematics versus $|\Delta\phi_{\ell\ell}|$, in slices of $m_{4\ell}$. 178

A.32.Unfolded systematics versus $|\Delta\phi_{\mathrm{pairs}}|$, in slices of $m_{4\ell}$. 179

A.33.Unfolded systematics versus $|\Delta y_{\mathrm{pairs}}|$, in slices of $m_{4\ell}$. 180

A.34.Unfolded systematics versus m_{12}, in slices of $m_{4\ell}$. 181

A.35.Unfolded systematics versus m_{34}, in slices of $m_{4\ell}$. 182

A.36.Unfolded systematics versus $p_{\mathrm{T},12}$, in slices of $m_{4\ell}$. 183

A.37.Unfolded systematics versus $p_{\mathrm{T},34}$, in slices of $m_{4\ell}$. 184

List of tables

4.1. Fiducial region definition at truth level. 49

4.2. The four $m_{4\ell}$ regions dominated by the single Z, Higgs, on-shell ZZ and off-shell ZZ processes. 51

4.3. Definition of the reconstruction-level event selection. This table is from Reference [66]. 53

4.4. Definition of the baseline lepton event selection. This Table is from Reference [66] 53

4.5. Definition of the signal lepton selection criteria applied to data. This table is from Reference [66]. 54

4.6. Predicted reconstruction-level yields per process and in total, compared with observed data counts, over the full fiducial phase space and in the following regions of $m_{4\ell}$: $Z \rightarrow 4\ell$ ($60 < m_{4\ell} < 100$ GeV), $H \rightarrow 4\ell$ ($120 < m_{4\ell} < 130$ GeV), off-shell ZZ ($20 < m_{4\ell} < 60$ GeV or $100 < m_{4\ell} < 120$ GeV or $130 < m_{4\ell} < 180$ GeV) and on-shell ZZ ($180 < m_{4\ell} < 2000$ GeV). The background row is events with non-prompt leptons, including those from $Z + Y$ events. The $H \rightarrow 4\ell$ row includes only the on-shell Higgs boson contribution, with off-shell contributions included in $gg \rightarrow 4\ell$. This table is from Reference [66]. 62

4.7. Efficiency correction taking into account the pre-unfolding weights and fiducial fraction for the full fiducial phase space and the $m_{4\ell}$ slices. The quoted uncertainties take into account the full set of systematics discussed in Section 4.9 67

4.8. Efficiency correction and fiducial fraction for the full fiducial phase space and the $m_{4\ell}$ slices, without the pre-unfolding weights applied. The quoted uncertainties take into account the full set of systematics discussed in Section 4.9 67

4.9. Two different versions of binning with varying event count and purity criteria. The nominal version is what is for the unfolded results. The high statistics version is used as a cross-check for interpretation studies. . . . 71

4.10. The binning used in the $m_{4\ell}$ distribution. Each bin satisfies the minimum number of events and purity criteria. The bins containing resonance peaks are symmetric around the peak. 72

4.11. Modifications made to the nominal SM prediction for injection studies. . 77

4.12. Uncertainties on the unfolded fiducial cross-section inclusively as well as in the four $m_{4\ell}$ slices studied in this analysis, split by source. Uncertainty contribution larger than 1% are marked in bold to guide the eye. This table is from Ref. [66]. 83

4.13. Fiducial cross-sections in the full fiducial phase space and in the $Z \to 4\ell$, $H \to 4\ell$, on-shell ZZ, and off-shell ZZ dominated regions in femtobarns. They are compared with two particle-level predictions and their uncertainties where the $q\bar{q} \to 4\ell$ process is simulated with either SHERPA or with POWHEG + PYTHIA8. 86

4.14. The expected and observed confidence intervals at 95% CL for the SMEFT Wilson coefficients, including both the linear and quadratic terms. The most sensitive observable indicated for each coefficient is used for the constraints. Only one coefficient is fitted at a time, with all others set to zero. This table is from Ref. [66]. 108

4.15. The expected and observed confidence intervals at 95% CL for the SMEFT Wilson coefficients, including only linear terms. The most sensitive observable indicated for each coefficient is used for the constraints. Only one coefficient is fitted at a time, with all others set to zero. This table is from Ref. [66]. 109

5.1. B-L model parameters set for scenario C of the gauge sector and scenario E of the scalar sector, as defined in Reference [2]. 136